Universität Potsdam

Properties and radiative effect of aerosol and cirrus clouds over the European Arctic

Dissertation with the aim of achieving the academic degree Doctor of Natural Sciences (Dr. rer. nat.) submitted to the Faculty of Science, Institute of Physics and Astronomy

by **Konstantina Nakoudi**

Potsdam, 3 December 2021

Konstantina Nakoudi
Properties and radiative effect of aerosol and cirrus clouds over the European Arctic,
© 3 December 2021
Reviewers: Prof. Dr. Markus Rex, Dr. Christoph Ritter, Prof. Dr. Lucas Alados–Arboledas

Published online on the
Publication Server of the University of Potsdam:
https://doi.org/10.25932/publishup-53036
https://nbn-resolving.org/urn:nbn:de:kobv:517-opus4-530366

DECLARATION

I hereby declare that I have conducted and written this thesis on my own, without contributions from other parties and with no other material than referenced. Graphics, quotes or ideas from other resources that are directly or indirectly included in this thesis, are unequivocally referenced to the original work. I moreover declare that this thesis has never been submitted for examination in this or in any other form.
Potsdam, 3 December 2021

Konstantina Nakoudi

ABSTRACT

Over the last decades, the rate of near-surface warming in the Arctic is at least double than elsewhere on our planet (*Arctic amplification*). However, the relative contribution of different feedback processes to *Arctic amplification* is a topic of ongoing research, including the role of aerosol and clouds. Lidar systems are well-suited for the investigation of aerosol and optically-thin clouds as they provide vertically-resolved information on fine temporal scales. Global aerosol models fail to converge on the sign of the Arctic aerosol radiative effect (ARE). In the first part of this work, the optical and microphysical properties of Arctic aerosol were characterized at case study level in order to assess the short-wave (SW) ARE. A long-range transport episode was first investigated. Geometrically similar aerosol layers were captured over three locations. Although the aerosol size distribution was different between Fram Strait (bi-modal) and Ny-Ålesund (fine mono-modal), the atmospheric column ARE was similar. The latter was related to the domination of *accumulation mode aerosol*. Over both locations top of the atmosphere (TOA) warming was accompanied by surface cooling.

Subsequently, the sensitivity of ARE was investigated with respect to different aerosol and spring-time ambient conditions. A 10% change in the single-scattering albedo (SSA) induced higher ARE perturbations compared to a 30% change in the aerosol extinction coefficient. With respect to ambient conditions, the ARE_{TOA} was more sensitive to solar elevation changes compared to $ARE_{surface}$. Over dark surfaces the ARE profile was exclusively negative, while over bright surfaces a negative to positive shift occurred above the aerosol layers. Consequently, the sign of ARE can be highly sensitive in spring since this season is characterized by transitional surface albedo conditions.

As the inversion of the aerosol microphysics is an ill-posed problem, the inferred aerosol size distribution of a low-tropospheric event was compared to the in-situ measured distribution. Both techniques revealed a bi-modal distribution, with good agreement in the total volume concentration. However, in terms of SSA a disagreement was found, with the lidar inversion indicating highly scattering particles and the in-situ measurements pointing to absorbing particles. The discrepancies could stem from assumptions in the inversion (e.g. wavelength-independent refractive index) and errors in the conversion of the in-situ measured light attenuation into absorption. Another source of discrepancy might be related to an incomplete capture of fine particles in the in-situ sensors. The disagreement in the most critical parameter for the Arctic ARE necessitates further exploration in the frame of aerosol closure experiments. Care must be taken in ARE modelling studies, which may use either the in-situ or lidar-derived SSA as input.

Reliable characterization of cirrus geometrical and optical properties is necessary for improving their radiative estimates. In this respect, the detection of sub-visible cirrus is of special importance. The total cloud radiative effect (CRE) can be negatively biased, should only the optically-thin and opaque cirrus contributions are considered. To this end, a cirrus retrieval

scheme was developed aiming at increased sensitivity to thin clouds. The cirrus detection was based on the wavelet covariance transform (WCT) method, extended by dynamic thresholds. The *dynamic WCT* exhibited high sensitivity to faint and thin cirrus layers (less than 200 m) that were partly or completely undetected by the existing static method. The optical characterization scheme extended the Klett–Fernald retrieval by an iterative lidar ratio (LR) determination (*constrained Klett*). The iterative process was constrained by a *reference value*, which indicated the aerosol concentration beneath the cirrus cloud. Contrary to existing approaches, the aerosol-free assumption was not adopted, but the aerosol conditions were approximated by an initial guess. The inherent uncertainties of the *constrained Klett* were higher for optically-thinner cirrus, but an overall good agreement was found with two established retrievals. Additionally, existing approaches, which rely on aerosol-free assumptions, presented increased accuracy when the proposed *reference value* was adopted. The *constrained Klett* retrieved reliably the optical properties in all cirrus regimes, including upper sub-visible cirrus with COD down to 0.02.

Cirrus is the only cloud type capable of inducing TOA cooling or heating at daytime. Over the Arctic, however, the properties and CRE of cirrus are under-explored. In the final part of this work, long-term cirrus geometrical and optical properties were investigated for the first time over an Arctic site (Ny-Ålesund). To this end, the newly developed retrieval scheme was employed. Cirrus layers over Ny-Ålesund seemed to be more absorbing in the visible spectral region compared to lower latitudes and comprise relatively more spherical ice particles. Such meridional differences could be related to discrepancies in absolute humidity and ice nucleation mechanisms. The COD tended to decline for less spherical and smaller ice particles probably due to reduced water vapor deposition on the particle surface. The cirrus optical properties presented weak dependence on ambient temperature and wind conditions. Over the 10 years of the analysis, no clear temporal trend was found and the seasonal cycle was not pronounced. However, winter cirrus appeared under colder conditions and stronger winds. Moreover, they were optically-thicker, less absorbing and consisted of relatively more spherical ice particles. A positive CRE^{net} was primarily revealed for a broad range of representative cloud properties and ambient conditions. Only for high COD (above 10) and over tundra a negative CRE^{net} was estimated, which did not hold true over snow/ice surfaces. Consequently, the COD in combination with the surface albedo seem to play the most critical role in determining the CRE sign over the high European Arctic.

ZUSAMMENFASSUNG

Seit den letzten Jahrzehnten erwärmt sich die arktische, oberflächennahe Luft mindestens doppelt so schnell, wie anderswo auf unserem Planeten (*arktische Verstärkung*). Der relative Beitrag verschiedener Rückkopplungsprozesse zu dieser *arktischen Verstärkung* ist ein Thema laufender Forschung, einschließlich der Rolle von Aerosol und Wolken. Lidarsysteme eignen sich gut zur Untersuchung von Aerosolen und optisch dünnen Wolken, da sie vertikal aufgelöste Informationen auf kurzen Zeitskalen liefern. Globale Aerosolmodelle können das Vorzeichen des Aerosolstrahlungseffekts (ARE) in der Arktis nicht erfassen. Im ersten Teil dieser Arbeit, wurden die optischen und mikrophysikalischen Eigenschaften des arktischen Aerosols auf Fallstudienebene charakterisiert, um das kurzwellige ARE zu bestimmen. Ein Ferntransportereignis von Aerosol wurde zuerst untersucht. An drei Standorten wurden geometrisch ähnliche Aerosolschichten erfasst. Obwohl die Aerosolgrößenverteilung zwischen der Framstraße (bimodal) und Ny-Ålesund (monomodal im Akkumulationsmode) unterschiedlich war, ergaben sich ähnliche Werte für das ARE in der atmosphärische Säule. Letzteres hängt mit der Dominanz des Akkumulationsmodus-Aerosols zusammen. Über beiden Standorten ergab sich am Oberrand der Atmosphäre (TOA) eine Erwärmung; diese wurde von einer Oberflächenkühlung begleitet.
Anschließend wurde die Abhängigkeit der ARE in Bezug auf verschiedene Aerosole und Umgebungsbedingungen im Frühling untersucht. Eine Änderung der Einfachstreualbedo (SSA) um 10% induzierte höhere ARE-Änderungen im Vergleich zu einer 30%igen Änderung des Aerosol-Extinktionskoeffizienten. In Bezug auf die Umgebungsbedingungen war die TOA-ARE im Vergleich zur Oberflächen-ARE empfindlicher gegenüber Änderungen der Sonnenhöhe. Über dunklen Oberflächen war das ARE-Profil ausschließlich negativ, während über hellen Oberflächen oberhalb der Aerosolschichten eine Verschiebung von negativen zu positiven Werten auftrat. Entsprechend ist das Vorzeichen der ARE im Frühjahr hochempfindlich, da diese Jahreszeit durch starke Änderung der Oberflächenalbedo gekennzeichnet ist.
Da die Inversion der Aerosolmikrophysik aus optischen Daten ein schlecht-gestelltes Problem ist, wurde die abgeleitete Aerosolgrößenverteilung eines Aerosol-Ereignisses in der niederen Troposphäre mit der einer aus in situ Verfahren abgeleiteten Verteilung verglichen. Beide Techniken ergaben zwei Aerosolmodi mit guter Übereinstimmung in Bezug auf die Gesamtvolumenkonzentration. In Bezug auf die SSA wurde jedoch ein Unterscied festgestellt, wobei die Lidarinversion auf stark streuende Partikel und die in-situ Messungen auf absorbierende Partikel hinwiesen. Die Abweichungen könnten auf Annahmen bei der Inversion (z.B. wellenlängenunabhängiger Brechungsindex) und auf Fehler bei der Umrechnung der in-situ gemessenen Lichtdämpfung in Absorption zurückzuführen sein. Eine weitere Ursache der Diskrepanz könnte auf eine unvollständige Erfassung von Feinpartikeln in den in-situ-Sensoren zurückzuführen sein. Die Unstimmigkeit über diesen wichtigsten Parameter für die arktische ARE macht weitere Untersuchungen im Rahmen von Aerosolschließungs-

Experimenten erforderlich. Vorsicht ist bei der ARE-aus Modellierungsstudien geboten, bei denen entweder in-situ- oder lidar-abgeleitete SSA als Input verwendet werden.
Eine zuverlässige Charakterisierung von Zirruswolken ist erforderlich, um die Abschätzung ihrer Strahlungswirkung zu verbessern. Von besonderer Bedeutung ist dabei der Nachweis von sub-visible Zirrus. Der Wolkenstrahlungseffekt (CRE) fällt zu negativ aus, wenn nur der optisch dünne und opake Zirrus berücksichtigt werden. Daher wurde ein Zirrus-Erkennungsschema basierend auf Lidardaten entwickelt. Das Schema verwendet die Wavelet–Kovarianz–Transformation (WCT), erweitert um dynamische Schwellenwerte. Die *dynamische WCT* zeigte eine hohe Empfindlichkeit gegenüber schwachen und dünnen Zirrusschichten von weniger als 200 m Mächtigkeit. Das optische Charakterisierungsschema erweiterte die Klett–Fernald–Retrieval durch iterative Lidar-Ratio (LR) Bestimmung (*constrained Klett*). Der iterative Prozess wurde durch einen Referenzwert eingeschränkt, der die Aerosolkonzentration unterhalb der Zirruswolke angab. Im Gegensatz zu bisherigen Ansätzen brauchte keine Aerosolfreiheit angenommen zu werden. Stattdessen wurden realistischere Annahmen unter der Wolke verwendet. Die inhärenten Unsicherheiten des eingeschränkten Kletts waren bei optisch dünneren Zirren höher, aber insgesamt wurde eine gute Übereinstimmung mit zwei etablierten Retrievals gefunden. Darüber hinaus konnten die bestehenden Ansätze, die auf aerosolfreien Annahmen beruhen, ebenfalls verbessert werden, wenn der vorgeschlagene Referenzwert verwendet wurde. Der *constrained Klett* konnte die optischen Eigenschaften in allen Zirrusregimen zuverlässig abrufen, einschliesslich der oberen sub-visible Zirren mit COD bis hinunter zu 0,02.
Zirrus ist die einzige Wolkengattung, die tagsüber am Atmosphärenoberrand entweder eine Kühlung oder eine Erwärmung hervorrufen kann. Über der Arktis sind die Eigenschaften und das CRE von Zirrus bislang nur wenig erforscht. Im letzten Teil dieser Arbeit wurden erstmals mit dem neuentwickelten Retrieval-Schema deren langfristige geometrische und optische Eigenschaften an einem arktischen Standort untersucht. Zirruswolken über Ny-Ålesund schienen im sichtbaren Spektralbereich absorbierender zu sein als in den niedrigen Breiten und mehr kugelförmige Eispartikel zu enthalten. Solche merididididialen Unterschiede könnten mit Diskrepanzen der absoluten Luftfeuchtigkeit und der Eiskeimbildung zusammenhängen. Tendenziell sank die COD bei weniger kugelförmigen und kleineren Eispartikeln, was wahrscheinlich auf eine geringere Wasserdampfablagerung an der Partikeloberfläche zurückzuführen ist. Die optischen Eigenschaften des Zirrus zeigten eine geringe Abhängigkeit von Umgebungstemperatur und Windbedingungen. In den 10 Jahren der Analyse konnte kein eindeutiger zeitlicher Trend und kein ausgeprägter saisonaler Zyklus festgestellt werden. Ein positives netto-CRE wurde für ein breites Spektrum von repräsentative Wolkeneigenschaften und Umgebungsbedingungen festgestellt. Für hohe COD (über 10) wurde jedoch ein negatives netto-CRE über der Tundra ermittelt, im Gegensatz zu Schnee- / Eisoberflächen. Folglich scheint die COD in Verbindung mit der Oberflächenalbedo die kritischste Rolle bei der Bestimmung des CRE über der hohen europäischen Arktis zu spielen.

PUBLICATIONS

Included in this dissertation:

Konstantina Nakoudi, Christoph Ritter, Christine Böckmann, Daniel Kunkel, Oliver Eppers, Vladimir Rozanov, Linlu Mei. , Vasileios Pefanis, Evelyn Jäkel, Andreas Herber, Marion Maturilli, and Roland Neuber. "Does the Intra-Arctic Modification of Long-Range Transported Aerosol Affect the Local Radiative Budget?(A Case Study)." Remote Sensing 12, no. 13 (2020): 2112. URL: https://www.mdpi.com/2072-4292/12/13/2112.

Contributions: **Konstantina Nakoudi** performed the lidar retrievals and the final SCIATRAN simulations, combined all the observational and simulated datasets, interpreted the results and wrote the original manuscript. Dr. Christoph Ritter provided scientific guidance on designing the study and interpreting the results. Prof. Christine Böckmann performed the microphysical retrievals. Dr. Daniel Kunkel and Oliver Eppers performed the backward trajectory calculations. Dr. Vladimir Rosanov and Dr. Linlu Mei provided scientific and technical support on SCIATRAN. Dr. Vasileios Pefanis supported the lidar data incorporation into SCIATRAN and performed sensitivity runs. Dr. Andreas Herber, Dr. Evelyn Jäkel, Dr. Marion Maturilli and Dr. Roland Neuber provided quality assured air-borne sun-photometer, air-borne and ground-based irradiance as well as the AMALi datasets, respectively.

Konstantina Nakoudi, Iwona S. Stachlewska and, Christoph Ritter. "An extended lidar-based cirrus cloud retrieval scheme: first application over an Arctic site." Optics Express 29, no. 6 (2021): 8553-8580. URL: https://www.osapublishing.org/oe/fulltext.cfm?uri=oe-29-6-8553&id=448923.

Contributions: **Konstantina Nakoudi** developed the algorithms under the supervision of Prof. Iwona Stachlewska and Dr. Christoph Ritter, performed the relevant sensitivity analysis and the multiple-scattering correction simulations, created the figures and wrote the original manuscript. Dr. Christoph Ritter developed the general purpose *constrained Klett* and **Konstantina Nakoudi** extended it to cirrus applications. All authors contributed to result interpretation and revisions of the manuscript.

Not included in this dissertation:

Fieke Rader, Rita Traversi, Mirko Severi, Silvia Becagli, Kim-Janka Müller, **Konstantina Nakoudi**, and Christoph Ritter. "Overview of Aerosol Properties in the European Arctic in Spring 2019 Based on In Situ Measurements and Lidar Data." Atmosphere 12, no. 2 (2021): 271. URL: https://www.mdpi.com/2073-4433/12/2/271.

Contribution: **Konstantina Nakoudi** performed part of the lidar measurements at AWIPEV. Additionally, contributed to result interpretation and wrote parts of the revised manuscript.

CONTENTS

1

INTRODUCTION

1.1 Motivation: Aerosol and cloud relevance to Arctic amplification

Over the last decades, the rate of near-surface warming in the Arctic is at least double than elsewhere on our planet (*Arctic amplification*) (Serreze and Barry, 2011; Wendisch et al., 2017). However, the relative contribution of different feedback processes to *Arctic amplification* is a topic of ongoing research, with climate models disagreeing on the sign of the total Arctic radiative feedback (Block et al., 2020). The radiative effect of aerosol and clouds depends among others on available solar radiation, surface albedo and atmospheric transport patterns (Willis, Leaitch, and Abbatt, 2018). Thus, aerosol and clouds play an inextricable role in the era of *Arctic amplification*.

Aerosol-induced cooling is suggested to counterbalance the greenhouse gas-induced warming by 1.3 to 2.2^oC over the past century (Najafi, Zwiers, and Gillett, 2015). In the same direction, climate models indicate that increased sulfate aerosol concentrations drove the sea ice expansion in the Eastern Arctic between 1950 and 1975 (Gagné et al., 2017). As the direct aerosol effect is estimated to be predominantly negative within the Arctic (Sand et al., 2017), the reduction of aerosol concentrations in the last decades is believed to have a significant impact on *Arctic amplification* and the state of sea ice (e.g. Najafi, Zwiers, and Gillett, 2015; Gagné, Gillett, and Fyfe, 2015; Acosta Navarro et al., 2016; Breider et al., 2017). Gagné, Gillett, and Fyfe (2015) suggested that under specific scenarios, the diminishing Arctic aerosol concentrations may contribute to a 10-year earlier ice-free Arctic than would otherwise occur. As aerosol – radiation interactions do not only depend on the aerosol type, a more comprehensive characterization of their radiative effect is needed under different solar geometry and surface albedo conditions. Ultimately, accurate climate projections necessitate a better understanding of aerosol direct and indirect radiative effects within the Arctic (Sand et al., 2017).

Lidar observations provide insights into the vertical variability of aerosol properties, an aspect that cannot be assessed by ground-based in-situ measurements. Besides aerosol, lidar systems are well-suited for cirrus cloud investigation as their operating wavelengths (i.e. at ultraviolet, visible and near-infrared) are more sensitive to small crystal sizes compared to millimeter radar systems (Heymsfield et al., 2017). Cirrus is the only cloud genus inducing either cooling or heating at the top of the atmosphere (TOA) during daytime, with the rest of the clouds producing a cooling effect (Lolli et al., 2017b; Campbell et al., 2018). The relative magnitude of short-wave (SW) cooling and infrared warming is highly dependent on the cloud properties, solar geometry, thermal contrast to the surface and surface albedo

(Kienast-Sjögren et al., 2016; Campbell et al., 2021). Over Ny-Ålesund, Svalbard, the annual average total cloud radiative effect (CRE) is suggested to be negative at TOA ($-16\ Wm^{-2}$) and positive at the surface ($+11\ Wm^{-2}$, Ebell et al., 2020. However, the contribution of Arctic cirrus clouds to the local radiation budget has not been quantified yet. To this end, the first necessary step is a better understanding of the cirrus geometrical and optical properties under different ambient conditions.

1.2 Theoretical background

1.2.1 Atmospheric aerosol

Atmospheric aerosol refers to suspended particles of micron or sub-micron sizes, emitted directly in solid or liquid form (*primary aerosol*) or resulting from the nucleation of gaseous precursors (*secondary aerosol*) (Bellouin et al., 2020a). In either case, the aerosol may originate from natural sources such as dust storms, volcanic eruptions, sea spray, natural fires as well as biogenic emissions such as pollen, bacteria and spores. Anthropogenic aerosol originate from biomass and fossil fuel combustion as part of agricultural and industrial activities, road traffic as well as domestic heating and cooking (Bellouin et al., 2020a). Aeolian dust, sea salt and pollen, which result from mechanical processes such as wind and erosion, are typically larger than 1 μm, while combustion generated particle sizes range from few nanometers to about 1 μm (Seinfeld and Pandis, 2016). However, a single aerosol particle can be an internal mixture of different chemical components of anthropogenic or natural origin (Bellouin et al., 2020b).

Particles with diameters larger than 2.5 μm are classified as *coarse particles*, while smaller particles that dominate the total aerosol number and a large fraction of mass are called *fine particles*. Particles with diameters smaller than 0.1 μm are often referred to as *ultra-fine particles* (Seinfeld and Pandis, 2016). Two aerosol size modes dominate the aerosol number distribution; the *nucleation mode* (with diameter smaller than 20 nm) and the *Aitken mode* (with diameter between 20 and 100 nm). *Nucleation mode* aerosol originate from gas-to-particle conversion processes such as homogeneous and heterogeneous nucleation. *Aitken nuclei* appear as primary particles, with secondary material condensing on them during their lifetime. The volume and mass distributions are mostly dominated by two modes; the *accumulation mode* (with diameter between 100 nm and 2 μm) and the *coarse mode* (with diameter between 2 and 50 μm). The main mechanisms that promote the transition of *Aitken mode* particles into the *accumulation mode* is coagulation and condensational growth (vapors from chemical reactions condense upon existing particles). Besides this, *accumulation mode* particles can be emitted as primary aerosol from combustion sources or form as secondary products (sulphates, nitrates, ammonium, organics) of chemical reactions (gas-to-particle conversion) (Seinfeld and Pandis, 2016, p. 342). Coagulation, however, is not an efficient

process for the promotion of *accumulation mode* particles towards the *coarse mode*.

Tropospheric aerosol concentration is highly variable in space and time compared to the well-mixed greenhouse gases. This is associated with their short tropospheric residence times, typically several days, as controlled by removal processes. Mechanisms that promote aerosol removal include coagulation, nucleation scavenging (activation to cloud condensation nuclei (CCN) and ice nucleating particles (INPs) as well as scavenging of interstitial aerosol) and dry or wet deposition (Garrett, Zhao, and Novelli, 2010). The short lifetime of aerosol necessitates observations on fine spatio-temporal scales, in the order of hours or even minutes. Lidar systems are capable of providing such information on a vertically-resolved framework. However, lidar systems operate from the ultraviolet to near-infrared spectral range and, therefore, are not sensitive to the whole aerosol size spectrum. The *Aitken mode* is too small to be observed by optical sensors. The *coarse mode* falls within the gray approximation region of the lidar operating wavelengths and, thus, lidar systems cannot provide spectrally-resolved information for this particle mode. The highest sensitivity of lidar systems corresponds to *accumulation mode* particles as investigated in this dissertation (Chapter 3).

Aerosol interact with radiation either directly, through scattering and absorption, or indirectly. More specifically, aerosol may act as CCN or INPs and thereby can impact on the cloud albedo and lifetime (Twomey, 1977). Another indirect effect, which is highly relevant for the Arctic, is the deposition of absorbing aerosol on bright surfaces such as snow and ice. This so-called *darkening effect* leads to albedo decrease and subsequent surface warming. On a global annual basis, the direct radiative effect of anthropogenic aerosol is suggested to be negative at TOA ($-1\ Wm^{-2}$) and the surface ($-2.1\ Wm^{-2}$), with the atmospheric effect estimated at $+1.1\ Wm^{-2}$ (Kinne, 2019).

1.2.2 Aerosol in the Arctic

Arctic aerosol can be of natural or anthropogenic origin and can be either long-range transported or locally produced. Long-range transported aerosol of natural or anthropogenic origin are more dominant in winter and spring, whereas local natural aerosol prevail in summer (Willis, Leaitch, and Abbatt, 2018). On the other hand, the presence of local anthropogenic aerosol is stronger in winter due to increased need for domestic heating and power generation (Schmale et al., 2018). Overall, the highest aerosol optical depth (AOD) within the Arctic appears in spring, with sulfate aerosol having the highest contribution, especially during late winter – spring (Fig. 1.1). Sulfate can be of crustal, biogenic, sea spray or anthropogenic origin. Anthropogenic sources have been identified as the most relevant ones for the Ny-Ålesund sulfate budget during springtime (Udisti et al., 2016). Sulfur from volcanic sources can also contribute to aerosol sulfate in the Arctic upper troposphere and stratosphere (e.g. (Hoffmann et al., 2010)). The second most significant contribution is attributed to organic carbon aerosol. In the Polar night organic carbon aerosol mainly originates from fossil fuel

sources but its peak is observed in late summer in connection with boreal forest fires (e.g. (Ritter et al., 2018; Zielinski et al., 2020)).

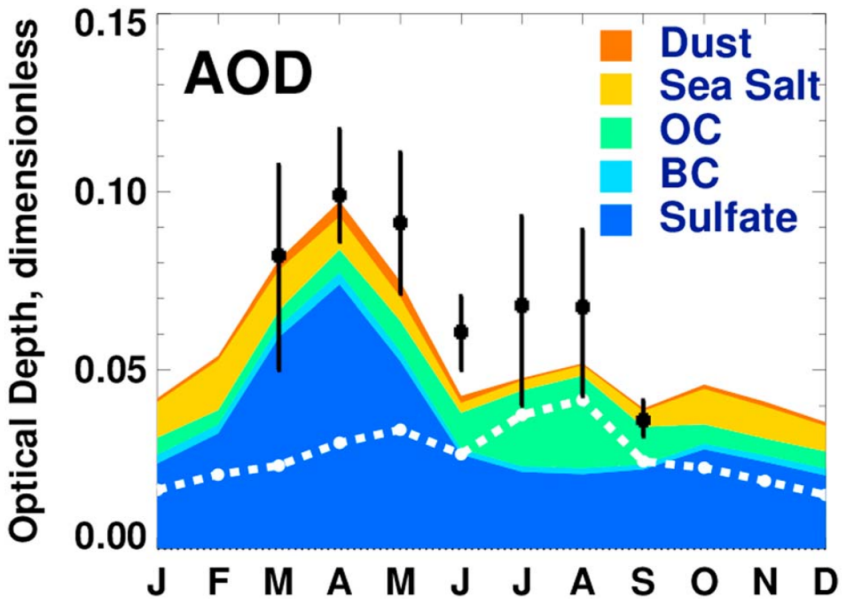

Fig. 1.1: Monthly cycle of AOD at 550 nm from eight different AERONET Arctic stations, averaged in the period 1997–2010. Black dots (bars) denote the monthly mean (one standard deviation) AOD. Stacked contours represent the contribution from different aerosol types, while the white dashed line shows the contribution from natural aerosol. BC: black carbon, OC: organic carbon. *Adapted from Breider et al. (2017), their Fig. 5.*

Sea salt comes next in importance, especially in winter and spring, when wind speeds peak in the northern oceans and facilitate its transport from open-water areas (Willis, Leaitch, and Abbatt, 2018). Two additional sea salt sources are suggested. The first one is wind-generated sea salt from frost flowers. Frost flowers are ice crystals that form on top of young sea ice and exhibit enhanced salinity compared to ocean water (Kaleschke et al., 2004). The second mechanism involves sea salt extraction from blowing snow, which can become saline through several processes (e.g. brine exclusion during freezing or sea salt deposition). Under strong winds the snow particles can be suspended in the air and upon their sublimation (if the air is sub-saturated with respect to water vapor) sea salt particles finally remain. Last in AOD contribution but not least in significance is dust and black carbon aerosol, with both of them known to produce a *darkening effect* (Flanner et al., 2009). The dust suspended in the Arctic troposphere does not only originate from remote sources (e.g. Gobi and Sahara deserts) but also from high-latitude (e.g. Iceland, Alaska, Canada, Greenland) and local sources (Zwaaftink et al., 2016; Moroni et al., 2018). Black carbon comprises a small but important component of long-range transported aerosol reaching the Arctic as it dominates the direct aerosol effect (DAE) in spring (Sand et al., 2017). Black carbon is the product of incomplete combustion from various industrial activities. In years with intense boreal forest fires, biomass burning can be the major source of deposited black carbon within the Arctic (Evangeliou et al., 2016).

Aerosol seasonality and transport regimes

Arctic aerosol properties exhibit a pronounced seasonal cycle in terms of concentration, size distribution and chemical composition. The seasonal variability of Arctic aerosol is driven by their sources, transport pathways, removal processes as well as meteorological conditions (Korhonen et al., 2008; Croft et al., 2016; Freud et al., 2017; Schmeisser et al., 2018). A typical annual cycle of Arctic aerosol number size distribution is presented in Fig. 1.2. On a pan-Arctic scale, the *accumulation mode* concentration gradually increases through winter and peaks in March – April, with median values between 100 and 200 cm^{-3} (Freud et al., 2017). This seasonality is reflected on the aerosol optical properties, with a maximization of the scattering coefficient (median values exceeding 10 Mm^{-1}) in late winter – spring (Schmeisser et al., 2018). The aerosol build-up during winter and early spring is supported by the low removal rates of ice-phase precipitation (Willis, Leaitch, and Abbatt, 2018).

In summer the *accumulation mode* abundance decreases, due to more efficient wet removal in the mid-latitudes and within the Arctic, and gives place to *Aitken aerosol mode* (Croft et al., 2016). The removal of *accumulation mode* aerosol provides also favorable conditions for new particle formation by limiting the condensation sink of particle-precursor gases and the coagulation sink of newly formed particles. New particle formation drives a second peak in total aerosol number concentration in summer (Dall' Osto et al., 2017). Autumn and winter are characterized by low concentration of *accumulation mode aerosol* and negligible presence of *nucleation* and *Aitken mode* particles (Tunved, Ström, and Krejci, 2013). Aerosol number and mass concentration typically reach their minimum between September and October (Tunved, Ström, and Krejci, 2013; Croft et al., 2016) as a result of decreased new particle formation, diminished poleward transport and more effective removal via liquid-phase precipitation (Croft et al., 2016).

The seasonal changes in Arctic aerosol properties are not limited near the surface but extend higher in the troposphere. While in winter the maximum extinction occurs in the lower troposphere, in spring its maximum progressively shifts towards the middle and upper troposphere (Di Pierro et al., 2013; Ritter et al., 2016; Shibata et al., 2018). The extinction enhancement in higher altitudes (*Arctic haze*) is associated with the isentropic poleward transport of polluted air masses from mid-latitudes (Klonecki et al., 2003; Stohl, 2006; Di Pierro, Jaeglé, et al., 2011). In recent years, however, *Arctic haze* tends to become indistinct at least over the European Arctic (Graßl and Ritter, 2019; Rader et al., 2021). *Arctic haze* comprises mostly aged *accumulation mode aerosol* of sulfate composition. However, chemical analysis has illustrated the presence of nitrate, chloride, sea salt, ammonium, dust, and carbonaceous compounds (Eleftheriadis, Vratolis, and Nyeki, 2009; Lisok et al., 2016; Moroni et al., 2018; Ferrero et al., 2019).

The dominating aerosol source regions vary on seasonal and vertical scales (Freud et al., 2017). For instance, north Eurasia is indicated as a major source of near-surface pollution at several Arctic sites, especially in winter (e.g. (Hirdman et al., 2010; Monks et al., 2015)). On

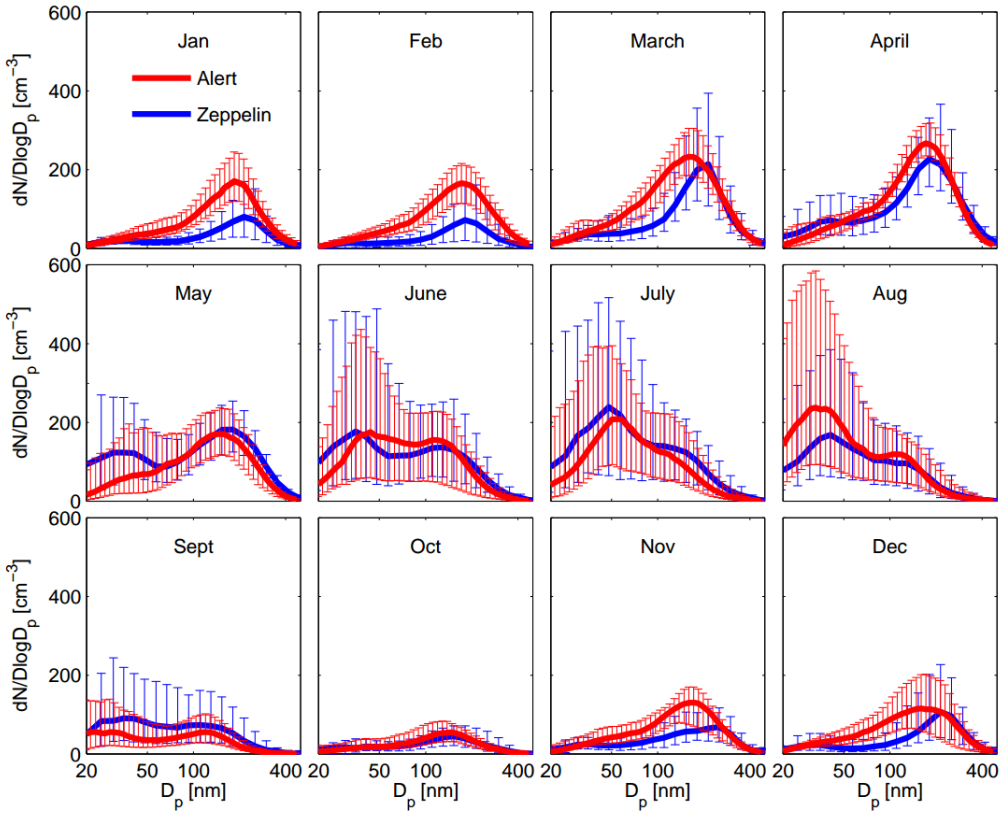

Fig. 1.2: Annual cycle of monthly median (errorbars represent 20–80th percentiles) aerosol number size distributions over two Arctic sites (Alert, Nunavut, Canada, and Zeppelin, Svalbard) in 2011–2013 for particle diameters between 20 and 500 nm. *Adapted from Croft et al. (2016), their Fig. 1.*

the other hand, north American and north-east Asian air masses are usually funneled into the middle and higher troposphere, especially in spring (e.g. Arnold et al., 2016; Sand et al., 2017). In the summer, middle and upper tropospheric air masses may originate from different geographic regions (Eurasia, north America and Asia, (Willis, Leaitch, and Abbatt, 2018)). During winter and spring, lower latitude air masses are more likely to be transported into the Arctic. In that time cold Arctic air masses are bordered by the *Arctic front* and minimum potential temperatures are frequently observed in the lower troposphere, which is isolated from the air aloft (Willis, Leaitch, and Abbatt, 2018). However, the *Arctic front* can extend southwards to approximately $40^{o}N$. Thereby, pollution in cold regions north of the *Arctic front*, such as north Eurasia, can be directly transported polewards (Klonecki et al., 2003). Moreover, the intrusion of air masses is promoted by strong diabatic cooling along transport over snow-covered areas or by blocking patterns (Klonecki et al., 2003; Stohl, 2006). In late winter and spring the *Arctic front* recedes polewards and, thus, lower tropospheric transport declines. Instead, middle and high troposphere transport tend to dominate since warm and moist air masses from north America and Asia ascend along the sloping isentropes (Stohl, 2006; Law and Stohl, 2007; Di Pierro, Jaeglé, et al., 2011). Lifting processes that facilitate the export of air masses from the boundary layer to these altitudes are related to the warm conveyor belts of extra-tropical cyclones. Subsequently, the air masses can penetrate the Polar dome from above through slow radiative cooling (1-5$^{o}C\ day^{-1}$, Klonecki et al., 2003).

In the summer, the *Arctic front* is shifted further polewards (Stohl, 2006). Wet removal is more pronounced along the summer transport pathways and, hence, the concentration of long-range transported aerosol declines (Croft et al., 2016).

Despite the overall distinct annual patterns, the seasonal cycle of aerosol properties presents differences across various Arctic sites (Freud et al., 2017). These differences result from the interplay of numerous parameters, such as proximity to aerosol source regions and the marginal ice zone, precipitation patterns and special features of each site (Freud et al., 2017). Hence, the Arctic cannot be treated as a uniform environment. Observations with high spatio-temporal coverage are essential for improving the representation of short-lived atmospheric constituents, such as aerosol, in climate models and reducing the uncertainties of future climate projections (Freud et al., 2017; Schmeisser et al., 2018).

Trends and future of aerosol over the Arctic

In the period 1980–2010, sulfate and black carbon mass concentrations have exhibited decreasing trends (-2 to -3% year^{-1}) across different Arctic stations (Breider et al., 2017). The decreasing sulfate trends were associated with declined sulfur emissions in Europe (by 80%), north America (by 70%) and Russia (by 50%) (Quinn et al., 2007; Hirdman et al., 2010; Breider et al., 2017). In contrast, the black carbon emissions have not decreased such notably, as China's contribution has doubled except for a 60% decline in Russia (Breider et al., 2017). Within the Arctic, a statistically significant shift towards more scattering particles (with higher single-scattering albedo (SSA)) is observed (Collaud Coen et al., 2020). However, the aerosol scattering coefficients exhibit a mix of positive and negative trends across different Arctic sites (Collaud Coen et al., 2020). At the same time, the increasingly, on spatial and temporal scales, ice-free Arctic Ocean is catalyzing the interest in commercial activities. The Arctic atmospheric composition is already affected by the opening of shorter shipping routes (Law et al., 2017), which together with natural resource extraction (gas and oil) they are likely to intensify in the future (Schmale et al., 2018).

Apart from anthropogenic aerosol, natural Arctic aerosol is subject to changes. Long-term observations have revealed an increasing occurrence of new particle formation events in anti-correlation with declining sea ice extent (Dall' Osto et al., 2017). The retreating sea ice may affect the emissions of particle-precursor gases (e.g. dimethylsulfide, organic compounds) as well as the production of primary marine aerosol (Willis, Leaitch, and Abbatt, 2018). In the context of receding sea ice, the spring-time AOD over Ny-Ålesund has diminished over the last two decades (Graßl and Ritter, 2019), possibly due to enhanced local humidity fluxes from the increasingly ice-free neighboring fjord (Dahlke et al., 2020). At the same time, the loss of land-based ice and snow may result in increased presence of local dust (Zwaaftink et al., 2016) and biogenic emissions from the exposed tundra (Kramshøj et al., 2016). Moreover, the intensification of boreal wildfires is expected to release large amounts of organic carbon aerosol and contribute to the natural particulate pollution in the Arctic (e.g. Warneke

et al., 2009; Evangeliou et al., 2016).

Diminished sulfate and black carbon concentrations have weakened the aerosol cooling effect, with the induced net TOA forcing estimated at $+0.48\ Wm^{-2}$ (Breider et al., 2017). Fig. 1.3 illustrates the multi-model mean Arctic DAE as attributed to total aerosol and to individual aerosol components. Pre-industrial emissions of anthropogenic aerosol and precursors were used as reference. Aerosol models fail to converge on the sign of annual mean DAE at TOA which ranges from -0.22 to $+0.01\ Wm^{-2}$ (25^{th}–75^{th} percentile). The discrepancies could be related to the assumptions of aerosol mixing state, size distribution and hygroscopicity (Sand et al., 2017). The annual mean DAE is estimated at $-0.12\ Wm^{-2}$ and black carbon is the only component that induces an exclusively positive effect. In late summer, the DAE shifts to a negative sulfate driven regime, while the effect of the remaining aerosol components is of variable sign. The presented estimates rely on monthly averaged model output, with horizontal resolution ranging from 1^o x 1^o to 5^o x 4^o. Therefore, they provide estimates on a spatio-temporally coarse framework. In order to reduce individual model uncertainties and the inter-model spread a better understanding of the parameters that determine the Arctic DAE is needed. In this work, a relevant sensitivity analysis is performed in Sec. 3.2.

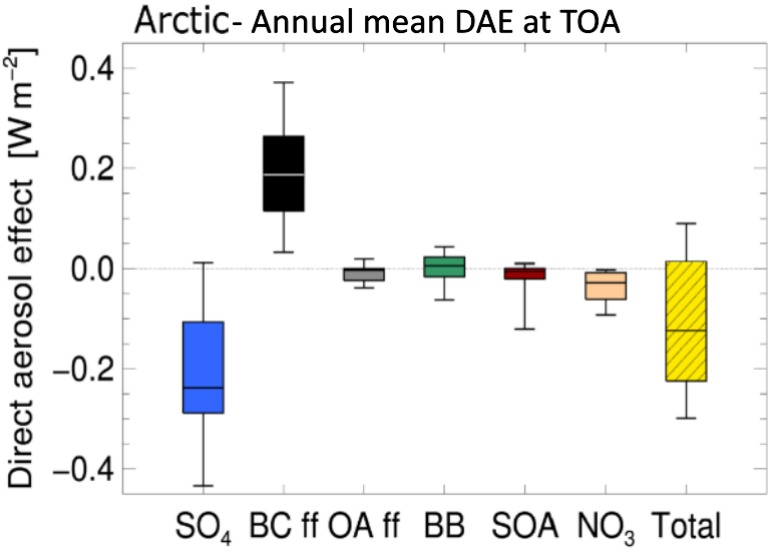

Fig. 1.3: Annual mean DAE at TOA over the Arctic for different aerosol components as derived from the AeroCom Phase II multi-model evaluation. SO_4: sulfate, BC: black carbon, BC ff: BC from fossil fuel and biofuel emissions, OA ff: organic aerosol from fossil fuel and biofuel emissions, BB: BC and organic aerosol from biomass burning emissions, SOA: secondary OA and NO_3: nitrate. *Adapted from Sand et al. (2017), their Fig. 8.*

1.2.3 Cirrus clouds

Accurate and precise geometrical and optical characterization of cirrus clouds is necessary for improving their radiative estimates (Lolli et al., 2018). The high uncertainty of the cirrus cloud radiative effect (CRE) is related to their wide range of cloud optical depth (COD) and occurrence altitudes (Heymsfield et al., 2017). In general, cirrus clouds exhibit decreasing geometrical thickness and appear at lower heights towards the Poles (Sassen, Wang, and Liu, 2008; Mace et al., 2009). Over the mid-latitudes a 40% cirrus average frequency is reported (Mace et al., 2009), which maximizes over the tropics (up to 70%, Nazaryan, McCormick, and Menzel, 2008) and decreases towards the Poles (Sassen, Wang, and Liu, 2008). Over different Arctic sites (Barrow, Eureka and SHEBA) ice clouds accounted for 30% of the total cloudiness above 6 km (Fig. 3 from Shupe, 2011), while over Ny-Ålesund the respective contribution was lower than 20% (Fig. 8 from Nomokonova et al., 2019). However, over the sub-Arctic site of Fairbanks, Alaska, a considerable annual average cirrus occurrence of 44% has been reported (Campbell et al., 2021). It should be noted that low-level Arctic ice clouds and ice fogs are not considered cirrus clouds (Heymsfield et al., 2017). In this work, the long-term geometrical and optical properties of cirrus clouds are investigated over the European Arctic site of Ny-Ålesund (Chapter 5).

Cirrus clouds can be classified in two categories depending on their formation (Krämer et al., 2016). The first one is *liquid origin cirrus* and refers to cirrus formed upon liquid droplet freezing of pre-existing mixed-phase or liquid clouds. Hence, the formation of *liquid origin cirrus* occurs if a mixed-phase or liquid cloud is completely glaciated when lifted by updrafts to cirrus formation altitude ranges (temperature below -38^oC). *Liquid origin cirrus* are mostly geometrically thick. Their occurrence is strongly related to warm conveyor belts as well as mesoscale convective systems and gravity waves (Krämer et al., 2016). The second category is *in-situ cirrus*, which form directly as ice, via homogeneous (temperature below -38^oC) or heterogeneous ice nucleation (temperature below 0^oC). *In-situ cirrus* are thinner than *liquid origin cirrus* and consist of smaller ice crystals (Krämer et al., 2020). Cirrus can also be classified according to their optical properties and more specifically their COD. Following the classification of Sassen and Cho (1992) cirrus can be categorized as *sub-visible* (COD < 0.03), *optically-thin* (0.03 < COD < 0.3) or *opaque* (0.3 < COD < 3). Sassen and Cho (1992) suggested a COD of 3 as an upper lidar attenuation limit for cirrus clouds.

The identification of *liquid origin* and *in-situ cirrus* is mainly feasible during their initial formation stage. Subsequent dynamic processes blur their distinct characteristics, such as ice crystal size. For instance, ice crystal growth may take place in timescales of several minutes when a large number of small ice crystals is embedded into a prevailing updraft. Additional dynamic processes include sedimentation as well as further ice formation. Sedimentation of bigger ice crystals can extend, for example, the cirrus lifetime since the RH_{ice} is sustained at high levels (less available ice surface for depleting the water vapor). At the dissipation stage, ice crystal evaporation or sublimation takes place. Smaller ice crystals experience rapid evaporation in timescales of minutes. However, the evaporation stage of cirrus comprising

big ice crystals (50 μm and larger) are simulated to several hours. Such cirrus survive in sub-saturated air for as long as the water released from the ice crystals sustains the RH_{ice} slightly below saturation (Kübbeler et al., 2011).

The geometrical and optical properties of cirrus clouds in the high Arctic are under-explored. Cloud-Aerosol lidar with Orthogonal Polarization (CALIOP) and Cloud Profiling Radar have significantly filled the observational deficit in the last 15 years, but provide observations up to 82^oN (Winker et al., 2009). At the same time, ice cloud identification over the Polar regions is still challenging. For instance, optically-thin ice layers are frequently miss-classified as aerosol layers (Di Biagio et al., 2018; Liu et al., 2019). Passive sensors exhibit, in general, reduced sensitivity to optically-thin clouds (Marquis et al., 2017). Besides this, over cold and bright surfaces it is challenging to detect ice clouds (Jafariserajehlou et al., 2019) and retrieve their optical properties (Mei et al., 2018) using infrared radiances. Campbell et al. (2021) found an exclusively negative daytime TOA CRE over Fairbanks based on MODIS radiances since only opaque cirrus could be detected. However, when considering all the cirrus regimes, as detected by lidar, the annual average CRE fluctuated between positive and negative values. Thus, the omission of sub-visible and optically-thin cirrus can lead to a negative CRE bias and the role of lidar systems is essential in reducing this bias. The development of a cirrus detection scheme with emphasis on geometrically- and optically-thinner cirrus clouds is presented in Chapter 4.

Cirrus is the only cloud genus capable of inducing warming or cooling at TOA during daytime (Lolli et al., 2017a). The cooling effect is related to the reflection of SW solar radiation (*SW albedo effect*). On the other hand, the warming effect is associated with the absorption of up-welling infrared radiation, originating from the surface and lower troposphere and its re-emission at lower temperatures that, finally, reduces the infrared radiation escaping into space (*infrared greenhouse effect*). Idealized simulations suggest that cirrus with low COD (below 0.4) produce a warming CRE ($+2$ to $+10\ Wm^{-2}$), while a shift towards a cooling effect was indicated for opaque cirrus ($-15\ Wm^{-2}$ for COD = 1 and $-250\ Wm^{-2}$ for COD = 12, Fig. 1.4). These scenarios were focused on local noon equinox mid-latitude (50^o) conditions over low reflecting surfaces (albedo = 0.3) of 15^oC temperature. Equinox conditions over the Arctic translate into higher solar zenith angle (SZAs) compared to mid-latitudes and are accompanied by higher albedo (snow- and ice-covered surfaces). Therefore, the simulations of Krämer et al. (2020) cannot be considered representative for the Arctic. The recent study of Campbell et al. (2021), investigating the daytime TOA cirrus CRE (annual average from -1.08 to $+0.78\ Wm^{-2}$) over Fairbanks (64.9^oN) is more representative. However, the surface albedo over Fairbanks ranged from 0.1 (snow-free conditions) to 0.4 (partly snow-covered conditions) and the SZAs were lower. Hence, it is still needed to extend the cirrus CRE investigation over the high Arctic and for snow/ice surface conditions. This is addressed in Chapter 5 for a broad range of representative cirrus properties and ambient conditions over Ny-Ålesund.

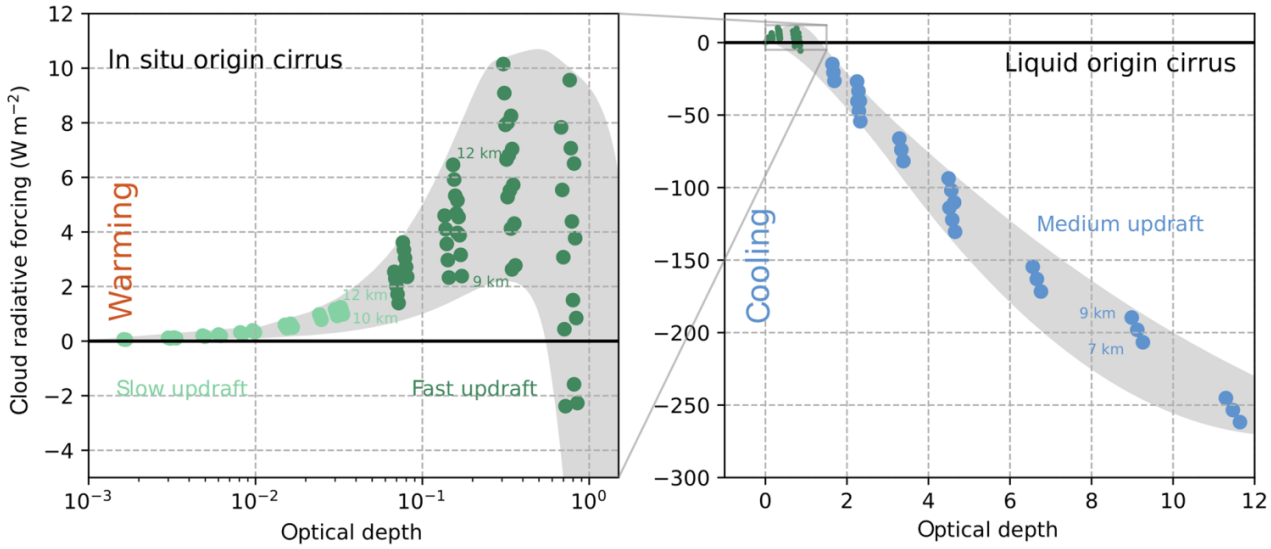

Fig. 1.4: Simulated cirrus CRE as a function of COD. See text for more information on the idealized scenarios. *Adapted from Krämer et al. (2020), their Fig. 5.*

1.3 Research questions

The goal of this work is a better understanding of aerosol and cirrus cloud properties and of their radiative effect over the high Arctic. The analysis is mainly focused on Ny-Ålesund, a coastal site in the European part of the Arctic. Ny-Ålesund (78.9^{o}N, 11.9^{o}E), Svalbard Archipelago, is embedded in the complex orography of fjord and mountain ranges, with micrometeorology playing an important role for aerosol patterns, especially in the lower troposphere (Jocher et al., 2015; Rader et al., 2021). Moreover, the warm West Spitsbergen Current affects the local conditions (Walczowski and Piechura, 2011). The Svalbard region is the hotspot of winter warming with up to 2^{o}C decadal near-surface temperature increase in the past 20 years (Gjelten et al., 2016; Dahlke and Maturilli, 2017). The positive temperature and humidity trends extend in the winter-time free troposphere, accompanied by an increasing occurrence of southerly flow (Maturilli and Kayser, 2017). Concurrently, the surface radiation budget experiences long-term changes. In winter the downward long-wave irradiance is amplified. The increased number of cyclones entering the Arctic as well as intensified local evaporation and thermal inversions have a potential contribution (Maturilli, Herber, and König-Langlo, 2015). In spring and summer, the short-wave reflected irradiance has decreased in connection with an earlier onset of snow melt (Maturilli, Herber, and König-Langlo, 2015). This work focuses on better characterizing the role of aerosol and cirrus clouds in the local radiation budget and addresses the following research questions:

- **RQ1: Which aerosol properties and ambient conditions play the most critical role in the local radiation budget? Are these properties retrieved precisely enough by optical remote sensing and how do they compare to in-situ measurements?**

  Aerosol models fail to agree on the sign of the direct Arctic ARE (Sand et al., 2017), which depends on the aerosol properties and ambient conditions. In the first part, the properties of Arctic aerosol are characterized at case study level. The optical and mi-

crophysical properties of a long-range transport episode are first analyzed (Sec. 3.1). Subsequently, the sensitivity of the ARE is investigated with respect to different aerosol and spring-time ambient conditions using radiative transfer simulations (Sec. 3.2). The inversion of aerosol microphysics is an ill-posed problem and up to now the comparison of remote sensing and in-situ techniques over Ny-Ålesund was focused on the aerosol optical properties (Tesche et al., 2014; Ferrero et al., 2019). In the final part, the comparison is extended to the microphysical properties of a low tropospheric event (Sec. 3.3).

- **RQ2: Is it possible to improve the detection of thin cirrus clouds? To which extent is the retrieval of their optical properties reliable?**

  The detection of sub-visible cirrus is of special importance as the total CRE can be negatively biased when the optically-thin and opaque cirrus contributions are only considered (Campbell et al., 2021). Even with active remote sensing, some discrepancies in thin cirrus detection occur. For instance, Pandit et al. (2015) demonstrated a 20% underestimation of sub-visible cirrus occurrence by satellite lidar observations in comparison to ground-based lidar. Consequently, there is a high need to reliably detect sub-visible cirrus and the contribution of ground-based lidar observations is essential in this respect. In the second part, the development of a cirrus detection and optical characterization scheme is described (Chapter 4). The cirrus detection is based on the wavelet covariance transform (WCT) method (Gamage and Hagelberg, 1993), extended by dynamic thresholds, aiming at increased sensitivity to thin cirrus layers. The cirrus optical characterization relies on the Klett–Fernald method (Klett, 1981; Fernald, 1984), extended by an iterative lidar ratio (LR). The iterative process is constrained by a reference value beneath the cirrus cloud. The reference value is designed more realistically as it is estimated from close cloud-free profiles or profiles with minimum cirrus influence. The inherent uncertainties and limitations of the proposed methodology are quantified and its performance is compared with two established methods.

- **RQ3: Which long-term geometrical and optical properties do Arctic cirrus clouds posses? Which properties and ambient conditions play the most critical role in the local radiation budget?**

  Cirrus is the only cloud type capable of inducing cooling or heating at TOA during daytime. The CRE sign depends on the cloud properties as well as on ambient conditions (Campbell et al., 2021). Over the Arctic, however, the properties and CRE of cirrus are under-explored. In the final part, the long-term cirrus geometrical and optical properties are investigated for the first time over an Arctic site (Ny-Ålesund, Chapter 5). To this end, the newly developed retrieval scheme (Chapter 4) is employed. Additionally, the cirrus CRE is investigated for a broad range of representative cloud properties and ambient conditions.

2

METHODS

2.1 lidar remote sensing technique

Lidar stands for light detection and ranging and is an active remote sensing technique. Lidar systems emit pulsed laser light at different wavelengths into the atmosphere. Part of this light is backscattered by air molecules and particles and, thus, can be collected by the system's telescope, whose optical axis is close to the laser beam axis. Subsequently, the light passes through the optical analyzing system, which consists of spectrally and polarization sensitive components. Finally, the light is transformed to photocurrent and it is counted by transient recorders. The transient recorders are triggered by a photodiode and, thus are synchronized with the laser flashing. The time difference between the laser flashing and the counting of the backscattered photons yields the ranging capabilities of lidar systems and allows the acquisition of profiles with high vertical and temporal resolution. In the following Section, the equations describing the working principle of elastic and Raman lidar are given. Then, the different signal corrections are explained (Sec. 2.1.2) and the derivation of particle optical properties is described (Sec. 2.1.3). More technical details about the components of the different lidar systems employed in this work are given in Sec. 2.2.

2.1.1 Elastic and Raman lidar equations

The majority of the emitted photons are scattered elastically i.e. there is no wavelength shift between the scattered and emitted photons. However, almost one out of 10^3 photons is scattered inelastically (Raman scattering) by air molecules. In the following the equations that describe the working principle of elastic (Eq. 2.1) and Raman lidar (Eq. 2.2) systems are presented. It should be noted that both lidar equations are valid under the assumptions of single-scattering processes, coherent and quasi-monochromatic light emission.

$$P(r,\lambda) = \underbrace{P(r_0,\lambda)\cdot\frac{c\cdot\tau}{2}\cdot A\cdot T_{\lambda}^{emis}\cdot T_{\lambda}^{rec}}_{C_{\lambda}}\cdot\underbrace{\frac{O(r,\lambda)}{r^2}}_{G(r,\lambda)}\cdot\beta(r,\lambda)^{tot}\cdot\underbrace{exp\left[-2\int_{r_0}^{r}\alpha(\hat{r},\lambda)^{tot}d\hat{r}\right]}_{T(r,\lambda)} \tag{2.1}$$

$$P(r,\lambda_{Ra}) = \underbrace{P(r_0,\lambda)\cdot\frac{c\cdot\tau}{2}\cdot A\cdot T_{\lambda}^{emis}\cdot T_{\lambda_{Ra}}^{rec}}_{C_{\lambda_{Ra}}}\cdot\underbrace{\frac{O(r,\lambda_{Ra})}{r^2}}_{G(r,\lambda_{Ra})}\cdot\beta(r,\lambda_{Ra})^{mol}\cdot \underbrace{exp\left[-\int_{r_0}^{r}\alpha(\hat{r},\lambda)^{tot}+\alpha(\hat{r},\lambda_{Ra})^{tot}d\hat{r}\right]}_{T(r,\lambda,\lambda_{Ra})} \tag{2.2}$$

$P(r,\lambda)$ and $P(r,\lambda_{Ra})$ denote the photon power received by the detector at a specific time and range bin at emitted wavelength λ and the Raman shifted wavelength λ_{Ra}. The received photon power is proportional to the photon energy E_o emitted at the pulse repetition frequency f_{rep}. Most of the remaining terms are range- and wavelength-dependent as denoted parenthetically in Eq. 2.1 and 2.2. For simplicity, these dependencies are hereafter omitted in the notation. The term $\frac{c\cdot\tau}{2}$ describes the *effective pulse length* that is the one-dimensional transect of the volume from which backscattered light is received. A is the area of the receiving telescope, while T^{emis} and T^{rec} is the transmission efficiency of the emission and receiving optics, respectively. The above mentioned system parameters are represented by the so-called *lidar constant* C.

The term G describes the *geometric factor*, which includes the *overlap function* O between the laser beam and the receiving telescope field of view (FOV). The *overlap function* represents in a range-resolved manner the number of photons arriving at the detector relative to those arriving at the telescope aperture. Usually, the *overlap function* is zero at the lidar, increases with range and becomes unity when the laser beam is fully imaged on the detector through the telescope aperture (Sicard et al., 2020). The *overlap function* depends on the relative position of the emitter and receiver optical axes, the laser beam diameter and divergence as well as the telescope diameter, FOV and aperture diameter (Sicard et al., 2020). The term r^2 represents the signal intensity decrease with range. This decrease is quadratic as the telescope surface A is only a part of the sphere surface enclosing the scattering volume. The r^2 term mainly accounts for the large dynamic range of the lidar signals (Weitkamp, 2006).

The terms β and T denote the backscatter coefficient and the transmission, respectively. The backscatter coefficient describes how much light is scattered in the backward direction ($\theta = 180^o$) i.e. towards the lidar (Weitkamp, 2006). The transmission term, following the *Beer–Lambert law*, accounts for the loss of photons due to extinction α as the laser pulses propagate from the lidar (located at r_0) up to a distance r and back. The extinction coefficient describes how much light is attenuated due to absorption and scattering into all directions. Within the atmosphere light is scattered and absorbed by molecules and particulate matter. However, in Eq. 2.2 only the molecular backscatter ($\beta(r,\lambda_{Ra})^{mol}$) is given since only the air molecules (N_2) account for the inelastic scattering at the selected wavelength λ_{Ra} (387 or 607 nm). The transmission term of Eq. 2.2 is split in two parts as the attenuation of the emitted light concerns a wavelength λ, while the backscattered light attenuation concerns the Raman shifted wavelength λ_{Ra}.

Finally, the backscatter (in $m^{-1}sr^{-1}$) and extinction coefficients (in m^{-1}), which are the primary lidar derived quantities, can be described by Eq. 2.3 and Eq. 2.4.

$$\beta(r,\lambda)^{tot} = \beta(r,\lambda)^{part} + \beta(r,\lambda)^{mol} = \sum_i N_i(r)\cdot\frac{d\sigma_i^{sca}}{d\Omega}(180^o,\lambda) \tag{2.3}$$

$$\alpha(r,\lambda)^{tot} = \underbrace{\alpha(r,\lambda)^{part}_{sca} + \alpha(r,\lambda)^{part}_{abs}}_{\alpha(r,\lambda)^{part}} + \underbrace{\alpha(r,\lambda)^{mol}_{sca} + \alpha(r,\lambda)^{mol}_{abs}}_{\alpha(r,\lambda)^{mol}} = \sum_i N_i(r) \cdot \left(\sigma_i^{sca} + \sigma_i^{abs}\right) \quad (2.4)$$

N_i denotes the number concentration (in m^{-3}) of different scatterer types i at range r and $\frac{d\sigma^{sca}}{d\Omega(180^o,\lambda)}$ is the differential scattering cross-section (in $m^2 sr^{-1}$) in the backward direction at wavelength λ. Respectively, σ_i^{abs} is the absorption cross-section (in m^2) of a scatterer i. The molecular contribution to scattering ($\alpha(r,\lambda)^{mol}_{sca}$) and absorption ($\alpha(r,\lambda)^{mol}_{abs}$) is pressure- and temperature-dependent and mainly originates from nitrogen and oxygen (Weitkamp, 2006). The particulate matter scattering ($\alpha(r,\lambda)^{part}_{sca}$) and absorption ($\alpha(r,\lambda)^{part}_{abs}$) can be attributed to different aerosol particle types and hydrometeors, such as liquid droplets and ice crystals, and depend on the particle size distribution, refractive index and shape. The focus of this work is placed on aerosol (Chapter 3) and ice particles (Chapters 4 and 5). Prior to solving the respective lidar equations and derive the particle backscatter and extinction coefficients, the lidar signals need to be calibrated and additional corrections need to be performed.

2.1.2 lidar signal corrections

The first step in the lidar signal pre-processing accounts for the incomplete overlap effect. The so-called *overlap correction* is applied on the signals so as to compensate for any irregular gradients, especially in the near-range. For the Koldewey Aerosol Raman Lidar (KARL, technical description follows in Sec. 2.2.1), clear-sky ceilometer observations are used as reference.

Subsequently, the lidar signals need to be corrected for the *electronic* and *atmospheric background* effects (Hoffmann, 2011), which are superimposed on the received signal intensity. The *electronic noise* corresponds to the detector's *dark current signal*, which is produced even in absolute darkness and it is temperature sensitive. The *atmospheric background* originates from any light source other than the laser beam and it is dependent on the surface albedo. It mainly represents the solar illumination but it can include lunar illumination and artificial light. The *atmospheric background noise* can be reduced by a narrow FOV receiver telescope and narrow interference filters in front of the detectors. However, background effects still need to be corrected, with two usual approaches existing. In the first approach, the background noise is estimated from the signal in the far-range. In the far-range the number concentration of molecules and particles is negligible and, thus, any measured intensity is the result of either atmospheric or electronic noise. Therefore, at each time step the average signal in the far-range is subtracted from the remaining range bins. For KARL, signals from 60 to 120 km are used for calculating the *electronic* and *atmospheric background*. In the second approach, the background signal is determined at each time step by delaying the laser beam emission into the atmosphere with respect to data acquisition. During the delay period, which is in the order of μs, only the background signal is detected without the influence of scattered laser radiation. Thus, the background is determined as the average signal in the first part

of the near-range region (*pre-trigger region*). This approach is adopted in the pre-processing of the Air-borne Mobile Aerosol Lidar (AMALi, technical description in Sec. 2.2.2) signals (Stachlewska et al., 2010). In the zenith AMALi configuration that is used in this work, the *pre-trigger region* is equal to 105 near-range bins (787.5 m). Finally, it should be noted that insufficient handling of the *background correction* leads to artificial signal gradients, which in extreme cases might be mistaken for real aerosol layers.

If the signals are recorded in photon-counting (PC) and analog (A) mode, the two components need to be glued. The *signal gluing* is performed within an interval (several hundred meters) selected as such that both signals are of high quality. In PC acquisition single photons can be counted as long as their photocurrent exceeds a pre-defined threshold. However, there is a small time interval (*dead-time*) in which no other photon can be detected. This limits the maximum count rate of the recorders and when this is reached the PC signal gets saturated, which usually holds true for strong near-range signals. Therefore, for near-range signals the A mode is preferred, which records the integrated photocurrent within each range bin. Nevertheless, the A signal can get very noisy in the far-range. Hence, non-saturated PC signal and A signal of high signal-to-noise ratio (SNR, Eq. 2.9) are required within the *gluing interval*. First, a *dead-time correction* is applied on the PC signal by using a theoretical model of photon statistics (D'Amico et al., 2016). Then, the A signal is scaled towards the PC signal by demanding their minimum deviation within the *gluing interval*. The *signal gluing* starts at the range bin of minimum difference and gradually proceeds as a weighting function (Hoffmann, 2011). Finally, a large dynamical detection range is achieved through hybrid signal profiles that combine the benefits of the PC and A components. Upon performing the aforementioned steps, the corrected signals can be obtained. However, the arbitrary units of lidar signals only provide qualitative information on the vertical distribution of different atmospheric features, such as aerosol and cloud particles. In order to derive the particle backscatter and extinction coefficients, which have a physical meaning, the lidar equations (Eq. 2.1 and 2.2) need to be solved.

2.1.3 Derivation of particle optical properties and related uncertainties

Starting with elastic backscatter lidar, such as AMALi (Sec. 2.2.2), one equation (Eq. 2.1) with two unknown terms, namely $\beta(r,\lambda)^{tot}$ and $\alpha(r,\lambda)^{tot}$, needs to be solved. In cases of homogeneous and turbid atmosphere ($\alpha(r,\lambda)^{part} >> \alpha(r,\lambda)^{mol}$), the so-called *slope method* can be applied (Collis, 1966). In reality, however, such conditions are rarely met. The *Klett–Fernald approach* works even when the atmosphere is heterogeneous, comprising aerosol rich and aerosol-free layers (Klett, 1981; Fernald, 1984). This approach is based on the formalism of Hitschfeld and Bordan (1954), applied on meteorological radar observations, with Klett (1981) stating that it can be conveniently extended to lidar observations. In the *Klett–Fernald approach* both particulate and molecular scatterer contributions need to be taken into account. The $\beta(r,\lambda)^{mol}$ and $\alpha(r,\lambda)^{mol}$ can be estimated from radiosounding temperature and pressure data or modelled standard atmosphere profiles. In order to obtain an analytical

solution, the $\beta(r,\lambda)^{part}$ and $\alpha(r,\lambda)^{part}$, which remain unknown, need to be replaced by one term. This term is the so-called *lidar ratio* (in sr)

$$LR(r,\lambda)^{part} = \frac{\alpha(r,\lambda)^{part}}{\beta(r,\lambda)^{part}}. \tag{2.5}$$

One problem arising from this assumption is the fact that in reality the LR is vertically-variable, as it depends on the aerosol particle size distribution, refractive index and shape. More specifically, depending on the aerosol type the LR may start from approximately 20 sr in the lower troposphere, if marine aerosol is present (e.g. (Burton et al., 2013)) and may reach 100 sr if combustion aerosol particles are lofted at higher altitudes (e.g. Giannakaki et al., 2016). The accuracy of the Klett–Fernald method is deteriorating in the presence of optically-thin clouds as their LR differs to that of aerosol and the lidar solution cannot efficiently converge due to their low optical depth. In these cases, an iterative LR selection can be implemented. The development and testing of such an approach is described in Chapter 4.

A final step before proceeding with the solution of the lidar equation is the *backscatter calibration*. The *backscatter calibration range* (r_{cal}) is usually set at a high atmospheric altitude, where particulate scattering can be considered negligible compared to the molecular one. In this work the *backscatter calibration range* was set in the lower stratosphere (in most cases 13–15 km). Subsequently, the *calibration value* for the backscatter ratio (BSR, Eq. 2.6 [1]) needs to be assumed (in most cases $BSR_{cal}^{355} = 1.01$ and $BSR_{cal}^{532} = 1.05$) and serves as a boundary condition for the lidar differential equation. The equation can be solved either towards the lidar system (backwards) or from the lidar system (upwards), with the former solution being numerically stable (Fernald, 1984). Therefore, this approach is followed here. In order to derive the aerosol backscatter coefficient, the elastic lidar equation is re-arranged with respect to the so-called *range-corrected signal* $S(r,\lambda)$

$$S(r,\lambda) = P(r,\lambda) \cdot r^2. \tag{2.7}$$

Subsequently, a logarithm is set in the two parts of the equation, followed by differentiation with respect to range r. This gives a non-linear differential equation of 2^{nd} degree with respect to $\beta(r,\lambda)$. The intermediate steps for reaching the solution, such as the linearization of the differential equation, are omitted here for the sake of brevity. The reader is directed to Weitkamp (2006) for the detailed steps. The backscatter coefficient solution is obtained by

$$\beta(r,\lambda)^{part} = -\beta(r,\lambda)^{mol} + \frac{S(r,\lambda)\cdot T(r,r_{cal})}{\frac{S(r_{cal},\lambda)}{\beta(r_{cal},\lambda)^{tot}} - 2\int_{r_{cal}}^{r} LR(\hat{r},\lambda)^{part}\cdot S(\hat{r},\lambda)\cdot T(r,r_{cal})d\hat{r}}. \tag{2.8}$$

[1]

$$BSR(r,\lambda) = \frac{\beta(r,\lambda)^{part} + \beta(r,\lambda)^{mol}}{\beta(r,\lambda)^{mol}} \tag{2.6}$$

$T(r, r_{cal})$ is described by $exp\left[-2\int_{r_{cal}}^{r}\left(LR(\hat{r},\lambda)^{part} - LR^{mol}\right)\cdot\beta(\hat{r},\lambda)^{mol}d\hat{r}\right]$. $LR^{mol} = 8\pi/3$ sr is the molecular LR that is range-independent.

The assumptions of the lidar equation and other uncertainties affect the retrieval of $\beta(r,\lambda)^{part}$. The a priori LR selection is very important as the impact of an inaccurate LR increases with the equation integration path (towards the system). However, the more turbid the atmosphere the lower is such an impact (Fernald, 1984). Concerning the *BSR calibration value* (BSR_{cal}), its impact on the solution decreases with the integration path as long as the backward approach is followed (Fernald, 1984). In this work, uncertainties of 10 sr and 3% were assumed for the LR and BSR_{cal}, respectively. Errors are also introduced due to statistical signal noise as well as signal temporal averaging and vertical smoothing. A small systematic error might also be introduced by the radiosounding or modelled derived molecular profiles. Finally, the positioning of the *calibration range* introduces additional uncertainty (Mattis et al., 2016). In this work, an average SNR (Eq. 2.9 [2]) higher than 3 was required in the *calibration range*.

Working with a Raman lidar system such as KARL (Sec. 2.2.1) allows the independent retrieval of $\beta(r,\lambda)^{part}$ and $\alpha(r,\lambda)^{part}$, without any LR assumption (Ansmann et al., 1992). Starting with $\alpha(r,\lambda)^{part}$, it can be derived by substituting the molecular part of Eq. 2.3 into Eq. 2.2, after logarithmizing and differentiating with respect to r (Ansmann, Riebesell, and Weitkamp, 1990). This yields an equation (not shown here) that includes the molecular and particle backscatter coefficient at the elastic wavelength λ and Raman shifted wavelength λ_{Ra}. The molecular extinction and number concentration can be estimated from radiosoundings or a modeled atmospheric profile. Obtaining the $\alpha(r,\lambda)^{part}$ solution, requires to know the extinction-related Ångström exponent at λ and λ_{Ra} ($\text{Å}_\alpha(\lambda/\lambda_{Ra})$). This is assumed equal to unity as the λ – λ_{Ra} pairs (355 – 387 nm and 532 – 607 nm) used in Raman lidars are spectrally close. This assumption is valid, especially for particles, whose size is comparable to the emitted light wavelengths. An uncertainty of 0.5 in the $\text{Å}_\alpha(\lambda/\lambda_{Ra})$ contributes to 5% error in the $\alpha(r,\lambda)^{part}$ (Weitkamp, 2006). Finally, the $\alpha(r,\lambda)^{part}$ can be derived as

$$\alpha(r,\lambda)^{part} = \frac{\frac{d}{dr}ln\frac{N(r)^{mol}}{P(r,\lambda_{Ra})\cdot r^2} - \alpha(r,\lambda)^{mol} - \alpha(r,\lambda_{Ra})^{mol}}{1+\left(\frac{\lambda}{\lambda_{Ra}}\right)^{A_\alpha(\lambda/\lambda_{Ra})}} \tag{2.10}$$

Concerning the $\beta(r,\lambda)^{part}$, it can be derived from the ratio of the elastically- over the inelastically-backscattered signal (Ansmann et al., 1992). Similar to the elastic lidar equation, the solution

2 The signal noise consists of the statistical noise and the background noise (P_{bg}, see also Sec. 2.1.2). The photon detection events, i.e. the measured signal intensity P in PC mode, follow a *Poisson distribution* and, thus, the associated statistical uncertainty equals to $\sqrt{P}$. The SNR can be estimated as

$$SNR(r,\lambda) = \frac{P(r,\lambda)}{\sqrt{P(r,\lambda)+P_{bg}(\lambda)}}. \tag{2.9}$$

necessitates a BSR_{cal} assumption at the *calibration range*. Finally, the $\beta(r,\lambda)^{part}$ can be derived as

$$\beta(r,\lambda)^{part} = -\beta(r,\lambda)^{mol} + \left[\beta(r_{cal},\lambda)^{part} + \beta(r_{cal},\lambda)^{mol}\right] \cdot \frac{P(r_{cal},\lambda_{Ra}) \cdot P(r,\lambda) \cdot N(r)^{mol}}{P(r_{cal},\lambda) \cdot P(r,\lambda_{Ra}) \cdot N(r_{cal})^{mol}} \cdot \frac{exp\left[-\int_{r_{cal}}^{r} \alpha(\hat{r},\lambda_{Ra})^{part} + \alpha(\hat{r},\lambda_{Ra})^{mol} d\hat{r}\right]}{exp\left[-\int_{r_{cal}}^{r} \alpha(\hat{r},\lambda)^{part} + \alpha(\hat{r},\lambda)^{mol} d\hat{r}\right]}. \quad (2.11)$$

In summary, working with Raman lidar systems allows the independent derivation of $\beta(r,\lambda)^{part}$ and $\alpha(r,\lambda)^{part}$ and, thus, the LR (Eq. 2.5) can also be derived. A limitation of the Raman technique lies on the weak Raman scattering cross-sections. This means that long temporal averaging of the backscattered signals is needed in order to reduce the statistical uncertainties of the solutions. Besides the $\beta(r,\lambda)^{part}$ and $\alpha(r,\lambda)^{part}$, which are extensive parameters, some additional optical properties can be derived using the ratio of $\beta(r,\lambda)^{part}$ at different wavelengths and polarization states. The derived properties are intensive, which means they do not depend on the particle number concentration. Some of the most common intensive optical properties are the following:

- Color ratio (CR, decreasing with particle size)

$$CR(r)^{part} = \frac{\beta(r,\lambda_1)^{part}}{\beta(r,\lambda_2)^{part}},\ with\ \lambda_1 < \lambda_2. \quad (2.12)$$

- An alternative definition is the backscatter (or extinction) related Ångström exponent (decreasing with particle size), which is more commonly used in aerosol studies

$$A(r)^{part}_{\beta(\lambda_1/\lambda_2)} = -\frac{ln\left[\frac{\beta(r,\lambda_1)^{part}}{\beta(r,\lambda_2)^{part}}\right]}{ln\left(\frac{\lambda_1}{\lambda_2}\right)},\ with\ \lambda_1 < \lambda_2. \quad (2.13)$$

- Linear particle depolarization ratio (LPDR, increasing with particle asphericity)

$$LPDR(r,\lambda) = \frac{\beta(r,\lambda)^{\perp,part}}{\beta(r,\lambda)^{\parallel,part}}. \quad (2.14)$$

To some extent it is possible to classify aerosol based on their intensive optical properties. As demonstrated in Fig. 2.1, pollution, smoke and marine aerosol are nearly-spherical (LPDR below 10%), while dust and volcanic ash are characterized by high LPDR. Mixtures of dust and smoke exhibit intermediate LPDR and their properties overlap with those of dust. It should be noted that the properties of pollution aerosol fall within the range of smoke aerosol since both of them are combustion particles. Finally, it should be noted that for KARL and AMALi observations, the depolarization ratio of molecules was considered equal to 1.43% following Behrendt and Nakamura (2002).

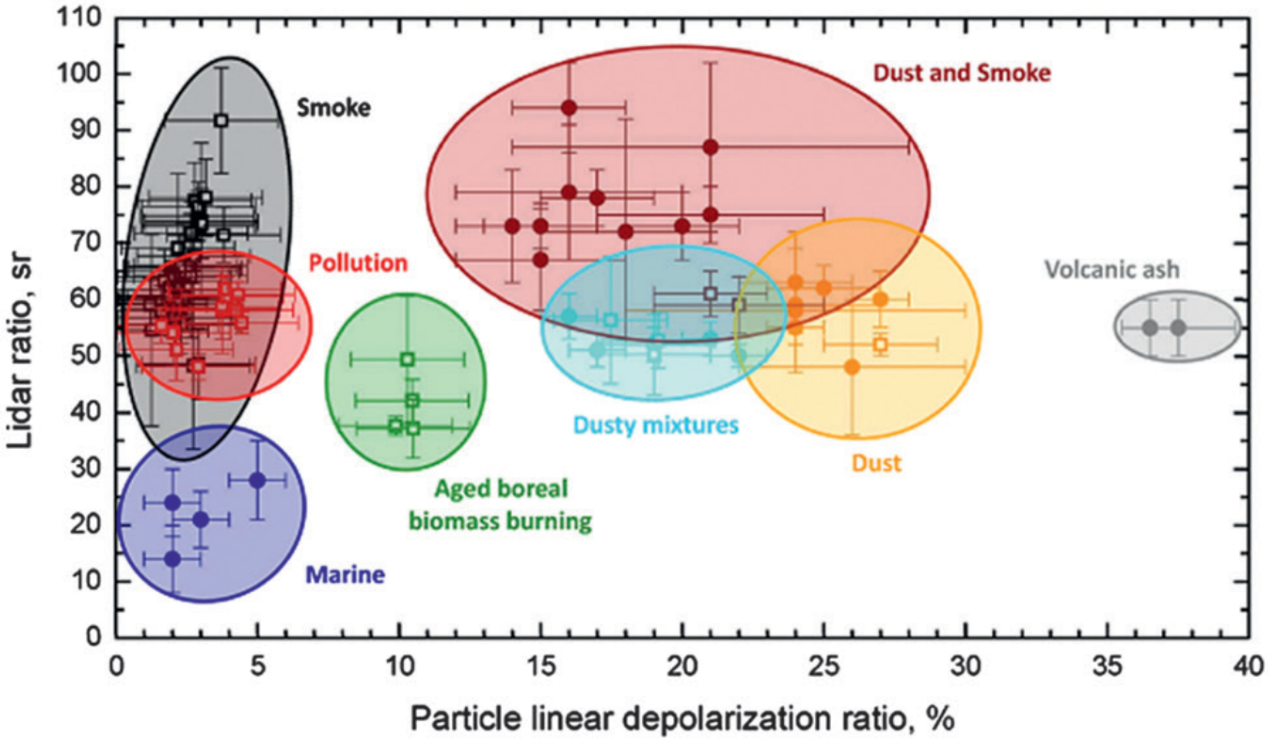

Fig. 2.1: Aerosol classification based on LR and LPDR at 355 nm as obtained from different measurement campaigns. *Adapted from Illingworth et al. (2015), their Fig. 8.*

2.2 lidar systems

In this work, observations from three lidar systems were exploited. The combined analysis of ground-based, air-borne and space-borne lidar observations gives insight into the spatio-temporal variability of aerosol layers and provides an overview on the aerosol conditions over a broad region. In the following, a summary description of each system and its connection to this work is provided.

2.2.1 Ground-based system KARL

KARL is a multi-wavelength system operated at the Alfred Wegener Institute Emille Victor (AWIPEV) research base [3], Ny-Ålesund (Fig. 2.2). In this work, KARL is employed for investigating the properties of aerosol (Chapter 3) and cirrus clouds (Chapter 5). The technical development along with a detailed description of KARL is given in the dissertation of Hoffmann (2011). KARL is a $3\beta + 2\alpha + 2\delta + 2wv$ system. The laser head includes an oscillator and an amplifier, each of them consisting of two Nd:YAG crystal rods pumped at 50 Hz by flash lamps. The light (1064 nm) exiting the amplifier is directed towards a harmonic generation crystal, which generates light at 532 nm and 355 nm after frequency doubling and tripling. KARL is a powerful system emitting approximately 10 W in each wavelength (approximately 200 mJ per pulse). Before emitted into the atmosphere the laser beam is expanded

3 https://www.awipev.eu/

by a beam widening telescope so as to reduce its angular divergence (about 0.8 mrad).

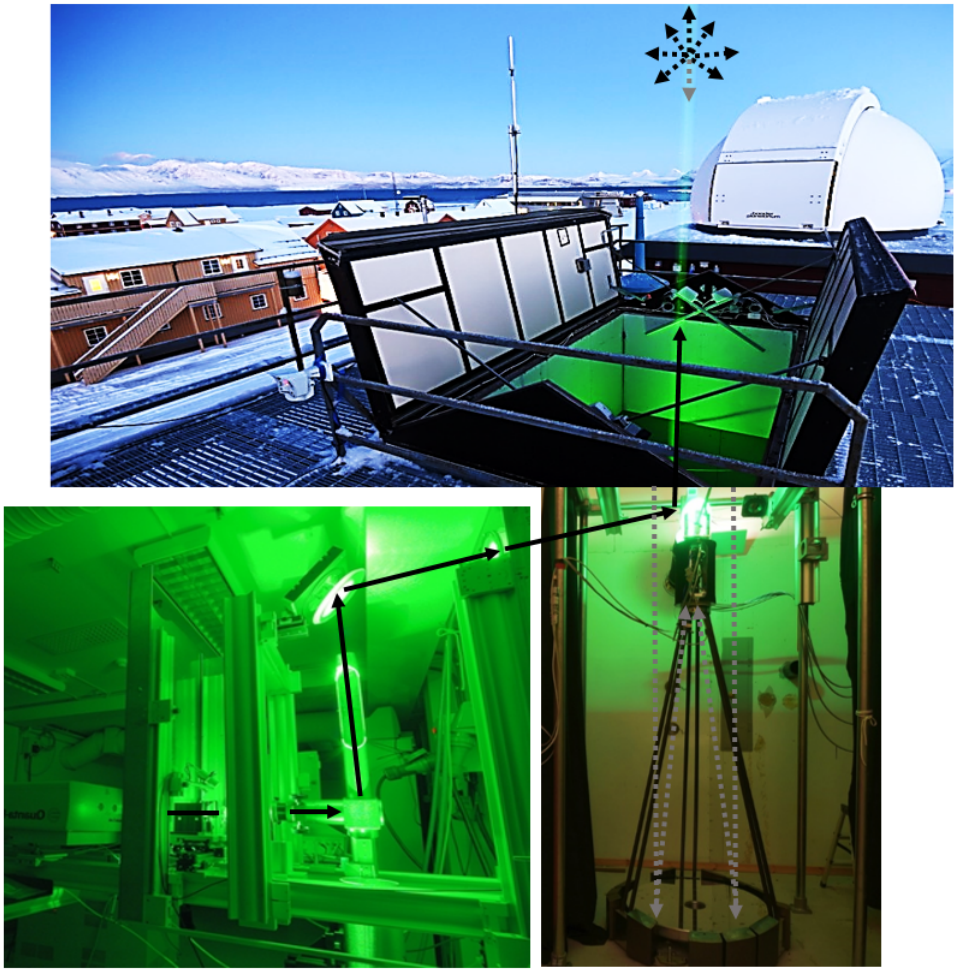

Fig. 2.2: The main components of KARL. Emitting unit, hatch with outgoing laser beam and receiving telescope.

KARL's receiver consists of a 70 cm diameter Newtonian telescope with a 2.28 mrad FOV, which is in co-axial configuration with the emitted laser beam. The light collected by the telescope passes through a pinhole as well as a collimation lens and, finally, it is transferred to the optical analyzing system via quartz fibers. The optical analyzing system consists of four boxes located above the telescope. The spectral separation is performed by dicroic mirrors and the light is subsequently filtered by neutral density and interference filters. The 1^{st} box filters the components of 355 nm light that are inelastically-scattered (at 387 and 407 nm). Ultraviolet light may produce fluorescence inside the glass fibers and, thus, it is desirable to isolate any artifacts as early as possible in the optical path. The two following boxes separate 355 and 532 nm light into orthogonal polarization planes. The 4^{th} box separates the 1064 nm from the 532 nm inelastically-scattered light (at 607 and 660 nm). After passing through another collimation lens the light components are directed into a photomultiplier tube (PMT, 355 and 532 nm elastic and Raman channels) or an avalanche photodiode (APD, 1064 nm), which are located in a temperature stabilized room. Both devices rely on the photoelectric effect and current amplification to obtain an output voltage within a dynamic range that is

linear to the number of incident photons. PMTs are affected by low dark current noise but their quantum efficiency is modest. APDs are usually used for detecting light at 1064 nm due to their high quantum efficiency in this wavelength, which compensates for their high dark current (Hunt et al., 2009). Finally, the output photocurrent is counted by transient recorders at 20 MHz digitization frequency, which corresponds to a vertical resolution of 7.5 m. The photocurrent acquisition is performed in PC and A modes (Sec. 2.1.2. KARL signal returns are obtained with 1.5 min resolution (4096 pulses). It should be noted that KARL is not in *24/7* operation. In general, more KARL observations are available in late winter – spring thanks to dedicated *Arctic haze* measurement campaigns. On the other hand, fewer measurements are performed in the summer due to the frequent presence of low-level clouds and the increased air traffic over Ny-Ålesund (KARL should be turned off for eye safety reasons).

2.2.2 Air-borne system AMALi

AMALi is a dual-wavelength elastic backscatter system installed on the research aircraft Polar5, operated by the Alfred Wegener Institute (AWI). The optical assembly of AMALi is depicted in Fig. 2.3. The system development and technical specifications are described in detail by Stachlewska et al. (2010). AMALi observations were used for investigating a long-range transport event over Fram Strait and its modification with respect to neighboring locations (Sec. 3.1). AMALi can be operated in zenith or nadir configuration, with the former one used in this work.

AMALi is equipped with an Nd:YAG laser that emits pulses at 355 and 532 nm with a repetition rate of 15 Hz and has to be switched off above 3 km, which is the maximum nominal operation height for the laser. A 10 cm off-axis telescope mirror of 3.1 mrad FOV collects the backscattered light, which is in co-axial configuration with the laser beam. A full overlap is achieved at a range of about 235 m. The received light is directed into the optical analyzing system, after passing through two folding mirrors with a pinhole in between and, finally, it is collimated by an achromatic lens. The wavelength separation is performed by dicroic mirrors, while a polarizing beamsplitter cube separates light at 532 nm in two orthogonal polarization components. The spectral purity of the light is assured by narrow-band interference filters. Cross-talk from the co- to the cross-polarization sensitive channel is suppressed by a thin film polarizing filter. Additionally, neutral density filters adjust the light intensity to the dynamical range of the detectors. PMTs are used for the detection of the different light components. AMALi signal returns are acquired with 1 s – 7.5 m resolution by transient recorders, in PC and A mode. In addition to the corrections described in Sec. 2.1.2, the AMALi profiles are corrected for the aircraft attitude (pitch and roll angles).

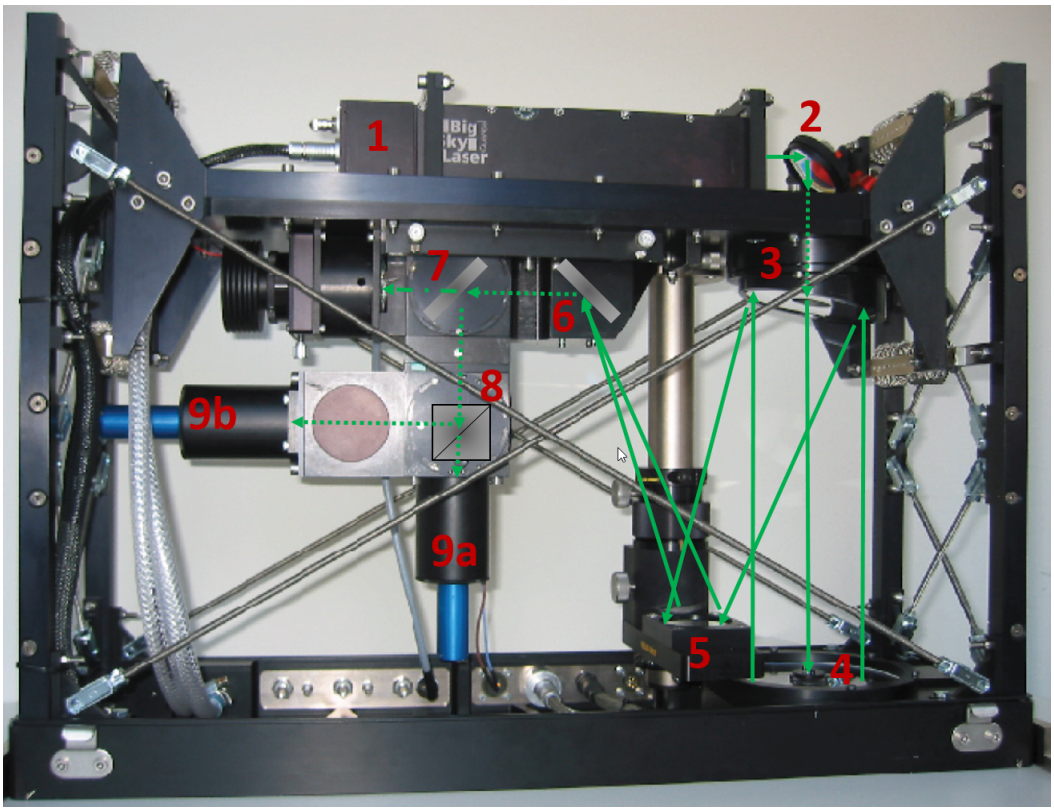

Fig. 2.3: The optical assembly of AMALi comprising the laser head (1), directing mirror (2), off-axis parabolic mirror (3), window with Brewster's angle (4), first folding mirror (5)and pinhole (6). The optical analyzing system consists of wavelength (7) and polarization state separation components (8) with each light component detected by a PMT (9a and 9b). *Adapted from Stachlewska et al. (2010).*

2.2.3 Space-borne system CALIOP

Cloud-Aerosol lidar with Orthogonal Polarization (CALIOP) is a space-borne system on board of Cloud-Aerosol lidar and Infrared Pathfinder Satellite Observations (CALIPSO). Near-global coverage, with 16-day revisit time, is provided up to $81.8^{o}N$ owing to CALIPSO's orbital configuration (98.2^{o} inclination). CALIOP is a dual-wavelength polarization sensitive elastic backscatter lidar, emitting linearly polarized light at 532 and 1064 nm. The separation of the backscattered light at 532 nm into two orthogonal polarization components (parallel and perpendicular polarization planes with respect to the emitted light) enables the derivation of the volume depolarization ratio. CALIOP produces ground footprints of 70 m diameter every 355 m along track (20.6 Hz pulse repetition rate, Winker et al., 2009), which move at nearly 7 kms^{-1}. In this work, CALIOP observations provide a broad picture of the aerosol conditions during the investigated spring-time (Sec. 3.1) and winter-time events (Sec. 3.3).

The latest version (4^{th}) of CALIOP products, released in November 2016, is used here. Several improvements have been implemented relative to the 3^{rd} product version. One substantial change relevant to the Polar regions is the raise of any aerosol classification constraints. While in the previous versions the aerosol classification algorithm was limited to

clean continental and polluted continental aerosol over ice, snow and tundra, the current algorithm is allowed to select any of the available aerosol sub-types (Kim et al., 2018). CALIOP provides three main categories of L2 products (profile products, the vertical feature mask and layer products). The derivation of layer products requires horizontal averaging (5, 20 or 80 km) in order to obtain a higher SNR. Weakly scattering features, such as thin aerosol and cirrus clouds, are usually reported at coarser horizontal resolution. The L2 processing chain consists of three main steps. Firstly, the identification of aerosol and cloud layers is performed by means of an iterative boundary locator, which is applied on the profiles of attenuated backscatter at 532 nm (Winker et al., 2009). Subsequently, a scene classification algorithm is used for typing the detected layers. In the final step, particle backscatter and extinction profiles are retrieved (Winker et al., 2009).

In the analysis performed here different L2 products were used, depending on their availability and quality level [4]. Data quality control is necessary prior to any further investigation. A quality filter is related to distinguishing aerosol from cloud layers. The efficiency of cloud – aerosol discrimination (CAD) is expressed by a confidence function, with negative values corresponding to aerosol features and non-negative ones to cloud features (ranging from -1 to $+1$). Subsequently, the confidence function is converted to the $CAD\ score$ (ranging from -100 to $+100$), whose absolute value provides a confidence level for the classification (Liu et al., 2019). In this work, only layers with $CAD\ score$ between -100 and -80 were selected for the analysis of aerosol (Chapter 3). Another quality control flag is related to the type and outcome of the extinction retrievals ($Extinction - QC$ flag). The $Extinction - QC$ flag, provided in the L2 aerosol layer and aerosol profile products, was examined and only values equal to 0, 1, 16 or 18 were kept (Winker et al., 2013). In brief, a value of 0 denotes unconstrained extinction retrievals, i.e. retrieval with unmodified LR. A value of 1 corresponds to retrievals constrained by the measured two-way transmittance (Young et al., 2018). A value of 16 (18) refers to unconstrained (constrained) retrievals for opaque layers (Winker et al., 2013). In this work, the majority of screened $Extinction - QC$ values were 0 and 1. Additionally, the $opacity\ flag$ was checked but very few layers were affected. Finally, unrealistic values were screened out from the L2 aerosol profile products. More specifically, Ångström exponent values lower than -0.5 or higher than 4 as well as negative LPDR or higher than 100% values were discarded.

4 More details on the L2 aerosol layer and profile products are available at https://www-calipso.larc.nasa.gov/resources/calipso_users_guide/data_summaries/layer/ and https://www-calipso.larc.nasa.gov/resources/calipso_users_guide/data_summaries/profile_data_v420.php, respectively.

2.3 Ancillary instrumentation

2.3.1 Radiosondes

Radiosondes are launched daily from AWIPEV at 11 UTC. Moreover, during dedicated campaigns, such as the Year of Polar Prediction, radiosondes are launched four times per day i.e. 5, 11, 17 and 23 UTC. The radiosondes provide useful meteorological information up to about 30 km. Concerning the analysis of aerosol and cirrus optical properties, the pressure and temperature information is necessary for the estimation of the molecular scattering and extinction profiles. Additionally, temperature is a crucial parameter for masking cirrus clouds, using the homogeneous nucleation temperature criterion (Chapter 4). Temperature, wind speed and wind direction information is also useful for investigating the meteorological dependencies of cirrus properties (Chapter 5). In this work two different types of radiosondes were used. The Vaisala RS92 was applied for years before 2018, while the Vaisala RS41 was used afterwards. The manufacturer provides estimates of the combined uncertainties, these being 0.2–0.4 K for temperature as well as 1 hPa (>100 hPa) and 0.6 hPa (100–3 hPa) for pressure. The daily radiosonde ascent data is available via the Pangea repository (e.g. (Maturilli, 2019b)).

2.3.2 Sun-photometers

Over Ny-Ålesund the aerosol optical depth (AOD) was measured by a SP1a type sun-photometer in 10 wavelengths between 369 and 1023 nm. The instrument has a 1^o FOV. The 1-min time resolution provides sufficiently high data quality due to the low random noise of the instrument and the total AOD uncertainty amounts to 0.01 (Graßl and Ritter, 2019). A cloud screening procedure that relies on the short-term AOD variability was applied to the data (Alexandrov et al., 2004). Additionally, an air-borne sun-photometer with an active tracking system (SPTA) is operated under a quartz dome on the top of Polar5 aircraft. The AOD is provided at 10 wavelengths between 396 and 1026 nm every 30 sec. Unfortunately, the 369–414 nm channels presented calibration issues during Polar Air-borne Measurements and Arctic Regional Climate Model Simulation Project (PAMARCMiP) 2018 and, thus, they were not used for further evaluation here. Moreover, the 946 nm channel, which is dedicated to water vapor absorption, was not used.

2.3.3 Radiation sensors

Ground-based and air-borne irradiance observations were utilized for evaluating modeled irradiances at the surface and at flight level (Sec. 3.1.3). At Ny-Ålesund, radiation measurements are performed within the frame of the Baseline Surface Radiation Network (BSRN) since 1992 (Maturilli, Herber, and König-Langlo, 2015). Short-wave (SW) broadband radiation in the range of 0.2–3.6 μm is measured with CMP22 pyranometers by $Kipp\ \&\ Zonen$, installed in up- and down-ward orientation for global and reflected radiation, respectively. In

addition, the diffuse radiation is obtained by ball-shaded similar instrumentation. The basic surface radiation and meteorological measurements with 1-min resolution applied here are available via the Pangaea data repository (e.g. (Maturilli, 2019a)). Radiation sensors were also installed on the top and bottom of the Polar5 fuselage during PAMARCMiP2018. More specifically, a CMP22 Pyranometer by $Kipp\ \&\ Zonen$ was measuring broadband (0.2–3.6 μm) global and reflected solar irradiances. The measurement repetition rate was 20 Hz.

2.4 Modeling tools

2.4.1 Air mass backward trajectories

In order to assess the origin of aerosol transport events and link the evolution of aerosol properties with intruding air masses, 10-day LAGRANTO backward trajectories were performed (Wernli and Davies, 1997; Sprenger and Wernli, 2015). Three-dimensional wind field data from ECMWF reanalysis was used to calculate kinematic trajectories with LAGRANTO. The ECMWF data for this study had a horizontal grid spacing of 0.5^o x 0.5^o with 137 hybrid sigma pressure levels in total. Analysis fields were available every six hours. For the flight locations over Fram Strait (Fig. 3.2), trajectories were initialized in a small region around the flight track (Sec. 3.1.1). Trajectories from Ny-Ålesund were initialized every 0.05^o in the horizontal within a 0.5^o x 0.5^o box centered at Ny-Ålesund (Fig. 3.4). Trajectory information was then available every hour. Ancillary meteorological parameters, such as pressure and relative humidity (RH), were calculated along the trajectories. The spatial variability of the trajectories was taken into account by using a box, instead of a single point, for initializing the calculations. Moreover, the influence of atmospheric variability was considered by analyzing coherent bundles of trajectories instead of single trajectories. Due to the complex orography of the Spitsbergen island, with the highest peak at 1.7 km, and the challenging to parameterize Arctic boundary layer, higher altitude trajectories are considered more reliable. Therefore, trajectory calculations were only performed for a high tropospheric transport event (Sec. 3.1).

2.4.2 Aerosol microphysics retrieval algorithm

The aerosol microphysics can be inverted from the aerosol optical parameters. In the inversion schemes, developed in the University of Potsdam, the extinction and backscatter coefficients are used to derive the complex refractive index and the aerosol volume size distribution by means of Mie theory. In this work, the input for the microphysics retrieval was obtained from KARL (AMALi – sun-photometer synergistic) observations, comprising β_{355}, β_{532}, β_{1064}, α_{355} and α_{532} (β_{355}, β_{532}, α_{496}, α_{675}, α_{779}, α_{861} and α_{1026}). The inversion of particle microphysics is an ill-posed problem. More specifically, even small errors in the input might be amplified in the solution. Therefore, the inversion of the volume distribution requires discretization, regularization and a parameter choice rule. Statistical noise and systematic uncertainties in the input together with mathematical approximation errors (regularization and

fitting procedures) contribute additively to the total solution uncertainties. The best solution is provided as the least residuum between the backward (input) and forward Mie calculated optical parameters, for each combination of the real and imaginary refractive index. It should be noted that the refractive index was considered as wavelength-independent, which is a common assumption. More information on the uncertainties is given for each individual retrieval (Sec. 3.1 and 3.3).

The total number, surface-area and volume concentration as well as the effective radius were derived separately for the fine and coarse aerosol modes by performing log-normal fits to the inverted volume distribution. Simulations with synthetic optical data have revealed that a retrieval accuracy of 20% can be achieved in the size parameters, with the total surface-area concentration being the most stable retrieved parameter (Müller et al., 2016). More details about the aerosol microphysics inversion algorithms can be found in Böckmann (2001), Samaras et al. (2015), and Müller et al. (2016).

The model relating the optical parameters $\Gamma(\lambda)$ with the volume size distribution $v(r)$ is described by a Fredholm integral operator of the first kind with a kernel function $K(r, \lambda, m)$

$$\Gamma(\lambda) = \int_{rmin}^{rmax} K(r, \lambda, m) \cdot v(r) dr. \tag{2.15}$$

with $K(r, \lambda, m) = \frac{3 \cdot Q(r, \lambda, m)}{4 \cdot r}$. In Eq. 2.15, λ denotes the wavelength, r the particle radius, $\Gamma(\lambda)$ stands for the aerosol extinction (or backscatter) coefficient, while $Q(r, \lambda, m)$ stands for the extinction (or backscatter) Mie efficiency (dimensionless). Identifying $\Gamma(\lambda)$ as the measurement data and $v(r)$ as the unknown volume distribution, the problem reduces to the inversion of Eq. 2.15. Knowing the volume distribution, the following microphysical parameters can be derived:

- total surface-area concentration ($\mu m^2 cm^{-3}$)

$$s_t = 3 \cdot \int_{rmin}^{rmax} \frac{v(r)}{r} dr \tag{2.16}$$

- total volume concentration ($\mu m^3 cm^{-3}$)

$$v_t = \int_{rmin}^{rmax} v(r) dr \tag{2.17}$$

- total number concentration (cm^{-3})

$$n_t = \frac{3}{4\pi} \cdot \int_{rmin}^{rmax} \frac{v(r)}{r^3} dr \tag{2.18}$$

- effective radius (μm)

$$r_{eff} = 3 \cdot \frac{v_t}{s_t} \tag{2.19}$$

By utilizing Mie theory together with the retrieved $n(r)$ and refractive index, forward calculations of the aerosol scattering ($\alpha(\lambda)_{sca}^{part}$) and absorption coefficients ($\alpha(\lambda)_{abs}^{part}$) can be performed. Hence, the single-scattering albedo (SSA) can be calculated as

$$SSA(\lambda) = \frac{\alpha(\lambda)_{sca}^{part}}{\alpha(\lambda)_{sca}^{part} + \alpha(\lambda)_{abs}^{part}}. \tag{2.20}$$

The lower the SSA the more absorbing aerosol is and vice versa. Additionally, using the scattering phase function ($P(cos\theta)$), the asymmetry parameter (g) can be derived as

$$g = \frac{1}{2} \cdot \int_{-1}^{1} P(cos\theta) \cdot cos\theta dcos\theta. \tag{2.21}$$

The g provides an indication on the angular distribution of scattered light. For isotropic scattering (Rayleigh scattering) g is zero, while for the scattering from aerosol, g denotes the relative strength of forward-scattering (bigger aerosol exhibit higher g, (Schmeisser et al., 2018)).

2.4.3 Radiative transfer model SCIATRAN

In order to quantify the altitude-dependent aerosol radiative effect (ARE) and its uncertainties, simulations were performed with the radiative transfer model SCIATRAN (Rozanov et al., 2014) [5]. To this end, the derived aerosol optical and microphysical properties were incorporated into the model. For evaluating the simulated irradiances, a spectral integration within the range of the BSRN and air-borne pyranometers (Sect. 2.3.3) was performed.

The radiative transfer equation is solved by means of the scalar discrete ordinate technique, using a plane-parallel atmosphere approximation. The simulations were performed from the local surface up to 40 km, which can be considered as the top of the atmosphere (TOA) since it includes the contribution from the whole stratospheric ozone (O_3) layer as well as the whole water vapor (WV) column. The vertical resolution varied from 50 m (below 10 km) to 1 km (above 10 km). The absorption contribution of line absorbers was computed in line-by-line mode of 0.01 nm spectral resolution, based on the wavelength-, pressure- and temperature-dependent spectroscopic parameters of the HITRAN 2008 database (Rothman et al., 2003). The surface albedo over Fram Strait and Ny-Ålesund was obtained from air-borne and BSRN pyranometer observations, respectively. A surface albedo of approximately 0.7 was found for both locations, revealing the presence of sea ice at Fram Strait and snow-covered tundra at Ny-Ålesund. For Fram Strait, thermodynamic profiles were constructed as a combination of appropriately selected air-borne meteorological observations below 5 km and radiosonde ascents from Ny-Ålesund aloft (approximately 500 km distance from flight operations). Between 5 and 8 km, a hybrid air-borne – radiosonde profile was constructed, which gradually shifted from the highest air-borne towards the radiosonde observations. For Ny-Ålesund, pressure, temperature, WV mixing ratio and O_3 concentration

5 The SCIATRAN model is written in FORTRAN and it is available at https://www.iup.uni-bremen.de/sciatran/ upon request to the developers.

profiles were taken from a collocated ozonesonde ascent. For both Arctic locations, further trace gases profiles (CO_2, CO, CH_4, NO_2 and O_2) were obtained from climatological profiles for the given month and latitude, computed with the Bremen-2D chemical transport model (Sinnhuber et al., 2009).

The aerosol related input comprised the spectrally-resolved aerosol extinction coefficient, the SSA as well as the asymmetry parameter. The aerosol optical and microphysical properties were extrapolated (from 355–1026 nm) to the model's spectral range by forward Mie calculation. More specifically, using the aerosol refractive index and number size distribution as input, the aerosol extinction coefficient can be calculated at any wavelength. In order to distinguish the altitude-dependent ARE (Eq. 2.23) from the total atmospheric effect, an aerosol scenario together with an off-aerosol scenario was simulated. In Eq. 2.22 and Eq. 2.23, F denotes the broadband SW irradiances (in W m^{-2}). The ARE within the atmospheric column (Eq. 2.24) was defined as the difference between the TOA (source term) and surface ARE (sink term). Here the definition of ARE is closer to the instantaneous forcing, which is the net irradiance due to an imposed change, without taking into account any rapid adjustments (Bellouin et al., 2020b).

$$F(z)^{net} = F(z)^{global} - F(z)^{reflected} \tag{2.22}$$

$$ARE(z) = F(z)^{net}_{total} - F(z)^{net}_{off-aerosol} \tag{2.23}$$

$$ARE_{atm.column} = ARE_{TOA} - ARE_{surface} \tag{2.24}$$

The net irradiances can also be used to estimate the atmospheric heating rate (HR in $Kday^{-1}$, Quinn et al., 2007). The $HR(z)$ is derived from the F^{net} at two different atmospheric levels (z and $z + \Delta z$) as

$$HR(z)_{tot} = \frac{\Delta T}{\Delta t}(z) = \frac{g}{C_p} \cdot \frac{F(z+\Delta z)^{net} - F(z)^{net}}{P(z+\Delta z)^{net} - P(z)^{net}} \cdot 86,400. \tag{2.25}$$

In Eq. 2.25 g denotes the gravitational acceleration (9.81 ms^{-2}), while C_p refers to the specific heat capacity of air (C_p = 1006 $JK^{-1}kg^{-1}$ at 300 K). P is the atmospheric pressure. Finally, in order to derive the contribution of aerosol (Eq. 2.26), the off-aerosol HR was subtracted from the total HR as in Donth et al. (2020).

$$HR(z)_{aer} = HR(z)_{tot} - HR(z)_{off-aer} \tag{2.26}$$

2.4.4 Multiple-scattering correction model

Big particles, such as ice crystals, exhibit a strong forward-scattering peak due to light diffraction. Thereby, the forward-scattered photons remain within the lidar receiver's FOV and travel with the laser pulse. As a result, some of the backscattered photons can be further scattered (one or multiple times) in the forward direction before reaching the lidar detector. The multiple-scattering effect needs to be corrected as the lidar equation assumes that each detected photon originates from a single-scattering event in the atmosphere (Weitkamp, 2006). A first parameterization of the multiple-scattering effect, introduced by Platt (1973), assumed a sole dependence on the cloud optical depth (COD). Eq. 2.27 describes the simple multiple-scattering correction (MSC) factor n, with the MSC COD being the ratio of the apparent COD over the factor n.

$$n = \frac{COD}{e^{COD} - 1} \tag{2.27}$$

However, the multiple-scattering effect does not only depend on the COD but also on the ice crystal effective radius (r_{eff}) and laser beam cloud penetration depth. Additionally, the effect is more pronounced if the lidar system has a wide receiver FOV and a non-negligible laser beam divergence. For this reason, an analytical model is needed in order to correct for high order scattering events. In this work, the MSC model of Eloranta (1998) was used [6]. The Eloranta model assumes the presence of hexagonal ice crystals for phase function calculations. Additionally, a mono-disperse ice crystal vertical distribution was applied. The ice crystal r_{eff} was estimated as a quadratic function of temperature, following the parameterization of Wang and Sassen (2002)

$$r_{eff} = 90.14 + 0.659 \cdot T - 0.004 \cdot T^2. \tag{2.28}$$

The model simulates the ratio of up to 7^{th} order (P_{tot}) to single-scattering photon power (P_1) as a function of range (r) and wavelength (λ). Sensitivity tests revealed that higher than 4^{th} order scattering events contributed negligibly to the total photon power. Therefore, the first four scattering orders were finally taken into account as a compromise between accuracy and computational speed. Initially, the apparent extinction (α_{app} or β_{part} multiplied by the LR_{ci}) was incorporated into the model and a first estimation of the MSC factor $F(r, \lambda)$ (Eq. 2.29) as well as the quasi-corrected extinction $(\alpha(r, \lambda))$ (Eq. 2.30) were obtained. Subsequently, the quasi-corrected extinction was re-incorporated into the MSC model and this recursive procedure was repeated until the model converged to a stable $F(\lambda$,r). Usually, only two iterations provided sufficient convergence (Nakoudi, Stachlewska, and Ritter, 2021).

$$F(r, \lambda) = \frac{\frac{d}{dr} \ln \frac{P_{tot}(r)}{P_1(r)}}{2 \cdot \alpha_{app}(r, \lambda) + \frac{d}{dr} \ln \frac{P_{tot}(r)}{P_1(r)}} \tag{2.29}$$

$$\alpha(r, \lambda) = \frac{\alpha_{app}(r, \lambda)}{1 - F(r, \lambda)} \tag{2.30}$$

6 The Eloranta MSC model written in C and the software is available at http://lidar.ssec.wisc.edu/multiple_scatter/ms.htm.

In this work, the MSC was applied on the extinction of cirrus layers (Sec. 5.2). Additionally, the LR and COD quantities were corrected using a vertically averaged $F(\lambda)$. The analytical and simplified MSC approaches are compared in App. C.

2.4.5 Simplified cloud radiative effect model

Apart from the ARE, the cirrus cloud radiative effect (CRE) is also assessed in this work. To this end, the simplified model of Corti and Peter (2009) was employed, which provides CRE estimates at TOA. The Corti–Peter model uses simple parameterizations of the SW and long-wave (LW) CRE with a few free parameters, aiming at acceptable accuracy with the lowest possible complexity [7]. The free parameters were estimated from the Fu–Liou radiative transfer model (Fu and Liou, 1992; Fu and Liou, 1993) using regression analysis. The parameterization was developed using a broad range of atmospheric conditions and cloud properties from reanalysis data (Corti and Peter, 2009). A plane-parallel atmosphere approximation is used. Additionally, all ice crystals are assumed to be hexagonal columns along with a cloud geometrical thickness of 1 km. The input parameters of the model include the COD, the surface albedo, the solar zenith angle (SZA), the surface temperature (T_{surf}) as well as the temperature at the cloud top ($T_{C_{top}}$). The Corti–Peter model has been applied to multi-year cirrus cloud observations over three mid-latitude sites (Kienast-Sjögren et al., 2016).

SW irradiances originate mainly from the Sun and they are represented in the visible and near-infrared spectral regions (0.4–4 μm). LW irradiances are mainly of terrestrial origin and they correspond to wavelengths longer than 4 μm in the parameterization. Comparisons with Fu-Liou radiative estimates revealed a mean error of 7% (10%) in the CRE^{SW} (CRE^{LW}, Corti and Peter, 2009). Lolli et al. (2017b) underlined that differences can be significantly higher for T_{surf} above 15^oC due to the decreased accuracy of the Corti–Peter regression analysis in this temperature regime. However, the T_{surf} over Ny-Ålesund does not exceed 5^oC on a seasonal basis (Maturilli, Herber, and König-Langlo, 2013) and, thus, the derived CRE is believed to be reliable as a first order estimate. The CRE^{SW} and CRE^{LW} are computed as the difference in TOA irradiance between an *all-sky* and a *cloud-free scenario*. Under a *cloud-free scenario* the SW irradiance can be expressed as

$$F^{SW}_{cloud-free} = I \cdot (1 - R - t \cdot t' \cdot \alpha). \tag{2.31}$$

In Eq. 2.31 I is the incident solar irradiance at TOA and R is the reflectivity of the atmosphere. The direct solar irradiance is propagated downwards in the atmosphere with transmittance t and it is reflected by a surface of albedo a. The diffuse irradiance is propagated upwards with transmittance t'. Under *all-sky conditions* the atmosphere is approximated by a three-layer (above cloud, cloud and below cloud layer) plane-parallel model. Multiple reflections between the cloud and the surface are taken into account but multiple reflections within each individual layer are neglected. Additionally, all atmospheric reflection and absorption is

7 An online version of the Corti–Peter model is available at http://www.iac.ethz.ch/url/crf.

assumed to occur above the cloud and the cloud layer is considered non-absorbing in the SW spectrum. Thus, $T_c = 1 - R_c$, with T_c (R_c) denoting the cloud transmittance (reflectivity). Under *all-sky conditions* the SW irradiance can be approximated as

$$F^{SW}_{all-sky} \approx I \cdot \left(1 - R - t \cdot t' \cdot \alpha - (1-\alpha) \cdot t \cdot t' \cdot \frac{R_c - \alpha \cdot R'_c}{1 - \alpha \cdot R'_c}\right). \tag{2.32}$$

The reflectivity R_c of the cloud layer with respect to the incident irradiance can be approximated as

$$R_c \approx \frac{COD_{eff}}{\gamma^* + COD_{eff}}. \tag{2.33}$$

The effective COD is corrected for the SZA as $COD_{eff} = COD/cos(SZA)$. Regarding the reflectivity R'_c of the cloud layer with respect to the upward diffuse irradiance (assumed isotropic), it can be approximated as

$$R'_c \approx \frac{2 \cdot COD}{\gamma^* + 2 \cdot COD}. \tag{2.34}$$

In Eq. 2.33–2.34 γ^* depends on the asymmetry parameter of the cloud particles. The regression analysis of Corti and Peter (2009) yielded an optimal γ^* = 7.7. Finally, by combining Eq. 2.31 and 2.32, the CRE^{SW} at TOA can be expressed as

$$CRE^{SW} = F^{SW}_{all-sky} - F^{SW}_{cloud-free} \approx -I \cdot t \cdot t' \cdot (1-\alpha) \cdot \frac{R_c - \alpha \cdot R'_c}{1 - \alpha \cdot R'_c}. \tag{2.35}$$

In Eq. 2.35 the two-way transmittance $t \cdot t'^*$ above the cloud layer was approximated for daily average SZA conditions. In the Corti–Peter parameterization a typical value of $t \cdot t'^*$ = 0.73 is used.

Under a *cloud-free scenario* the LW irradiance emitted by the Earth surface can be approximated by

$$F^{LW}_{cloud-free} \approx \sigma^* \cdot T^{k^*}_{surf}. \tag{2.36}$$

The regression analysis of Corti and Peter (2009) applied to the computed Fu–Liou irradiances revealed best estimates of σ^* = 1.607 $\cdot$ 10^{-4} $Wm^{-2}K^{-2.528}$ and k^* = 2.528. Under *all-sky conditions* the LW irradiance at TOA can be expressed as

$$F^{LW}_{all-sky} \approx (1 - \epsilon^*) \cdot \sigma^* \cdot T^{k^*}_{surf} + \epsilon^* \cdot \sigma^* \cdot T^{k^*}_{C_{top}}. \tag{2.37}$$

In Eq. 2.37 ϵ^* is the effective cloud emissivity. In the Corti–Peter parameterization the cloud emissivity is assumed to only depend on the COD according to $\epsilon^* \approx 1 - e^{-\delta^* \cdot COD}$. The regression analysis revealed a best estimate of δ^* = 0.75 for the photon diffusivity, a parameter depending on the cloud SSA. The first term in Eq. 2.37 represents the irradiance transmitted through the cloud, while the second term expresses the irradiance emitted by the cloud. By combining Eq. 2.36 and 2.37, the CRE^{LW} can be expressed as

$$CRE^{LW} = F^{LW}_{all-sky} - F^{LW}_{cloud-free} \approx \epsilon^* \cdot \sigma^* \cdot (T^{k^*}_{surf} - T^{k^*}_{C_{top}}) \tag{2.38}$$

Finally, the CRE^{net} at TOA can be simply obtained as the sum of CRE^{SW} (Eq. 2.35) and CRE^{LW} (Eq. 2.38).

3

ARCTIC AEROSOL PROPERTIES AND RADIATIVE EFFECT (CASE STUDIES)

In this Chapter the properties of Arctic aerosol are investigated within the high and low troposphere at case study level. Overall, the aerosol optical and microphysical properties have been thoroughly characterized across different ground stations in the Arctic (Freud et al., 2017; Schmeisser et al., 2018). However, these properties are mostly representative for the near-surface aerosol conditions. Lidar-based studies provide information on the vertical variability of aerosol optical properties (Di Pierro et al., 2013; Ritter et al., 2016). Additional insights can be gained into the aerosol microphysics but their inversion is a complex and non-automated task. Therefore, the microphysics inversion is usually performed at case study level, such as *Arctic haze* (Hoffmann et al., 2009; Stock et al., 2012) and biomass burning events (Ritter et al., 2018).

Here two recent events are selected, one in spring-time high troposphere and one in winter-time low troposphere. Besides the aerosol optical and microphysical properties, the short-wave (SW) aerosol radiative effect (ARE) is characterized in spring (Sec. 3.1). The main results were published in Nakoudi et al. (2020) but here they are extended with CALIOP observations and sensitivities on the ARE and heating rates (HR, Sec. 3.2). In the low-tropospheric event the microphysical properties were obtained from remote sensing inversion and in-situ measurements with the aim to assess their agreement (Sec. 3.3).

3.1 Aerosol in the upper troposphere (Spring)

3.1.1 Overview of aerosol observations and air mass origin

This section focuses on a long-range transport episode, which was identified in high tropospheric altitudes over three parts of the Arctic (North Greenland – East Canadian Archipelago, Fram Strait and Ny-Ålesund) in April 2018 (Fig. 3.1–3.4). Measurements from air-borne, ground-based and space-borne platforms were exploited. Remote sensing observations were used for retrieving the aerosol optical and microphysical properties. The goal is to investigate the modification of aerosol properties across the different locations and, upon their incorporation into a radiative transfer model, to assess the ARE.

Air-borne observations were performed within the frame of Polar Air-borne Measurements and Arctic Regional Climate Model Simulation Project (PAMARCMiP2018) in the vicinity of Villum research station, Greenland (81.6^{o}N, 16.7^{o}W), in March–April 2018. AMALi was operated in zenith configuration on 9 flights (25 March – 4 April for approximately 32 h). The

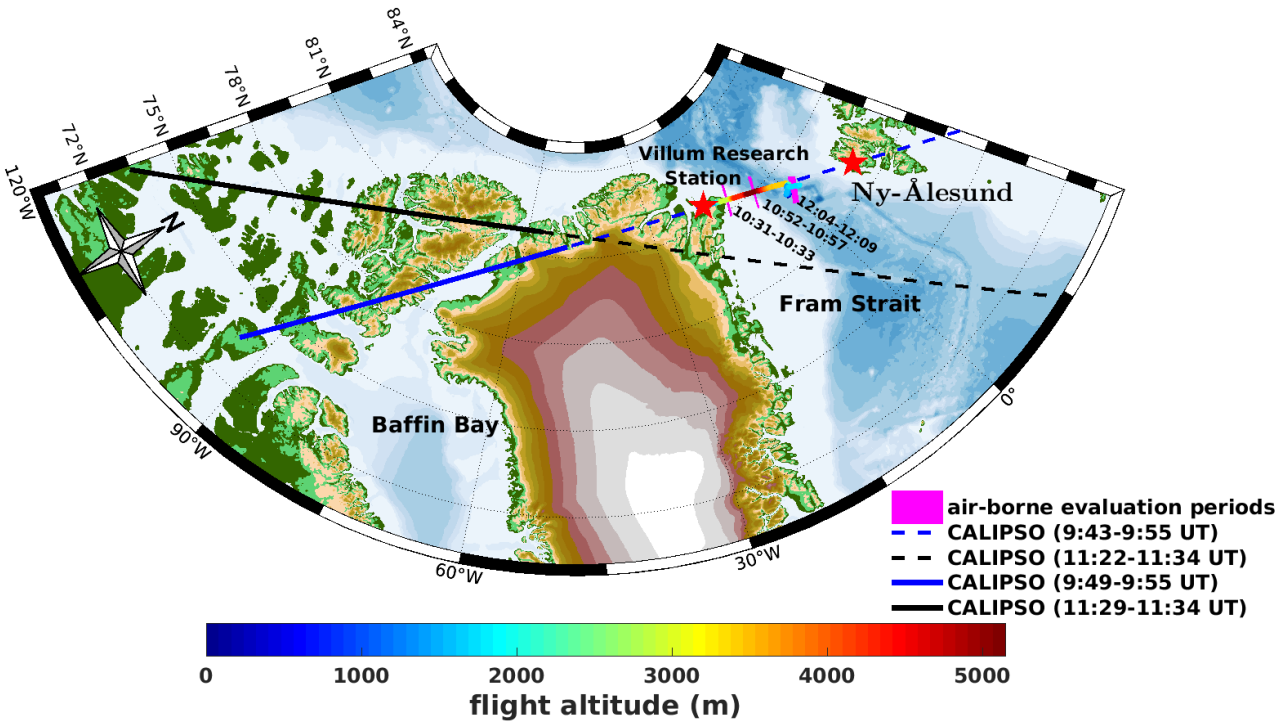

Fig. 3.1: Flight track of Polar 5 (multi-color line) over north Fram Strait on 2 April 2018. The flight altitude is color-indicated. AMALi (10:31-10:33 and 12:04-12:09) and sun-photometer (10:52-10:57) observations were exploited during selected periods (magenta shading). The two spatio-temporally closest CALIPSO ground tracks (selected evaluation periods) are overlaid in blue/black dashed (solid) lines.

PAMARCMiP2018 period was characterized by a high-pressure system over the North Pole, while some weak lows occurred over northeast Greenland. On 2 April, the Polar5 aircraft took off from Villum research station and performed a transect flight over Fram Strait. Along this flight a well-defined aerosol layer was identified by AMALi (Fig. 3.2) and sun-photometer at high tropospheric altitude over the region 81.5, $15.5^{o}NW$ – 80, $5^{o}NE$ (Fig. 3.1). Three short air-borne observation periods (magenta shading in Fig. 3.1) were extracted for aerosol optical retrievals as limited by the changing flight altitude. More specifically, two periods were derived from AMALi observations (red rectangles in Fig. 3.2) and one from the sun-photometer.

During PAMARCMiP2018 the CALIPSO satellite overpassed several times the region of flight operations. On 1–2 April a mixture (polluted dust, smoke and clean continental) of thin elevated aerosol layers was discernible over North Greenland – East Canadian Archipelago. For a detailed investigation of the aerosol optical properties, two CALIPSO overpass periods (indicated in Fig. 3.1) were selected on 2 April as the spatio-temporally closest to the air-borne operations. Geographically extended aerosol layers were identified between 4 and 8 km along both overpasses (Fig. 3.3) [1]. In the earlier period CALIPSO overpassed at a

1 An overview can be found in https://www-calipso.larc.nasa.gov/products/lidar/browse_images/show_v4_detail.php?s=production&v=V4-10&browse_date=2018-04-02&orbit_time=09-02-37&page=4&granule_name=CAL_LID_L1-Standard-V4-10.2018-04-02T09-02-37ZD.hdf and https://www-calipso.larc.nasa.gov/products/lidar/browse_images/show_v4_detail.php?s=production&v=V4-10&

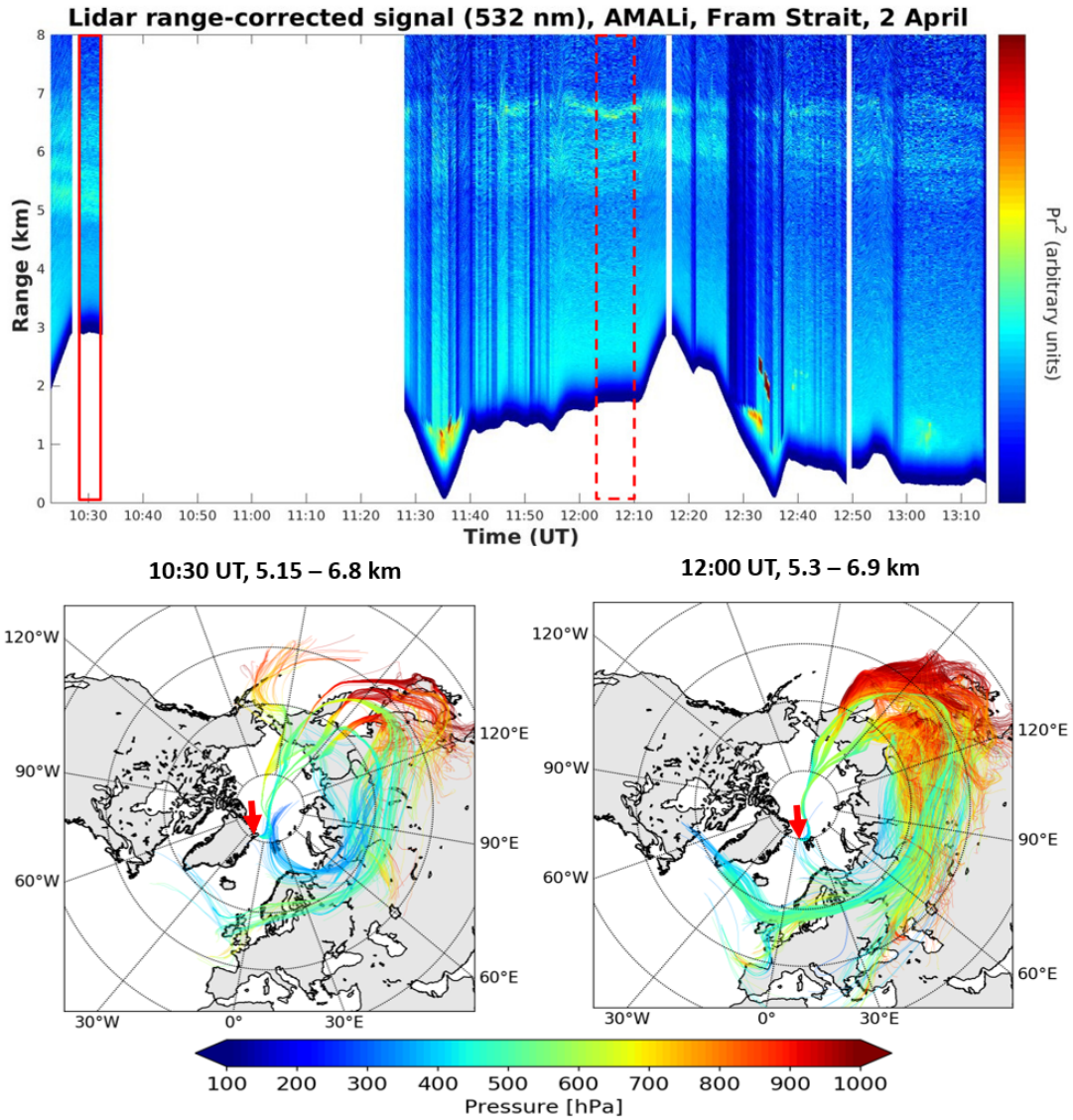

Fig. 3.2: AMALi range-corrected signal and evaluation periods of aerosol optical (and microphysical) properties indicated with dashed (solid) rectangles (upper panel). In some periods (dashed rectangles) only optical properties were available due to the lack of photometer observations. LAGRANTO 10-day backward trajectories ending at the aircraft position (red arrows) for each evaluation period are also presented (lower panels). For the sake of clarity a subset of trajectories is shown.

very close distance from Ny-Ålesund (minimum 1.4 km) and the flight activities region (1.6-26 km). Unfortunately, along this overpass only sparse and weakly scattering aerosol layers were detected over Ny-Ålesund and Fram Strait. Nevertheless, a higher number of stronger scattering layers were identified southwest of the flight operations. The second overpass revealed a higher number of layers but the ground track distances were greater (minimum 424 km from Ny-Ålesund and 218-295 km from flight operations).

browse_date=2018-04-02&orbit_time=10-41-32&page=4&granule_name=CAL_LID_L1-Standard-V4-10.2018-04-02T10-41-32ZD.hdf (last access: 19-04-2021).

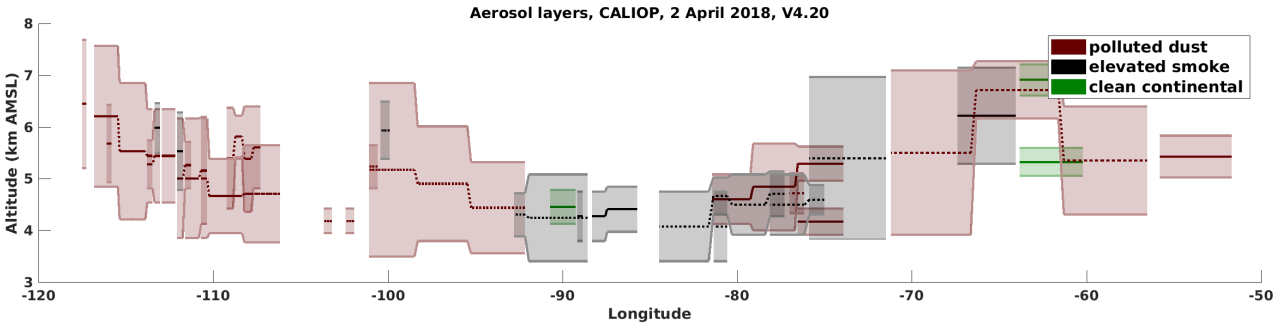

Fig. 3.3: CALIOP-derived aerosol layer base and top over North Greenland – East Canadian Archipelago on 2 April. Different aerosol subtypes are color indicated. Two CALIPSO overpasses were selected. Solid (dashed) lines correspond to layers detected along the earlier (later) overpass.

In the following days (3–4 April), AMALi captured clouds and aerosol remnants in the interim of North Greenland and Ny-Ålesund, in the same altitude and geographical region as the aerosol layers (Fig. S1 from Nakoudi et al. (2020)[2]). Likewise, CALIOP detected clouds over Svalbard and Fram Strait. However, on 5 April geometrically similar aerosol layers (at 4-7 km) were observed over Ny-Ålesund by KARL and Micro-pulse lidar (MPL; technical description given in Shibata et al. (2018)) at 200-600 km from the flight operations (Fig. 3.4). Although the MPL provided a continuous evolution of the layer, its optical products cannot be used for inversion of the aerosol microphysics due to the lack of Raman channel information. Therefore, the optical and microphysical aerosol properties were only inverted for available KARL observation periods (on 5 and 6 April, rectangles in Fig. 3.4). The synoptic situation on the days when the aerosol layer was observed over Ny-Ålesund, was characterized by the passing of a weak low-pressure system. According to radiosonde ascents moderate N-NW winds (3-7 ms^{-1}) prevailed, while wind shear and RH were enhanced (RH of 47-58% on 5 April and 55-65% on 6 April) at the layer altitude range.

A significant number of air mass trajectories ending at Fram Strait and Ny-Ålesund originated from the lower troposphere, implying, thus, a connection to surface aerosol sources. According to LAGRANTO backward trajectories (Sec. 2.4.1), the air masses arriving at 5–7 km over Fram Strait were associated with northeast Chinese surface sources (Fig. 3.2). The air masses were at least 9 days old (last contact with main aerosol source region) (Fig. 3.5a). Over Ny-Ålesund (5 April) air masses were funneled from north Scandinavia (lower part of the plume) and northeast China (upper part of the plume, Fig. 3.4). On their arrival at Ny-Ålesund, the Chinese air masses were at least 9 days old, while the north Scandinavian ones had last contact with surface sources 4 days ago (Fig. 3.5b). One–two days before reaching Ny-Ålesund (Fig. 3.5), the air masses passed over North Greenland – East Canadian Archipelago and Fram Strait at 500–600 hPa (greenish trajectories, Fig. 3.4). In the next Section, the aerosol layer properties over the different regions will be investigated

2 https://www.mdpi.com/2072-4292/12/13/2112/s1

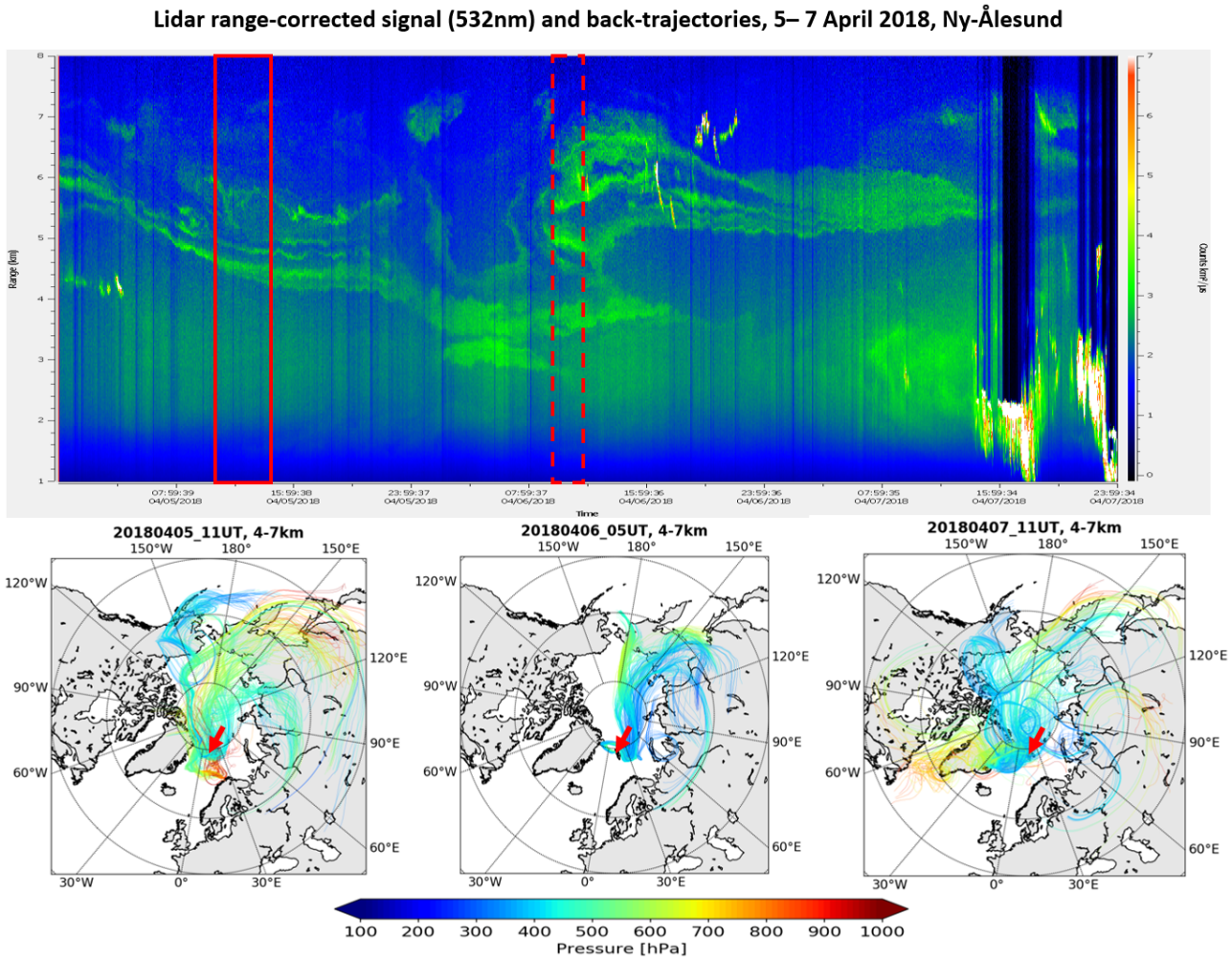

Fig. 3.4: Same as Fig. 3.2 but for trajectories ending over Ny-Ålesund (red arrow) on 5-7 April. A connection to northeast Chinese and north Scandinavian surface sources is discernible for 5 April.

from a comparative perspective as their history seems to be related.

Finally, an overview of the aerosol load (in terms of aerosol optical depth (AOD)) over the different regions is given (Fig. 3.6). The highest AOD was reported over Fram Strait (blue shading), corresponding to the upper limit of the CALIOP derived AOD. However, it should be noted that the AOD from CALIOP refers to specific aerosol layers and not to the total atmospheric column. Over Ny-Ålesund the AOD (black line) was lower by 50% relative to Fram Strait (on 5 and 7 April), indicating the effect of aerosol removal. The AOD over Ny-Ålesund was higher than for clean continental layers (green shading), indicating the departure from background aerosol conditions. On 6 April the aerosol layer over Ny-Ålesund was vertically perturbed (Fig. 3.4), possibly due to the passing of a weak low-pressure system at that time. The AOD fluctuated and maximized some hours later. This rapid increase is potentially related to aerosol hygroscopic effects, supported by increased RH (55-65%) and short-lived clouds around 12 UT (Fig. 3.4). In the following days, low-level clouds did not allow for investigating the event any further.

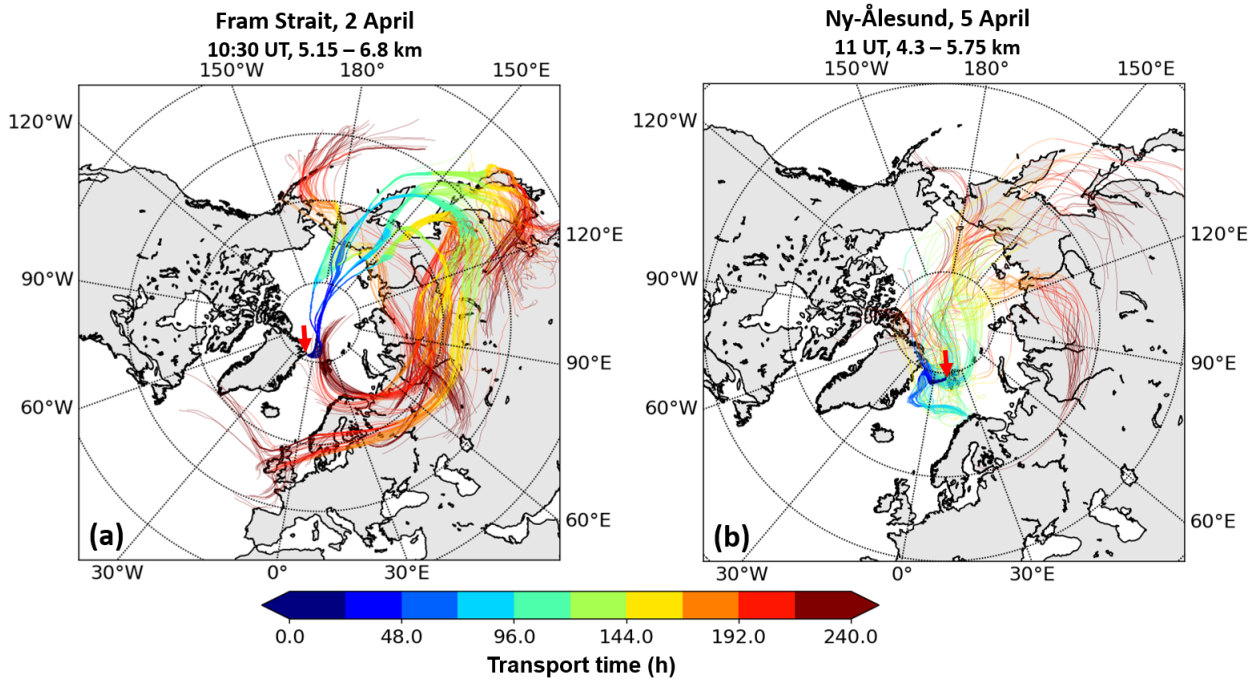

Fig. 3.5: LAGRANTO backward trajectories ending at the aerosol layer altitude range over west Fram Strait (a) and Ny-Ålesund (b). The air mass transport time is color indicated and the ending locations are denoted by red arrows. For the sake of clarity a subset of trajectories is shown.

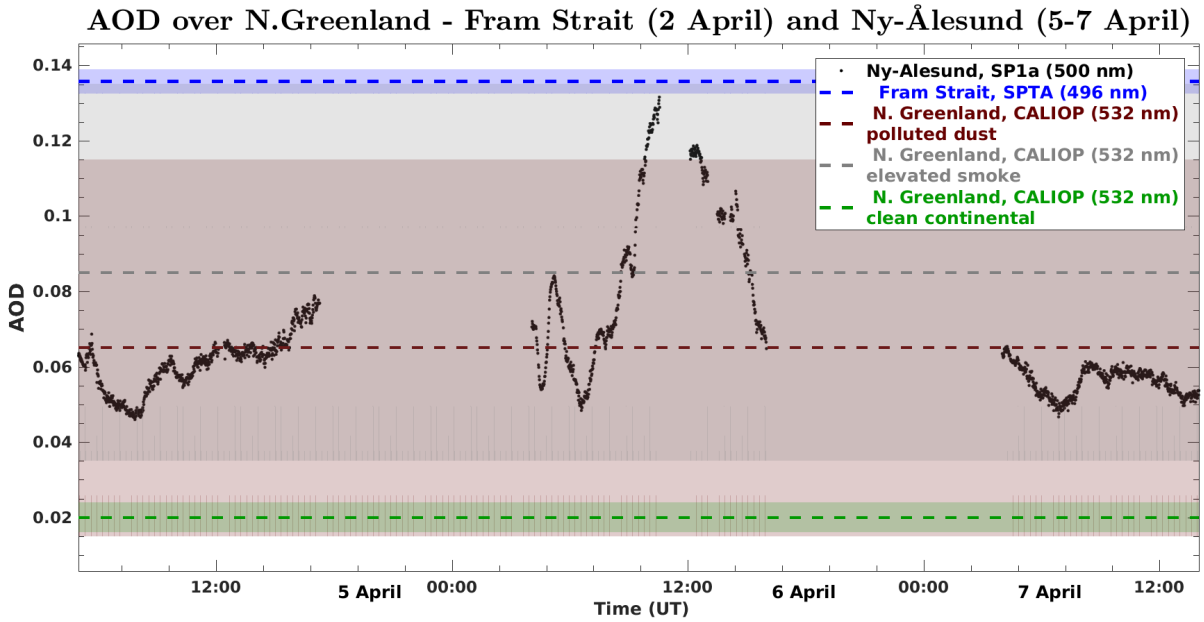

Fig. 3.6: Evolution of columnar AOD over Ny-Ålesund after cloud screening. For comparison, the AOD over Fram Strait is given (mean ± standard deviation). Similarly, the AOD over North Greenland for different aerosol sub-type layers is presented.

3.1.2 Modification of aerosol optical and microphysical properties

The aerosol properties over North Greenland, Fram Strait and Ny-Ålesund are investigated in this Section. Profiles of aerosol backscatter coefficient (Eq. 2.8), linear particle depolarization ratio (LPDR; Eq. 2.14) and backscatter related Ångström exponent (Eq. 2.13) are illustrated in Fig. 3.7. The aerosol extinction coefficient (Eq. 2.10) and extinction related Ångström exponent are presented in Fig. 3.8. Since the extinction over Ny-Ålesund was derived by the Raman technique (Sec. 2.1) during daytime, only layer-mean values were obtained that allowed tolerable statistical uncertainties. Over Fram Strait the extinction was estimated by subtracting the AMALi AOD (above the aerosol layer) from the sun-photometer columnar AOD (more details given in Nakoudi et al. (2020)). The CALIOP derived optical properties are summarized in Tab. 3.1, while the air-borne and ground-based remote sensing derived properties are presented in Tab. 3.2.

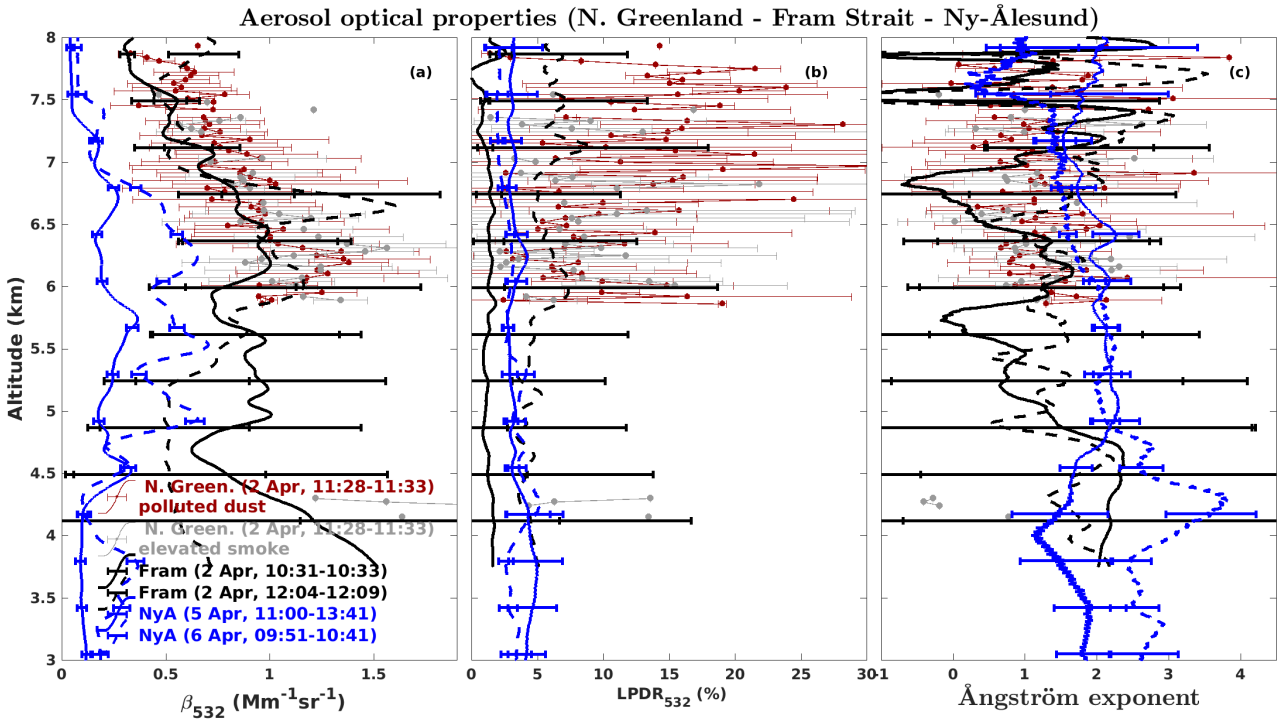

Fig. 3.7: Aerosol optical properties over North Greenland, Fram Strait and Ny-Ålesund. Errorbars represent retrieval uncertainties. Air-borne (space-borne) derived profiles exhibit higher uncertainties due to changing flight altitude (satellite position) that constrained the temporal averaging. For the sake of clarity only properties from the second CALIPSO overpass are shown.

Over North Greenland – Fram Strait, the aerosol concentration was higher (enhanced aerosol backscatter coefficient, Fig. 3.7a). As expected, the highest departure from spherical shape was found for the polluted dust mixture (brown line in Fig. 3.7b), followed by the elevated smoke (gray line). Over Fram Strait, the aerosol was characterized by lower but variable LPDR (1.1–5.5%), while low values (approximately 3%) appeared over Ny-Ålesund. The higher LPDR over mid-Fram Strait (dashed black line) could be attributed to a spherical

– non-spherical aerosol mixture. The non-spherical component was likely dust from Gobi desert (as indicated by backward trajectories, Fig. 3.2). A mixture of 60% smoke and 40% dust (Tesche et al., 2009) could account for the upper range of the LPDR observed over Fram Strait. On the other hand, anthropogenic aerosol from industrial and biomass burning sources could account for the lower LPDR over west Fram Strait (solid black line) and Ny-Ålesund. Finally, a shift towards smaller particles was indicated (increasing Ångström exponent) between Fram Strait and Ny-Ålesund (Fig. 3.7c).

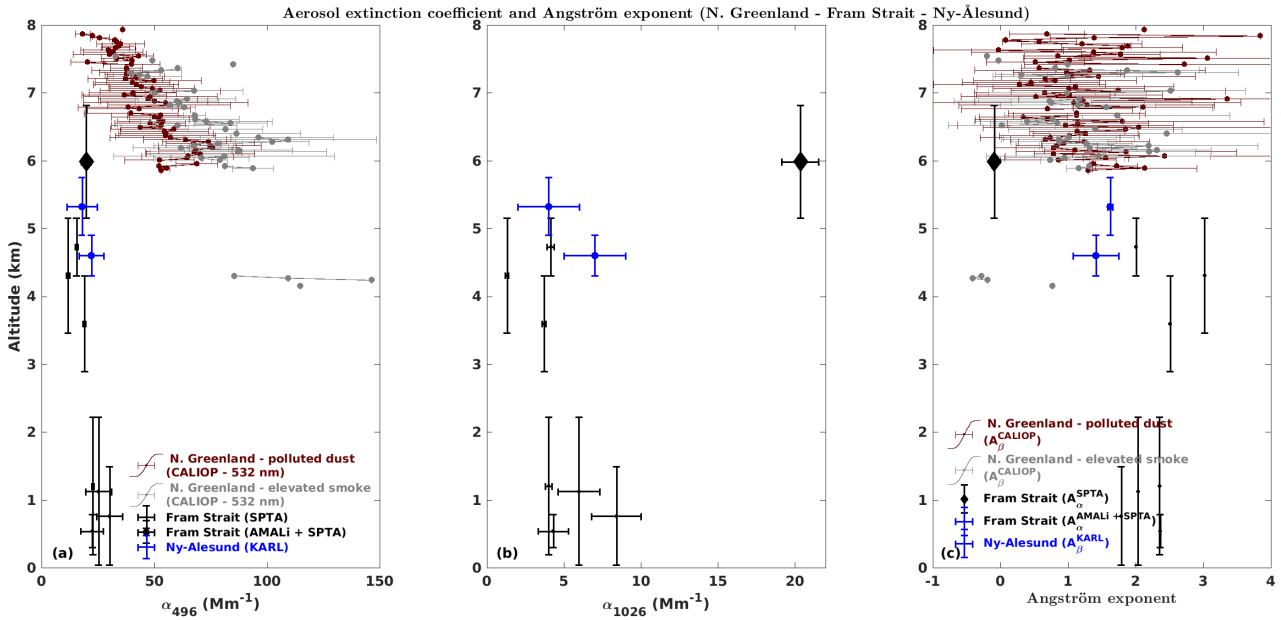

Fig. 3.8: Aerosol extinction coefficient α (at 496 nm for SPTA, KARL and AMALi and 532 nm for CALIOP) and Ångström exponent (532/1064 nm for CALIOP and KARL and 496/1026 nm for SPTA and AMALi). Horizontal errorbars indicate the corresponding uncertainties, while vertical errorbars indicate the layer altitude range. For the sake of clarity only properties from the second CALIPSO overpass are shown.

The highest aerosol extinction coefficient was derived over North Greenland for the elevated smoke layers (Fig. 3.8a), while the extinction over Fram Strait and Ny-Ålesund was at least one time lower. This discrepancy is partly related to the lower LR_{532} over Fram Strait (Tab. 3.2). Additionally, the illustrated CALIOP profiles correspond to the second overpass (black line in Fig. 3.1) that was in greater distance from the flight operations and exhibited extinction 2-3 times higher than the first overpass (Tab. 3.1). Indeed, a better agreement was found between Fram Strait and the first CALIPSO overpass in terms of AOD (AOD = 0.03–0.05, Tab. 3.1 and AOD = 0.035, Tab. 3.2). Thus, the extinction and AOD discrepancies between Fram Strait and North Greenland are not related to instrumental effects (e.g. different detection sensitivities of CALIOP and AMALi) but reflect the aerosol spatio-temporal variability. Finally, the aerosol extinction in the visible spectrum was similar over Fram Strait and Ny-Ålesund (Fig. 3.8a) but in the near-infrared the extinction over Ny-Ålesund was significantly lower (Fig. 3.8b). This aspect will be discussed later in connection with the modifi-

cation of the aerosol size distribution.

Tab. 3.1: Summary of aerosol optical properties (mean ± standard deviation) as derived by CALIOP for each aerosol sub-type along two overpasses. Properties derived by the L2 5km Aerosol profile (layer) product are given in plain (italic).

Aerosol Optical Properties, North Greenland, 2 April				
CALIOP (L2_05kmAlay and L2_05kmApro)				
time (UT)	**9:49–9:54**		**11:28–11:33**	
aerosol subtype	**polluted dust**	**elevated smoke**	**polluted dust**	**elevated smoke**
geom. limits (km)	*3.9–5.8*	*3.8–7.1*	*3.5–7.7*	*3.4–7*
$\beta_{532}(Mm^{-1}sr^{-1})$	0.6 ± 0.2	0.7 ± 0.5	0.9 ± 0.2	1.1 ± 0.3
$Å_{\beta532/\beta1064}$	1.3 ± 0.8	1.1 ± 0.9	1.3 ± 0.7	1.1 ± 0.8
$LPDR_{532}$ (%)	*10 ± 2*	*8 ± 3*	*10 ± 3*	*5 ± 2*
$\alpha_{532}(Mm^{-1})$	32 ± 9	51± 35	47 ± 14	75 ± 23
LR532 (sr)	*55 ± 22*	*70 ± 16*	*55 ± 22*	*70 ± 16*
AOD_{532}	*0.03 ± 0.01*	*0.05 ± 0.01*	*0.1 ± 0.04*	*0.12 ± 0.06*

The inverted aerosol microphysical properties and summarized in Tab. 3.3 (for details see Sec. 2.4.2). As the inversion requires a minimum set of 5 input optical parameters, it was not feasible to infer the aerosol microphysics from CALIOP data. For Fram Strait the input was obtained from synergistic AMALi – sun-photometer observations. Collocation discretization and an iterative Padé-regularization method with a fixed number of 30 iterations were employed (Böckmann and Kirsche, 2006; Osterloh et al., 2011). For Ny-Ålesund the input was derived from KARL and a truncated singular value decomposition regularization algorithm was used (Böckmann, 2001). The total number, surface-area and volume concentration, as well as the effective radius (r_{eff}) were derived for the fine and coarse modes by log-normal fits to the volume distribution. Fitting errors amounted to 10% for the total concentrations and 5% for the r_{eff} estimation. The single-scattering albedo (SSA) and asymmetry parameter uncertainties were estimated by sensitivities based on Mie calculations with different refractive indices.

The inverted particle size distributions are illustrated in Fig. 3.9, with the transition towards a fine particle domination being evident. Over Fram Strait a bi-modal distribution was present, whereas over Ny-Ålesund the coarse mode was nearly absent. A fine mode was inverted for the upper sub-layer, while a weak bi-modal distribution characterized the lower one. The Ångström exponent indicated smaller particles over Ny-Ålesund, which is in line with the coarse mode depletion. The differences in aerosol size distribution could be related to the source regions and transport time of the layers, indicating discrepancies in the aerosol composition and aging state. As ice clouds were observed over Fram Strait by CALIOP and

Tab. 3.2: Summary of aerosol optical properties (mean ± standard deviation) over two parts of Fram Strait and Ny-Ålesund.

Aerosol Optical Properties, Fram Strait and Ny-Ålesund					
	AMALi		**KARL**		
	2 April		**5 April**		**6 April**
time (UT)	**10:31–10:33**	**12:04–12:09**	**11:00–13:47**		**9:51–10:41**
geom. limits (km)	**5.15–6.8**	**5.3–6.9**	**4.3–4.9**	**4.9–5.75**	**4.6–5**
$\beta_{532}(Mm^{-1}sr^{-1})$	0.9 ± 0.1	1 ± 0.2	0.2 ± 0.05	0.3 ± 0.06	0.4 ± 0.2
$Å_{\beta355/\beta532}$	0.8 ± 0.6	1.3 ± 0.4	1.8 ± 0.2	2.2 ± 0.1	2.4 ± 0.3
$Å_{\beta532/\beta1064}$	-	-	1 ± 0.1	1.1 ± 0.04	1.2 ± 0.3
$LPDR_{532}$ (%)	1.3 ± 0.2	5.5 ± 1	3.2 ± 0.3	3 ± 0.2	3.4 ± 0.4
$\alpha_{496}(Mm^{-1})$	21 ± 2	-	20 ± 5	16 ± 6	-
$\alpha_{1026}(Mm^{-1})$	20 ± 1	-	7 ± 2	4 ± 2	-
	AMALi + sun-photometer		**KARL**		
LR_{355} (sr)	-	-	35 ± 15	48 ± 4	-
LR_{532} (sr)	15 ± 3	-	82 ± 25	64 ± 37	-
AOD_{496}	0.035	-	0.012	0.014	-

AMALi in the interim time (Fig. S1 from Nakoudi et al. (2020)[2]), the modification of the size distribution could be attributed to nucleation scavenging and subsequent dry/wet deposition. Nucleation rates (Fletcher, 1958) and sedimentation velocities favor the depletion of bigger particles.

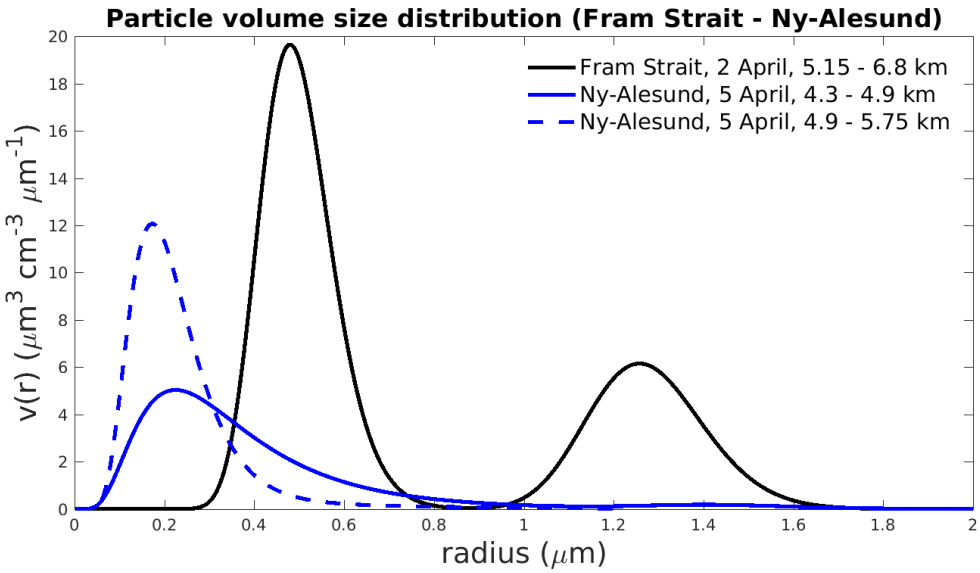

Fig. 3.9: Particle volume size distributions over west Fram Strait and Ny-Ålesund.

Tab. 3.3: Aerosol microphysical properties over west Fram Strait and over Ny-Ålesund.

Aerosol Microphysical Properties, Fram Strait and Ny-Ålesund						
	AMALi + sun-photom.		**KARL**			
	2 April		**5 April**			
time (UT)	**10:31–10:57**		**11:00–13:47**			
geom. limits (km)	**5.15–6.8**		**4.3–4.9**		**4.9–5.75**	
Refractive Index ri (mean ± 1 σ)						
ri	1.5 + 0.008 $\cdot i$		1.54 + 0.019 $\cdot i$		1.49 + 0.007 $\cdot i$	
	± 0.02 + 0.006 $\cdot i$		± 0.04 + 0.01 $\cdot i$		± 0.02 + 0.004 $\cdot i$	
single-scattering albedo SSA (mean ± uncertainty)						
SSA_{355}	0.84 ± 0.1		0.88 ± 0.06		0.96 ± 0.02	
SSA_{532}	0.91 ± 0.06		0.9 ± 0.05		0.96 ± 0.02	
asymmetry parameter g (mean ± uncertainty)						
g_{355}	0.69 ± 0.04		0.71 ± 0.04		0.72 ± 0.02	
g_{532}	0.7 ± 0.05		0.69 ± 0.03		0.68 ± 0.01	
effective radius r_{eff}, number n_t, surface s_t and volume v_t concentration						
	fine	coarse	fine	coarse	fine	coarse
$r_{eff}(\mu m)$	0.49	1.26	0.26	1.43	0.19	-
$n_t(cm^{-3})$	8.78	0.24	65.2	0.005	132.9	-
$s_t(\mu m^2 cm^{-3})$	24.09	4.68	21.6	0.13	36.4	-
$v_t(\mu m^3 cm^{-3})$	3.9	1.97	1.9	0.06	2.3	-

The asymmetry parameter, which is indicative of the aerosol size, was similar for all the layers and corresponded to big particles. More specifically, the asymmetry parameter was higher than the monthly average in different Arctic ground stations (mostly between 0.55 and 0.65 (Schmeisser et al., 2018)). Such high values are usually related to long-range transported aerosol (Schmeisser et al., 2018). The accumulation aerosol mode over Fram Strait was untypically large (Mei et al., 2020), but over Ny-Ålesund it was close to other events ((Hoffmann et al., 2009), r_{eff} = 0.18 µm; (Stock et al., 2012), r_{eff} = 0.19 µm). Typically, the aerosol size distribution in spring peaks around radii of 0.15 μm (according to in-situ measurements with a 0.5 μm cut-off diameter) as illustrated in Fig. 1.2. The refractive index values were slightly lower in comparison to other *Arctic haze* events, comprising either polluted aerosol ((Hoffmann et al., 2009), 1.56 + $0.01 \cdot i$) or a mixture of industrial pollution and biomass burning aerosol from Siberia ((Stock et al., 2012), 1.6 + $0.007 \cdot i$). Furthermore, those events were characterized by higher total number concentration ((Hoffmann et al., 2009), $343 \pm 30\%\ cm^{-3}$; (Stock et al., 2012), 480–950 cm^{-3}), probably due to more efficient aerosol sources or less effective removal processes along the transport paths (from central

and east Siberia).

Finally, the spectral dependency of LR (higher LR_{532} than LR_{355}) over Ny-Ålesund is similar to that of aged biomass burning aerosol (Nicolae et al., 2013; Janicka et al., 2017; Ortiz-Amezcua et al., 2017). The LR_{532} (15 sr) over Fram Strait was lower compared to literature values of biomass burning and industrial pollution particles. In order to interpret this finding Mie calculations were performed, which produced the highest LR in the near-infrared (LR_{1064} = 36 sr) and lower values in the visible (LR_{532} = 19 sr). As illustrated in Fig. S3 from Nakoudi et al. (2020) [2], the coarse mode dominated the extinction and backscatter cross-sections. Therefore, the particle size distribution exhibited less sensitivity to the visible light. Thus, the similar extinction at 532 nm over Fram Strait and Ny-Ålesund but the lower extinction at 1064 nm over Ny-Ålesund can be attributed to the absence of the coarse aerosol mode.

3.1.3 Aerosol radiative effect (ARE)

The SW direct effect of aerosol on the local radiation budget was assessed using the radiative transfer model SCIATRAN (Sec. 2.4.3). The vertically-dependent irradiances and ARE are depicted in Fig. 3.10. For evaluation, the observed irradiances at the surface and at flight level are displayed. Additionally, profiles of total (HR_{tot}, Eq. 2.25) and aerosol heating rates (HR_{aer}, Eq. 2.26) are presented (Fig. 3.11). The solar zenith angle (SZA) was set at 73^o over Ny-Ålesund and 78^o over Fram Strait in accordance with the solar geometry conditions during the aerosol observations. The surface was highly reflective over both locations (broadband albedo = 0.7). Further input parameters and settings are described in Sec. 2.4.3.

At surface, a *shadowing effect* ($-3.5\ Wm^{-2}$ at Fram Strait and $-1.5\ Wm^{-2}$ at Ny-Ålesund) was produced. Above the aerosol layer, the upward irradiance was diminished, producing a warming effect at the top of the atmosphere (TOA, $+0.9\ Wm^{-2}$ over Fram Strait and $+3\ Wm^{-2}$ over Ny-Ålesund). The irradiance difference between TOA and surface accounted for the warming of the atmospheric column ($+4.4\ Wm^{-2}$ over Fram Strait and $+4.5\ Wm^{-2}$ over Ny-Ålesund). Compared to air-borne radiation observations, the simulated irradiances over Fram Strait presented a maximum bias of 3%, 8%, and 13% in the SW down-welling, up-welling, and net components, respectively. These differences can be attributed to uncertainties in the thermodynamic and trace gas profiles, as well as the high SZA values, which could introduce additional errors in the radiative transfer calculations, especially under the plane-parallel assumption. In comparison to BSRN observations, the simulated irradiances at the surface of Ny-Ålesund exhibited agreement mostly with the range of uncertainty. Quinn et al. (2007) estimated the ARE and HR of *Arctic haze* (AOD_{500} = 0.12 and SSA = 0.94) for SZA of 62.6^o at Barrow, Alaska (over a highly reflecting surface). Similar to here, the ARE was negative at the surface ($-0.9\ Wm^{-2}$) and positive at TOA ($+2.5\ Wm^{-2}$).

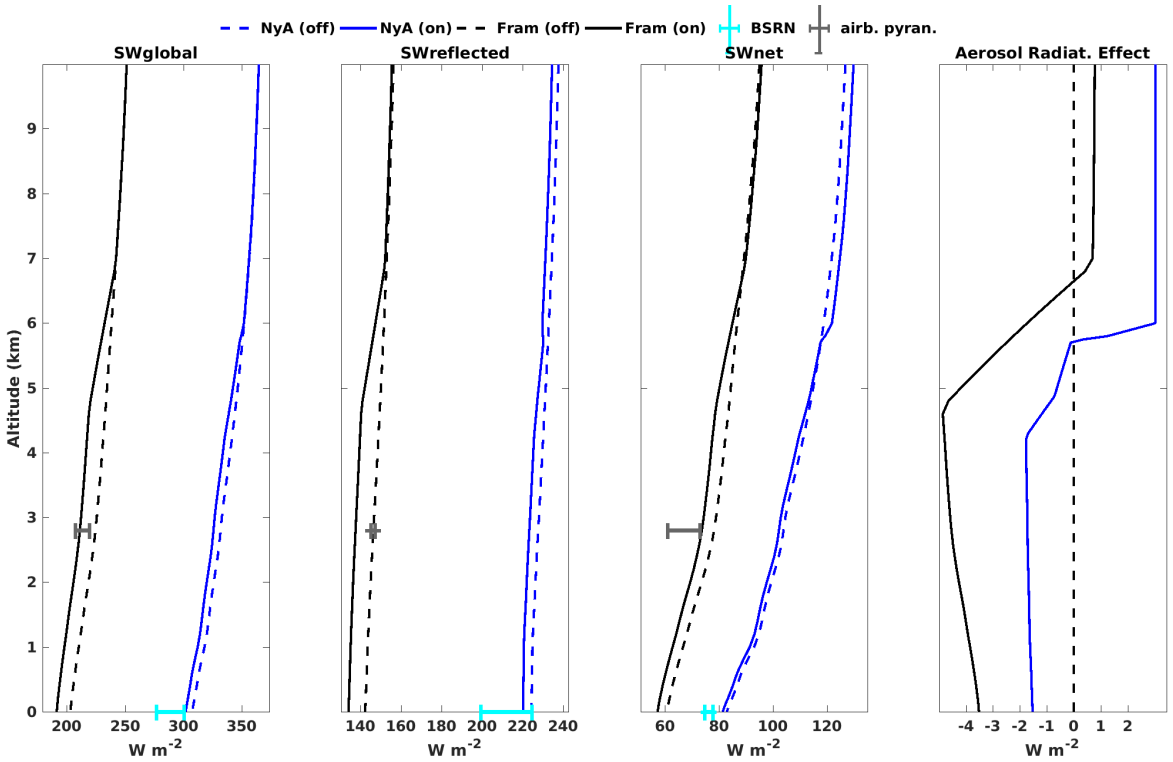

Fig. 3.10: Profiles of simulated irradiances and ARE over Ny-Ålesund (blue) and Fram Strait (black). Observed irradiances at Ny-Ålesund (cyan) and aboard Polar 5 (grey) are given for comparison (average ± one standard deviation).

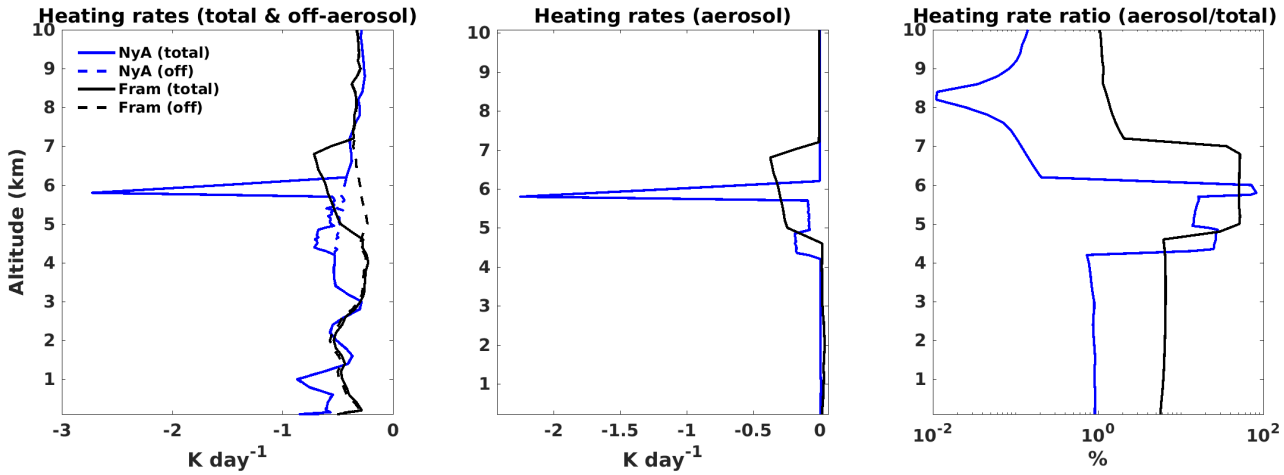

Fig. 3.11: Profiles of simulated HR over Ny-Ålesund (blue) and over Fram Strait (black). The HR_{tot} and $HR_{off-aer}$ are presented (left panel) along with the HR_{aer} (middle panel) as well as the contribution of HR_{aer} to the HR_{tot} (right panel).

Regarding the HR_{aer}, it was slightly positive below the aerosol layers (Fig. 3.11, middle panel) and turned negative aloft. The average (± standard deviation) HR_{aer} within the atmospheric column of Fram Strait (Ny-Ålesund) amounted to $-0.02 \pm 0.08\ Kday^{-1}$ ($-0.014 \pm 0.13\ Kday^{-1}$). Maximum rates were observed within the aerosol layers, reaching $-0.32 \pm 0.04\ Kday^{-1}$ ($-0.16 \pm 0.19\ Kday^{-1}$) over Fram Strait (Ny-Ålesund). The contribution of aerosol to the HR_{total} was small (less than 7%) beneath the aerosol layers (Fig. 3.11, right

panel) and maximized, as expected, within the aerosol layers (80% at Ny-Ålesund and 50% at Fram Strait). In the study of Quinn et al. (2007) the HR_{aer} amounted to $+0.25\ Kday^{-1}$, in the same order to here. Their opposite sign is probably related to a different HR reference system.

3.2 Sensitivities of the spring-time Arctic ARE

3.2.1 Sensitivity on aerosol related parameters

In this section a set of sensitivity tests is performed in order to investigate the effect of different aerosol parameters on the simulated ARE. To this end, the scenario over Ny-Ålesund was selected and the aerosol input was perturbed by its uncertainties, as presented in Tab. 3.2 and 3.3. In each perturbed scenario, the rest of the input parameters was kept as in the control scenario. The perturbed parameters included the extinction coefficient (increased by 30%), SSA (decreased by 10%) and asymmetry parameter (decreased by 8%). The resulting irradiances and HR_{aer} are presented in Fig. 3.12 and the differences with respect to the control scenario are summarized in Tab. 3.4.

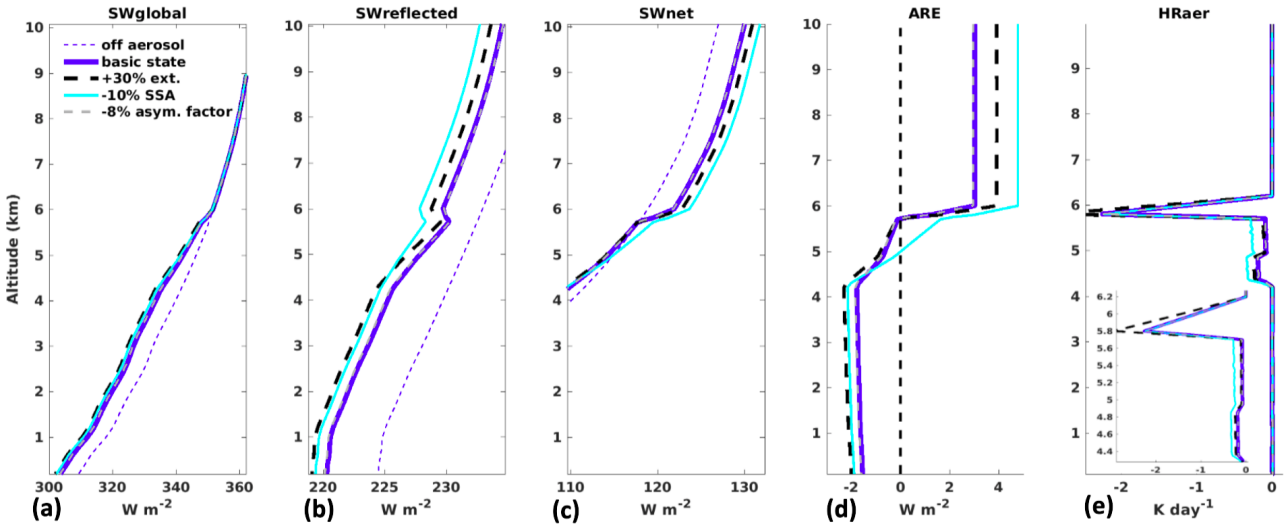

Fig. 3.12: SW irradiances (a-c), ARE (d) and HR_{aer} (e). Apart from the control scenario (blue) and the off-aerosol scenario (dashed blue), three perturbed scenarios are presented. The inset figure in panel (e) is a zoom-in of the HR_{aer} within the aerosol layers.

The most pronounced changes occurred in terms of SW_{refl} irradiance above the aerosol layers (Fig. 3.12b), especially for the perturbed SSA (cyan) and extinction (black) scenarios. The positive ARE above the aerosol layers displayed a greater enhancement ($+57\%$ in the SSA and $+30\%$ in the extinction scenario) than the negative ARE beneath ($+27\%$ in both scenarios). Hence, the retained irradiance within the atmospheric column increased. Overall, the highest sensitivities corresponded to changes in the SSA. A 10% SSA change induced more intense perturbations than a 30% extinction change. The high sensitivity of ARE_{TOA} on SSA was also highlighted by Quinn et al. (2007), reporting a 3.1% perturbation as a result of

Tab. 3.4: Overview of ARE and HR_{aer} changes (absolute and relative to the control scenario over Ny-Ålesund) for different aerosol perturbation scenarios. The highest changes are given in **bold**.

scenario	ΔARE_{TOA}	$\Delta ARE_{surf.}$	ΔARE_{column}	ΔHR_{aer}^{column}	$\Delta HR_{aer}^{aer.layer}$
+30% ext.	$+0.9\ Wm^{-2}$	$-0.4\ Wm^{-2}$	$+1.3\ Wm^{-2}$	$-0.004\ Kday^{-1}$	$-0.05\ Kday^{-1}$
	+30%	**+27%**	+29%	+29%	+31%
−10% SSA	$+1.7\ Wm^{-2}$	$-0.4\ Wm^{-2}$	$+2.1\ Wm^{-2}$	$-0.005\ Kday^{-1}$	$-0.16\ Kday^{-1}$
	+57%	**+27%**	**+47%**	**+36%**	**+100%**
−8% g	$-0.1\ Wm^{-2}$	$-0.1\ Wm^{-2}$	–	$-6 \cdot 10^{-5}\ Kday^{-1}$	$+3 \cdot 10^{-4}\ Kday^{-1}$
	+3%	+7%	–	+0.4%	+0.2%

1% SSA change. Respectively, a doubling of the AOD (and thus extinction) resulted in 80% change (Quinn et al., 2007). The asymmetry parameter did not bring any significant changes. Additionally, a sensitivity on the layer altitude was performed (not shown). Although for higher aerosol layers the ARE intensified, its overall sensitivity proved to be very small. For 1 km altitude change the ARE_{TOA} and $ARE_{atm.column}$ ($ARE_{surface}$) changed by $O(10^{-1})\ Wm^{-2}$ ($O(10^{-2})\ Wm^{-2}$). Additionally, small HR_{aer} changes ($O(10^{-3})\ Kday^{-1}$) were found. Finally, it should be noted that throughout the performed sensitivities the ARE sign was not modified. Thus, a qualitative assessment of the ARE is feasible under the given aerosol uncertainties.

At this point the role of different aerosol parameters for the resulting ARE can be better understood. More specifically, it can be explained why despite the modification of the aerosol size distribution, the SW radiative footprint was similar over Fram Strait and Ny-Ålesund. Starting with the SSA, its differences were not high enough to be reflected on the ARE. The asymmetry parameter was not sensitive to the modification of the size distribution and, as shown, it has the lowest impact on the ARE. Finally, despite the extinction decline in the near-infrared (Fig. 3.8b), the impact on the spectrally integrated irradiance was insignificant since this spectral region corresponds to low solar irradiance. At the same time, the visible extinction, which is sensitive to the dominating visible solar irradiance, was almost constant (Fig. 3.8a). Consequently, the SW radiative footprint remained nearly constant at the two locations as the most relevant aerosol properties were hardly modified.

3.2.2 Sensitivity on ambient conditions

Sensitivity on solar zenith angle (SZA)

In the following the sensitivities are extended to representative SZA and albedo spring-time conditions. The aerosol input as well as other parameters were kept as in the control scenario. Fig. 3.13 presents profiles of ARE and HR_{aer} for typical spring-time SZA values. For

the sake of brevity, the profiles of SW_{global}, $SW_{reflected}$ and SW_{net} are not shown as their shape is similar to those of Fig. 3.10. In order to illustrate the dependence on SZA more clearly, the ARE and HR_{aer} are also given at selected altitudes (Fig. 3.14).

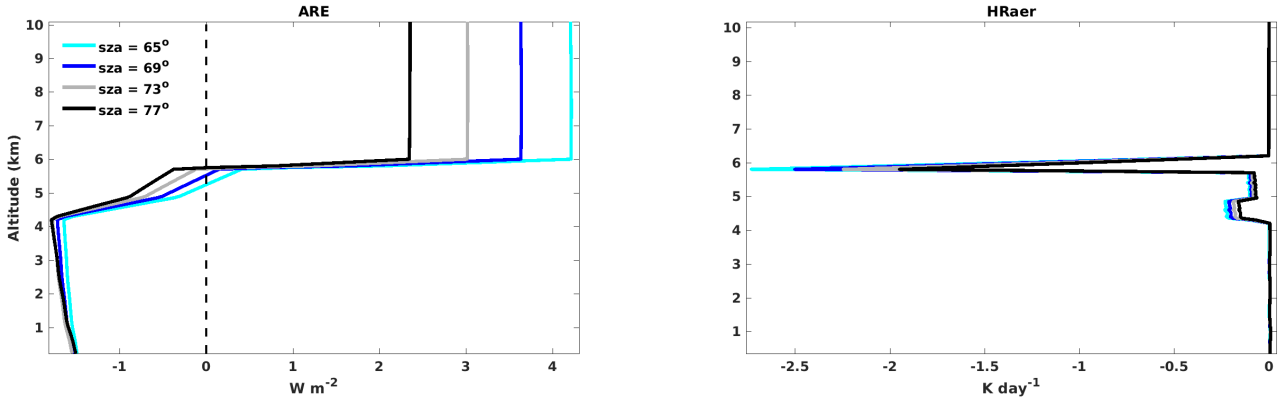

Fig. 3.13: Profiles of ARE and HR_{aer} for typical spring-time SZA values over Ny-Ålesund.

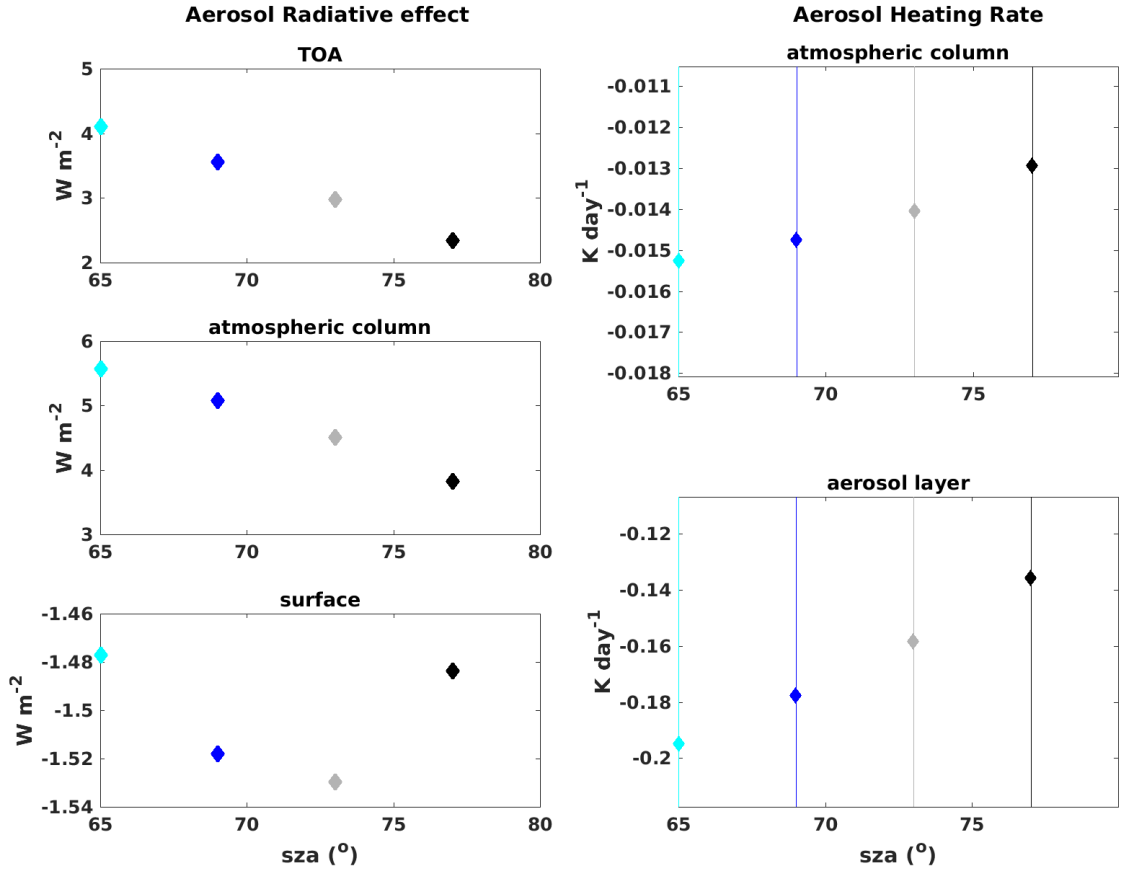

Fig. 3.14: ARE and HR_{aer} as a function of SZA at different atmospheric levels as derived from the profiles of Fig. 3.13.

As expected, the ARE profiles (Fig. 3.13) were shifted towards more positive values as the solar elevation increased (SZA decreased). The higher sensitivity was displayed above the aerosol layers. The irradiances beneath the aerosol layer showed a weak dependence on

SZA, with the $ARE_{surface}$ being one order of magnitude lower than the ARE_{TOA} (Fig. 3.14). The absolute value of $ARE_{surface}$ decreased with increasing SZAs up to 73^o. For the highest SZA of 77^o the relation was reversed. However, as the changes in $ARE_{surface}$ were small, the inherent uncertainties of the SCIATRAN model, which increase for higher SZA, might be responsible for the different response to SZA. Regarding the HR_{aer}, it intensified (in absolute terms) as the solar elevation increased and, expectantly, the main perturbations occurred within the aerosol layers.

Sensitivity on surface albedo

The sensitivity with respect to surface albedo is presented in Fig. 3.15 and 3.16. The selected albedo values represent a wide range of surface conditions; from open-water (a = 0.05) and tundra (a = 0.1 (Maturilli, Herber, and König-Langlo, 2015)) to transition conditions between tundra and snow (a = 0.45) as well as snow/ice cover (a = 0.73). In general, more SW_{global} remained over highly reflective surfaces, possibly due to increased multiple reflections between atmospheric constituents and the surface (Fig. 3.15a). Over highly reflective surfaces, the SW_{net} was diminished within the whole atmospheric column due to higher SW_{refl}.

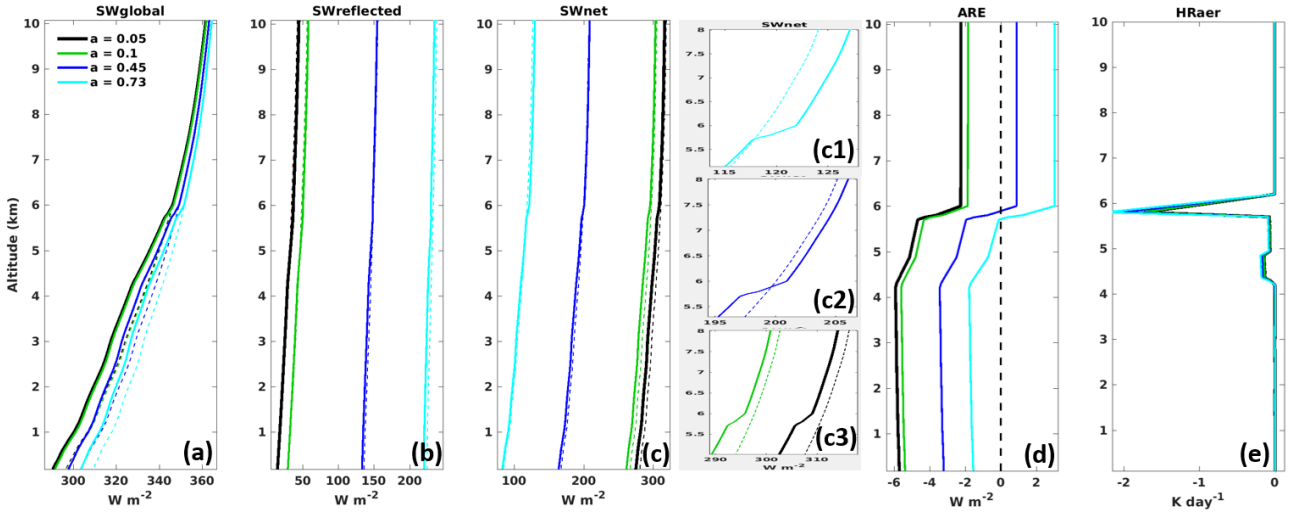

Fig. 3.15: Same as Fig. 3.13 but for surface albedo sensitivity. Apart from ARE and HR_{aer}, SW irradiances are presented for aerosol (solid lines) and off-aerosol scenarios (dashed lines). Panels (c1-c3) are zoom-ins of (c) showing the different behavior of SW_{net} above the aerosol layer.

For higher reflective surfaces the $ARE_{atm.column}$ intensified (Fig. 3.16) as a combination of higher ARE_{TOA} (source term) and lower $ARE_{surface}$ (sink term). The ARE remained negative throughout the atmospheric column for dark surfaces (Fig. 3.15d). In contrast, over bright surfaces a shift from negative to positive ARE occurred. This can be explained by comparing the respective aerosol (solid lines) and off-aerosol scenarios (dashed lines). Over bright surfaces, more SW_{net} remained above the aerosol layers relative to aerosol-free conditions (Fig. 3.15c1–c2), whereas the opposite held true over dark surfaces (Fig. 3.15c3). Bright

surfaces seemed to promote multiple reflections within the aerosol layer, resulting in more trapped SW_{net} aloft (less SW_{refl} relative to the aerosol-free scenario). However, over dark surfaces the shadowing role of the aerosol layer (more SW_{refl} relative to the aerosol-free scenario) seemed to dominate, resulting in less SW_{net} aloft. For bright surfaces, the HR_{aer} intensified within the aerosol layer, whereas within the atmospheric column it weakened.

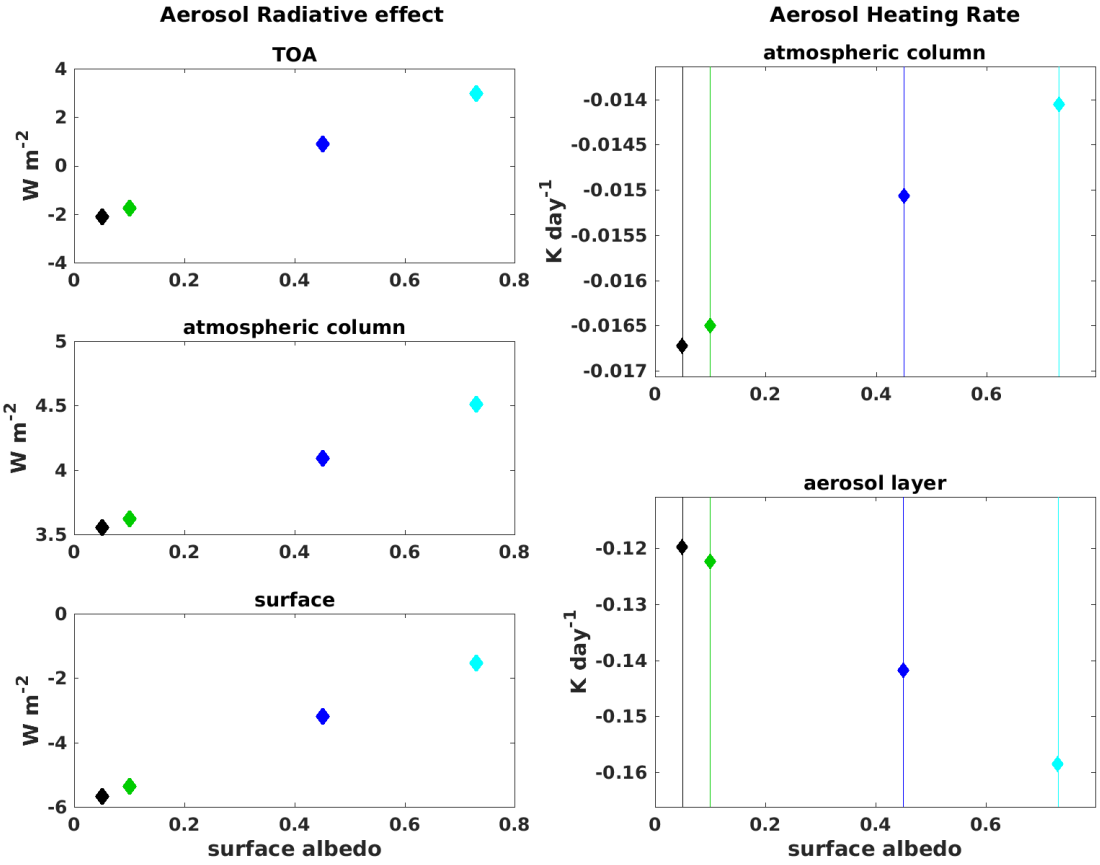

Fig. 3.16: Same as Fig. 3.14 but for surface albedo sensitivity.

Finally, the sensitivity on water vapor (WV) was investigated in order to assess its effect comparatively to aerosol. The water vapor mixing ratio was reduced by 30%, corresponding to maximum weekly fluctuations at 5–15 km over Ny-Ålesund (2–9 April 2018). The resulting atmospheric column WV effect amounted to $-3.8\ Wm^{-2}$, which was lower than the corresponding ARE ($+4.5\ Wm^{-2}$), and the same held true for the surface and TOA. Consequently, the WV effect was weaker than the instantaneous aerosol effect.

3.3 Aerosol in the lower troposphere (Winter)

3.3.1 Overview of remote sensing and in-situ measurements

In the Arctic the maximum aerosol extinction in winter and early spring appears within the lower 2 km of the troposphere (Di Pierro et al., 2013). Therefore, this period is ideal for performing lidar observations in coordination with tethered-balloon measurements, as the latter are typically limited within the first kilometer above ground. To this end, the first Polar night coordinated lidar and tethered-balloon aerosol measurements were performed at Ny-Ålesund in January 2019. The tethered-balloon and the lidar were operated in close proximity to each other (Fig. 3.17, upper right photograph). From 18 to 28 January 2019, 20 tethered-balloon profiles were obtained in parallel to 72 h of lidar observations, with several aerosol layers identified.

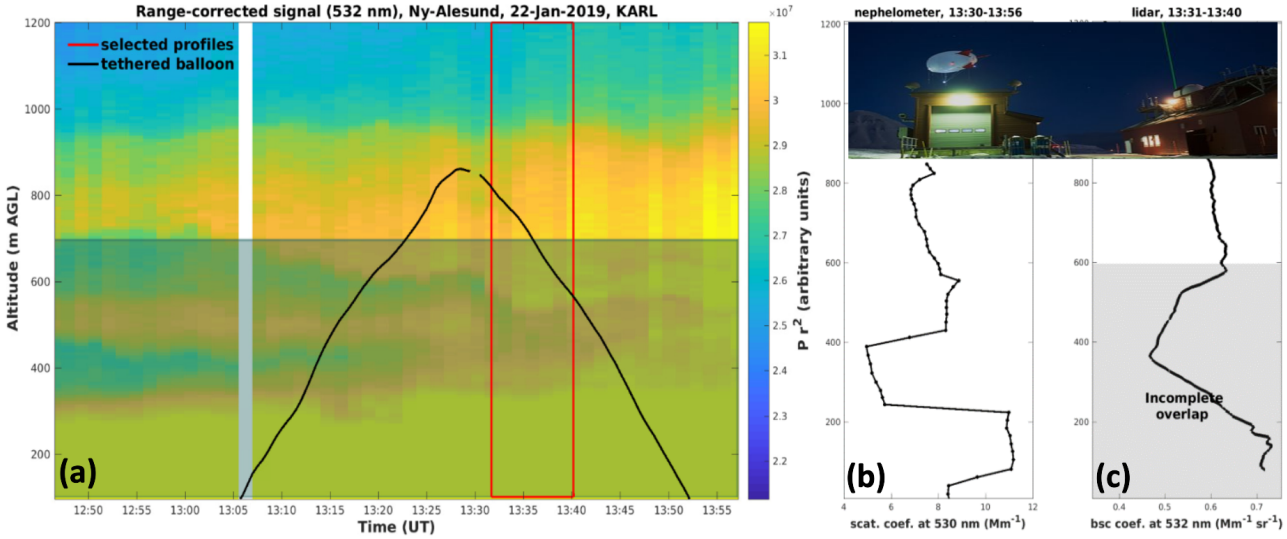

Fig. 3.17: Overview of lidar range-corrected signal on 22 January 2019 (a) and overlaid tethered-balloon position. The grey shading indicates the incomplete overlap region. The red rectangle indicates the period used for the aerosol microphysical retrieval. Profiles of particle scattering (b) and backscatter coefficient (c) are also presented. The setup of the experiment is depicted in the inset photograph (provided by Gregory Tran, AWIPEV station leader).

Here the properties of an aerosol layer, which was captured on 22 January at 600–900 m, are analyzed in detail. Following a similar approach to the *Arctic haze* case study (Sec. 3.1), the lidar derived optical parameters were incorporated into the aerosol microphysics algorithm so as to invert the aerosol size distribution. Additionally, the size distribution was measured in-situ. An overview of the lidar range-corrected signal together with the tethered-balloon position is given in Fig. 3.17. The tethered-balloon payload included, among others, an optical particle counter (OPC), a Minidisc sensor, a nephelometer and a particle soot absorption photometer (PSAP). More details about the instrumental payload can be found in Mazzola et al. (2016). The tethered-balloon data, which are presented here were provided

by Dr. Mauro Mazzola (CNR-ISP).

Fig. 3.17b and 3.17c depict profiles of aerosol scattering coefficient from the nephelometer and aerosol backscatter coefficient from KARL. These profiles correspond to the balloon descent period. A double layer aerosol structure (approximately 400–550 m and 600–1000 m) was identified, with the scattering and backscatter coefficient gradients being in good agreement. This also held true within the range of incomplete overlap (gray shaded area). However, within this range the optical retrievals are not always reliable (see Sec. 2.1.2 for details). Therefore, the analysis was focused on the higher aerosol layer. The tethered-balloon reached the base (572 m) of this layer at 13:18 UTC, ascended up to 855 m and then started its descent. During that period, the lidar revealed stable aerosol conditions. During the balloon ascent the nephelometer presented a small lag with respect to the OPC measurements (not shown here). Therefore, the aerosol size distribution comparison was only performed for the descending period.

3.3.2 Aerosol properties from the remote sensing perspective: KARL and CALIOP

In this section, the aerosol optical properties are analyzed using ground-based and satellite lidar observations. The optical properties were derived from KARL for the closest period to balloon descent. The selected layer (642–814 m) is denoted with cyan shading (Fig. 3.18), with its top chosen to match with the maximum height of the tethered-balloon. The aerosol backscatter coefficient at 355 ($1.08 \pm 0.01\ Mm^{-1}sr^{-1}$), 532 ($0.6 \pm 0.01\ Mm^{-1}sr^{-1}$) and 1064 nm ($0.15 \pm 0.01\ Mm^{-1}sr^{-1}$) as well as the extinction coefficient at 355 ($24.7 \pm 6.6\ Mm^{-1}$) and 532 nm ($19.5 \pm 11.4\ Mm^{-1}$) served as input for the aerosol microphysics retrieval.

Some hours earlier (5:36 UT) the CALIPSO satellite overpassed in the north-east of Ny-Ålesund (minimum distance of 250 km). CALIOP identified several weak aerosol layers in the lower troposphere [3]. More specifically, in the closest overpass distance an extended marine layer was observed (with 80 km horizontal resolution) at 322–1280 m. Additionally, 8 marine layers were detected (with 20 or 80 km horizontal resolution) from 53 to 801 m over the region 81.84^oN, 27.5^oE – 80.85^oN, 5^oE. Over a broader region, a limited number of polluted smoke layers was also observed in the lower troposphere. Fig. 3.19 and 3.20 present the properties of the closest aerosol layers. Only the Level2 Aerosol Layer product was used (1^{st} and 2^{nd} layers) as the Aerosol Profile product was too noisy (see Sec. 2.2.3). Tab. 3.5 summarizes the aerosol optical properties as derived by KARL and CALIOP, which mostly lay within the range of one another uncertainties. Only the AOD from KARL was lower compared to CALIOP. However, this can be attributed to the lower geometrical thickness (642–814 m)

3 https://www-calipso.larc.nasa.gov/products/lidar/browse_images/show_v4_detail.php?s=production&v=V4-10&browse_date=2019-01-22&orbit_time=05-32-22&page=1&granule_name=CAL_LID_L1-Standard-V4-10.2019-01-22T05-32-22ZN.hdf (last access: 18 February 2021)

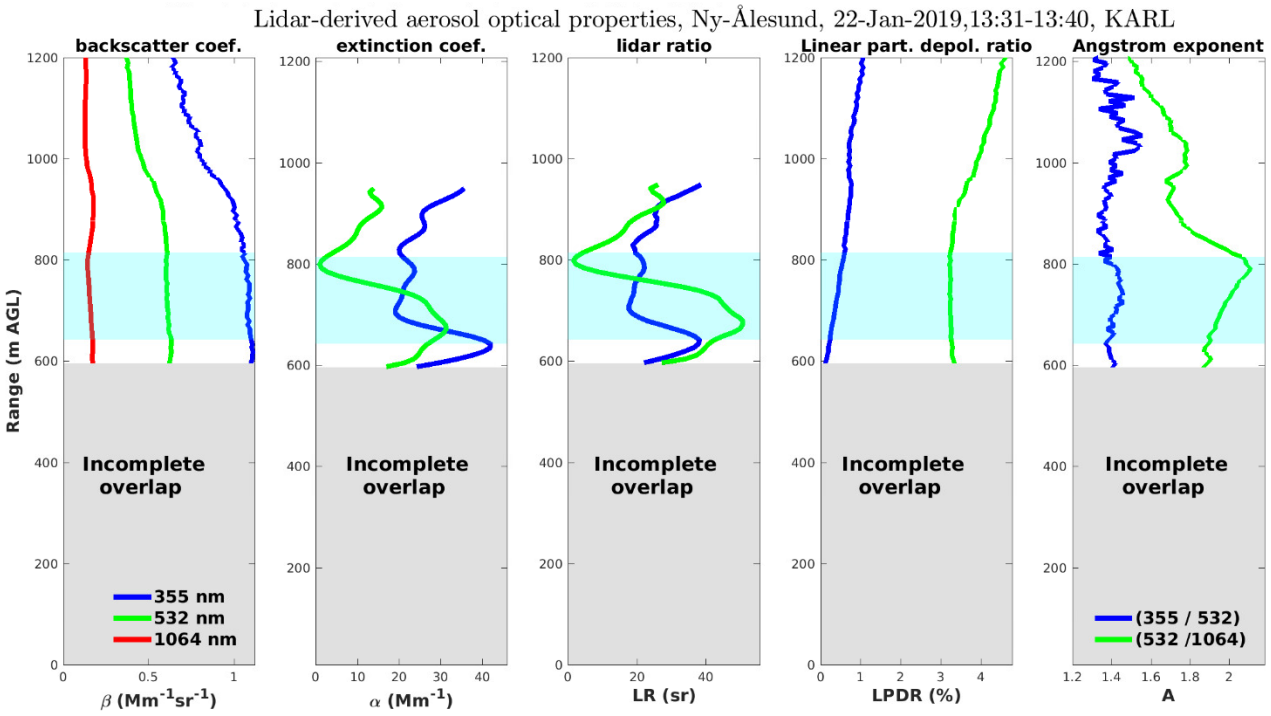

Fig. 3.18: Profiles of aerosol optical properties as derived by KARL. The layer selected for the aerosol microphysics retrieval is denoted with cyan shading.

of the analyzed layer compared to CALIOP (e.g. 322–1280 m for the closer layer).

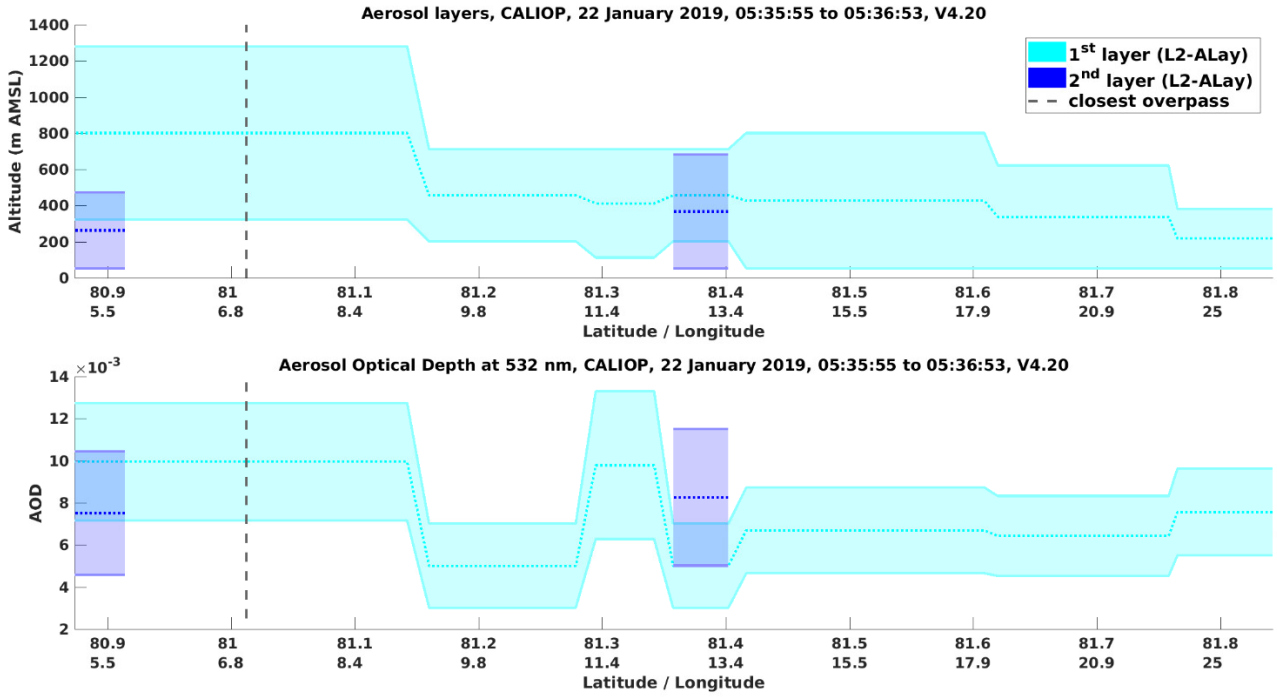

Fig. 3.19: CALIOP-derived aerosol layer base and top (upper panel) and AOD (lower panel). The closest overpass over Ny-Ålesund (250 km) is also given (dashed vertical line).

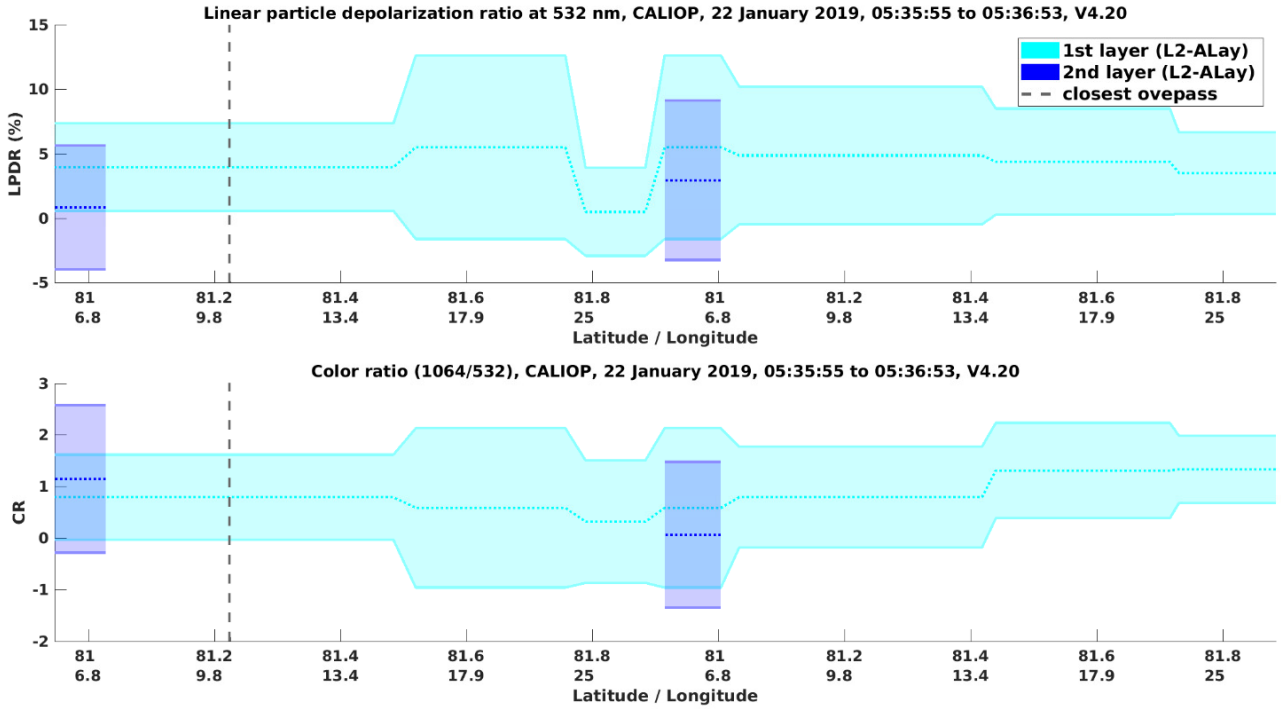

Fig. 3.20: Same as 3.19 but for LPDR (upper panel) and CR (lower panel).

The aerosol LR_{532} and CR are in line with marine aerosol studies. Groß et al. (2013) (Burton et al. (2013)) reported a LR_{532} of 18 $\pm$ 5 sr (17–27 sr) and $CR_{(532/1064)}$ of 1.64 $\pm$ 0.1 (1.3–1.6). Dawson et al. (2015) derived from satellite observations a global mean LR_{532} of 26 sr, which decreased with wind speed over the ocean surface (U_{10}). More specifically, for calm wind conditions (U_{10} < 4 ms^{-1}) the LR_{532} was estimated at 32 $\pm$ 17 sr, while under strong winds (U_{10} > 15 ms^{-1}) the LR_{532} dropped to 22 $\pm$ 7 sr. At Ny-Ålesund calm wind conditions prevailed in the first 800 m above ground (wind speed lower than 3 ms^{-1} from radiosonde measurements) with south-east flow. This could explain the slightly higher LR from KARL compared to CALIOP. It should be noted that the CALIOP derived LR was equal to 23 $\pm$ 5 sr for all of the marine layers as the extinction retrieval was obtained by prescribed LR values (Kim et al., 2018).

The LPDR from KARL and CALIOP is slightly lower compared to marine aerosol studies. Groß et al. (2013) (Burton et al. (2013)) reported a $LPDR_{532}$ of 3 $\pm$ 1% (4–9%). Haarig et al. (2017) derived the LPDR of marine aerosol as a function of RH, finding less spherical aerosol under low RH conditions. Under dry conditions (RH around 40%) the $LPDR_{355}$ ($LPDR_{532}$) reached 12 $\pm$ 8% (15 $\pm$ 4%) as a cubic-like particle shape appeared, while a transition to spherical shapes occurred at higher RH (50-80%) with $LPDR_{355}$ ($LPDR_{532}$) lower than 3% (2%). The RH over Ny-Ålesund amounted to approximately 40% within the layer. However, the LPDR is closer to the wet aerosol regime of Haarig et al. (2017), indicating the presence of an additional more spherical aerosol component.

Tab. 3.5: Aerosol optical properties over Ny-Ålesund and along the closest CALIPSO overpass.

Aerosol optical properties			
lidar system	**KARL**	**CALIOP (closest layer)**	**CALIOP (adjacent layers)**
geolocation	78.9^oN, 11.9^oE	81^oN, 7.1^oE	81.84^oN, 27.5^oE
			to $80.85^oN, 5^oE$
time (UTC)	13:31–13:40	05:36:47	5:36–5:37
geom. limits (m)	642–814	322–1280	53–801
LR_{355} (sr)	23 ± 6	–	–
LR_{532} (sr)	32 ± 19	23 ± 5	23 ± 5
$LPDR_{355}$ (%)	0.4 ± 0.1	–	–
$LPDR_{532}$ (%)	3.2 ± 0.01	3.96 ± 3.39	0.5 ± 3.4–5.5 ± 7
$CR_{\beta355/\beta532}$	1.8 ± 0.02	–	–
$CR_{\beta1064/\beta532}$	0.25 ± 0.01	0.79 ± 0.82	0.06 ± 1.4–1.33 ± 0.65
AOD_{532}	0.0034	0.01 ± 0.003	0.006 ± 0.002–0.01 ± 0.004

3.3.3 Aerosol microphysical properties from in-situ and remote sensing perspectives

This section focuses on the inversion of aerosol microphysics and its comparison to in-situ measurements. The aerosol microphysics were inverted from the aerosol optical properties using spline collocation and an iterative Padé regularization method (see Section 2.4.2). Several sensitivity tests were performed regarding the spline basepoints. More specifically, their number (9, 12, 15 and 18) as well as their position was iteratively changed. Finally, the volume distribution was inverted from 18 basepoints, with their number not found to affect the inversion performance. The in-situ aerosol size distribution was derived from the OPC, which measured the aerosol number concentration (average, standard deviation and number of measurement points) at 21 diameter ranges (0.34–9.5 μm). For finer particles (diameters of 0.014–0.3 μm) the Minidisc sensor provided the total number concentration. Measurements from 12 altitude levels (642–814 m) with a resolution of about 15 m were extracted for further analysis.

The particle volume and number size distributions are presented in Fig. 3.21. Initially, the volume distribution was assessed, since it is numerically more stable. Both the in-situ and lidar derived distributions were bi-modal. The two modes of the inverted distribution appeared around 0.2 and 0.5 μm. Regarding the in-situ distribution, its finer mode appeared around 0.17 μm and its coarse mode was shifted to bigger radii (0.68 μm). Despite the location shift, the two coarse modes agreed on the peak magnitude.

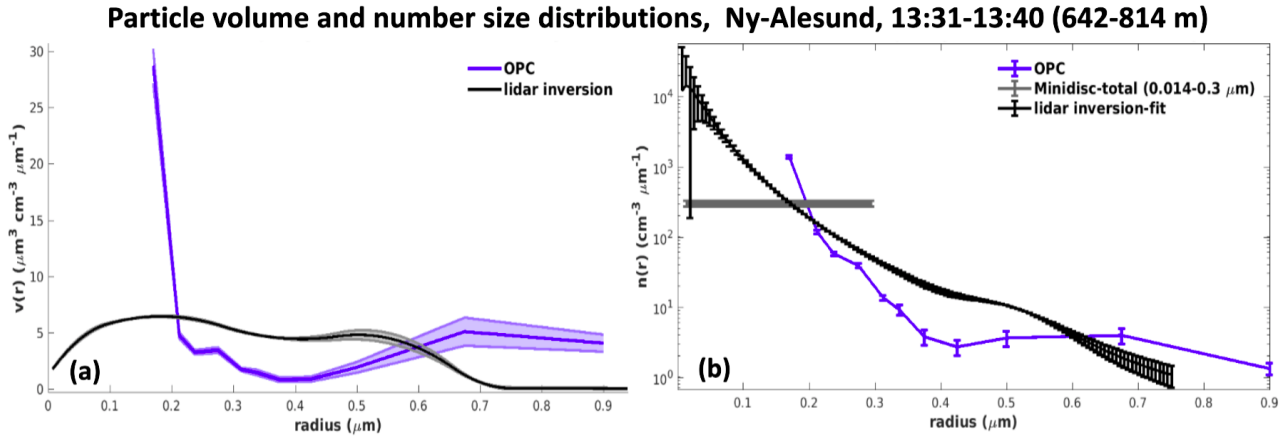

Fig. 3.21: Particle volume (a) and number size distributions (b) derived in-situ (blue) and inverted from lidar observations (black). Total particle number concentration from the Minidisc sensor is also given (gray). Shaded areas denote one standard deviation (fitting errors) of the distributions (inverted number distribution).

Upon gaining confidence in the agreement of the volume distributions, the particle number size distribution was assessed. The in-situ distribution is presented as mean $\pm$ one standard deviation (Fig. 3.21b), while the inverted number distribution was derived by log-normal fits to the two modes of the inverted volume distribution (see Sec. 2.4.2). The fitting approach was selected over the inversion of the number distribution (using Eq. 2.18) due to the numerical instability of the latter approach in the low radii limit. Still errors stem from the fitting, with the procedure being more sensitive to the lower and upper radii limits (higher errorbars). For radii 0.007–0.15 μm the total number concentration from the Minidisc sensor is also given (gray line). For radii bigger than 0.2 μm the in-situ and lidar number distributions differed by less than one order of magnitude. However, for smaller radii higher differences (1–2 orders of magnitude) were observed, which can be attributed to the more challenging to measure and invert fine particles. The aerosol microphysical properties are summarized in Tab. 3.6. The lidar inverted number, surface and volume concentration is given for two modes, while the respective total concentrations from in-situ are also presented. The best agreement was achieved in terms of volume concentration. Moreover, the sum of OPC and Minidisc number concentrations agreed with the inverted number concentration within the range of uncertainties. The surface concentrations were in the same order of magnitude but they lay out of each other uncertainty.

The SSA was estimated from forward Mie calculations of the aerosol scattering and absorption coefficients (SSA = 0.96) as well as from the combination of nephelometer and PSAP measurements (SSA = 0.8). The remote sensing derived SSA indicated highly scattering particles, whereas the in-situ derived SSA pointed to absorbing particles. The in-situ SSA lay out of the 25^{th}–75^{th} percentile of long-term Arctic site statistics (Schmeisser et al., 2018). For instance, the SSA at Zeppelin, the closest station to Ny-Ålesund, is above 0.85 even at the 5^{th} percentile level. Additionally, the absorption coefficient uncertainty (and, thus, the SSA uncertainty) is primarily determined by the uncertainty of the correction scheme,

Tab. 3.6: Aerosol microphysical properties. For the remote sensing inversion, uncertainties represent the standard deviation of the best complex refractive index solutions. For the inverted number, surface and volume concentrations the fitting errors are given.

Aerosol Microphysical Properties, Ny-Ålesund			
22 January 2019, 13:31–13:40, 642–814 m			
	remote sensing inversion		**in-situ**
refractive Index ri (mean ± standard deviation)			
ri	$1.52 + 0.005 \cdot i \pm 0.01 + 0.002 \cdot i$		–
single-scattering albedo SSA (mean ± standard deviation)			
SSA_{355}	0.96 ± 0.02		-
SSA_{532}	0.96 ± 0.01		0.8 ± 0.02
effective radius r_{eff}, number n_t, surface s_t and volume v_t concentration			
	fine	coarse	total (0.17-0.9 μm)
r_{eff} (μm)	0.21	0.52	-
$n_t(cm^{-3})$	637.3 ± 426.7	0.64 ± 0.16	39.4 ± 2.5 (301 ± 29 at 0.007-0.150 μm)
$s_t(\mu m^2 cm^{-3})$	42.6 ± 4.9	2.1 ± 0.5	24.9 ± 2.9
$v_t(\mu m^3 cm^{-3})$	3 ± 0.3	0.36 ± 0.09	2.9 ± 0.5

which converts the measured light attenuation to light absorption coefficient. The latter uncertainty ranges from 20% at sites with high loading of strongly absorbing particles up to 100% or more at sites with low loading of weakly absorbing particles (Ogren et al., 2017). Other sources of discrepancy might be related to an incomplete capture of fine particles in the in-situ sensors or assumptions in the remote sensing inversion (e.g. wavelength-independent refractive index).

From a physical point of view, the discrepancies could be related to the effects of micrometeorology and hygroscopicity. Ny-Ålesund is characterized by complex orography, which can perturb the boundary layer structure (Jocher et al., 2015). In winter and early spring the boundary layer height over Ny-Ålesund rarely exceeds 100 m (Rader et al., 2021). Hence, both the lidar and in-situ measurements were most likely performed in the lower free-troposphere but small scale changes in the aerosol concentration and properties cannot be ruled out. Additionally, aerosol remote sensing is performed in ambient conditions, while aerosol are sampled in-situ under nearly dry conditions (RH of 30-40%). However, the RH was approximately 40% within the layer altitude and, thus, hygroscopic effects were rather unlikely.

Finally, the bi-modal size distribution may indicate the presence of two different aerosol components. The real part of the refractive index (1.52 ± 0.01) was closer to literature values

of ammonium sulphate (1.52–1.55 at 400–700 nm, (Toon, Pollack, and Khare, 1976)) and slightly higher than that of sea salt (1.49 at 633 nm, (Shettle and Fenn, 1979)). Therefore, it can be argued that apart from marine aerosol (coarse mode), an anthropogenic aerosol component (fine mode), most likely combustion aerosol, was present. It should be mentioned that marine and smoke aerosol exhibit partly overlapping optical properties since they are characterized by low LPDR (0–5%, Fig. 2.1). Additionally, in some cases their LR marginally overlaps and, therefore, it might be difficult to distinguish these two aerosol components.

3.4 Discussion and Conclusions

In this Chapter the optical, microphysical and radiative properties of Arctic aerosol were investigated at case study level. In the first part, a long-range transport episode was investigated (Sec. 3.1). Geometrically similar aerosol layers were observed over three neighboring locations (North Greenland – East Canadian Archipelago, Fram Strait and Ny-Ålesund, Fig. 3.1-3.4). Overall, nearly spherical aerosol was found. Air mass backward trajectories indicated northeast China as the source of aged aerosol within the Fram Strait and the upper part of the Ny-Ålesund layer (Fig. 3.2 and 3.4). However, the lower part of the Ny-Ålesund layer originated from north Scandinavia. Therefore, it be argued that the upper Ny-Ålesund sub-layer was the aged version of the Fram Strait layer, while the lower sub-layer comprised relatively fresh aerosol.

The aerosol size distribution was different over Fram Strait and Ny-Ålesund, with depletion of the coarse mode (Fig. 3.9). In the interim transport, the presence of ice clouds indicated the potential action of nucleation scavenging. Despite the modification of the aerosol size distribution, the short-wave (SW) radiative footprint was similar over both locations due to the domination of accumulation mode aerosol. However, the aerosol radiative effect (ARE) was not negligible, amounting to $+4.4\ Wm^{-2}$ ($+4.5\ Wm^{-2}$) in the atmospheric column over the highly reflective surface of Fram Strait (Ny-Ålesund). Top of the atmosphere (TOA) warming was accompanied by surface cooling, with implications for atmospheric stratification. The maximum aerosol heating rate (HR_{aer}) amounted to $-0.32 \pm 0.04\ Kday^{-1}$ ($-0.16 \pm 0.19\ Kday^{-1}$) over Fram Strait (Ny-Ålesund). In the context of retreating sea ice (Doscher, Vihma, and Maksimovich, 2014), the radiative footprint may exhibit higher variability along transport episodes due to increasingly diverse surface albedo conditions (e.g. more leads and polynyas). Apart from the aerosol physical variability, the aerosol retrieval uncertainties and limitations deserve thorough exploration in order to better constrain the vertically-resolved ARE.

In the second part, the sensitivity of ARE and HR_{aer} was assessed with respect to aerosol uncertainties and ambient conditions (Sec. 3.2). Concerning the aerosol uncertainties, the highest sensitivity emerged in response to the single-scattering albedo (SSA). More specifically, a 10% SSA change induced higher perturbations than a 30% change in the extinction coefficient. The sign of ARE was not modified under the given aerosol uncertainties. In

this sense, a qualitative assessment of the ARE is feasible. With respect to ambient conditions, the ARE_{TOA} was more sensitive to solar elevation changes compared to $ARE_{surface}$ (Fig. 3.13). A solely negative ARE appeared only for dark surfaces, whereas a negative to positive shift was found for bright surfaces (Fig. 3.15d). Over bright surfaces, more net irradiance remained above the aerosol layers relative to aerosol-free conditions (multiple reflection domination), while the opposite held true over dark surfaces (shadowing domination). Consequently, the sign of the ARE can be highly sensitive in spring, which is characterized by transitional surface albedo conditions.

In the final part, a low tropospheric aerosol event was investigated using remote sensing and in-situ techniques (Sec. 3.3). The aerosol size distribution was inverted from the optical input parameters and it was compared to in-situ measurements. From the remote sensing perspective, the intensive optical properties as derived from KARL and CALIOP presented good agreement (Tab. 3.5). Spherical and highly scattering particles were found, with CALIOP attributing them to marine aerosol. Both the lidar inversion and the in-situ measurements revealed a bi-modal aerosol size distribution (Fig. 3.21) and high agreement was found in the total volume concentration (Tab. 3.6). However, disagreement was found in the SSA, with the lidar inversion indicating highly scattering particles and the in-situ measurements pointing to absorbing particles. The discrepancies could stem from assumptions in the inversion (e.g. wavelength-independent refractive index) and errors in the conversion of the in-situ measured light attenuation into absorption. Another source of discrepancy might be related to an incomplete capture of fine particles in the in-situ sensors. The disagreement in the most critical parameter for the Arctic ARE necessitates further exploration in the frame of aerosol closure experiments. Care must be taken in ARE modelling studies, which may use either the in-situ or lidar-derived SSA as input.

4

DEVELOPMENT OF A CIRRUS CLOUD RETRIEVAL SCHEME

Accurate and precise detection of cirrus cloud boundaries is of high necessity as the geometrical cloud thickness is essential for parameterizing the cirrus cloud optical depth (COD, Sassen and Comstock, 2001; Wang and Sassen, 2002). In turn, the accuracy of cloud optical properties is critical for cloud phase classification and cloud – aerosol discrimination. Different lidar-based retrievals of cirrus cloud optical properties exist, each one with its own strengths and limitations. For instance, the transmittance (Platt, 1979) and backward – total optical depth methods (Elouragini and Flamant, 1996) cannot be applied to optically-thinner cirrus (COD < 0.05 and COD < 0.1, respectively). The Raman technique (Ansmann et al., 1992) provides a vertically-dependent cirrus lidar ratio (LR_{ci}) but is limited to night-time applications, contrary to the double-ended Klett method (Ansmann et al., 1992) that, however, yields a layer-mean LR_{ci}.

In this chapter, the development of a cirrus cloud retrieval scheme is presented using representative cases over Ny-Ålesund. The scheme consists of cirrus detection (*dynamic WCT*) and optical characterization (*constrained Klett*). Sensitivities related to cirrus detection are performed (App. A) and their effect on the cirrus optical properties is examined (Sec. 4.5). Additionally, the limitations of the proposed *constrained Klett* are investigated (App. B.1) and its inherent uncertainties are quantified (App. B.2). The *constrained Klett* is compared with two established optical retrievals (Sec. 4.4), with their limitations and strengths discussed (Sec. 4.6). Hereafter, the term cirrus cloud will refer to a set of consecutive cirrus layers. This chapter is based on the results of Nakoudi, Stachlewska, and Ritter (2021) but the comparison to established methods is extended to a long-term dataset. The code for the retrieval scheme is publicly available (Nakoudi and Ritter, 2020).

4.1 Fine-scale cirrus cloud detection

4.1.1 Selection of cirrus clouds

The specifications of KARL enable signal acquisition at fine vertical and temporal scales (7.5 m, 1.5 min), which are well-suited for the investigation of cloud properties. As here the focus is on cirrus clouds, the presence of supercooled liquid-water layers needed be excluded. Therefore, only clouds with cloud base (C_{base}) temperature lower than -40^oC (homogeneous nucleation temperature) were considered (Delanoë and Hogan, 2010; Ceccaldi et al., 2013). Temperature profiles were obtained by the daily radiosondes launched from AWIPEV (Sec. 2.3.1). The utilized temperature criterion is strong as Shupe (2011) reported only 3–5% liquid-water occurrence between -40 and -30^oC within Arctic clouds. Thus, the

possibility of liquid-water presence is very low, even within the range of temperature uncertainty (Sec. 2.3.1) or errors due to radiosonde drift and temporal discrepancy with the lidar observations. In the following section all the steps of cirrus detection are presented in detail, including the revised method.

4.1.2 Wavelet Covariance Transform method

In order to detect the cirrus C_{base} and C_{top}, the Wavelet Covariance Transform (WCT) method (Brooks, 2003) was extended by dynamic thresholds. The WCT is sensitive to signal gradients and has been employed for detecting either cirrus clouds (Dionisi et al., 2013; Voudouri et al., 2020) or the planetary boundary layer top height (Nakoudi et al., 2019; Wang et al., 2020). Following the signal calibration and corrections (see Sec. 2.1), the lidar range-corrected signal (Pr^2) was normalized (with respect to the median signal between the range of full overlap and 12 km). The latter step was essential for making the WCT profiles comparable to literature thresholds (Baars et al., 2008) but did not affect the Pr^2 signal and WCT gradients.

In Fig. 4.1 the Pr^2 signal and WCT profiles corresponding to the lower part of a cirrus layer are presented. The WCT profiles (Eq. 4.1) can be perceived as the low-pass filtered version of the Pr^2 signal (Kokkalis et al., 2020) as they are based on its convolution with a Haar step function (Eq. 4.2) of specific step width (dilation, α) and step location (b). The Pr^2 signal was integrated below (outer zone, green shading) and above (inner zone, gray shading) each range bin. Each zone's width was equal to $\alpha/2$.

$$W_f(\alpha, b) = \frac{1}{\alpha} \int_{C_{base}}^{C_{top}} P(r) \cdot r^2 \cdot h\left(\frac{r-b}{\alpha}\right) dr \tag{4.1}$$

$$h\left(\frac{r-b}{\alpha}\right) = \begin{cases} +1, & b - \frac{\alpha}{2} \leq r \leq b \\ -1, & b \leq r \leq b + \frac{\alpha}{2} \\ 0, & \text{elsewhere} \end{cases} \tag{4.2}$$

The knowledge of cloud presence below the targeted cirrus layers is important. For this reason, underlying cloud layers were also screened with the WCT method. Lidar profiles were retained for further evaluation on condition that the signal quality was high. Otherwise, if above the low- or mid-level clouds the signal-to-noise ratio (SNR, Eq. 2.9) was low (< 3 as in Elouragini and Flamant (1996)), the profiles were discarded. Likewise, the signal quality was checked above the cirrus C_{top}.

An appropriate dilation is crucial for accurate cirrus detection. A relatively narrow dilation produces more noisy WCT profiles, while a too wide dilation may not resolve small-scale

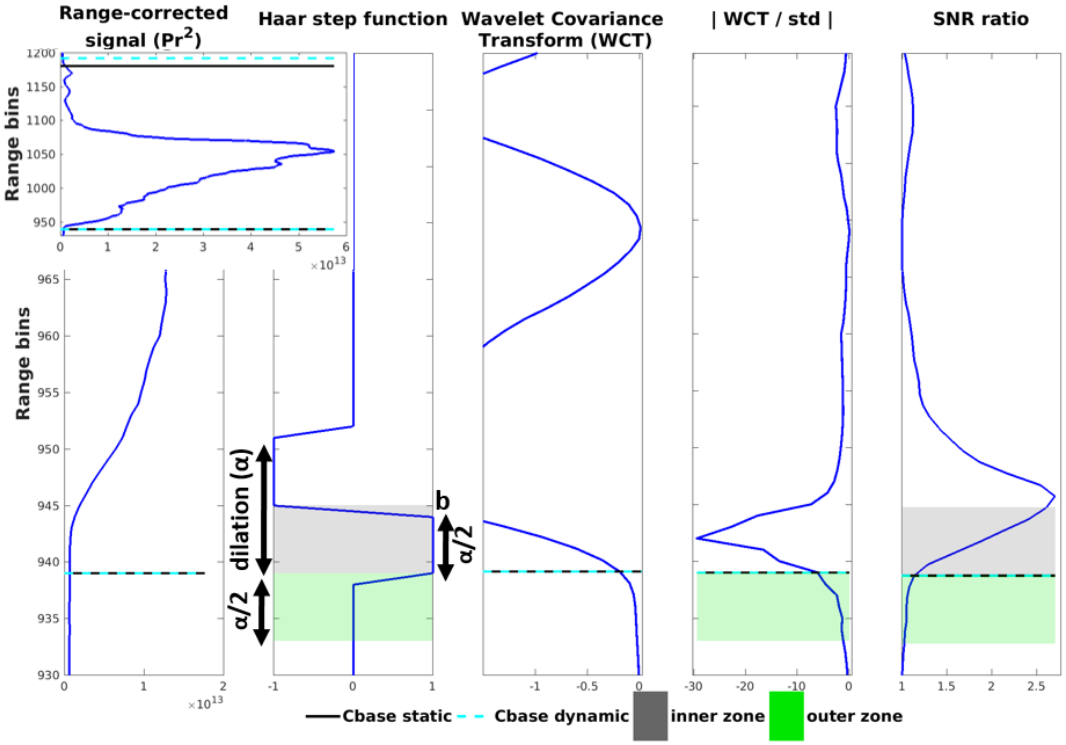

Fig. 4.1: Exemplary profiles of Pr^2 signal, Haar step function, WCT, WCT to signal standard deviation ratio ($|WCT/std|$) and *SNR ratio*, which correspond to the lower part of a cirrus layer observed at 7-9 km. Horizontal lines denote the dynamic (cyan) and static (black) derived C_{base}. Gray (green) shading denotes the inner (outer) zone of the cirrus layer. The whole cirrus layer Pr^2 profile is given in the upper left inset figure.

features such as thin clouds. In order to select an appropriate dilation, its effect on cirrus detection was assessed through a sensitivity analysis and finally a value of 90 m was chosen (App. A.1).

4.1.3 Revised detection method: Dynamic Wavelet Covariance Transform

Another crucial parameter for cirrus detection is the WCT threshold, which determines whether a signal gradient denotes a cloud boundary or not. Static WCT thresholds have been proposed so far (Baars et al., 2008; Baars et al., 2016). However, in this work dynamic thresholds were introduced, which assess the strength of the signal gradients with respect to the given signal variability. Two dynamic thresholds are introduced here; the first depends on the ratio of WCT over the signal standard deviation ($|WCT/std|$) and the second relies on the SNR. The main steps of the *dynamic WCT method* are outlined in Fig. 4.2. This approach has a higher robustness potential, since it is adaptable to the given cloud strength and lidar specifications. After examining a significant number of profiles, it was found that cirrus peaks were related to WCT values exceeding the signal standard deviation ($|WCT/std| > 1$, e.g. Fig. 4.1). $|WCT/std|$ thresholds of 1.5 and 2 were also investigated, but they mostly de-

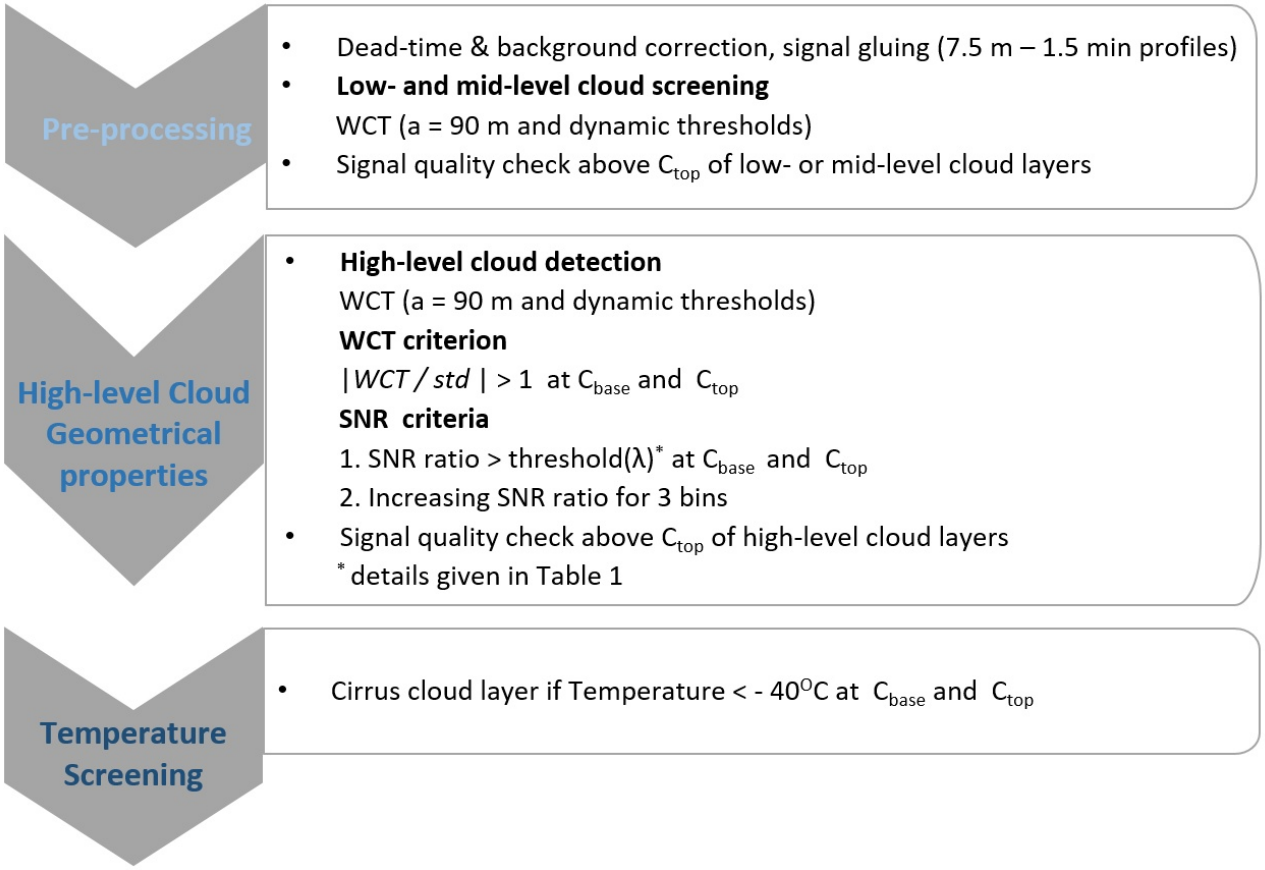

Fig. 4.2: Flowchart of the revised cirrus detection.

tected stronger parts of the cirrus layers, leaving out the faint marginal parts. A candidate C_{base} (C_{top}) was finally identified one bin below (above), where $|WCT/std| > 1$, by inspecting the profiles in the upward (downward) direction.

In order to discriminate cirrus related peaks from noise, an SNR criterion was introduced. Within the inner and outer zones of bins, where $|WCT/std| > 1$, the median SNR was calculated. Then, the algorithm checked whether the inner to outer zone $SNR\ ratio$ exceeded a given threshold. Additionally, an increasing $SNR\ ratio$ was demanded for three consecutive bins above the C_{base} (below the C_{top}). Slightly different $SNR\ ratio$ thresholds were found for each wavelength due to discrepancies in the SNR of each channel. The thresholds are summarized in Tab. A.1. The wavelength dependency of the WCT was also investigated (App. A.2) and the 532 channel with perpendicular polarization (532_s) was finally selected for cirrus detection. In the next Section an assessment of the dynamic thresholds with respect to the static ones is performed.

4.2 Comparison of dynamic and static cirrus detection

Firstly, the *dynamic WCT* method is compared to the static one on a systematic basis, using cirrus layers with variable geometrical depth, occurrence altitude and vertical structure. In total 832 layers were identified by the dynamic WCT, while the static WCT identified the C_{base} (C_{top}) of 779 (805) layers. The distributions of C_{base} (in blue) and C_{top} (in gray) differences are shown in Fig. 4.3. The static WCT provided the C_{base} higher and the C_{top} lower than the *dynamic WCT*. Thus, the static WCT tended to identify the cloud boundaries towards the centre of the cirrus layers as it was less sensitive to their marginal parts. The difference of the two methods was mostly less than 500 m, while in few cases it exceeded 1000 m. Optically-thin and sub-visible layers were characterized by higher C_{base} differences, whereas for the C_{top} the difference was higher in opaque layers.

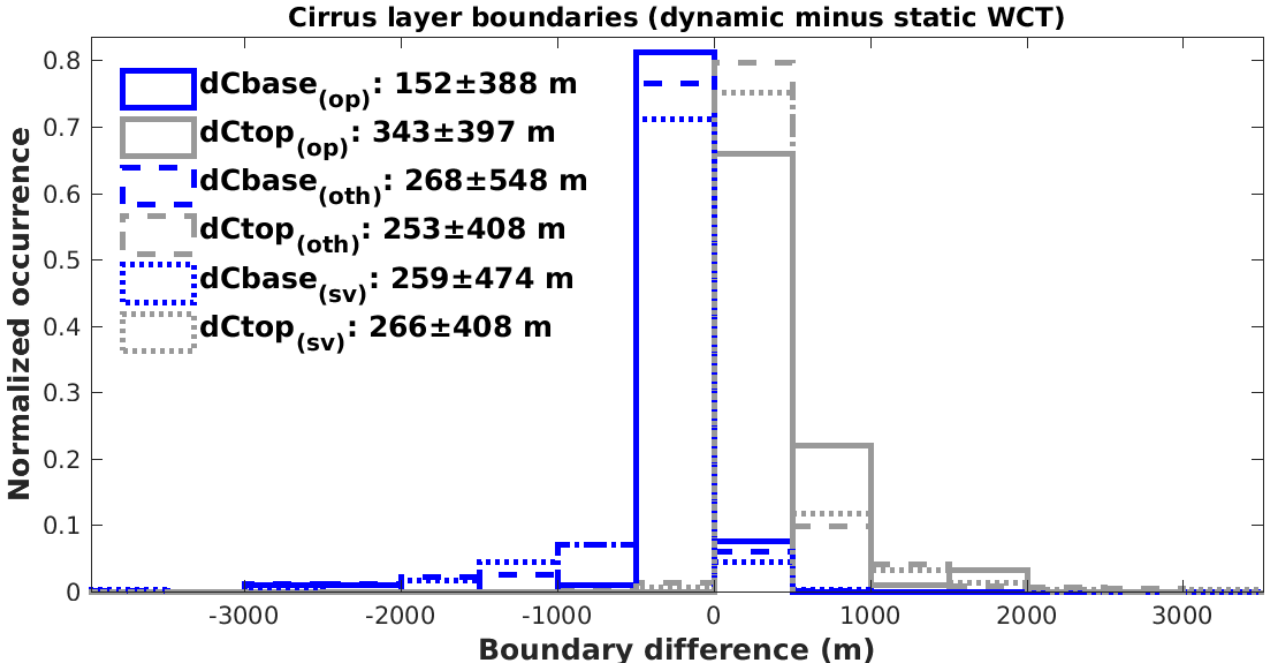

Fig. 4.3: Distribution of C_{base} and C_{top} difference (dynamic minus static WCT). Separate distributions are given for each apparent COD regime, defined with respect to the *dynamic WCT* derived properties.

In addition to the overall comparison, a daytime cirrus cloud case (affected by background illumination) was analyzed (Fig. 4.4). The dynamic method proved more sensitive to weak signal gradients and marginal parts of cirrus layers. Instead, the static method did not always detect the boundaries of faint layers. For instance, the WCT at the C_{base} of the layer depicted in Fig. 4.4b was equal to -0.07 and, therefore, it was not captured by the less sensitive static threshold (0.3, Baars et al., 2016). Moreover, as demonstrated in Fig. 4.4c, the static method was only sensitive to stronger cirrus parts, while the dynamic method detected the C_{base} (C_{top}) 278 m (285 m) out of the static-derived boundaries. Hence, the static method underestimated the cirrus geometrical thickness by more than 500 m in this given cirrus layer. Finally, it should be mentioned that for some faint layers both methods failed to detect the cirrus boundaries, as for 8:00–9:00 UT on 25 April 2015 (Fig. 4.4a). Overall, the

dynamic method detected faint layers that could otherwise not have been detected by the static method.

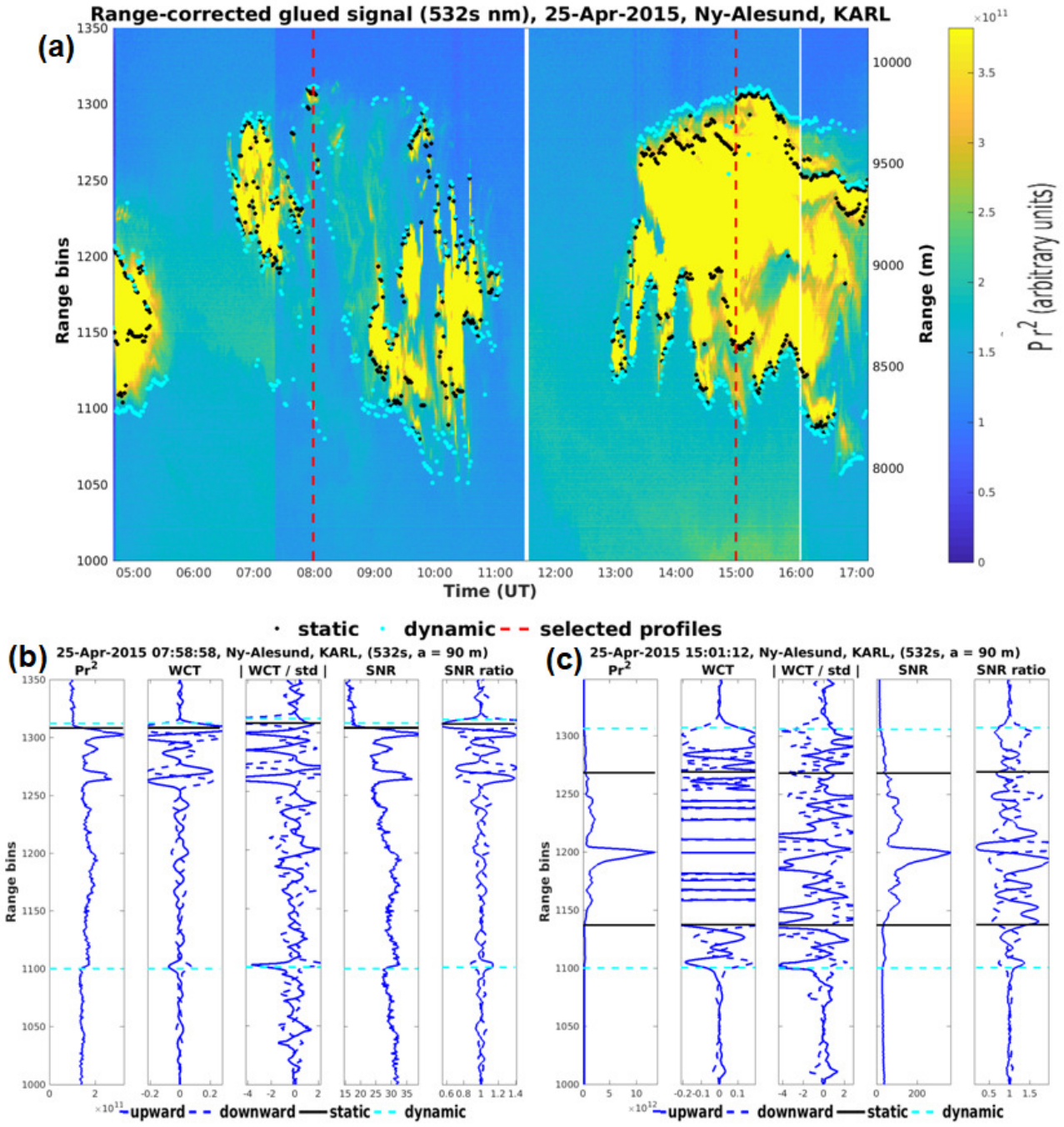

Fig. 4.4: Lidar Pr^2 signal with overlaid dynamic (cyan) and static (black) WCT derived cirrus boundaries. Signal normalization accounts for background color changes. Selected profiles (red vertical lines) are presented in panels (b) and (c), where horizontal lines indicate the dynamic and static cirrus boundaries. Solid (dashed) blue lines correspond to upward (downward) profiles used for C_{base} (C_{top}) detection. For better readability, please refer to the digital version.

4.3 Cirrus cloud optical retrievals

In this Section existing cirrus optical retrievals are first presented (Sec. 4.3.1). Subsequently, the proposed *constrained Klett* method (Sec. 4.3.3) is described, including the newly introduced parameters, i.e. the *convergence range*, the *reference value* as well as the factor used to adjust the LR_{ci} after each iteration (Eq. 4.3). The main steps are outlined in Fig. 4.6.

4.3.1 Existing cirrus optical retrievals: double-ended Klett and Raman

In order to gain confidence in the proposed *constrained Klett* method, two established retrievals were also applied. Concerning the double-ended Klett (Ansmann et al., 1992), sets of backward and forward Klett–Fernald retrievals (Klett, 1981; Fernald, 1984) were performed with changing LR_{ci}. The LR_{ci} with the lowest *root mean square error* between the backward and forward particulate backscatter coefficient profiles (β^{part}) was selected. The LR_{ci} was modified within a wide range of values (5–90 sr) in order to avoid an a priori exclusion of physically possible solutions. The selection was based on experimental (Ansmann et al., 1992; Chen, Chiang, and Nee, 2002) and modeling studies (Okamoto et al., 2019; Okamoto et al., 2020). For instance, Ansmann et al. (1992) reported values between 5 and 15 sr over a marine mid-latitude site using the Raman technique. Okamoto et al. (2019) and Okamoto et al. (2020) performed simulations and reported a LR_{ci} from 5 sr to 100 sr and higher. The Klett–Fernald calibration range was set in the stratosphere for the backward retrieval (Sec. 2.1.3) and in the *convergence range* for the forward retrieval (more details follow in Sec. 4.3.3). In this way, the retrievals were made as comparable as possible to the *constrained Klett*. However, it should be noted that the classical double-ended Klett assumes aerosol-free conditions below and above the cirrus cloud (Ansmann et al., 1992). The impact of the aerosol-free assumption is investigated in Section 4.4.

The cirrus optical characterization and the *reference value* estimation was also performed via the Raman technique (Sec. 2.1.3). Although this technique provides a vertically-dependent LR_{ci}, here a vertically-mean LR_{ci} is reported so as to facilitate the comparison with the double-ended and *constrained Klett*. The Raman technique was limited to night-time cases. However, in order to reduce the noise of the weak Raman signals, profiles were smoothed with a Savitzky–Golay filter. The smoothing window was equal to one-third of the minimum cirrus cloud thickness. The comparison among the *constrained Klett*, double-ended Klett and Raman retrievals is presented in Sec. 4.4 and their limitations and strengths are discussed in Sec. 4.6.

4.3.2 Temporal averaging within stationary periods

The high vertical and temporal resolution profiles allowed for reliable cirrus detection. However, the precision of optical properties was affected by statistical uncertainties and, thus,

temporal averaging was necessary. Care should be taken with long temporal averaging to avoid smearing out the cloud physical variability. Otherwise, cloud and cloud-free range bins might be averaged and produce physically unrealistic profiles. More importantly, distorted particulate extinction profiles affect the accuracy of radiative estimates (Lolli et al., 2018).

Bearing the aforementioned aspects in mind, a temporal averaging that is constrained by periods of stationarity was adopted following Lanzante (1996). This procedure is based on the Mann–Wilcoxon–Whitney test, such that the data points of one stationary period share the same COD statistical distribution. This method has been applied to time-series of cirrus COD and geometrical thickness by Larroza et al. (2013). Here the procedure was applied on the integrated backscatter coefficient (β_{int}) time-series , which was obtained from an initial guess Klett–Fernald retrieval (more details follow in Sec. 4.3.3). The designation of stationary (yellow lines) and temporal averaging periods (red lines) is shown for the case of 23 January 2019 in Fig. 4.5. The β_{int} was selected instead of the COD because the latter might be influenced by the assumed LR_{ci} (Sec. 4.3.3). However, in the majority of the analyzed cases (2011-2020) the β_{int} and COD exhibited similar variability.

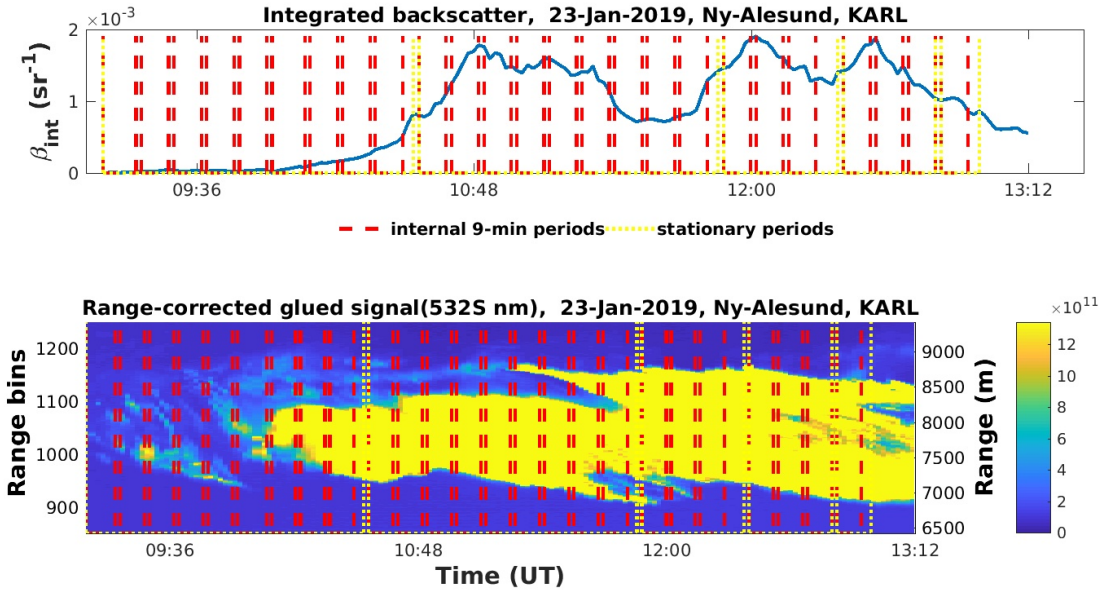

Fig. 4.5: Time-series of integrated backscatter coefficient (β_{int}, upper panel) and Pr^2 signal (lower panel) with overlaid stationary (yellow lines) and temporal averaging periods (red lines). Temporal averaging was only performed within each stationary period.

As expected the stationary periods had variable duration since they reflect the physical variability of the investigated parameter. For instance, on 23 January 2019, each of the first two periods was over 1 h long, while the subsequent two periods did not exceed 30 min each. However, one should keep in mind that the β_{int} is a columnar parameter and, thus, the cirrus vertical variability cannot be accounted for by the stationary periods. Therefore, shorter averaging periods were obtained for ensuring non-distorted profiles. In order to obtain homogeneous statistical uncertainties temporally-averaged profiles of equal duration

were constructed (9 min by averaging 6 consecutive raw profiles) within each stationary period. Periods shorter than 9 min were discarded. Finally, the cirrus C_{base} and C_{top} were newly determined based on the averaged signal profiles by the *dynamic WCT* method.

4.3.3 Revised optical retrieval: constrained Klett method

In the revised optical retrieval, the backward Klett–Fernald method (Klett, 1981; Fernald, 1984) was constrained by a *reference value*. The *reference value* represents the aerosol concentration beneath the cirrus cloud by means of the backscatter ratio (BSR_{ref}, Eq. 2.6). Then, the LR_{ci} is iteratively adjusted until the BSR matches with the BSR_{ref}. The aerosol concentration beneath the cirrus cloud was assumed as temporally constant. In order to enhance the validity of this assumption, the *reference value* was set within the range of minimum signal variance (*convergence range*). The *convergence range* is a 500 m–zone, where the median signal presents minimum temporal variance. The *convergence range* was bounded by the full overlap range (600 m) and 1 km beneath the minimum C_{base}. In this way, artificial signal gradients as well as cirrus adjacent areas, where turbulence and ice seeding are more likely, were avoided to the greatest possible extent. If the variance was equally low in more than one zones, the highest one was selected, because the Klett errors increase with the integration from the far-range (Sec. 2.1.3). Finally, profiles not highly correlated (r < 0.98) with the temporal median profile were discarded.

Firstly, an initial guess Klett–Fernald retrieval was performed in two LR zones, one within the cirrus layer (assumed LR_{ci}^{355} = 20 sr and LR_{ci}^{532} = 28 sr) and one outside (assumed LR^{355} = 35 sr and LR^{532} = 36 sr). Using the assumed LR_{ci}, the Newton-Raphson method (described in Ryaben'kii and Tsynkov (2006)) was initialized. The assumed LR_{ci} can be arbitrary provided that it is close enough to the unknown quantity and, therefore, it was selected close to literature values (e.g. (Giannakaki et al., 2007; Gouveia et al., 2017; Voudouri et al., 2020)). Regarding the LR outside the cirrus layer, background values for the site of Ny-Ålesund were taken from Ritter et al. (2016). The background values should be adapted accordingly for different research sites.

Subsequently, using the initial guess retrieval, the β_{int} was estimated within the cirrus range. Although the β_{int} was a first approximation, its minimum corresponded to layers with minimum COD. The lower the COD the less is the Klett–Fernald solution affected by a wrongly chosen LR_{ci}. Therefore, a *reference profile* was chosen as the profile of minimum β_{int} or, if available, as the temporally-closest cloud-free profile. Then, the BSR_{ref} was calculated as the median BSR within the *convergence range* of the *reference profile*. However, an accurate BSR_{ref} can only be obtained from *reference profiles* of low COD. This limitation is investigated in App. B.1, where an upper COD threshold of 0.2 was found to provide sufficient accuracy. The effect of BSR_{ref} statistical uncertainties on the derived optical properties is

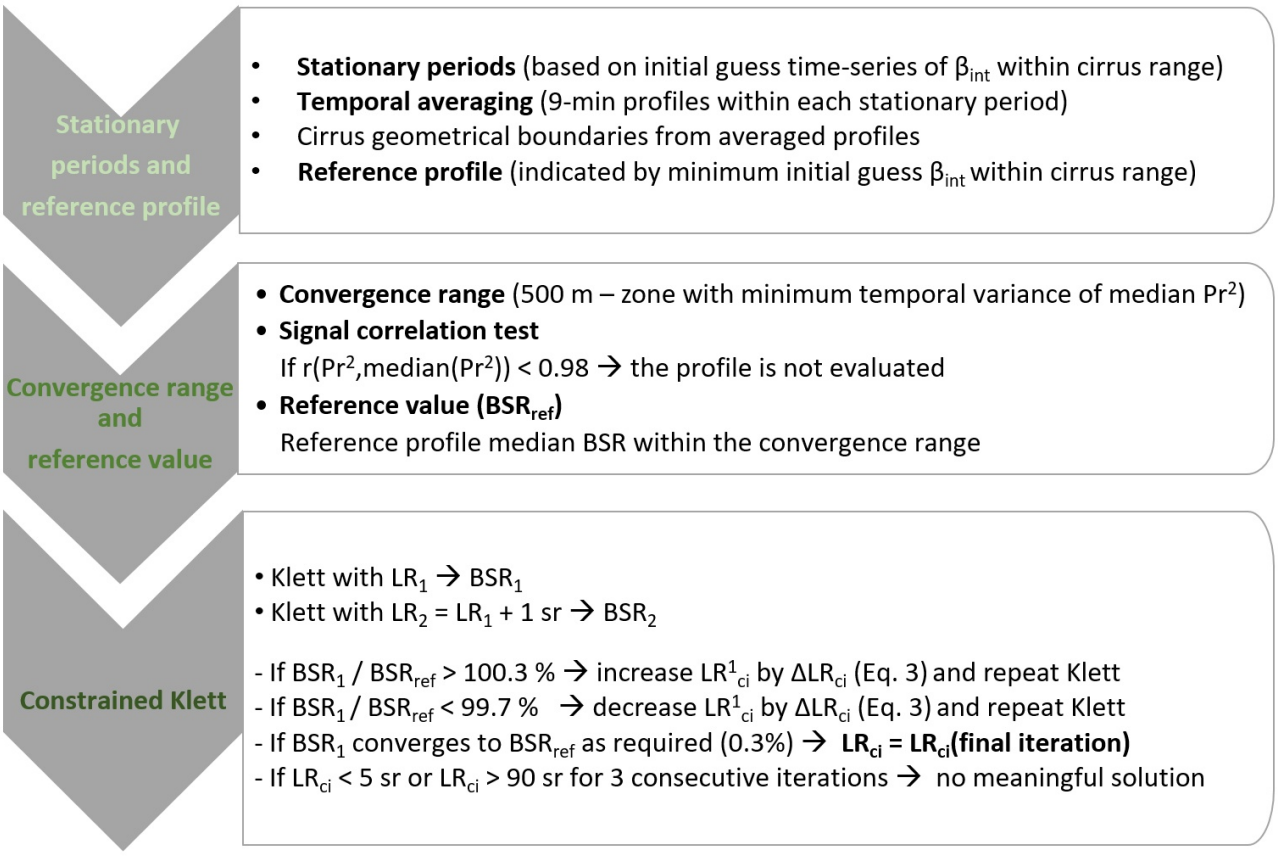

Fig. 4.6: Flowchart of the revised cirrus optical retrieval.

also investigated (App. B.2).

Once the *convergence range*, the *reference profile* and the BSR_{ref} are defined, the recursive Klett–Fernald retrieval can be initiated. In each iteration two retrievals were performed, one with LR^1_{ci} and another with $LR^2_{ci} = LR^1_{ci} + 1$ sr (see lower module of Fig. 4.6) and the median BSR within the *convergence range* was estimated (denoted by BSR_1 and BSR_2 for the respective retrievals). The BSR_1 was adjusted by a factor ΔLR_{ci} (Eq. 4.3) until it converged satisfactorily to BSR_{ref}. The *convergence percentage* was set to 0.3% after sensitivity analysis (App. B.2). Following the Newton–Raphson method, the ΔLR_{ci} factor was formulated as the difference of BSR_{ref} and BSR_1 over the partial derivative $\frac{\partial BSR}{\partial LR}$ with $dLR = 1\ sr$. The iterative process was bounded by physically meaningful LR_{ci} values (5–90 sr), similarly to the double-ended Klett (Sec. 4.3.1).

$$\Delta LR_{ci} = \frac{BSR_{ref} - BSR_1}{\frac{\partial BSR}{\partial LR}} \tag{4.3}$$

Finally, the COD was estimated from the best matching LR_{ci} and the respective β^{part} solution as

$$\text{COD} = \int_{C_{base}}^{C_{top}} LR_{ci} \cdot \beta^{part}(r) dr. \tag{4.4}$$

4.4 Comparison to established optical retrievals

Firstly, a systematic comparison of the *constrained Klett* with the established double-ended Klett and Raman (when applicable) retrievals is presented (Fig. 4.7). The assessment was performed on a large number of cirrus layers with variable vertical structure, geometrical and optical thickness for daytime and night-time conditions. The apparent LR_{ci} as obtained from the different retrievals displayed agreement within the range of statistical uncertainties (legend of Fig. 4.7). The uncertainties were higher for the Raman retrievals. When aerosol-free conditions were assumed beneath the cirrus clouds, the LR_{ci} was systematically overestimated as the distribution (gray line) was shifted towards higher values.

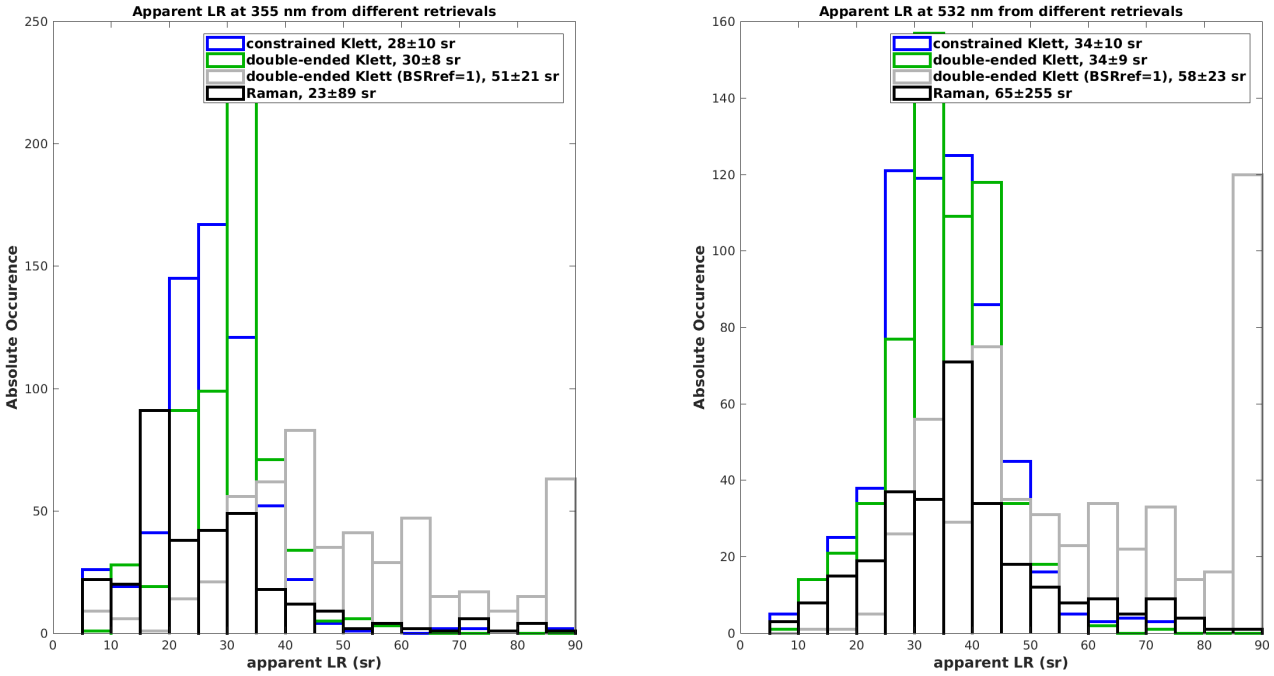

Fig. 4.7: Distribution of apparent LR_{ci} at 355 nm (left panel) and 532 nm (right) as derived from different retrievals. The presented LR_{ci} correspond to cirrus layers with COD > 0.02.

The aforementioned comparison was performed for cirrus layers with COD higher than 0.02. For lower COD (not shown), the *constrained Klett* derived LR_{ci} was shifted towards lower values ($LR_{ci}^{355} = 22 \pm 15\ sr$ and $LR_{ci}^{532} = 23 \pm 13\ sr$). The same held true for the double-ended Klett ($LR_{ci}^{355} = 28 \pm 10\ sr$ and $LR_{ci}^{532} = 26 \pm 11\ sr$). At the same time, the LR_{ci} overestimation due to the aerosol-free assumption was higher ($LR_{ci}^{355} = 51 \pm 27\ sr$ and $LR_{ci}^{532} = 69 \pm 24\ sr$) together with the Raman statistical uncertainties ($LR_{ci}^{355} = 8 \pm 44\ sr$ and $LR_{ci}^{532} = 51 \pm 337\ sr$). As cirrus detection and optical characterization proved more challenging for low COD (see also App. B.2), care will be taken in the long-term cirrus properties statistics (Chapter 5).

In order to better understand how the optical discrepancies depend on the COD regime a more detailed comparison was performed. The cirrus cloud of 23 January 2019 was selected

as it consisted of different COD regimes, from sub-visible to lower opaque. The MSC LR_{ci}^{355} and COD^{355} as derived from the different retrievals are presented in Fig. 4.8. More details on the multiple-scattering effect are given in Sec. 2.4.4. The three retrievals exhibited agreement within the range of uncertainties in terms of the mean cloud optical properties (legend of Fig. 4.8). However, in terms of individual cirrus layer retrievals only the constrained and double-ended Klett closely agreed. The Raman technique provided mostly lower LR_{ci} and COD solutions, probably because of the vertical smoothing process. Higher LR_{ci} discrepancies occurred for layers with low COD (time bins 1–5). This could be attributed to less efficient convergence of the *constrained Klett* as well as to higher Raman statistical uncertainties.

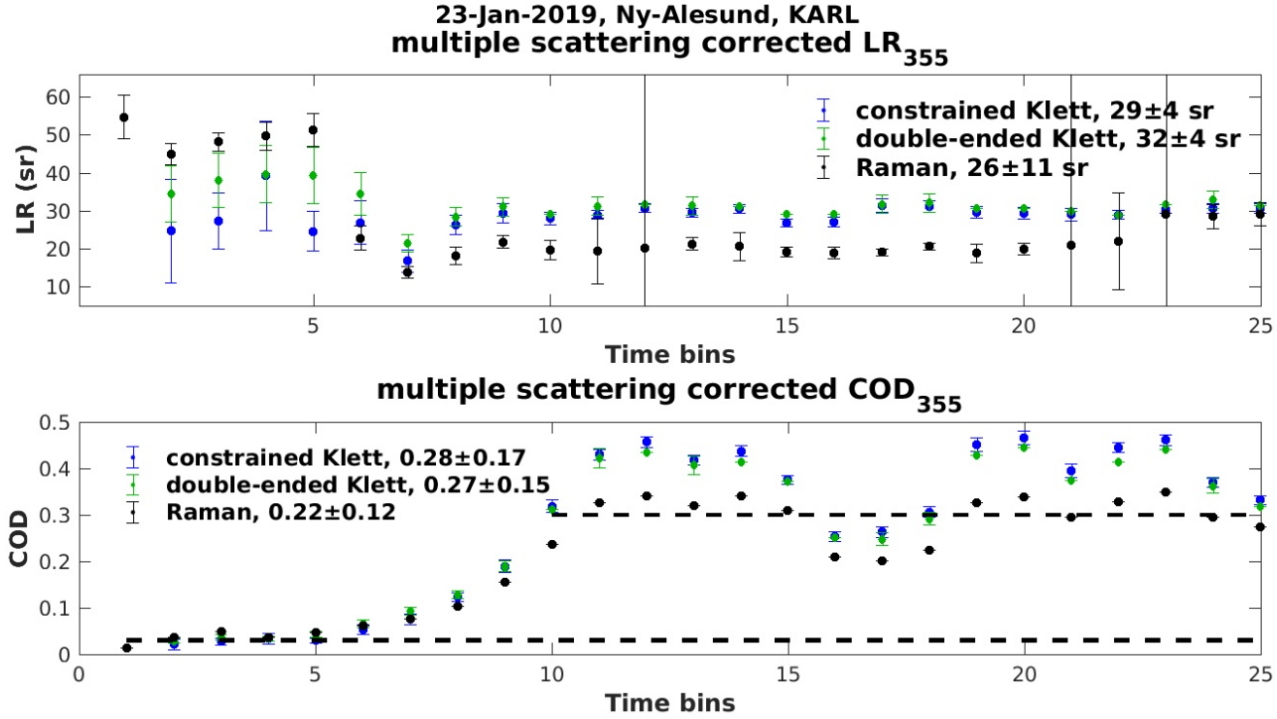

Fig. 4.8: Comparison of MSC optical properties at 355 nm (mean ± standard deviation given in the legend). For Klett retrievals, errorbars represent uncertainties due to 0.01 *reference value* error. For the Raman retrieval, LR_{ci} errorbars represent the standard error of the mean (extremely high for vertically-inhomogeneous layers), while COD errorbars represent the integral-propagated particulate extinction uncertainty. Dashed horizontal lines denote the different COD regimes.

The high agreement between double-ended and *constrained Klett* can be readily attributed to the fact that both rely on elastic signals. It should also be noted that identical far- and near-range *reference values* were applied in order to make the two retrievals as comparable as possible (Sect. 4.3.1). However, as already mentioned, the classical double-ended Klett is based on aerosol-free assumptions above and below the cirrus clouds (Ansmann et al., 1992). A sensitivity analysis was performed in order to assess the impact of the latter assumption. In Fig. 4.9 the optical properties are presented as in Fig. 4.8 but the aerosol-free

assumption (BSR = 1) was additionally applied on the double-ended Klett (green circle and cross symbols). Optically-thinner layers (time bins 1–5) were the ones mostly affected by the aerosol-free assumption, displaying LR_{ci} of 75 ± 7 sr (mean ± standard deviation). Previously, the LR_{ci} was estimated at 31 ± 2 sr by the double-ended Klett, 24 ± 5 sr by the *constrained Klett* and 38 ± 5 sr by the Raman retrieval. For optically-thicker layers, positive discrepancies (2–8 sr) were also found, while the overall COD discrepancies lay between 0.01 and 0.03 (not shown). Hence, the aerosol-free assumption led to a significant overestimation of the LR_{ci} since the neglected amount of extinction was instead attributed to the cirrus layers.

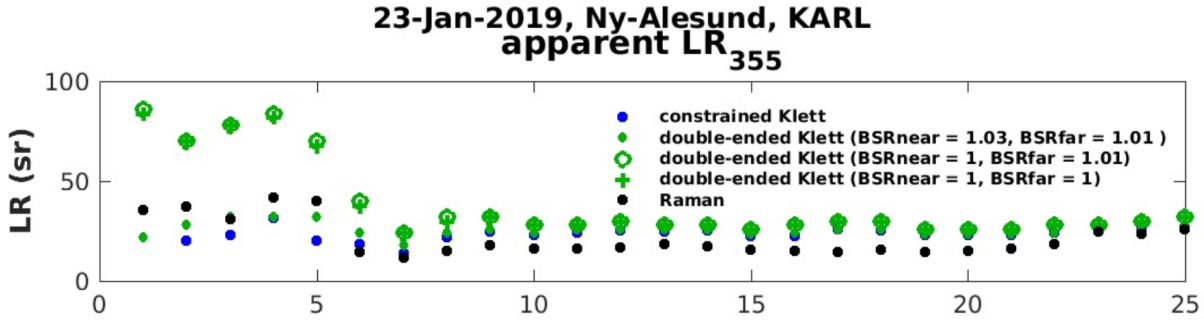

Fig. 4.9: Same as Fig. 4.8 except for apparent optical properties and double-ended Klett with aerosol-free assumption (BSR = 1). Non-realistic *reference values* can introduce biases in the optical properties, especially for optically-thinner layers.

4.5 How uncertainties in cirrus detection affect the optical retrievals?

In the following the effect of cirrus detection uncertainties on the apparent optical properties is assessed. To this end, the cirrus geometrical properties were determined via the dynamic (Fig. 4.10a, cyan symbols) and static WCT methods (black symbols). Based on the dynamic and static derived boundaries, the optical properties were retrieved via the *constrained Klett* and the resulting discrepancies were investigated (Fig. 4.10b). The optical differences are illustrated (blue dots referring to the right axis of Fig. 4.10b) as a function of the geometrical difference (dot size, defined as the cumulative difference of C_{base} and C_{top} between the static and dynamic method). Higher geometrical discrepancies mostly occurred for faint cirrus layers (Fig. 4.10a). Accordingly, higher optical discrepancies arose for upper sub-visible and optically-thin layers. The highest LR_{ci} and COD differences (45% or 17 sr and 93% or 0.037, respectively) appeared for the layer with the maximum geometrical discrepancy (1613 m). However, the geometrical discrepancy was a necessary but not sufficient condition for optical discrepancies to occur. For instance, in opaque layers although the geometrical discrepancies were non-negligible (up to 490 m), the resulting LR_{ci} and COD discrepancies were low (less than 1 sr and 0.025, respectively). This indicates that the solution already converged sufficiently within the main part of the layers and, thus, the role of marginal parts was less critical. Overall, for optically-thin and opaque layers the LR_{ci} difference was lower than 10%

(3 sr) and the COD difference did not exceed 8% (0.025).

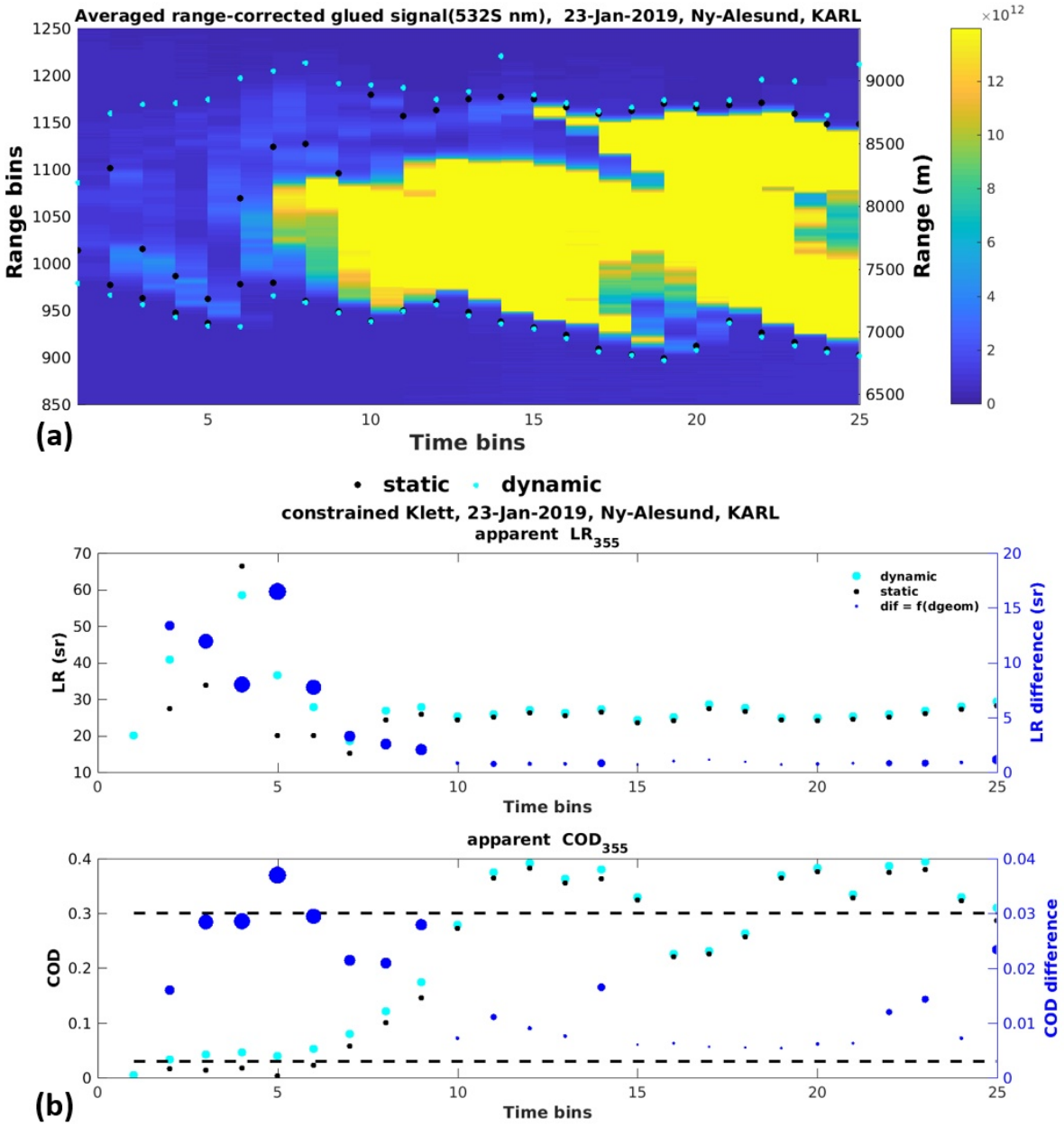

Fig. 4.10: Temporally averaged signal with overlaid dynamic and static WCT derived cirrus boundaries (a). Corresponding optical properties as retrieved from the *constrained Klett* method (b) and differences (blue dots referring to the right axis) as a function of the geometrical discrepancy (dot size). The geometrical discrepancies varied from 30 to 1613 m.

The impact of detection uncertainties was also assessed using the double-ended Klett and Raman retrievals (Fig. 13 from Nakoudi, Stachlewska, and Ritter (2021)). The resulting discrepancies were higher for optically-thinner layers as in the *constrained Klett*. In the double-ended Klett, the maximum LR_{ci} and COD differences amounted to 20% (8 sr) and 90% (0.04), while for opaque layers the respective differences did not exceed 10% (2 sr and 0.025). In the Raman retrievals, maximum discrepancies amounted to 65% (25 sr) for the

LR_{ci} and to 95% (0.034) for the COD, while for optically-thicker layers the corresponding discrepancies did not exceed 30% (6 sr) and 12% (0.03). Overall, the Raman discrepancies were higher probably due to the higher impact of noise on the retrievals.

4.6 Discussion

4.6.1 Limitations of cirrus retrieval schemes

The limitations of the applied retrieval schemes are briefly discussed here. From a numerical viewpoint, the *constrained Klett* cannot always provide a robust LR_{ci}. More specifically, the light attenuation within optically-thinner layers was not sufficiently strong to adjust the LR_{ci} (Sec. 4.3.3). Likewise, the double-ended Klett solutions exhibited lower absolute differences and, hence, the best matching LR_{ci} was challenging to find. Based on systematic analysis, the *constrained Klett* adjusted effectively the LR_{ci} for apparent COD as low as 0.02. Further limitations of the *constrained Klett* relate to the assumed as vertically-independent LR_{ci}. However, this is a common limitation in existing methods such as the double-ended Klett. Finally, the aerosol content stability assumption beneath the cirrus cloud proved valid (Fig. B.1) based on independent Raman estimates. Concerning the Raman signals, they usually require vertical smoothing even for night-time applications. Smoothing acts at the expense of effective resolution (Iarlori et al., 2015). As a result, distorted particulate extinction profiles might be produced, with ice crystal related peaks being suppressed and a critical impact on the accuracy of radiative estimates (Lolli et al., 2018). Exemplarily, vertical smoothing of 780 m can lead to biases of 64% (7.7 Wm^{-2}) at the surface and 39% (11.8 Wm^{-2}) at TOA for opaque cirrus layers (Lolli et al., 2018). Similarly, long temporal averaging, which smears out the cirrus physical variability, is expected to induce radiative effect biases.

4.6.2 Strengths of the revised retrieval scheme

The proposed *dynamic WCT* method proved more sensitive to faint cirrus layers that were partly or completely overlooked by the static method (Sec. 4.2). A similar advancement has been achieved in the 4^{th} version of CALIOP cloud - aerosol discrimination algorithm (Liu et al., 2019), which shows increased sensitivity to cirrus fringes (optically-thinner layers adjacent to cirrus clouds). Additionally, fine-scale temporal averaging was performed, based on periods of physical stationarity, in order to obtain non-distorted particulate backscatter coefficient profiles (Sec. 4.3.2). In the *constrained Klett* the *reference value* was not simply assumed but approximated by an initial guess. This approach proved to agree with independent Raman estimates (Sec. B.1) on condition that cloud-free or low COD (below 0.2) *reference profiles* were available. The upper COD limit was rarely reached in the analyzed cases (2011-2020). Since KARL is not in *24/7* operation, cirrus clouds were neither monitored from their formation nor clear-sky observations were always available prior to the cirrus passing. However, for continuously operating lidar systems as those of the Micro-Pulse Lidar Network (MPLNET) the upper COD limitation can be lifted more easily. The more realistic *reference*

value was of benefit to established methods such as the double-ended Klett. Instead, the aerosol-free assumption led to positive LR_{ci} biases (Fig. 4.9), especially in optically-thinner layers.

4.7 Conclusions

In this Chapter, the development of a cirrus cloud retrieval scheme was presented, with its limitations and strengths thoroughly explored. The scheme comprised cirrus detection (*dynamic WCT*) and optical characterization (*constrained Klett*). The Wavelet Covariance Transform (WCT) method was revised for C_{base} and C_{top} detection (Sec. 4.1.2). For the first time, two dynamic criteria were introduced (Sec. 4.1.3). The cirrus optical properties were derived by an iterative Klett–Fernald retrieval, called *constrained Klett* (Sec. 4.3.3). The main conclusions can be summarized as follows:

- The *dynamic WCT* method was more sensitive to faint cirrus layers, which were partly or completely undetected by the static method (Sec. 4.2). Increased sensitivity to thin layers (less than 200 m) was achieved with appropriate tuning (App. A.1).
- In the *constrained Klett* the LR_{ci} was iteratively adjusted to match with a *reference value*, which indicated the aerosol concentration beneath the cirrus cloud. The *constrained Klett* was applicable to cirrus layers with COD down to 0.02. Contrary to existing approaches, the *reference value* was not simply assumed but was approximated by an initial guess. The proposed approach was in agreement with independent Raman estimates. Even without any available cloud-free profile, an accurate *reference value* was estimated from profiles with COD up to 0.2 (App. B.1).
- The main inherent uncertainty of *constrained Klett* was related to the *reference value* selection (App. B.2). Optically-thinner layers displayed higher sensitivities (up to 50% in the COD and 60-74% in the LR), whereas in opaque layers the uncertainties were lower (10% in the COD and 15% in the LR).
- The *constrained Klett* presented agreement with the existing double-ended Klett and Raman retrievals within the range of uncertainties. The double-ended Klett, which relies on aerosol-free assumptions, presented increased accuracy when the proposed *reference value* was adopted.
- Cirrus detection uncertainties affected more critically the retrievals of optically-thinner layers (Sec. 4.5).

In the next chapter, the long-term variability of cirrus properties will be investigated over Ny-Ålesund employing the revised retrieval scheme.

5.1 Overview of cirrus occurrence and meteorological conditions over Ny-Ålesund

This section provides an overview of cirrus occurrence (Fig. 5.1) and geometrical properties (Fig. 5.3 and Fig. 5.4) from 2011 to 2020 over Ny-Ålesund. Fig. 5.1 presents the vertically-resolved occurrence of cirrus on a monthly basis. Additionally, an overview of the prevalent meteorological conditions during the cirrus observations is given (Fig. 5.2, 5.5 and 5.6). Seasonal cirrus properties' statistics are summarized in Tab. D.1.

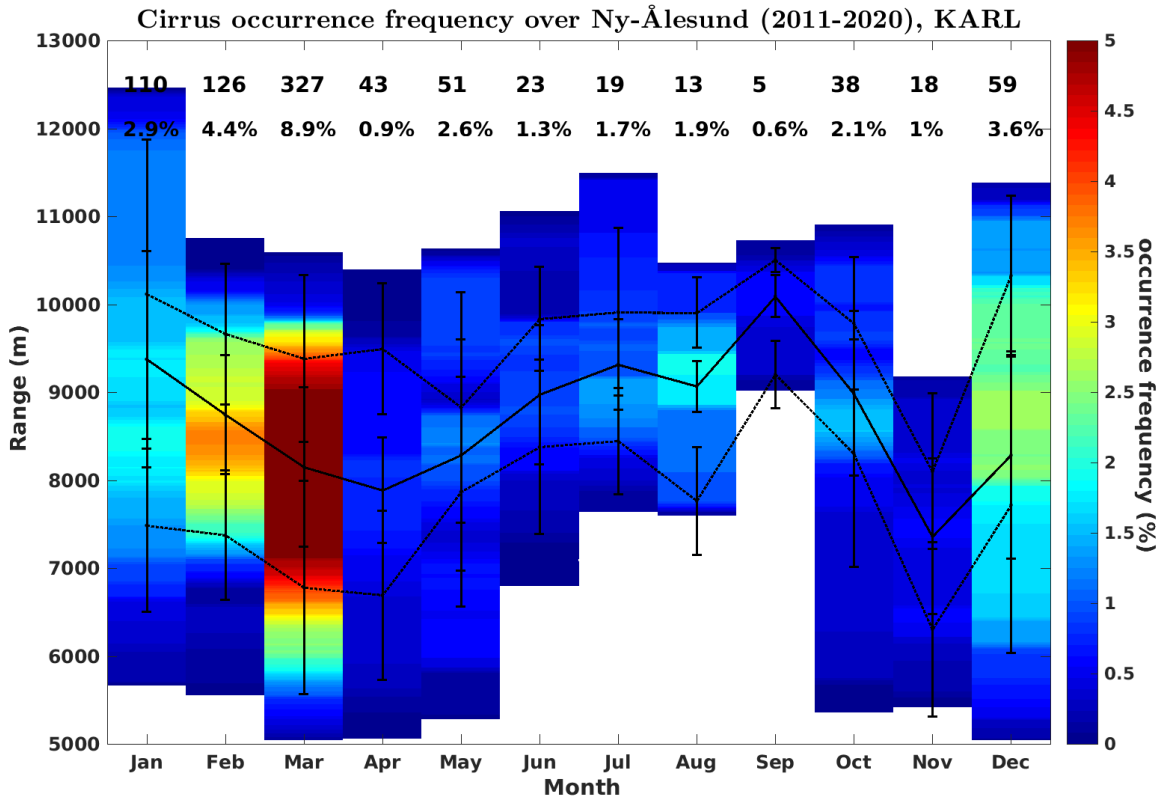

Fig. 5.1: Cirrus monthly occurrence frequency (9 min – 7.5 m cirrus observations normalized to KARL observation hours). The numbers on top denote the detected cirrus layers and the cirrus occurrence frequency. The C_{base}, effective C_{mid} and C_{top} are overlaid (median and standard deviation).

The cirrus occurrence frequency was higher in winter ($3.6 \pm 0.7\%$) and spring ($4.1 \pm 4.3\%$) relative to summer ($1.6 \pm 0.3\%$) and autumn ($1.2 \pm 0.8\%$). The seasonal cycle of cirrus occurrence is is accordance with Nomokonova et al. (2019), who examined the occurrence of hydrometeors over Ny-Ålesund using continuous remote sensing observations. In winter

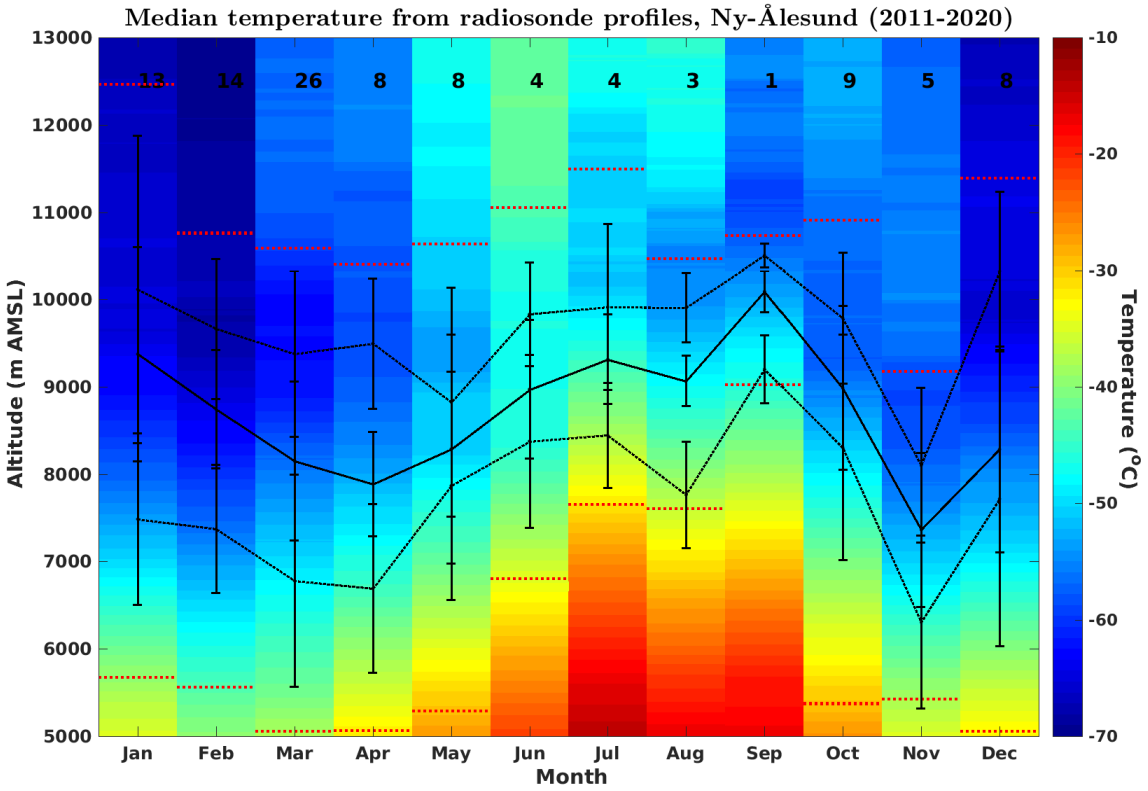

Fig. 5.2: Monthly median temperature as derived from radiosonde ascents. Note that only the temporally-closest radiosondes to lidar observations are included. The C_{base}, effective C_{mid} and C_{top} are overlaid (median and standard deviation). The numbers on top denote the number of utilized radiosondes. The red dashed lines indicate the monthly envelope of cirrus occurrence as given in Fig.5.1.

and spring ice clouds occurred on a 15–20% frequency, which did not exceed 5% in the rest of the year ((Nomokonova et al., 2019), their Fig. 10). Nevertheless, the occurrence frequencies of cirrus are lower compared to those of ice clouds as the latter include ice within the whole tropospheric column. With the majority of ice-phase appearing in the first 2 km ((Nomokonova et al., 2019), their Fig. 8), the lower occurrence of cirrus that mostly form above 5 km, can be explained. Additionally, the presented cirrus occurrence frequencies are negative biased as they only include layers that were possible to evaluate. However, this was not the case for weak and highly optically-thick layers (no C_{top} detection, Sec. 4.1.2). The same held true for cirrus with directly underlying mid-level clouds (not possible to define the *reference range*, Sec. 4.3.3) or multi-layered cirrus, which are not included in the analysis. Moreover, stationary periods shorter than 9 min were excluded (Sec. 4.3.2). Finally, there is a possible lidar operation bias, with the observations preferentially performed under clear-sky conditions and not on a *24–7 basis* as in Nomokonova et al. (2019) .

The cirrus C_{base} followed the seasonal cycle of temperature (Fig. 5.2) as it was constrained by the cirrus temperature regime (below $-40^{o}C$, Sec. 4.1.1). The C_{base} appeared lower in

winter and spring, while the C_{top} was shifted slightly downwards in spring (9.4 $\pm$ 1 km) and autumn (9.2 $\pm$ 1.1 km) relative to summer (9.9 $\pm$ 0.7 km, Tab. D.1). The C_{top} pattern can be attributed to the seasonality of the tropopause height. However, in December and January the C_{top} (9.9 $\pm$ 1.3 km for the whole winter) appeared in comparable or even higher altitudes than summer. This at first sight paradox is related to the frequent poorly-defined Polar night tropopause. Maturilli and Kayser (2017), using 22 years of radiosonde measurements over Ny-Ålesund, demonstrated that the winter-time thermal tropopause is often indistinguishable due to very low static stability. This regime is connected to radiative cooling in the absence of solar radiation and the governing polar vortex dynamics, while during the sun-lit period a well-defined tropopause regime appears (Maturilli and Kayser, 2017). Indeed, from Fig. 5.2 the tropopause and lower stratosphere are roughly distinguishable for April–October (vertical temperature gradients changing from negative to positive), which is not the case for the rest of the months. A more detailed analysis of cirrus occurrence altitude with respect to different tropopause regimes is presented in Sec. 5.5.1.

The cirrus C_{base} (C_{top}) varied from 5.5 to 8.5 km (from 8.5 to 10.5 km, Fig. 5.3). From a seasonal perspective, thicker layers were observed in winter (2.1 $\pm$ 1.3 km) and spring (1.9 $\pm$ 1.2 km) compared to summer (1.4 $\pm$ 0.9 km) and autumn (1.4 $\pm$ 0.9 km, Tab. D.1). The total geometrical thickness (GT) of cirrus layers amounted to 1.9 $\pm$ 0.6 km (median $\pm$ standard deviation) and their majority was thinner than 4.5 km (inset Fig. 5.4). Cirrus layers down to a thickness of 158 m were detected (in July), while the thickest layer extended over 6.3 km (in January). The distribution of GT was broader compared to mid-latitudes. This has also been demonstrated from satellite observations for the local winter of Polar regions (Fig. 7 from Nazaryan, McCormick, and Menzel (2008)).

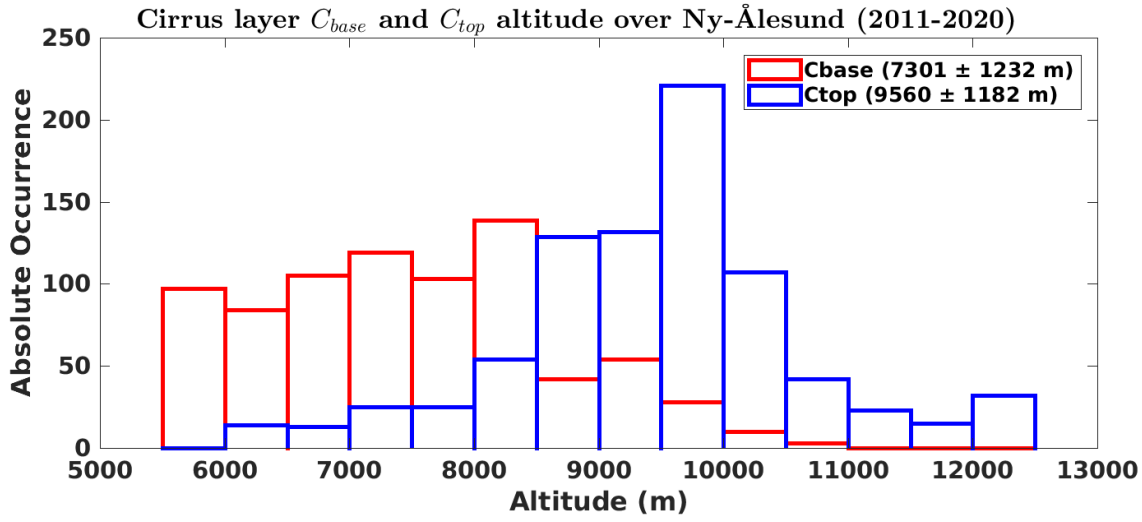

Fig. 5.3: Absolute occurrence distribution of C_{base} and C_{top} altitude. The median $\pm$ standard deviation are given in the legend.

Concerning wind speed, higher values were observed with the cirrus occurrence envelope (red horizontal lines, Fig. 5.5) compared to the rest of the atmospheric column. Between April

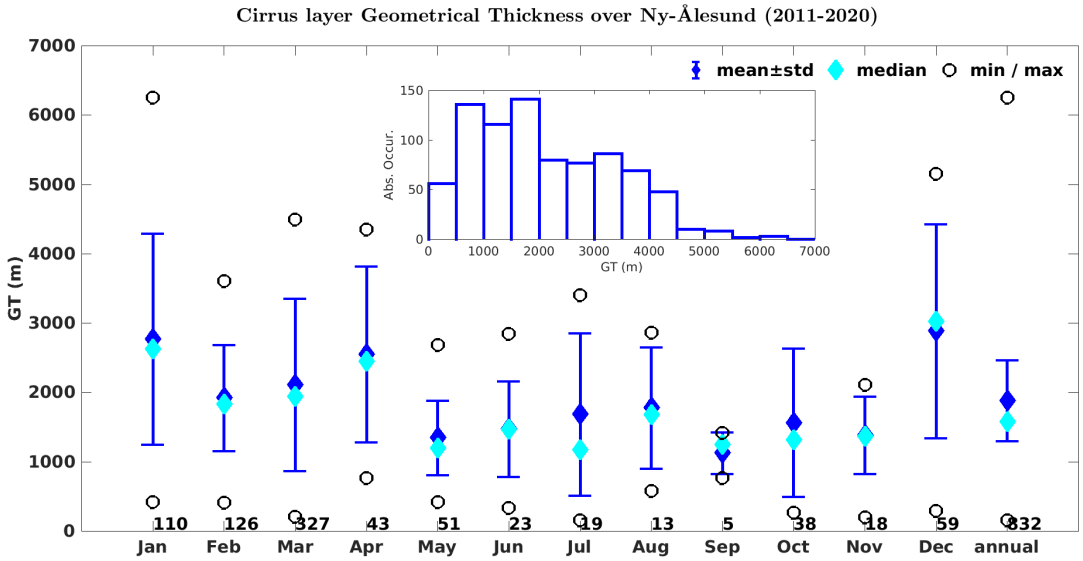

Fig. 5.4: Monthly and annual statistics on cirrus layer geometrical thickness. The overall absolute occurrence distribution is given in the inset figure.

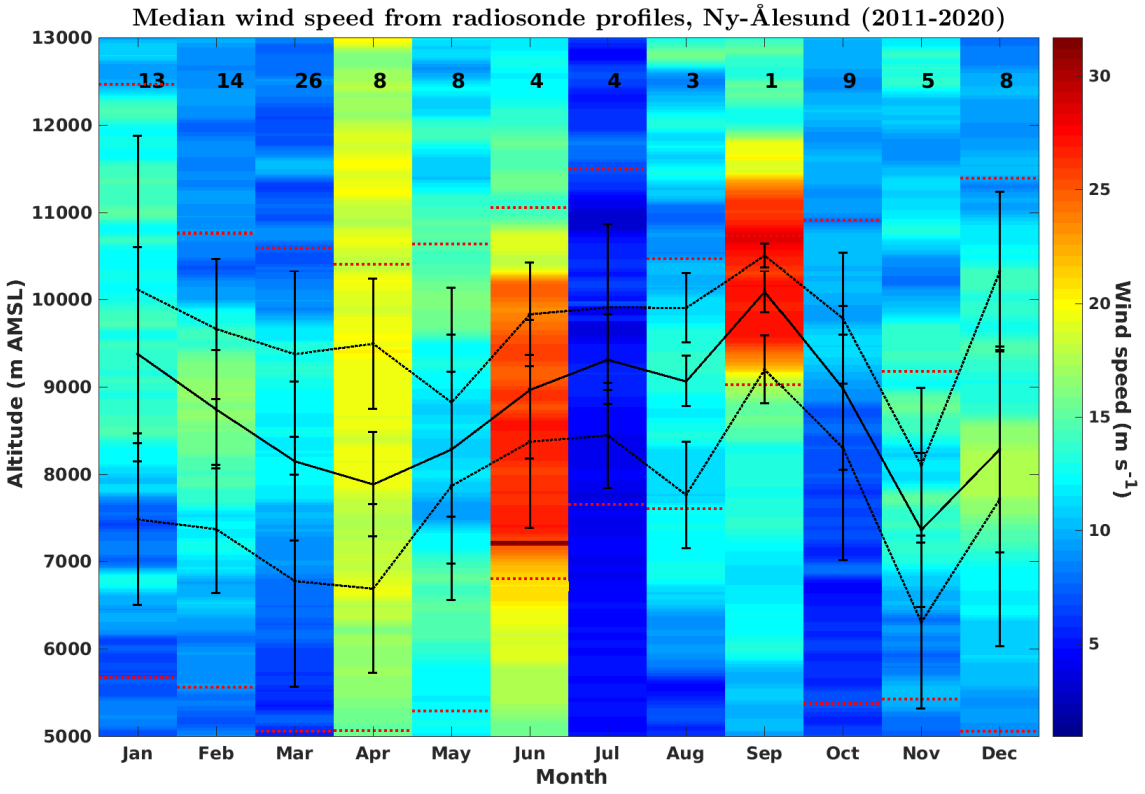

Fig. 5.5: Same as Fig. 5.2, except for wind speed.

and June, the wind speed started to increase at 3 km and high values sustained up to 13 km. In July and October the wind speed was lower within the whole free-troposphere. Over Ny-Ålesund the tropospheric wind speed is mostly below 15 ms^{-1} and rarely exceeds 20 ms^{-1} but maximizes around 7–8 km throughout the year (Maturilli and Kayser, 2017, their Fig. 2).

Hence, stronger winds are expected within the cirrus envelope but the high wind speeds observed in June and September are rare.

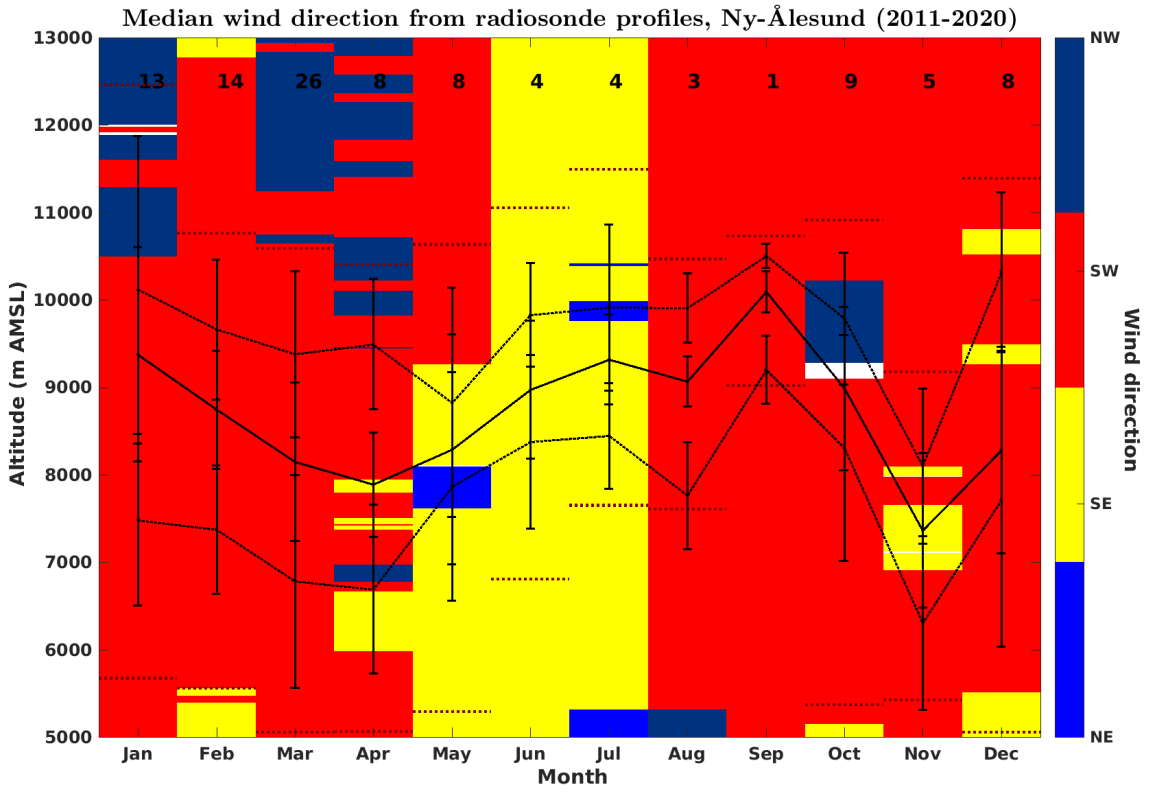

Fig. 5.6: Same as Fig. 5.2, except for wind direction.

Southerly flow (SW and SE) was dominant within the cirrus envelope and the majority of the free-troposphere (Fig. 5.6). Over Ny-Ålesund W–NW and W–SW flow prevails throughout the year between 5 and 12 km (Maturilli and Kayser, 2017, their Fig. 3). Consequently, southerly flow seemed more conducive to cirrus formation as warm and moist air from lower latitudes is advected towards Ny-Ålesund (Maturilli and Kayser, 2017). A stricter investigation of the meteorological conditions in the presence of cirrus clouds is performed in Sec. 5.5.

5.2 Quality assurance of optical properties

The quality of cirrus optical properties needs to be carefully evaluated prior to any further analysis. The first quality check is related to specular reflections (Sec. 5.2.1). Specular reflections occur on horizontally-oriented hexagonal ice crystals, with dimensions large enough for their falling attitude to be controlled by aerodynamic drag forces (Sassen, 1980). Specular reflections produce sharp increases in the backscatter coefficient along with decreased depolarization. Upon screening the potentially affected cirrus layers, an additional inspection of extreme lidar ratio (LR) values was performed (Sec. 5.2.2). As a final step, the cloud optical depth (COD) and LR were corrected for the effect of multiple-scattering (Sec. 5.2.3).

5.2.1 Specular reflection effect

First of all, let's make a short literature review on specular reflections. Noel and Chepfer (2010) found that horizontally-oriented ice crystals mainly occur within the -30 to -10^oC temperature range and were almost absent below -40^oC (using CALIOP data at 0.3^o off-nadir angle). Avery et al. (2020) confirmed that specular reflections occur between 0 and -40^oC, with a peak at -15^oC. In the lidar community a usual specular reflections work-around is to tilt the laser beam by some degrees (usually 3^o off-nadir). However, the laser beam of KARL is not tilted due to technical limitations related to its large receiving telescope (Sec. 2.2.1). Therefore, any potential influence from specular reflections needed to be identified. According to the simulations of Okamoto et al. (2019) and Okamoto et al. (2020) horizontally-oriented plates and columns produce lower than 10% linear particle depolarization ratio ($LPDR_{355}$) in combination with a wide range of LR_{355} (4 to 100 sr, Fig. 5.7).

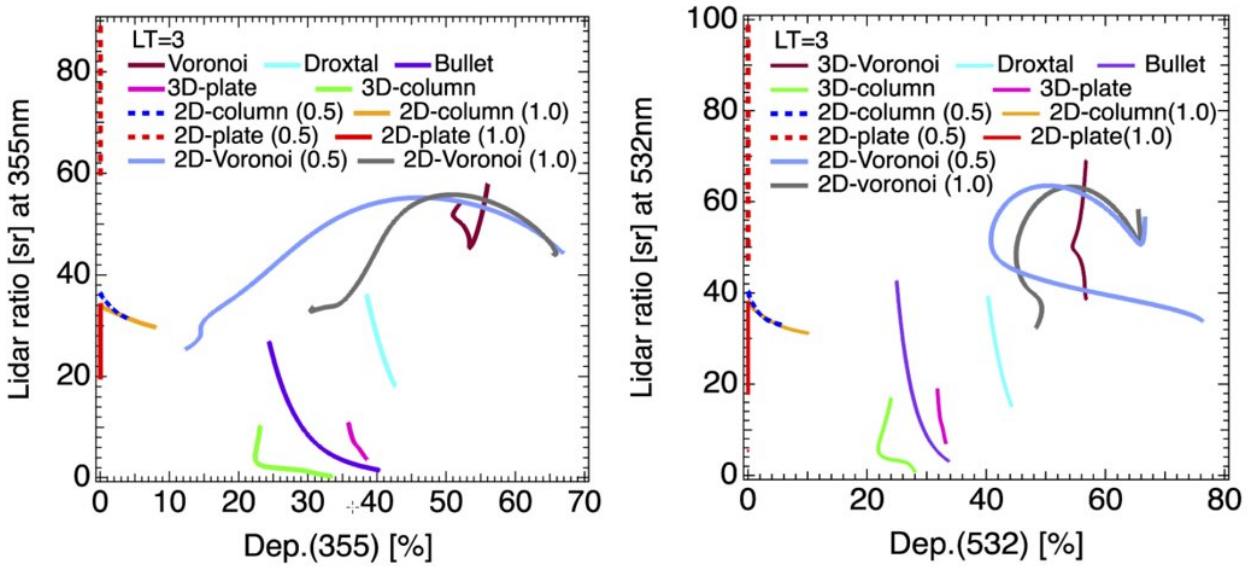

Fig. 5.7: Simulated LR versus LPDR at 355 and 532 nm for different types of ice crystals. Horizontally-oriented crystals are denoted as *2D*. *Adapted from Okamoto et al. (2020), their Fig. 8b and 9b.*

Although the cirrus analysis was restricted to temperatures below -40^oC, peaks in the backscatter coefficient profiles frequently coincided with low $LPDR$. Therefore, cirrus layers with $LPDR$ lower than 10% were inspected and, finally, indications of horizontally-oriented crystal layers were found. At the same time, the majority of them displayed low color ratio (CR), indicating bigger ice crystals, which are more likely to be horizontally-oriented (Sassen, 1980). Horizontal-orientation was mainly deduced within thin sub-layers, of thickness down to 100 m, as also reported by Borovoi et al. (2014). Such layers appeared as thin filaments with thickness of 500 m (8900–9400 m) and 250 m (9550–9800 m), respectively (Fig. 5.8). Even though these layers were vertically-limited, a distorted backscatter profile could impact on the vertically-mean LR and by extension on the COD. Therefore, the whole cirrus layers that were likely influenced by specular reflections were screened out. In total 38% (319 out

of 832) of the layers were screened out, indicating a significant presence of hexagonal plate and column ice crystals over Ny-Ålesund.

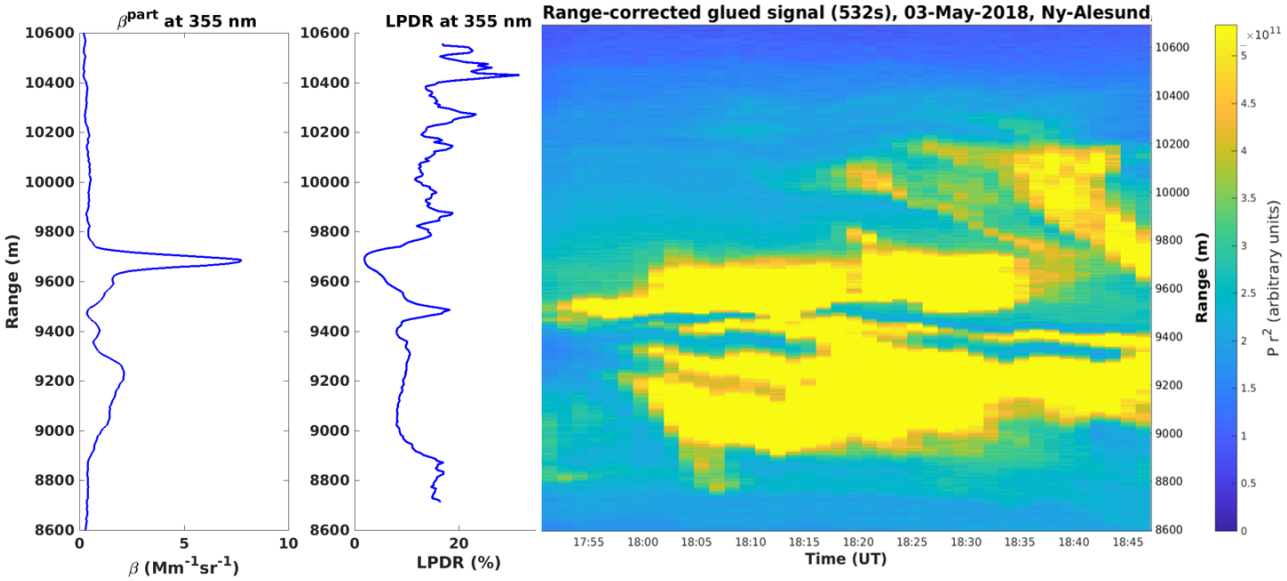

Fig. 5.8: Exemplary profiles of backscatter coefficient and LPDR for a cirrus layer containing sub-layers of horizontally oriented ice crystals. These sub-layers can be identified by backscatter peaks and LPDR local minima. For an overview, the lidar range-corrected signal is also given (right panel).

5.2.2 Investigation of extreme cirrus lidar ratio values

Despite the first screening of potential horizontally-oriented crystals, irregularly high LR were still present in the dataset. Therefore, the reasons behind the occurrence of extreme LR values were further investigated. According to the simulations of Okamoto et al. (2020) the LR of randomly-oriented crystals with LPDR lower than 40% (as for the present dataset) is not expected to exceed 50 sr (Fig. 5.7). On a second inspection, high LR values were observed in connection with low COD and GT (Fig. 5.9). As discussed in Sec. 4.5 and App. B, the optical retrievals of geometrically and optically-thinner cirrus were accompanied by higher uncertainties.

Another factor, possibly affecting the optical retrievals, is the high signal noise due to background illumination (Sec. 2.1.2). Extreme LR values mostly appeared in spring (Fig. 5.9). Their absence in summer, despite the high background illumination, can be attributed to higher cirrus GT (mostly above 500 m) compared to spring (down to 200 m). It should also be noted that in spring the solar elevation is lower but the surface albedo is higher as the ground around Ny-Ålesund is still partly snow- or ice-covered (Maturilli, Herber, and König-Langlo, 2015). Therefore, multiple surface reflections may produce higher background illumination in spring compared to summer. Additionally, the inspection of apparent (non-corrected) and

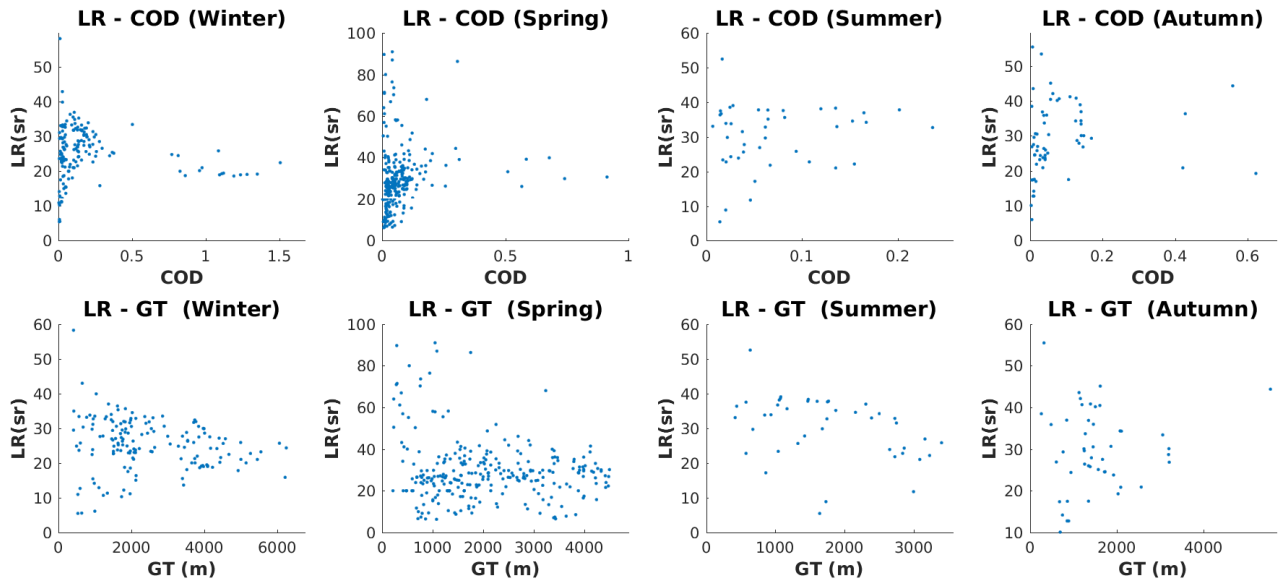

Fig. 5.9: Apparent LR versus apparent COD (upper panels) and versus GT (lower panels) on a seasonal basis. Only cirrus layers with LPDR higher than 10% were considered.

multiple-scattering corrected (MSC) extinction profiles revealed a connection between high LR and highly fluctuating MSC factor F (not shown). This indicates that the derivation of a vertically-mean LR is not a good approximation for vertically-inhomogeneous cirrus layers. Therefore, such profiles were also screened out from any further analysis. In total, 390 (71 with COD < 0.02) out of 832 cirrus layers passed the quality assurance procedure. In terms of cirrus clouds (defined as consecutive cirrus layers) 79 out of 112 were flagged as high quality ones.

5.2.3 Multiple-scattering correction

The final necessary correction is related to multiple-scattering. The MSC was applied on all the quality-assured extinction profiles using the analytical model of Eloranta (1998) and subsequently the LR and COD were also corrected (Sec. 2.4.4). A comparison to the simplified approach of Platt (1973) is presented in the App. C. In absolute terms the effect of multiple-scattering on the LR was comparable for all three cirrus regimes, while the effect on the COD was higher for the opaque regime (Tab. 5.1). The relative effect was slightly higher at 355 nm than at 532 nm, as the forward-scattering is stronger in the ultraviolet compared to the visible spectral region (Gouveia et al., 2017). In terms of relative differences, which actually represent the MSC factor F (Eq. 2.29), the effect was higher for the sub-visible regime. The MSC factor F maximizes near the C_{base} with the extinction underestimated by 50–60% and decreases to 20–30% within the cirrus layer ((Nakoudi, Stachlewska, and Ritter, 2021), their Fig. 14).

Tab. 5.1: Overview of MSC and apparent optical properties for different cirrus regimes. The absolute and percentage differences are calculated with respect to the MSC properties, which are also used for defining the cirrus regimes.

Multiple-scattering effect				
sub-visible	**LR355**	**LR532**	**COD355**	**COD532**
MSC properties	26 ± 13 sr	29 ± 14 sr	0.019 ± 0.007	0.018 ± 0.008
apparent properties	21 ± 10 sr	23 ± 11 sr	0.015 ± 0.006	0.015 ± 0.007
absolute difference	5 ± 4 sr	5 ± 3 sr	0.004 ± 0.002	0.003 ± 0.002
percentage difference	***20 ± 5%***	***17 ± 4%***	***20 ± 5%***	***17 ± 4%***

optically-thin	**LR355**	**LR532**	**COD355**	**COD532**
MSC properties	34 ± 9 sr	41 ± 10 sr	0.11 ± 0.07	0.11 ± 0.07
apparent properties	28 ± 7 sr	35 ± 8 sr	0.09 ± 0.06	0.1 ± 0.06
absolute difference	5 ± 3 sr	6 ± 3 sr	0.02 ± 0.01	0.01 ± 0.01
percentage difference	***15 ± 5%***	***14 ± 5%***	***15 ± 5%***	***14 ± 5%***

opaque	**LR355**	**LR532**	**COD355**	**COD532**
MSC properties	29 ± 8 sr	37 ± 7 sr	0.87 ± 0.41	1.03 ± 0.45
apparent properties	26 ± 8 sr	33 ± 6 sr	0.78 ± 0.37	0.93 ± 0.41
absolute difference	3 ± 1 sr	4 ± 1 sr	0.09 ± 0.04	0.1 ± 0.05
percentage difference	***10 ± 4%***	***10 ± 3%***	***10 ± 4%***	***10 ± 3%***

5.3 Overview of cirrus optical properties over Ny-Ålesund

An overview of cirrus optical properties from 2011 to 2020 is provided here. Data points, which passed the quality assurance (Sec. 5.2) are only taken into account. Therefore, only a subset of the layers discussed in the beginning of this Chapter (Sec. 5.1) are presented here. The majority of cirrus observed by KARL were optically-thin, followed by the sub-visible regime (Fig. 5.10). The domination of optically-thin cirrus is also observed in sub-Arctic sites (71% over Kuopio, Finland, (Voudouri et al., 2020) and 45% over Fairbanks, Alaska, (Campbell et al., 2021)). However, it should be noted that the derived distribution might be positively biased towards optically-thin cirrus. As the detection and optical evaluation of sub-visible cirrus was the most challenging (Sec. 4.5 and App. B), many of these layers displayed extreme LR (Fig. 5.9) and, thus, were screened out. Regarding the opaque regime, its underestimation is related to the instrumental limitations of lidar. More specifically, the lidar laser beam can be partly or completely attenuated within highly opaque layers. Sassen and Cho (1992) suggested a COD of 3 as an upper lidar attenuation limit for cirrus layers. The maximum

reported COD over Ny-Ålesund was equal to 1.8. Optically-thicker layers with SNR at the C_{top} lower than 3 were not evaluated (Sec. 4.1.1). Additionally, KARL is usually switched off in the presence of highly optically-thick clouds because the strong backscattered signal can damage its PMT detectors. Overall, it can be argued that even in the absence of the aforementioned bias sources, the relative contribution of the different cirrus regimes would not have changed.

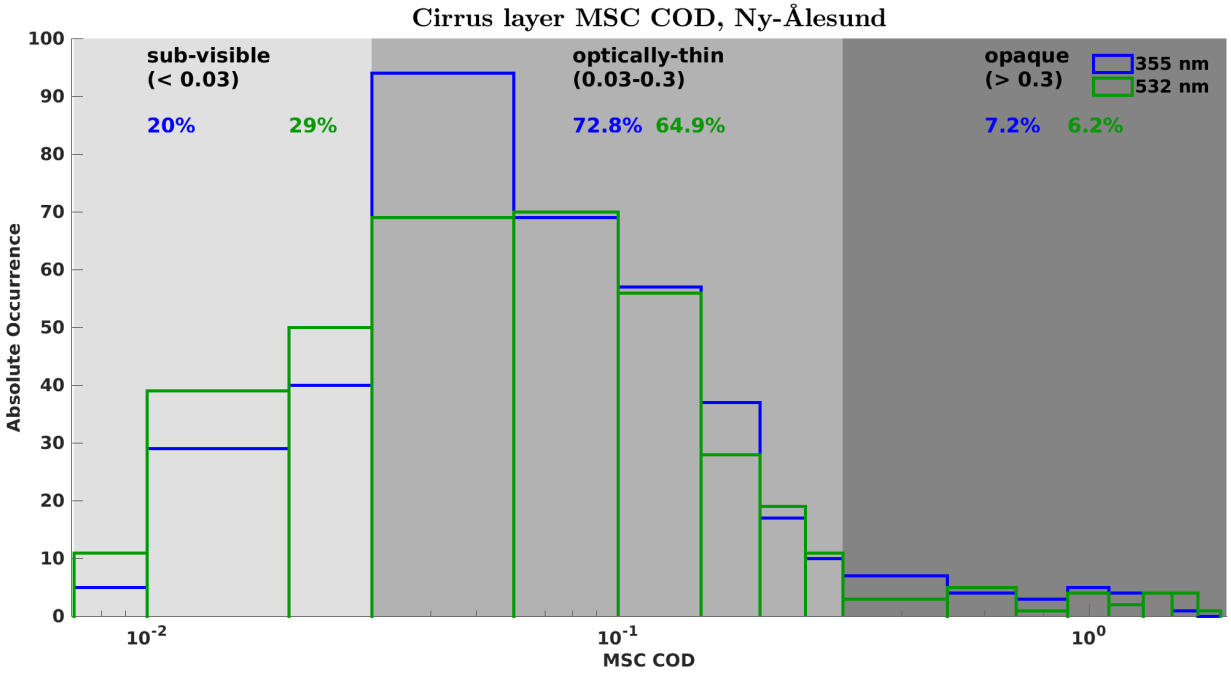

Fig. 5.10: Absolute occurrence of MSC COD_{355} and COD_{532}, considering only quality assured data. The different cirrus regimes are shade-indicated and their relative occurrence frequencies are given on the top side.

Keeping the aforementioned possible bias sources in mind, the MSC COD over Ny-Ålesund was equal to 0.07 $\pm$ 0.24 at 355 nm and 0.07 $\pm$ 0.26 at 532 nm (median $\pm$ standard deviation). These values are lower than those derived over the sub-Arctic site of Kuopio (COD_{355} = 0.25 $\pm$ 0.2), as the relative prevalence of opaque cirrus (26%) was higher there (Voudouri et al., 2020). Higher COD has been observed over the mid-latitudes (e.g. 0.31 $\pm$ 0.24 over Thessaloniki, (Giannakaki et al., 2007)), the sub-tropics (e.g. 0.3 $\pm$ 0.36 over Wuhan, (Wang et al., 2020)) and the Tropics (e.g. 0.25 $\pm$ 0.46 over Amazonia, (Gouveia et al., 2017)). From a seasonal perspective, the COD over Ny-Ålesund was higher in winter (Tab. D.1).

Hereafter, the optical properties of cirrus layers will be presented in two classes based on the *constrained Klett* sensitivity limit: COD higher than 0.02 (*high COD regime*) and lower than 0.02 (*low COD regime*). The optical retrievals were more challenging for the latter class and, therefore, they are treated with lower confidence. Moreover, the Wilcoxon rank sum test revealed statistically significant different distributions for the LR, LPDR and CR of the two COD regimes (null-hypothesis rejected at 5 % significance level and very small p-value).

The MSC LR distributions at 355 and 532 nm are presented in Fig. 5.11. The median LR_{532} was higher than the LR_{355}, indicating that cirrus were more absorbing in the visible spectral region. The *low COD regime* exhibited opposite spectral dependency and an overall lower LR than the *high COD regime*. In other words, the optically-thinnest cirrus (0.004 < COD < 0.02) seemed to be less absorbing than the optically-thicker ones and their absorption at the ultraviolet was higher compared to the visible spectral region. These findings will be discussed later in connection with other optical properties such as the CR and LPDR. In winter lower LR was found compared to the rest of the year (Tab. D.1).

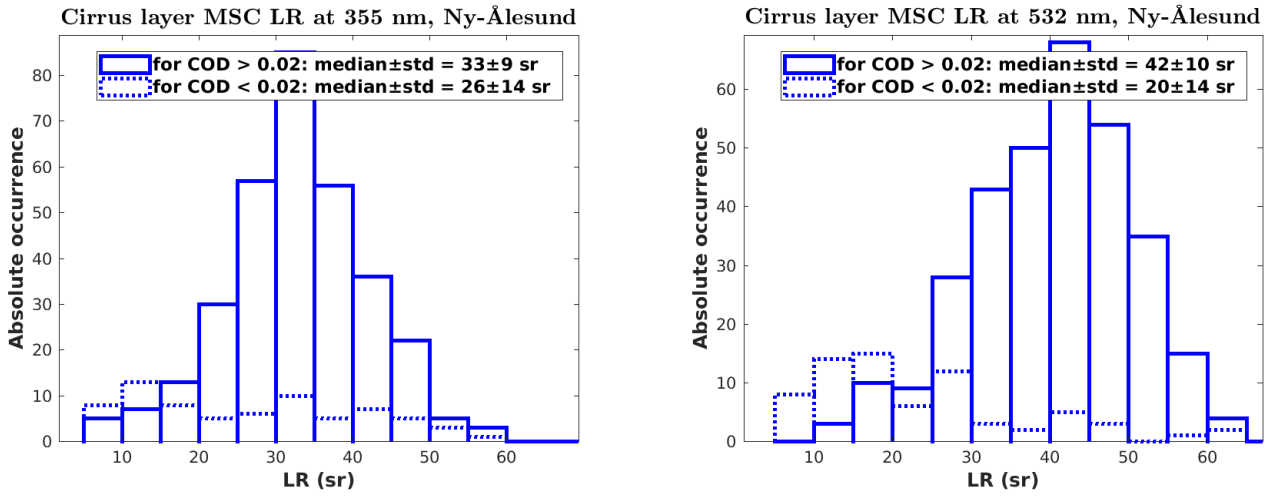

Fig. 5.11: MSC LR distributions at 355 nm and 532 nm, considering only quality assured data.

The LR_{355} (33 $\pm$ 9 sr) over Ny-Ålesund was in great agreement with the average LR_{355} (33 $\pm$ 7 sr) over Kuopio (Voudouri et al., 2020). Voudouri et al. (2020) reported a meridionaly-increasing LR towards higher latitudes (their Fig. 7c). The LR_{532} over Ny-Ålesund seemed to follow this tendency, while an asymptotic behavior was found for LR_{355}. A poleward increase of the LR has been reported over the Northern Hemisphere for opaque ice clouds (Young et al., 2018, using CALIOP observations). More specifically, the LR_{532} (following an increasing gradient of centroid temperature) started from approximately 25 sr over the Tropics and reached about 40 sr over the Arctic, with higher values in its Canadian and Russian parts (Young et al., 2018, their Fig. 7). However, a stable LR_{532} of 33 $\pm$ 5 sr has been derived over the 50^oS–50^oN ocean zone for semi-transparent cirrus (Josset et al., 2012, using CALIOP-CloudSat observations).

The $LPDR_{355}$ mainly varied between 10 and 20%, while in the *low COD regime* it was slightly increased (17 $\pm$ 5%, Fig. 5.12). The LPDR was higher in summer and autumn (Tab. D.1). The presented LPDR is lower compared to other cirrus studies. For instance, over Kuopio an annual mean $LPDR_{355}$ of 38 $\pm$ 7% was reported but the analysis was limited to clouds with LPDR higher than 25% (Voudouri et al., 2020). Wang et al. (2020) found an annual mean LPDR of 30 $\pm$ 9% over Wuhan, China. For cirrus clouds, which originated from heavy air traffic sectors over the Atlantic Ocean and Europe, higher LPDR (47 $\pm$ 7%) was

reported compared to cirrus from clearer regions (38 $\pm$ 6%, (Urbanek et al., 2018)). The decreasing LPDR tendency for clearer origin cirrus is in the same direction with the lower LPDR over Ny-Ålesund.

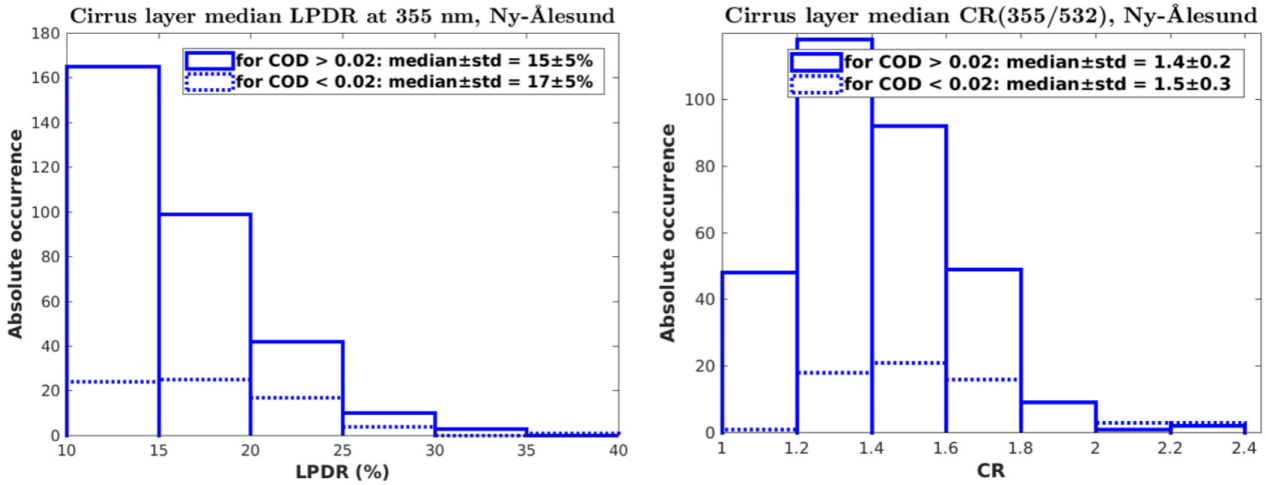

Fig. 5.12: $LPDR_{355}$ and CR distributions, considering only quality assured data.

As cirrus layers suspected of horizontal crystal orientation were screened out (Sec. 5.2.1), an attempt will be made to interpret the relatively low LPDR values. Low LPDR was also derived over Antarctica, Dumont d'Urville (Del Guasta et al., 1993) and Sondakyla, north Finland, (Del Guasta, 2001). The $LPDR_{532}$ was quite constant (13–23%, Fig. 7 from Del Guasta, 2001) as attributed to small and possibly columnar ice crystals, after excluding the presence of horizontal crystals and super-cooled droplets. Sassen and Zhu (2009) investigated the geographical distribution of linear volume depolarization ratio at 532 nm in ice clouds (using off-nadir CALIOP observations). Although the present findings cannot be quantitatively compared to Sassen and Zhu (2009), the latitudinal depolarization changes are worth mentioning. Sassen and Zhu (2009) highlighted a depolarization decrease towards the high latitudes of both hemispheres and attributed the differences to possible changes in the ice nucleation mechanisms. Over the high latitudes, ice clouds occur at lower heights and, thus, the availability and properties of aerosol that serve as ice nucleating particles (INPs) may differ (Sassen and Zhu, 2009). Another reason could be the lower absolute humidity in which cirrus clouds form in the Polar regions compared to lower latitudes.

Regarding the CR, it mainly varied between 1.2 and 1.6 (Fig. 5.12). The *low COD regime* exhibited slightly higher CR, indicating smaller ice crystals, which can partly explain the higher LR_{355} than LR_{532} (Fig. 5.11). The Ångström exponent amounted to 0.8 $\pm$ 0.4 (1.04 $\pm$ 0.4 in the *low COD regime*). Unfortunately, it is hard to find literature for the cirrus CR as various definitions and wavelength pairs are used. Voudouri et al. (2020) used the same CR definition as here (Eq. 2.12) and the same wavelength pair (355–532 nm) and reported an average CR of 1.1 $\pm$ 0.8 over Kuopio, indicating the presence of slightly bigger ice crystals compared to Ny-Ålesund. Finally, according to the simulations of Okamoto et al. (2020) the CR mainly lay between 0.7 and 2 (defined as in Eq. 2.12. Note that Fig. 9a from Okamoto et al. (2020)

uses the inverse definition). Overall, the *low COD regime* layers seemed to be less absorbing (lower LR) and comprise less spherical (higher LPDR) and smaller ice particles (higher CR).

5.4 Inter-relations of cirrus properties

In this section the cirrus properties are investigated in relation to one another. The relation of LPDR with CR and LR is examined (Fig. 5.13a and Fig. 5.13b). Individual measurements are demonstrated together with the median ± standard deviation of different CR and LPDR classes. The linear regression line on the median values was overlaid only if the coefficient of determination (R^2) exceeded 0.5. As in the previous Section the results are presented separately for the *high* and *low COD regime*.

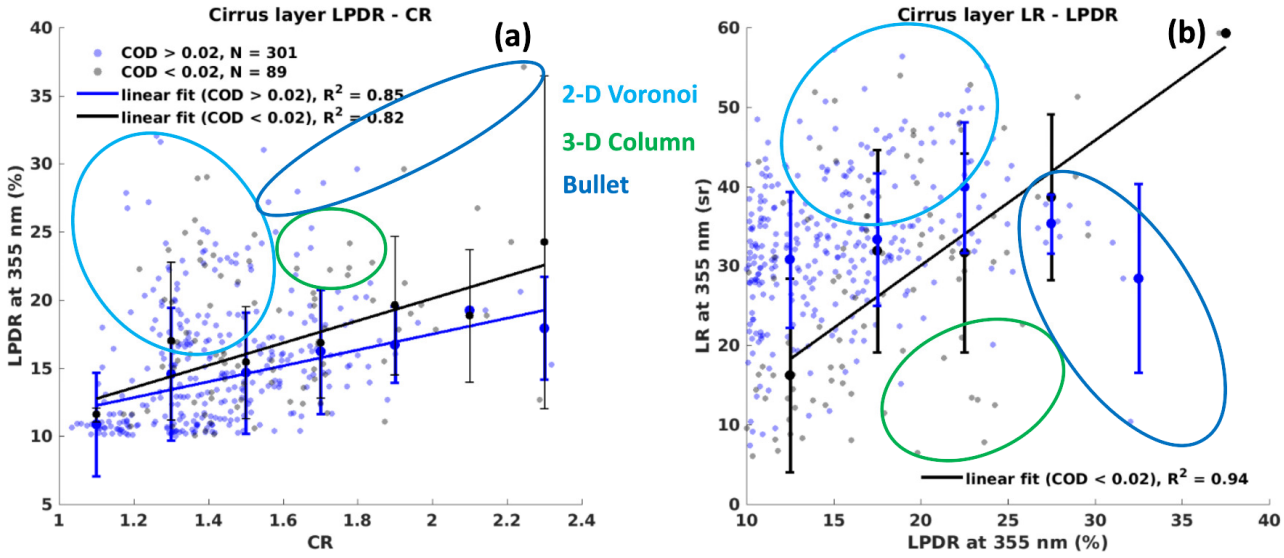

Fig. 5.13: LPDR versus CR (a) and LR versus LPDR (b) considering only quality assured data. The median ± standard deviation of LPDR (LR) in 0.2 CR (5% LPDR) classes is given together with the linear regression line. The closest matching ice crystal types from Okamoto et al. (2020) are indicated.

The LPDR and CR presented an overall proportional relation (Fig. 5.13a), which translates into bigger ice particles (lower CR) being more spherical (lower LPDR). Increased deposition of water vapor had probably occurred on the surface of bigger particles, rendering their shape more spherical. For LPDR below 25%, the LR and LPDR were also proportional (Fig. 5.13b). For LPDR above 25%, an inversely proportional relation was displayed. Only in the *low COD regime*, the LR – LPDR were exclusively proportional. An assignment to the closest matching ice crystal shapes will be attempted based on simulated properties from Okamoto et al. (2020). A part of the cirrus ice crystals closely matched to horizontally-oriented Voronoi particles ($LPDR_{355}$: 15–65% and CR: 1.2–1.5). To a lower extent, the observed particles could be attributed to column ($LPDR_{355}$: 20–30% and CR: 1.6–1.8) and bullet ice crystals ($LPDR_{355}$: 25–40% and CR: 1.5–2). Horizontally-oriented Voronoi particles

present relatively high LR, which is increasing with their LPDR (Fig. 5.7). Column crystals are characterized by low LR and weak dependence on the LPDR. Regarding bullet crystals, they exhibit intermediate to low LR, which is inversely proportional to LPDR. Finally, the majority of the measurements could not be assigned to any idealized crystal shape since in reality ice crystals mainly posses irregular shapes (e.g. facetted poly-crystaline particles, (Korolev, Isaac, and Hallett, 1999; Lawson et al., 2019)).

In the following, the dependence of COD on the cirrus geometrical and optical properties is investigated (Fig. 5.14 and 5.15). The linear regression was performed to all data points, as the *low* and *high COD regimes* are in physical continuity. The natural logarithm of COD seemed to be proportional to the cirrus layer median GT, which translates into an exponential increase of the COD with GT. Identical results were found for COD_{532} (not shown). The degree of the relation may differ across different sites. For instance, Sassen and Comstock (2001) demonstrated a linear proportionality between COD and GT over Utah (in their Fig. 8), while a higher relation (but not specified) was reported over Oklahoma ((Wang and Sassen, 2002), their Fig. 12). An inversely proportional relation was found between COD and LPDR as well as CR (Fig. 5.15). This indicates that the COD decreased exponentially for smaller (increasing CR) and less spherical ice particles (increasing LPDR), probably due to reduced water vapor deposition on the ice particle surface. Similar results were obtained for COD_{532} (not shown).

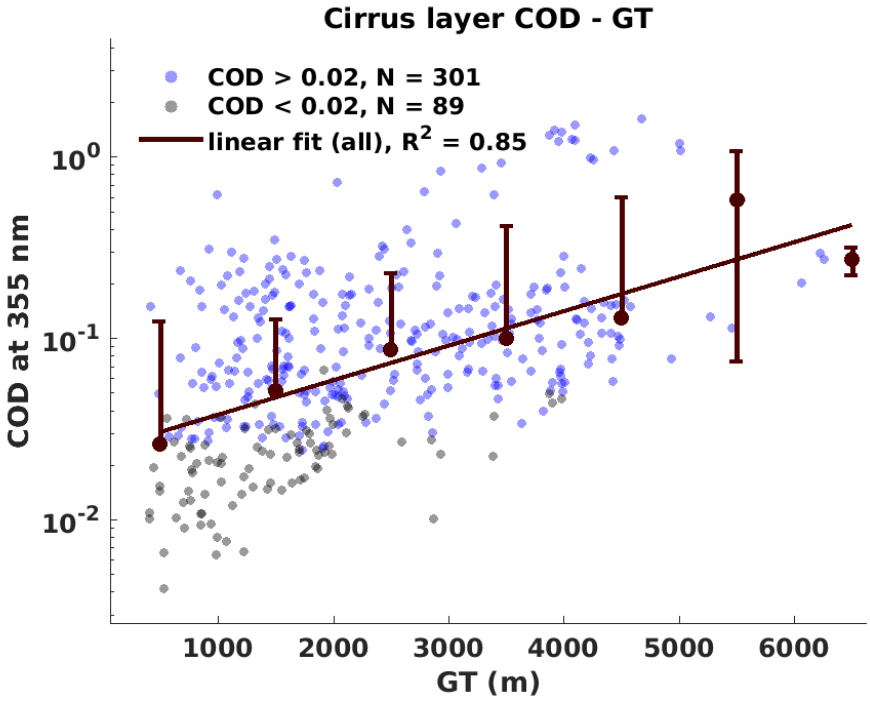

Fig. 5.14: Same as Fig. 5.13 but for COD versus geometrical thickness (GT, 500 m GT classes). The linear regression was performed on the whole dataset.

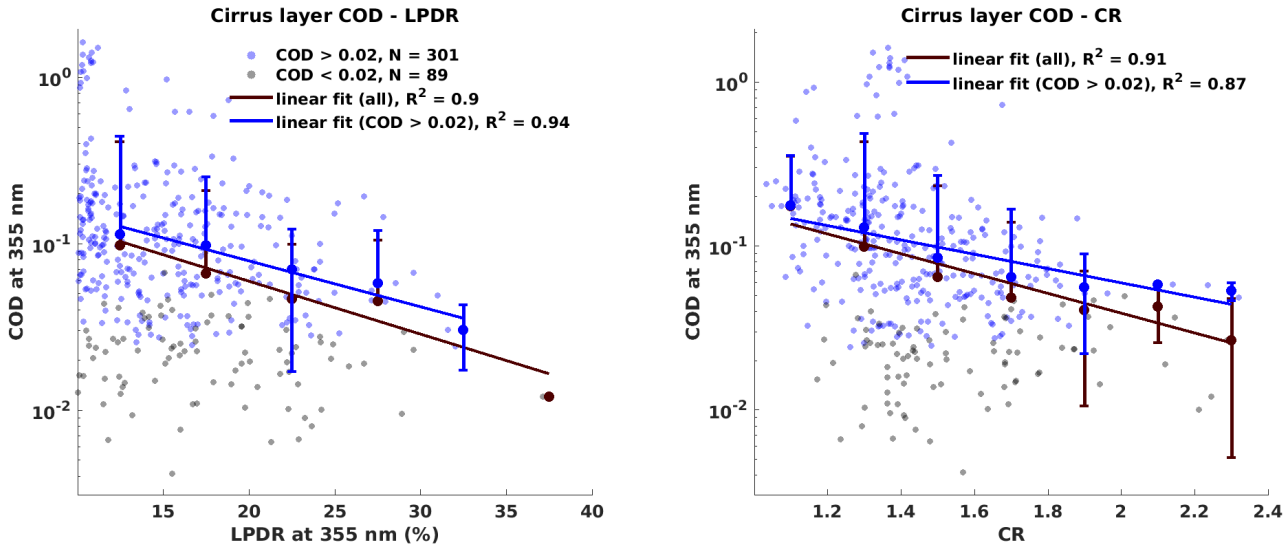

Fig. 5.15: Same as Fig. 5.14 but versus $LPDR_{355}$ (left) and CR (right).

5.5 Dependence on meteorological conditions

The dependence of cirrus geometrical and optical properties on the meteorological conditions is examined here. The dependency was investigated upon temperature, wind speed and wind direction. The meteorological parameters were derived from AWIPEV radiosonde ascents (Sec. 2.3.1). For days with multiple launches, each cirrus layer was matched with the temporally-closest radiosonde. An additional criterion was applied, limiting the difference between radiosonde and lidar measurements to 2 h. With this criterion, 148 cirrus layers (26 in the *low COD regime*) out of 390 remained for further analysis. An overview of the meteorological conditions within the cirrus altitude range is presented in Fig. 5.16. The median temperature was mainly between -65 and -50^oC, while the $T_{C_{base}}$ ($T_{C_{top}}$) varied from -55 to $-38\ ^oC$ (from -70 to $-55\ ^oC$). A broad range of wind conditions was found (mostly between 1 and 15 ms^{-1}), with an increasing wind speed tendency from the C_{base} towards the C_{top}. A similar tendency was also reported over mid-latitude (Utah, (Sassen and Campbell, 2001)) and sub-tropical sites (central China, (Wang et al., 2020)). Colder cirrus tended to appear in winter and spring and winter-time cirrus were accompanied by markedly stronger wind conditions (Tab. D.1). Winter- and spring-time cirrus were associated with W–SW flow, whereas a E–NE flow appeared in summer. The most variable wind conditions appeared in autumn (Tab. D.1).

The cirrus over Ny-Ålesund seemed slightly colder compared to Fairbanks (Campbell et al., 2021) and Kuopio (Voudouri et al., 2020). Over Fairbanks the $T_{C_{top}}$ rarely dropped below -60^oC, while over Kuopio the $T_{C_{top}}$ (-57 ± 9^oC for C_{top} of 9.8 $\pm$ 1.1 km) was about 8^oC higher compared to Ny-Ålesund (-65 ± 7^oC for C_{top} of 9.6 $\pm$ 1.2 m). Over Kuopio the $T_{C_{mid}}$ was -50 ± 10^oC (for C_{mid} of 9.2 km), while over Ny-Ålesund the median layer temperature amounted to -57 ± 6^oC (for C_{mid} of 8.3 km). It should be noted, however, that for Fairbanks and Kuopio warmer cirrus were a priori considered, as the $T_{C_{base}}$ threshold was set to -27^oC (over Ny-Ålesund it was set at -40^oC). Compared to tropical sites, the Ny-Ålesund

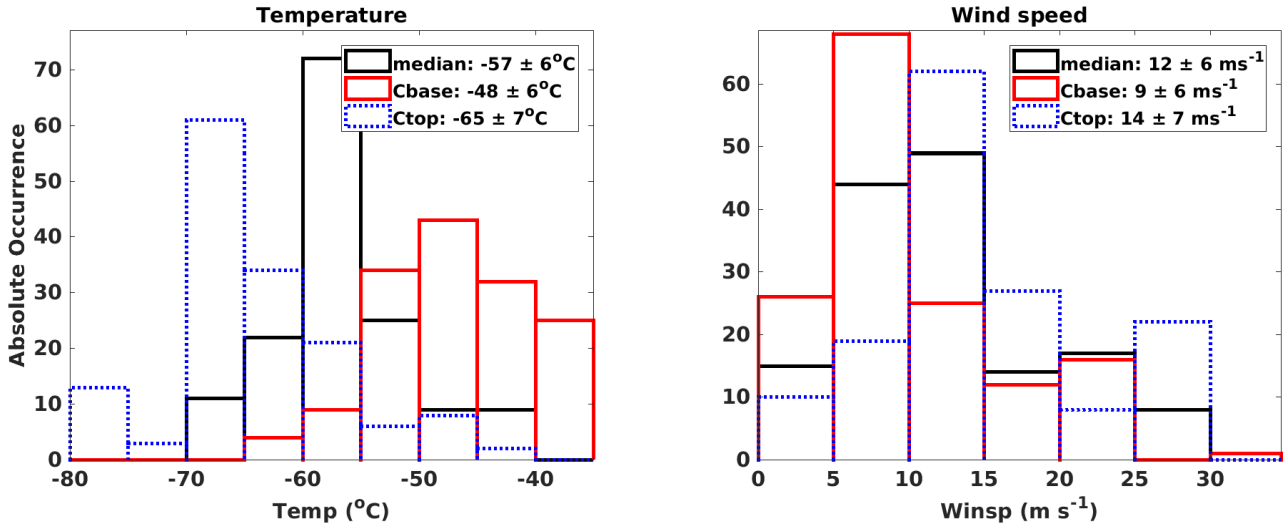

Fig. 5.16: Distribution of temperature and wind speed within the cirrus layer altitude range, presented as layer median, at C_{base} and at C_{top}. The median $\pm$ standard deviation is given in the legend. Only quality-assured data with 2 h temporal difference between the lidar and radiosonde measurements were considered.

cirrus tended to be slightly warmer due to their lower occurrence altitudes, constrained by the meridionally sloping tropopause. For instance, $T_{C_{mid}}$ of -65 ± 12^oC was reported at 14.1 $\pm$ 2 km over tropical India (Pandit et al., 2015).

Meteorological dependencies of cirrus geometrical thickness

The dependency of cirrus layer GT on temperature, wind speed and wind direction is explored in Fig. 5.17. In the *high COD regime* the GT decreased with temperature, which is surprising since layers forming at higher temperatures (lower altitudes) are expected to be geometrically-thicker due to their greater distance from the tropopause (Sassen and Comstock, 2001; Wang et al., 2020). Below -55^oC two branches appeared. The first one displayed increasing GT with temperature (GT lower than 2500 m and *low COD regime*), while the opposite held true for layers thicker than 2500 m. The high GT branch mainly represented winter and spring cirrus, with those thicker than 3000 m and colder than -50^oC related to a poorly-defined tropopause. A decreasing GT with temperature has also been observed over Kuopio below -50^oC (Fig. 8a from Voudouri et al., 2020). Over lower latitudes, such a relation has been reported for warmer cirrus (above -55^oC at tropical latitudes (Pandit et al., 2015) and above -50^oC in mid-latitudes (Giannakaki et al., 2007; Hoareau et al., 2013)).

Concerning wind speed, a proportionality to GT was found for winds up to 15 ms^{-1} in both COD regimes (Fig. 5.17, middle panel). For stronger winds no clear dependence was found any longer. An attempt to explain the GT – wind speed proportionality will be made using a simplified rationale. This assumes that wind speed is a proxy for horizontal advection of air masses. Assuming air masses of equal RH advected towards a region with similar INP

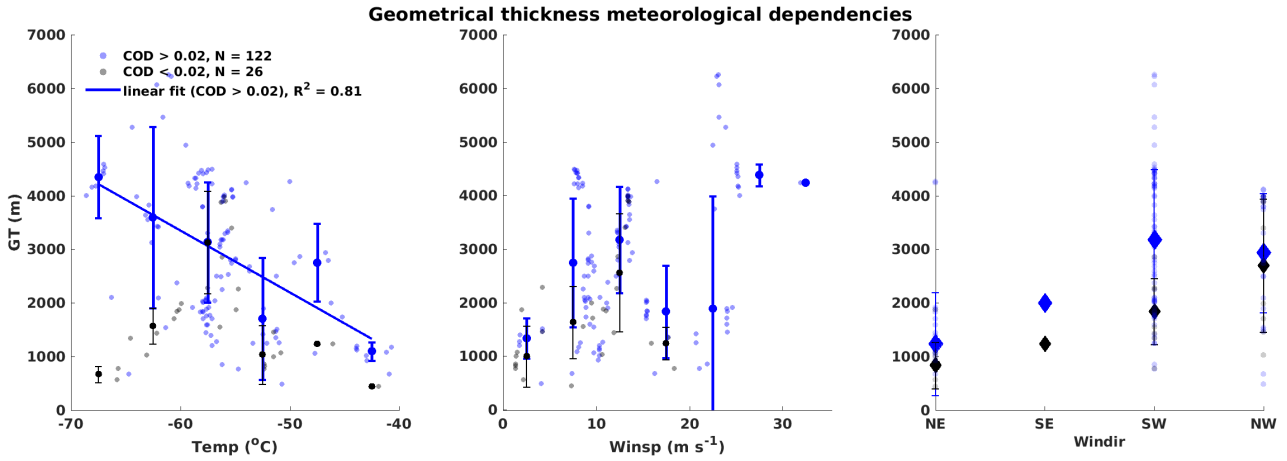

Fig. 5.17: Cirrus layer GT versus layer median temperature (left), wind speed (center) and wind direction (right). Overlaid is the median ± standard deviation of GT per temperature (5^oC), wind speed ($5\ ms^{-1}$) and wind direction classes. Only quality assured data were considered satisfying the 2 h temporal criterion.

type, number concentration and size distribution, a stronger wind regime will result in intensified ice nucleation. During intensified (condensation and) deposition of water vapor higher amounts of latent heat will be released, leading to ascending air motion within the cirrus and, thus, to higher vertical cirrus extent. It should be noted, however, that the cirrus lifetime is expected to differ as well in the different wind regimes. Unfortunately, it is difficult to expand on this aspect as KARL was not in continuous operation. Therefore, the simplified rationale could be valid only instantaneously. Regarding wind direction, geometrically-thicker cirrus appeared under westerly flow but different GT classes fell within each other's variability (Fig. 5.17, right panel). The SE regime was only represented by two cirrus layers although this wind sector was dominant in May–July (Fig. 5.6). As the SE origin cirrus seem geometrically-thinner, the derivation of their optical properties is expected to be challenging and probably most of these layers were screened out (Sec. 5.2).

Meteorological dependencies of cirrus optical properties

In the following, the dependence of cirrus optical properties on temperature (Fig. 5.18) and wind speed (Fig. 5.19) is investigated. Overall, the dependency of optical properties on temperature did not seem to be strong. The COD seemed to decrease with temperature below -55^oC (Fig. 5.18). Over Kuopio the COD also decreased with temperature between -70 and -50^oC. For cirrus warmer than -50^oC the COD dependence on temperature was weak over both sites. In contrast, over mid-latitude and sub-tropical sites the COD – temperature relation was closer to linearly proportional (Sassen and Comstock, 2001; Wang and Sassen, 2002; Wang et al., 2020). Concerning the LR, a clear dependence on temperature has not been established yet (Gouveia et al., 2017; Voudouri et al., 2020; Wang et al., 2020) as it was the case over Ny-Ålesund (Fig. 5.18, upper right panel). The dependency of LPDR was

also not clear, similar to Kuopio (Voudouri et al., 2020). However, over sub-tropical (central China, (Wang et al., 2020)) and tropical sites (south India, (Sunilkumar and Parameswaran, 2005)) the LPDR decreased with temperature. Finally, the CR slightly increased (smaller ice particles) with temperature below -55^oC, while the opposite occurred between -55 and -45^oC. Over Kuopio a weak dependency was reported, with increasing CR between -60 and -45^oC (Voudouri et al., 2020).

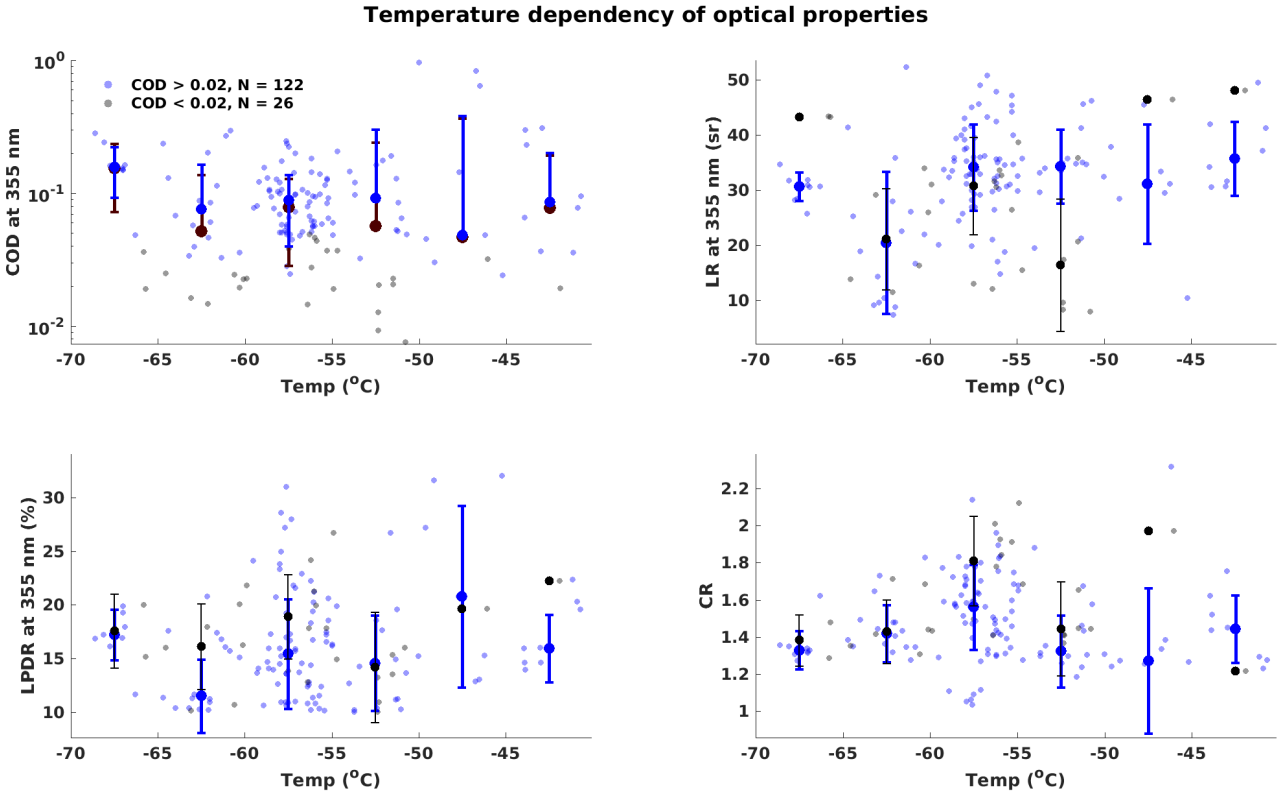

Fig. 5.18: Cirrus layer optical properties versus median temperature. LPDR and CR are reported as layer-median values. Overlaid are the median ± standard deviation optical properties per temperature (5^oC classes).

The relation of COD with wind speed was weakly proportional (Fig. 5.19). The LR slightly decreased with wind speed in the *high COD regime*, while the opposite was found in the *low COD regime*. The COD – wind speed relation could be explained by a similar rationale to the GT – wind speed relation (Fig. 5.17). However, the COD dependence on wind speed was weaker compared to the GT, as the LR exhibited an opposing dependence. The respective LPDR and CR relations were not clear. However, the ice particles were likely more spherical for stronger winds (in the *high COD regime*). More specifically, the LPDR decreased with different slopes under the 1–15 ms^{-1} and 15–35 ms^{-1} wind regimes. In contrast, in the *low COD regime* the LPDR slightly increased for winds up to 15 ms^{-1}. Finally, the optical properties were similar within different wind sectors (not shown).

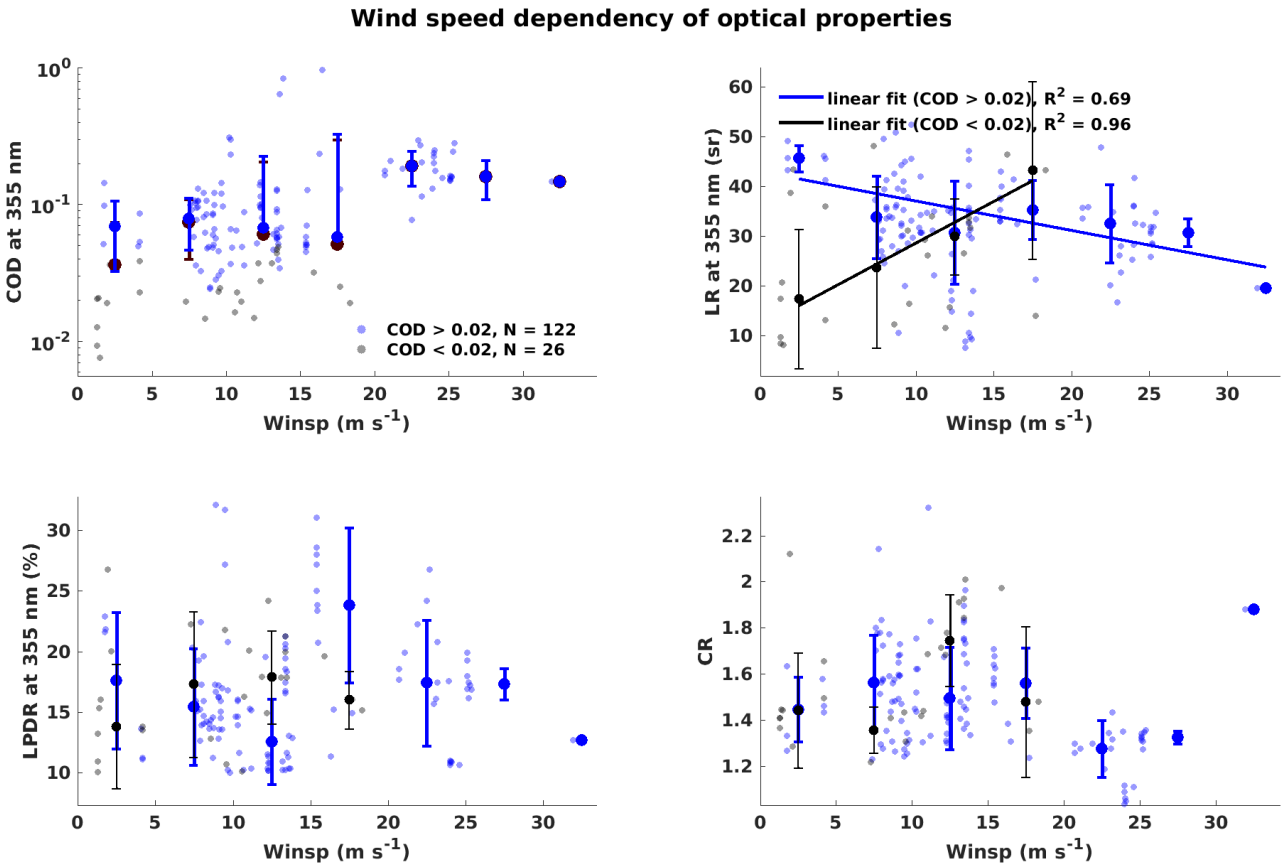

Fig. 5.19: Same as Fig. 5.18 except for dependence on wind speed (5 ms^{-1} classes).

5.5.1 Cirrus clouds in the tropopause

In the presented analysis the cirrus occurrence in the tropopause and lower stratosphere was examined and carefully distinguished from polar stratospheric clouds (PSCs) and aerosol layers. During the study period, 15 high winter-time cirrus clouds (C_{top} > 10 km) were observed in total. From a seasonal perspective, *stratospheric cirrus* (C_{top} at least 500 m above the lapse rate tropopause (Zou et al., 2020)) appear mostly in boreal and austral winter (Nazaryan, McCormick, and Menzel, 2008; Sassen, Wang, and Liu, 2008; Zou et al., 2020).

Using the radiosonde-derived temperature profiles, an effort was made to estimate the tropopause height via the lapse rate definition (WMO, 1957). Unfortunately, in the majority of the cases the determination of the tropopause height was not possible. However, two characteristic winter-time tropopause regimes were identified as presented in Fig. 5.20. Cirrus extended well above 10 km in the poorly-defined tropopause regime (upper panels). However, the cirrus C_{top} was constrained beneath the tropopause in the well-defined tropopause regime (lower panels). Additionally, the relative humidity (RH) profile differed. When the tropopause was well-defined the RH declined rapidly to nearly-zero levels, whereas for a poorly-defined tropopause the RH decline was smoother. A poor separation between the troposphere and the stratosphere is more likely to favor the intrusion of water vapor into the lowermost stratosphere. The latter in combination with the nearly-neutral temperature

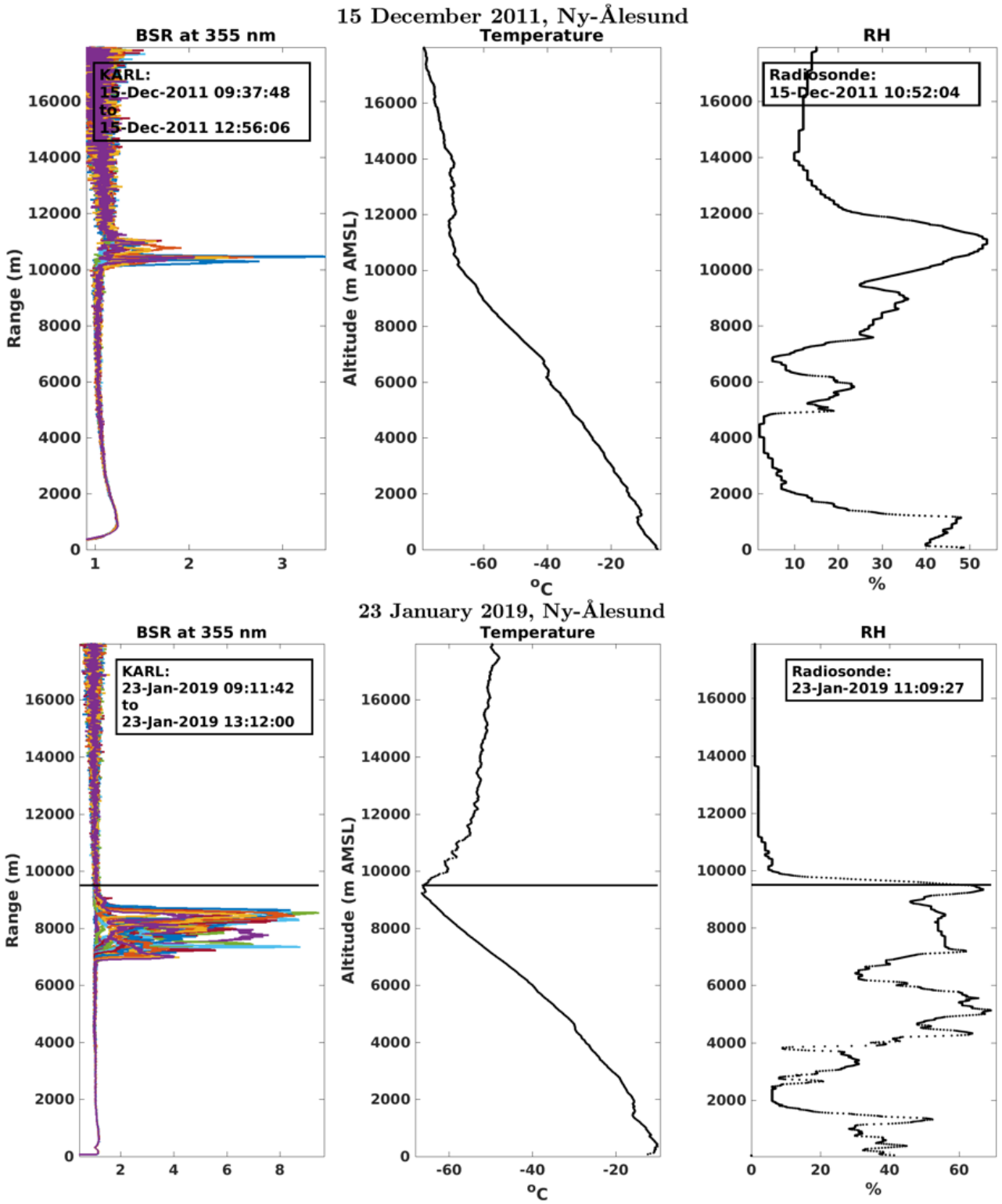

Fig. 5.20: Representative winter-time tropopause regimes. Profiles of BSR, air temperature and RH for poorly-defined (upper panels) and well-defined tropopause (lower panels).

gradient, sustains higher levels of RH, which is a key parameter for cloud formation and persistence. Conversely, a well-defined tropopause deters water vapor stratospheric intrusions and together with the positive temperature gradients leads to nearly-zero RH levels. Concerning the causal relation between cirrus occurrence and a poorly-defined tropopause, the

following can be stated: the poorly-defined regime is necessary but not sufficient for cirrus to extend within the tropopause.

It should be noted that cirrus clouds were carefully distinguished from aerosol layers in the upper troposphere – lower stratosphere region. Noteworthy are the Siberian fires' smoke layers of summer 2019. These layers were observed from 7–8 km up to 17–18 km between August 2019 and May 2020 over Ny-Ålesund as well as the central Arctic (Ohneiser et al., 2021). Thus, they partly overlapped with the cirrus occurrence altitude range. However, the optical properties of the smoke layers were different to those expected for cirrus clouds. The smoke layers consisted of nearly-spherical particles (LPDR lower than 4% both at 355 and 532 nm) that were in general more absorbing (LR_{355} = 55 sr and LR_{532} = 85 sr) than ice particles (Ohneiser et al., 2021). Regarding PSCs, they typically occur at higher altitudes than cirrus, mainly between 20 and 24 km over Ny-Ålesund (Massoli, Maturilli, and Neuber, 2006), and at lower temperatures (below -78^oC).

The occurrence of high and cold tropopause cirrus is of key importance with respect to cirrus radiative estimates. Campbell et al. (2021) hypothesized that the increasing tropopause heights over the Arctic in the last 40 years (especially in summer) have enabled the formation of higher and colder cirrus. This, in turn, implies an intensification of the daytime cloud radiative effect (CRE) at the top of the atmosphere (TOA). The authors proposed a positive feedback mechanism over land that is driven by the greater thermal contrast between the warming surface and the colder cirrus. However, the investigation of this hypothesis over open-water and ice-covered surfaces remains an open task. The hypothesis of Campbell et al. (2021) is tested to some extent in the following Section.

5.6 CRE estimation at TOA: sensitivity analysis

In this Section, the cirrus CRE is investigated at TOA through a sensitivity analysis using the simplified model of Corti and Peter (2009) (Sec. 2.4.5). In each sensitivity test one input parameter was perturbed, while the others were kept constant. The unperturbed parameters corresponded to average or median conditions encountered over Ny-Ålesund and amounted to: SZA = 67.5^o, T_{surf} = -5^oC, $T_{C_{top}}$ = -65^oC and COD = 0.07. Each sensitivity was performed for two surface albedo scenarios: over tundra (a = 0.1) and over snow/ice (a = 0.8). In the control scenario the CRE^{net} at TOA amounted to $+2.5\ Wm^{-2}$ (SW: $-2.8\ Wm^{-2}$, LW: $+5.4\ Wm^{-2}$) over tundra and $+5.1\ Wm^{-2}$ (SW: $-0.3\ Wm^{-2}$, LW: $+5.4\ Wm^{-2}$) over snow/ice.

Firstly, the dependency of CRE on the surface albedo was investigated (Fig. 5.21). The higher the surface albedo the lower was the negative CRE^{SW} (blue line), while the LW effect (red line) remained constant. Thus, the CRE^{net} (gray line) intensified over higher reflective surfaces. Multiple reflections between the cloud and the ground increase for higher albedo, resulting in decreased CRE^{SW} at TOA. This mechanism is easier to understand when consid-

ering Eq. 2.35 in two extreme scenarios. For albedo = 1 the perfect ground reflectivity cannot be further increased by the addition of a cloud (CRE^{SW} = 0). For albedo = 0 no multiple reflections occur and the negative CRE^{SW} maximizes (Eq. 2.35 reduces to $CRE^{SW} \approx -I \cdot t \cdot t'^{*} \cdot R_c$ (Corti and Peter, 2009)).

Over tundra (dot symbols) lower solar elevation (higher SZA) was accompanied by lower SW effect. As a result, the CRE^{net} increased due to the relatively higher contribution of the LW effect. Over snow/ice surfaces (hexagon symbols) the response of the SW effect to SZA was negligible (changes of 0.1 Wm^{-2}) and, thus, the same applied for the CRE^{net} (the LW effect remained constant). In general, under *high Sun conditions*, the *short-wave albedo* and *infrared greenhouse* effects compete one another, while under *low Sun conditions* there is little solar radiation to compensate for the infrared radiation emitted towards space.

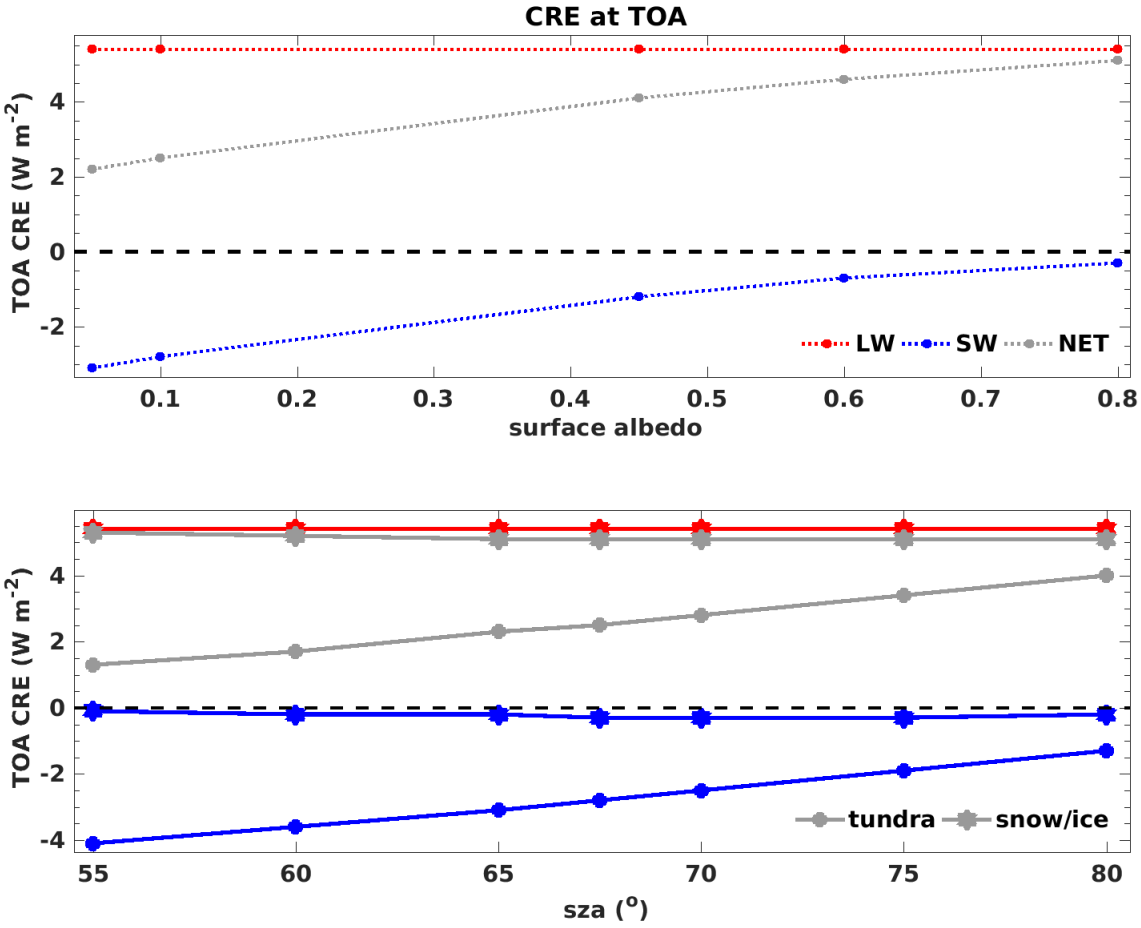

Fig. 5.21: CRE at TOA as a function of surface albedo and SZA. The SW, LW and net components are presented separately. Note that in each sensitivity the remaining parameters are kept constant.

The dependency of the CRE on $T_{C_{top}}$ and T_{surf} was also investigated (Fig. 5.22). Warmer cirrus were found to produce a lower net effect due to a diminished LW effect. More specifically, the higher the $T_{C_{top}}$ the more LW irradiance was emitted upwards and, hence, less irradiance remained at TOA. The net warming effect was less intense over tundra compared

to snow/ice surfaces since the CRE^{SW} had a greater counterbalancing contribution in the former scenario. Concerning T_{surf}, an increasing CRE^{net} was revealed. In order to interpret this response one has to examine the thermal contrast between the surface and the C_{top}, which drives the CRE^{LW} (Eq. 2.38). For warmer surfaces the thermal contrast to a cirrus cloud gets greater. The cloud receives more LW irradiance by the surface but re-emits less irradiance towards the TOA due to its lower temperature. Hence, more net irradiance remains at TOA. Based on the presented findings it seems that the hypothesis of Campbell et al. (2021) (Sec. 5.5.1) can be extended to tundra and snow/ice surfaces.

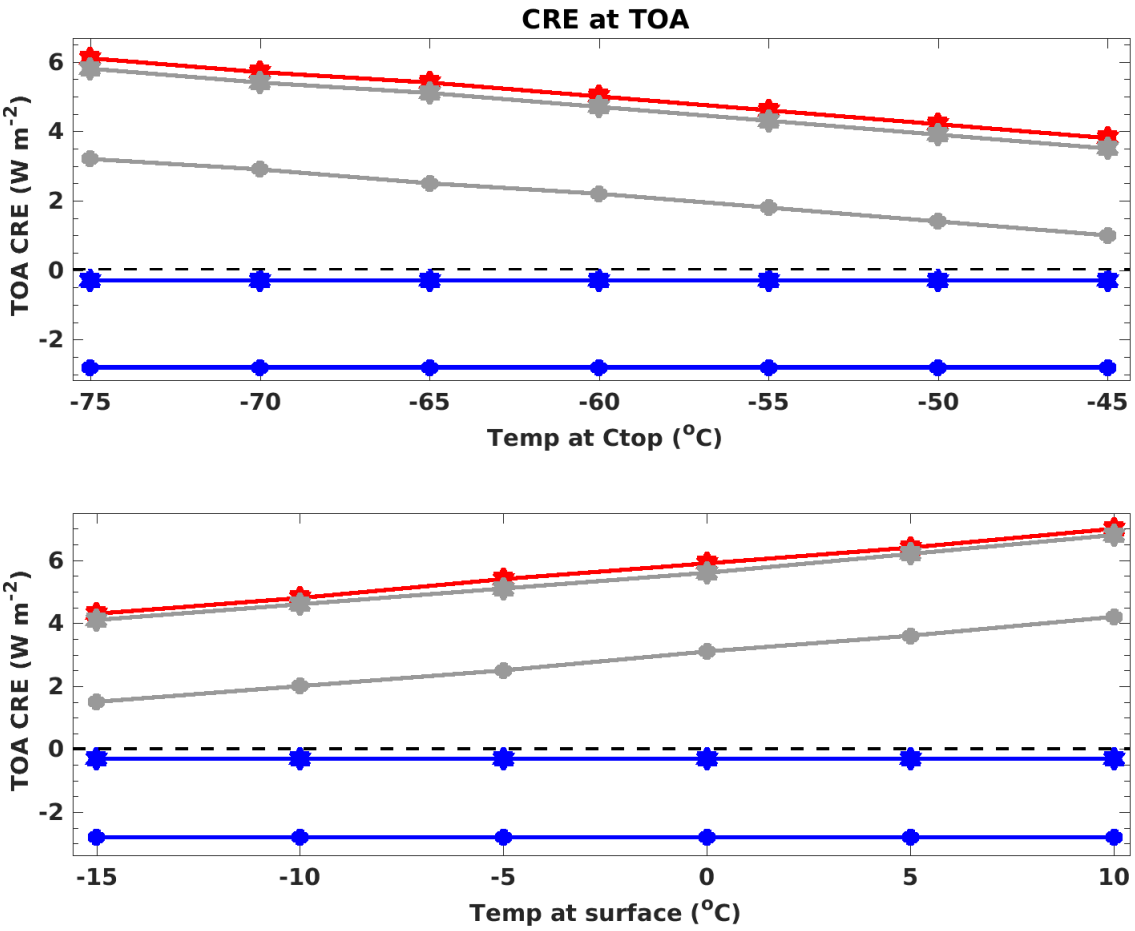

Fig. 5.22: Same as Fig. 5.21 but for C_{top} and T_{surf} sensitivities.

Finally, the response of the CRE on COD was examined (Fig. 5.23). It should be noted that over Ny-Ålesund a COD from 0.004 up to 1.8 was derived. Nevertheless, keeping in mind the lidar instrumental bias towards optically-thin clouds (Sec. 5.3), the sensitivity test was extended to higher COD scenarios. Both the CRE^{SW} and CRE^{LW} increased with COD but with opposite sign and at different rates. For low COD, the CRE^{LW} dominated (positive CRE^{net}). For COD higher than 10, however, a different response was found over snow/ice and tundra. Over snow/ice the LW domination persisted as the COD increased and, thus, the CRE^{net} was solely positive. Over tundra, nevertheless, the CRE^{SW} outweighed the CRE^{LW} for thicker clouds and the CRE^{net} displayed negative values of low magnitude (compared to

the same COD scenario over snow/ice).

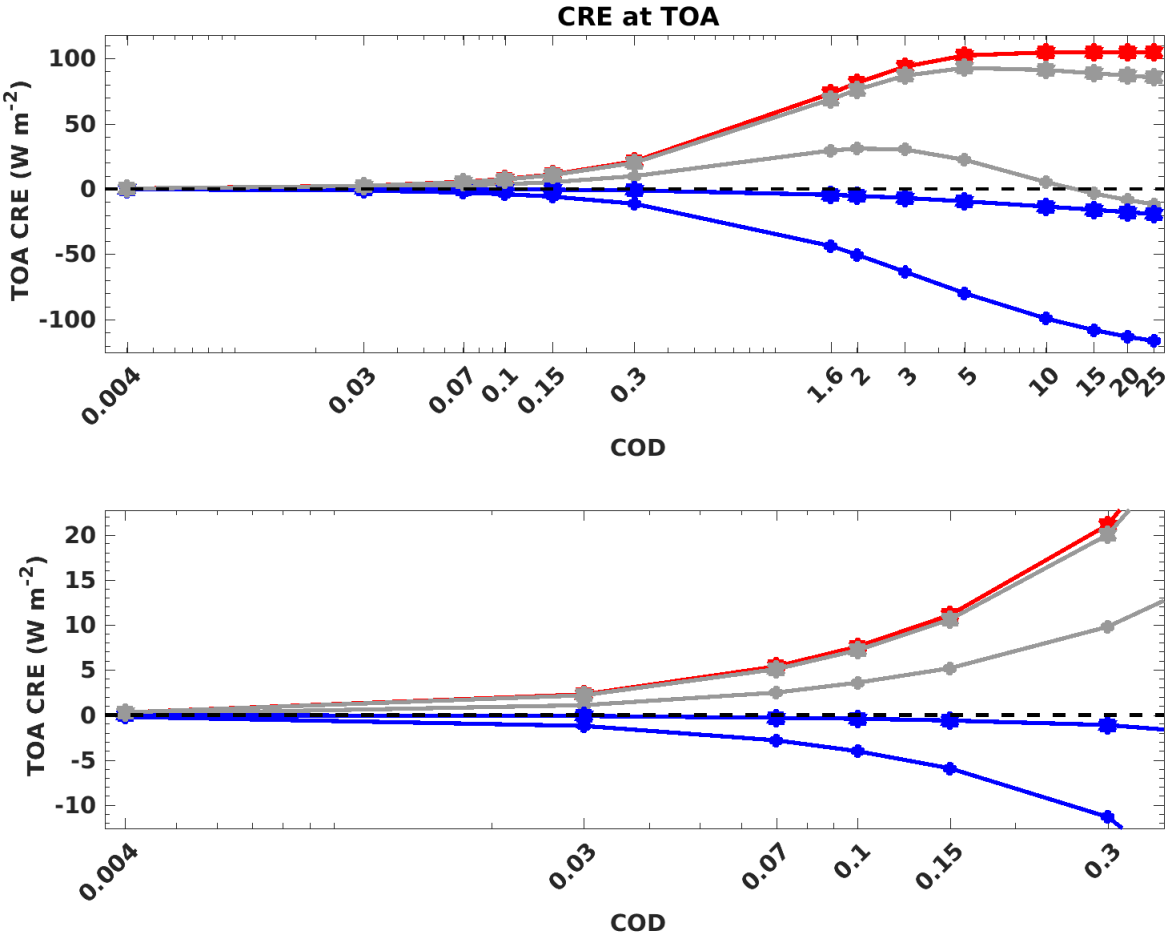

Fig. 5.23: Same as Fig. 5.21 but for COD sensitivity. The lower panel is a zoom-in of the upper panel for low COD scenarios.

Similar to Ny-Ålesund, sub-visible and optically-thin cirrus had a positive CRE contribution over mid-latitude (Krämer et al., 2020) and sub-Arctic sites (Campbell et al., 2021). However, the transition from positive to negative CRE^{net} occurred for lower COD (around 0.5) compared to Ny-Ålesund (above 10). There are two reasons behind this discrepancy. Firstly, higher SZA values are encountered over Ny-Ålesund and, thus, there is a higher tendency towards a domination of the positive LW effect. Secondly, the Corti–Peter model tends to shift the positive to negative CRE^{net} crossover point towards higher COD compared to comprehensive radiative transfer calculations (0.25 COD bias over Singapore, (Lolli et al., 2017b)). However, the bias reported by Lolli et al. (2017b) is small compared to the discrepancy between Fairbanks and Ny-Ålesund and, therefore, the first reason seems more likely.

5.7 Conclusions

In this Chapter the geometrical and optical properties of cirrus layers were analyzed over Ny-Ålesund on a long-term basis, using observations from 2011 to 2020. The inter-relations

of properties were examined together with their dependence on meteorological conditions. Finally, a sensitivity analysis on the top of the atmosphere (TOA) cloud radiative effect (CRE) was performed. The main findings can be summarized as follows:

- In winter and spring cirrus layers were geometrically-thicker, they appeared more frequently and their C_{base} was found lower (Fig. 5.1). The troposphere and tropopause thermodynamic structure seemed to control the seasonality of cirrus occurrence altitude.

- The multiple-scattering effect was found equally important for all cirrus regimes in terms of lidar ratio (LR). The effect on the cloud optical depth (COD) was higher for the opaque regime (Tab. 5.1). The correction of the multiple-scattering effect increases the confidence in optically-thicker cirrus retrievals. On that grounds, the lidar-derived properties are brought closer to the observational range of cloud radars.

- The majority of cirrus layers fell into the optically-thin regime, displaying a COD of 0.07 $\pm$ 0.24 (median $\pm$ standard deviation). However, lidar observations are known to be biased towards optically-thinner clouds. The LR in the ultraviolet spectral region (33 $\pm$ 9 sr) was in good agreement with a sub-Arctic study (Voudouri et al., 2020), while the LR in the visible region (42 $\pm$ 10 sr) was higher compared to lower latitudes. In winter optically-thicker cirrus of lower LR were observed compared to the rest of the year (Tab. D.1). The linear particle depolarization ratio (LPDR) was lower (more spherical ice particles) compared to lower latitudes. A meridionally decreasing depolarization ratio was also supported by satellite lidar observations (Sassen and Zhu, 2009). In summer and autumn the LPDR was higher (Tab. D.1).

- The LPDR and color ratio (CR) were found to be proportional (Fig. 5.13a), reflecting a tendency of bigger ice particles being more spherical. Increased deposition of water vapor had probably occurred on the surface of bigger particles, rendering their shape more spherical. The COD increased exponentially with GT (Fig. 5.14). Additionally, the COD tended to be lower for less spherical and smaller ice particles (Fig. 5.15) probably due to reduced deposition of water vapor on the ice particle surface.

- The $T_{C_{top}}$ (median cirrus temperature) mainly ranged from -70 to -55^oC (from -65 to -50^oC, Fig. 5.16). Across different regions (except for the Tropics) more than half of the cirrus are observed above -48^oC (Krämer et al., 2020). Therefore, the presented cirrus properties can be considered more representative for cold cirrus.

- The GT of cold (below -55^oC) and thin cirrus (less than 2500 m) increased with temperature, while the *high COD regime* cirrus exhibited the opposite behavior (Fig. 5.17). The GT increased for wind speeds up to 15 ms^{-1}. Winter cirrus occurred under colder conditions and stronger winds. Winter and spring cirrus were associated with W–SW flow, whereas E–NE flow appeared in summer (Tab. D.1).

- Below -55^oC COD decreased with temperature, while the ice particle size tended to be smaller (increased CR). Hardly any temperature dependence of LR and LPDR was

found (Fig. 5.18). Similar behavior was observed over a sub-Arctic site (Voudouri et al., 2020). The COD was weakly proportional to wind speed (Fig. 5.19), whereas the respective LPDR and CR relations were not clear. The properties of cirrus associated with different wind sectors were not distinguishable from one another.

- The CRE sensitivity analysis at TOA mostly revealed a positive net effect. The CRE^{net} amounted to $+2.5\ Wm^{-2}$ over tundra and $+5.1\ Wm^{-2}$ over ice in the control scenario (SZA = 67.5^o, $T_{surf} = -5^oC$, $T_{C_{top}} = -65^oC$ and COD = 0.07). Only for highly opaque cirrus (COD higher than 10) and over tundra the net effect turned negative. An intensified CRE^{net} is expected over Ny-Ålesund in winter (high SZA and high albedo) due to the relative domination of the *infrared greenhouse effect* (Fig. 5.21). Over the high European Arctic, the COD along with the surface albedo seem to be the most critical parameters in determining the CRE sign at TOA.

- The overall dependency of cirrus properties on temperature and wind speed was not pronounced and neither was a seasonal cycle. However, the properties of winter-time cirrus were distinctive. Winter cirrus tended to be geometrically- and optically-thicker. At the same time, they appeared under colder conditions and stronger winds, they seemed to be less absorbing (lower LR) and consisted of relatively more spherical ice particles (lower LPDR, Tab. D.1). Over the 10 years of the analysis, the cirrus properties have not exhibited any clear temporal trend. The Micro-pulse lidar (MPL) observations might be more suitable for detecting trends of cirrus occurrence and properties as they are provided on a continuous basis.

The lidar-derived cirrus properties can be compared to those from the cloud radar, which is installed at AWIPEV. More specifically, the geometrical boundary discrepancies between lidar and radar can be examined as well as discrepancies in the extinction coefficient. Additionally, it can be assessed to which extent the cirrus conditions over Ny-Ålesund are representative for the high European Arctic, using satellite lidar observations.

6

CONCLUSIONS AND OUTLOOK

Based on the outcome of Chapters 3-5, the formulated research questions can be addressed as follows:

- **RQ1: Which aerosol properties and ambient conditions play the most critical role in the local radiation budget? Are these properties retrieved precisely enough by optical remote sensing and how do they compare to in-situ measurements?**

  Firstly, the aerosol optical and microphysical properties were analyzed for a long-range transport event (Sec. 3.1). Although the aerosol size distribution was clearly modified (from bi-modal to fine mono-modal) between two European Arctic locations, the aerosol radiative effect (ARE) within the atmospheric column was similar. The latter was related to the domination of accumulation mode aerosol.

  As a next step, the response of ARE to different aerosol properties and spring-time ambient conditions was assessed by radiative transfer simulations (Sec. 3.2). Upon perturbing the aerosol properties by their highest uncertainties, the significant role of the single-scattering albedo (SSA) was revealed. A 10% change in the SSA perturbed the ARE more intensely than a 30% change in the aerosol extinction coefficient. As the ARE sign was not modified in the aforementioned sensitivities, the qualitative assessment of radiative estimates seems reliable. However, the ARE sign was found sensitive to the surface albedo. A solely negative ARE appeared only for dark surfaces, whereas a negative to positive shift was found for bright surfaces. Over bright surfaces, more net irradiance remained above the aerosol layers relative to aerosol-free conditions (multiple reflection domination), while the opposite held true over dark surfaces (shadowing domination). The present findings indicate that the ARE sign can be highly sensitive in spring, which is characterized by transitional surface albedo conditions.

  The inversion of aerosol microphysics from lidar-derived optical parameters is an ill-posed problem. In the final part, the inverted size distribution was compared to the in-situ measured distribution for a low-tropospheric event (Sec. 3.3). Both techniques revealed a bi-modal size distribution, with good agreement in the total aerosol volume concentration. However, in terms of SSA a disagreement was found, with the lidar inversion indicating highly scattering particles and the in-situ measurements pointing to absorbing particles. The discrepancies could stem from assumptions in the inversion (e.g. wavelength-independent refractive index) and errors in the conversion of the in-situ measured light attenuation into absorption. Another source of discrepancy might

be related to an incomplete capture of fine particles in the in-situ sensors. The disagreement in the most critical parameter for the Arctic ARE necessitates further exploration in the frame of aerosol closure experiments. Care must be taken in ARE modelling studies, which may use either the in-situ or lidar-derived SSA as input. In the future, the impact of the revealed discrepancies on the radiative effect can be quantified.

- **RQ2: Is it possible to improve the detection of thin cirrus clouds? To which extent is the retrieval of their optical properties reliable?**

  The detection of sub-visible cirrus is of special importance as the total cloud radiative effect (CRE) can be negatively biased, should only the optically-thin and opaque cirrus contributions are considered (Campbell et al., 2021). In the second part, a cirrus detection and optical characterization scheme was developed, aiming at increased sensitivity to thin cirrus clouds (Chapter 4). The detection scheme extended the Wavelet Covariance Transform (WCT) method (Gamage and Hagelberg, 1993) by dynamic thresholds (*dynamic WCT*). Finally, higher sensitivity was achieved to thin and faint cirrus layers that were partly or completely undetected by the existing static method.

  The optical characterization scheme extended the Klett–Fernald retrieval (Klett, 1981; Fernald, 1984) by an iterative lidar ratio (LR) determination (*constrained Klett*). The iterative process was constrained by a *reference value*, which indicated the aerosol concentration beneath the cirrus cloud. Contrary to existing approaches, the aerosol-free assumption was not adopted, but the aerosol conditions were approximated by an initial guess. Even without any available cloud-free profile, a sufficiently accurate *reference value* was obtained from profiles with cloud optical depth (COD) up to 0.2. The inherent uncertainties of the *constrained Klett* were higher for optically-thinner cirrus, but an overall good agreement was found with two established retrievals. Additionally, existing approaches, which rely on aerosol-free assumptions, presented increased accuracy when the proposed *reference value* was adopted. The *constrained Klett* retrieved reliably the optical properties in all cirrus regimes, including upper sub-visible cirrus with COD down to 0.02.

- **RQ3: Which long-term geometrical and optical properties do Arctic cirrus clouds posses? Which properties and ambient conditions play the most critical role in the local radiation budget?**

  Cirrus is the only cloud type capable of inducing a cooling or heating effect at the top of the atmosphere (TOA) during daytime. The CRE sign depends on the cloud properties as well as on ambient conditions (Campbell et al., 2021). Over the Arctic, however, the properties and CRE of cirrus are under-explored. In the final part, long-term cirrus geometrical and optical properties were investigated for the first time over an Arctic site (Chapter 5). To this end, the retrieval scheme developed in Chapter 4 was employed. Additionally, the cirrus CRE was investigated at TOA using a simplified model.

In winter and spring cirrus layers were thicker, their occurrence was more frequent and their cloud base was found lower. Cirrus clouds over Ny-Ålesund seemed to be more absorbing in the visible spectral region compared to lower latitudes and comprise more spherical ice particles. Such meridional differences could be related to discrepancies in absolute humidity and ice nucleation mechanisms. The COD tended to decline for less spherical and smaller ice particles probably due to reduced water vapor deposition on the particle surface. The cirrus optical properties presented weak dependence on ambient temperature and wind conditions. Over the 10 years of the analysis, no clear temporal trend was found and the seasonal cycle was not pronounced. However, winter cirrus appeared under colder conditions and stronger winds. Moreover, they were optically-thicker, less absorbing and consisted of relatively more spherical ice particles.

A positive CRE^{net} was primarily found for a broad range of representative cirrus cloud properties and ambient conditions over Ny-Ålesund. Only for high COD (above 10) and over tundra a negative CRE^{net} was estimated, which did not hold true over snow/ice surfaces. Consequently, the COD in combination with the surface albedo seemed to play the most critical role in determining the CRE sign over the high European Arctic. In the future, the cirrus properties can be incorporated into a comprehensive radiative transfer model in order to estimate the CRE in a vertically-resolved manner, which can subsequently be compared to estimates from regional climate and general circulation models.

A

CIRRUS DETECTION SENSITIVITIES

A.1 Wavelet Covariance Transform - dilation sensitivity

Since the WCT dilation is an important parameter for cirrus detection (section 4.1.2), a relevant sensitivity analysis is performed here. Thanks to the high vertical resolution (7.5 m) of KARL signals, small dilation values between 30 m and 120 m were explored, presented with different symbols in Fig. A.1. After analyzing a significant number of cirrus layers, it was observed that dilation values smaller than 90 m were less sensitive to smooth-shaped cirrus layers, as shown in Fig. A.1b (smooth signal gradients close to C_{top}). On the contrary, the 90 m dilation was more effective for faint layers and efficiently captured layers thinner than 200 m, as for 9:15–11:15 UT on 23 January 2019 (Fig. A.1a). Detecting faint layers near the C_{base} is important, since the multiple scattering effect is higher there (Wandinger, 1998). Overall, the discrepancies arising from the dilation selection were low, with the majority of inter-dilation spread being less than 50 m.

A.2 Wavelet Covariance Transform - wavelength dependency

The dependency of cirrus detection on wavelength was assessed in terms of the dynamic and static WCT methods. Since the SNR depends on background illumination conditions, both daytime (25 April 2015, Fig. A.2a) and night-time (23 January 2019, Fig. A.2b) cirrus clouds were investigated. In Fig. A.2a and A.2b the dynamic (circle symbols) and static (dot symbols) WCT derived boundaries are demonstrated for different wavelengths. The 355 nm channel with parallel polarization (355_p, cyan symbols) was not as sensitive to faint cirrus layers as the other wavelengths due to the strong Rayleigh scattering in the ultraviolet (Fig. A.2b, for example at 9:15–10:00 UT). This behavior was more pronounced for the static WCT method. Concerning the 355 nm channel with perpendicular polarization (355_s, black symbols), it was strongly affected by noise during daytime (Fig. A.2a) and noise peaks were frequently detected even with increased $SNR\ ratio$ thresholds. In the 532_p channel (green symbols) both the static and dynamic methods mostly detected the stronger cirrus parts (Fig. A.2a, for example at 14:00–16:00 UT).

The selected cirrus layer of Fig. A.2c was characterized by smooth-shaped C_{base} and strong-shaped C_{top}. Therefore, the discrepancies across different wavelengths were larger for the C_{base}. The static (dotted lines) and dynamic (dashed lines) WCT derived boundaries are given for the different channels. The 355_p and 532_p channels mostly detected the strongest cirrus parts. In contrast, the 355_s, 532_s (light green symbols) and 1064 nm

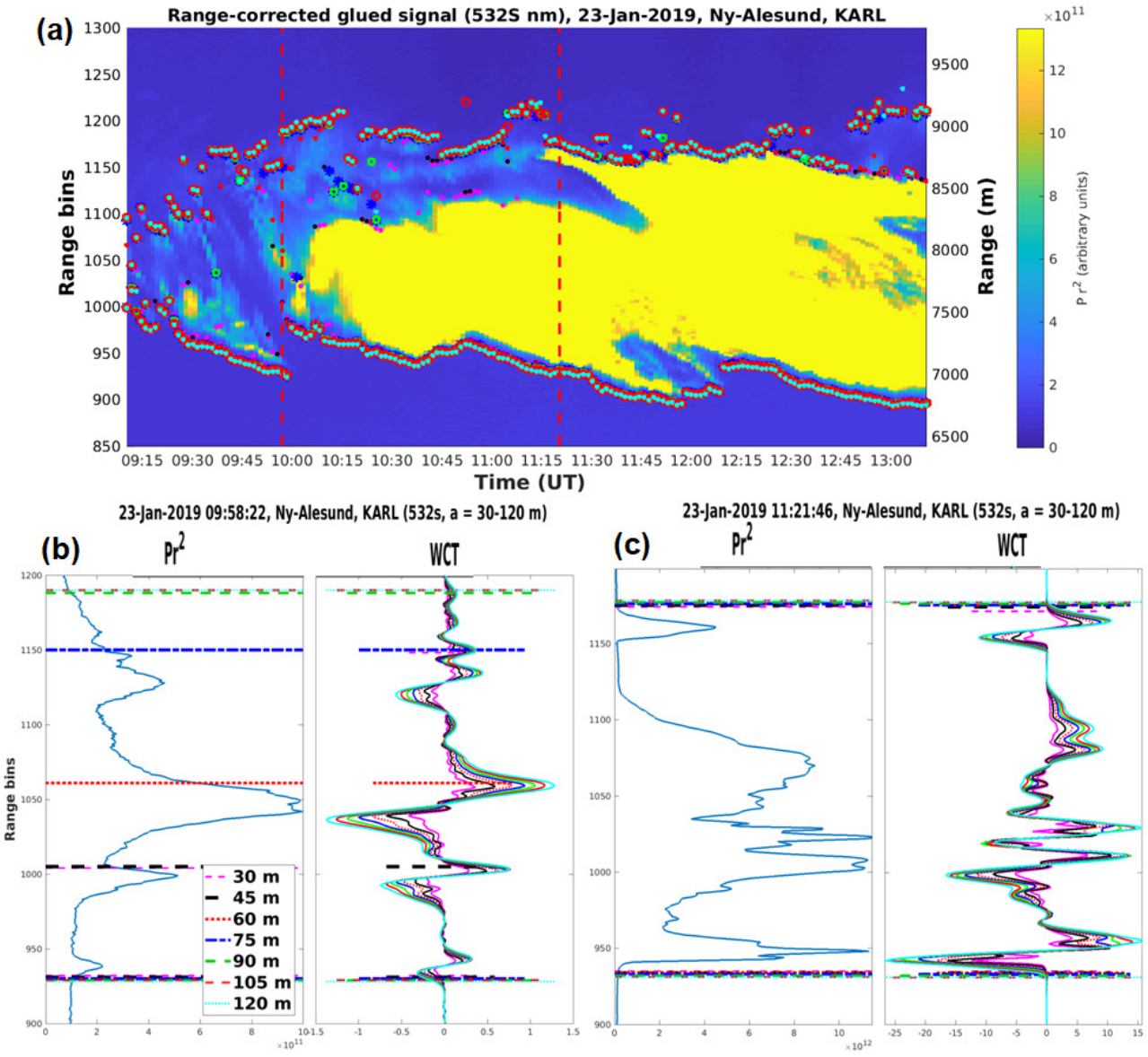

Fig. A.1: Lidar signal with overlaid C_{base} and C_{top} resulting from different dilation values (a). Selected profiles (red vertical lines) are presented in panels (b) and (c).

(red symbols) channels were more sensitive to faint marginal parts and showed better inter-agreement, especially in the dynamic method. Moreover, the SNR of the perpendicular polarization channels was higher compared to those with parallel polarization and the SNR_{532} was higher than SNR_{355}. In general, longer wavelengths perform better in discriminating clouds from aerosol. However, KARL records 1064 nm signals in analog mode, which is more prone to noise (Sec. 2.2.1).

For the aforementioned reasons, the 532_s channel was finally selected for cirrus detection as the highest quality channel. It should be mentioned, however, that under specific conditions the 532_s derived boundaries also presented variability. For instance, fluctuating geometrical boundaries can be seen at 10:00–10:30 UT (Fig. A.2b) due to weak gradients, especially close to the C_{top}. Variability was also found during 12:30–13:00 UT (Fig. A.2b), with

weak signal gradients overhead of strong ones. The variability was lower for the temporally-averaged signals thanks to higher SNR (see Fig. 4.5).

The proposed thresholds of $|WCT/std|$ and *SNR ratio* are summarized in Table A.1. The *SNR ratio* was investigated separately at C_{base} and C_{top} due to changes in the signal noise, with stricter ratios prescribed at C_{top}. Due to higher noise, stricter *SNR ratios* were selected for 1064 nm and daytime 355_s profiles. Less strict thresholds were assigned to the finally selected 532_s channel. The proposed thresholds worked well for cirrus clouds appearing in different altitudes. A sensitivity test is recommended before applying the *SNR ratio* thresholds to systems with different specifications than KARL, since the SNR is dependent on the operating wavelength, averaging time and background illumination conditions. A sensitivity on the $|WCT/std|$ threshold does not seem necessary as this parameter displayed high stability for different wavelengths and averaging periods.

Tab. A.1: Proposed dynamic $|WCT/std|$ and *SNR ratio* thresholds for each channel. Static thresholds from Baars et al. (2016) are also given.

	WCT threshold		**SNR ratio threshold**		**SNR**
channel (nm)	**dynamic**	**static**	**dynamic** C_{base}	**dynamic** C_{top}	**static**
355_p	$\|WCT/std\|$ >1	0.1	1.1	1.2	>2
355_s	$\|WCT/std\|$ >1	0.1	1.2 (d) / 1.1 (n)	1.5 (d) / 1.2 (n)	>2
532_p	$\|WCT/std\|$ >1	0.3	1.1	1.3	>2
532_s	$\|WCT/std\|$ >1	0.3	1.1	1.2	>2
1064	$\|WCT/std\|$ >1	0.3	1.2	1.5	>2

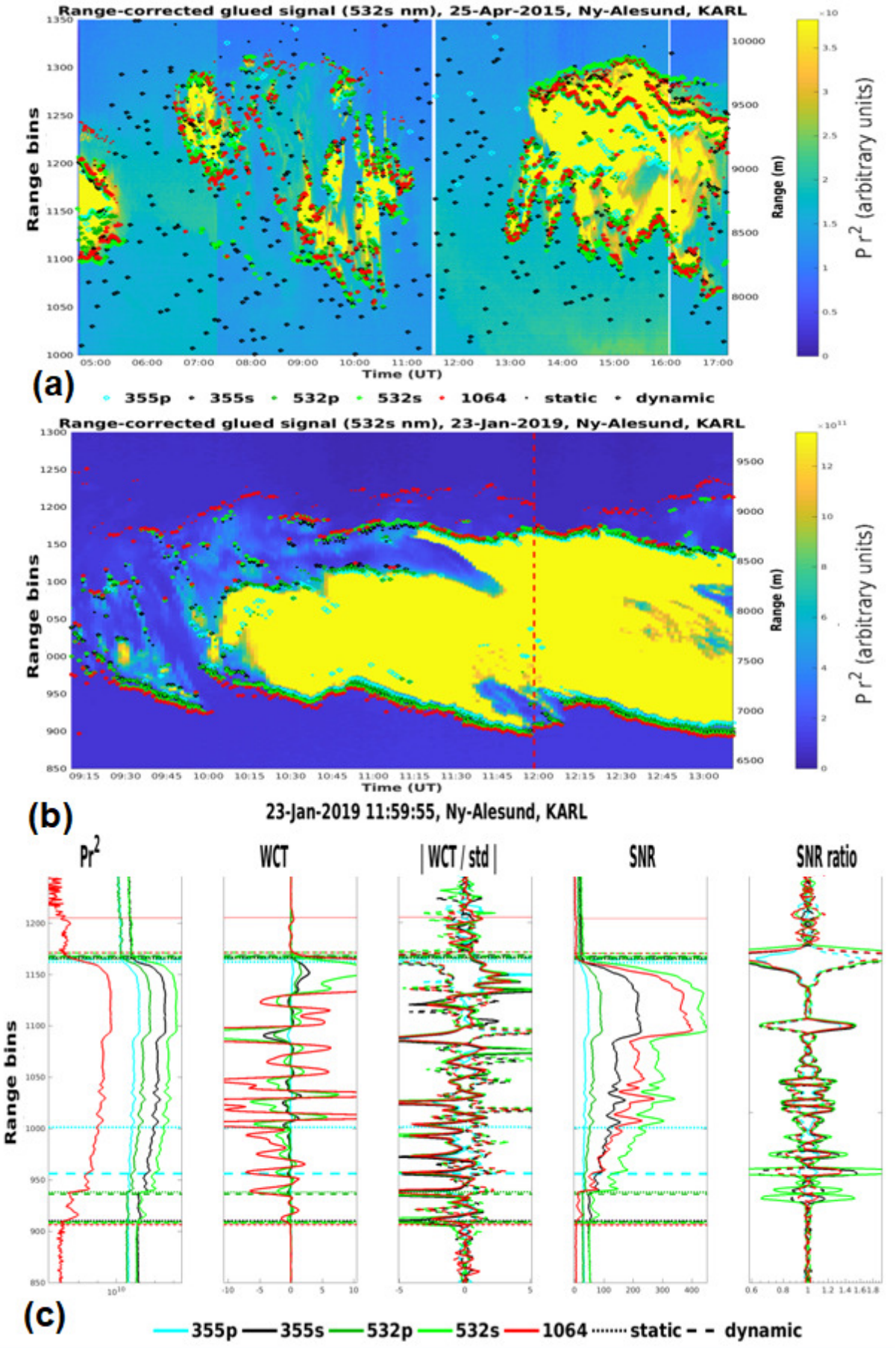

Fig. A.2: Lidar signal for daytime (a) and night-time (b) cirrus clouds with overlaid the geometrical boundaries as derived by the dynamic (circle symbols) and static (dot symbols) methods. Selected profiles are presented together with the dynamic (dashed lines) and static (dotted lines) WCT derived boundaries (c). The 532_s channel was finally selected for cirrus detection.

B

CIRRUS OPTICAL CHARACTERIZATION SENSITIVITIES

B.1 Reference value accuracy and limitations

The cirrus cloud of 23 January 2019 was selected for assessing the accuracy and inherent uncertainties of *constrained Klett* as it comprised different COD regime layers. Concerning the *reference value* (Sec. 4.3.3), it was first calculated from a cloud-free profile ($BSR_{ref}^{cloud-free}$) observed at 7:47–7:56 UT prior to the cirrus cloud passing over Ny-Ålesund. The BSR_{ref} accuracy was evaluated by estimating the same quantity via the Raman technique (BSR_{ref}^{Raman}). This analysis is illustrated in Fig. B.1. The blue line and shaded area (median $\pm$ standard deviation) denote the $BSR_{ref}^{cloud-free}$, while the BSR_{ref}^{Raman} (black symbols) are also presented. At 355 nm (532 nm, not shown) the $BSR_{ref}^{cloud-free}$ amounted to 1.03 ± 0.03 (1.07 ± 0.02), while the BSR_{ref}^{Raman} was equal to 1.06 ± 0.01 (1.06 ± 0.02). Thus, the $BSR_{ref}^{cloud-free}$ and BSR_{ref}^{Raman} were in agreement within the range of uncertainties, this being satisfactory, taking into account the high Raman statistical uncertainties especially for fine temporal scales (here 9 min).

The BSR_{ref} was also estimated from the minimum β_{int} profile (using the initial guess Klett, Sec. 4.3.3) in order to represent the scenario of no cloud-free profile availability. However, in this scenario the BSR_{ref} accuracy is subject to an upper COD limit. More specifically, the higher the cirrus COD the less accurate is the BSR_{ref}^{guess} expected to be, since the impact of a wrongly assumed LR_{ci} on the solution will be higher. In order to assess the effect of COD on the BSR_{ref}^{guess} (blue symbols) accuracy, a comparison to the BSR_{ref}^{Raman} was performed for every single profile of the 23 January 2019 case. Then, it was assessed up to which COD the BSR_{ref}^{guess} accuracy was acceptable. More specifically, the statistical uncertainty of the $BSR_{ref}^{cloud-free}$ (0.03) was considered as acceptable. As demonstrated in Fig. B.1, right axis, a sufficiently accurate BSR_{ref}^{guess} was obtained for COD up to 0.2. This is illustrated more clearly on the upper left inset figure, with the BSR_{ref}^{guess} lying within the $BSR_{ref}^{cloud-free}$ uncertainty (dashed line) for COD up to 0.2. Thus, even when profiles with COD up to 0.2 were selected, instead of a cloud-free profile, the resulting BSR_{ref}^{guess} agreed well enough with the $BSR_{ref}^{cloud-free}$ and BSR_{ref}^{Raman}.

A side remark concerns the aerosol content stability beneath the cirrus cloud, which is assumed in the constrained and double-ended Klett retrievals. As displayed in Fig. B.1, the BSR_{ref}^{Raman} mostly lied within the uncertainty of the $BSR_{ref}^{cloud-free}$, indicating that the stability assumption was valid. Finally, it should be clarified that the above discussed upper COD

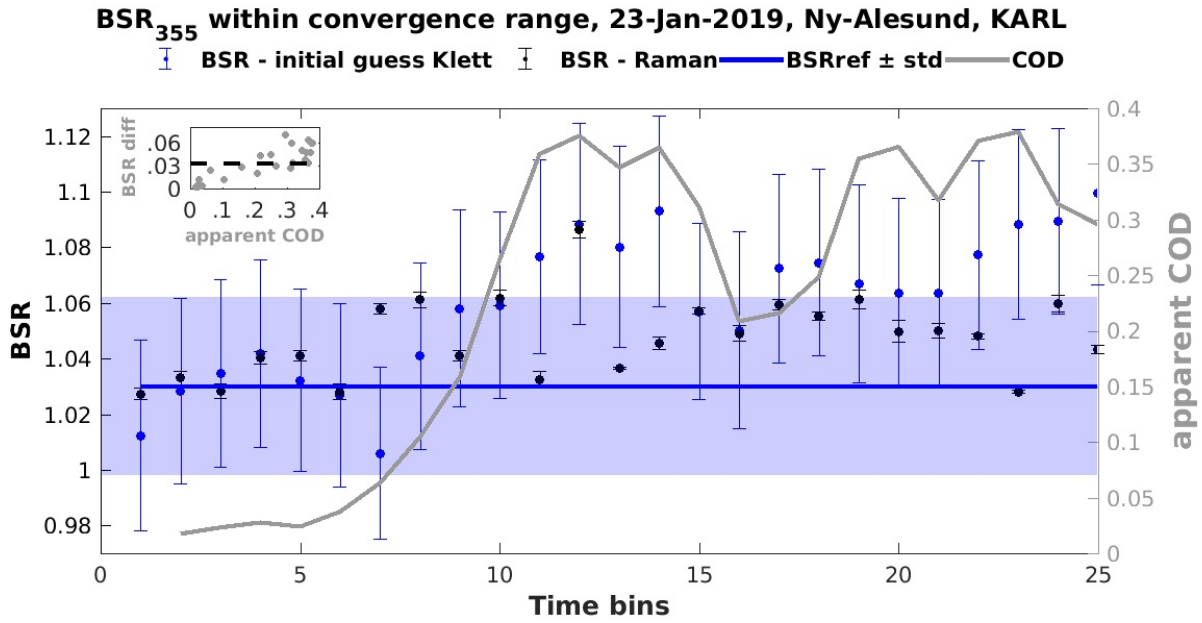

Fig. B.1: BSR_{ref}^{355} (median ± standard deviation) as derived by the initial guess Klett and Raman retrievals (BSR_{ref}^{Raman} errorbars are smaller due to a 75 m-smoothing of the BSR profile). The $BSR_{ref}^{cloud-free}$ (blue line and shaded area) is also provided from a preceding cloud-free profile. The apparent COD is given on the right axis. The difference between BSR_{ref}^{guess} and $BSR_{ref}^{cloud-free}$ versus the apparent COD are presented in the upper left inset figure. More details are given in the text.

limit only concerns the *reference value* estimation. Once a sufficiently accurate *reference value* is obtained, the *constrained Klett* can be applied on any cirrus cloud regime.

B.2 Inherent uncertainties of constrained Klett

In order to assess the inherent uncertainties of the *constrained Klett* method, the response of optical properties to the parameters of *convergence percentage* and *reference value* was investigated. In the first sensitivity analysis (Fig. B.2a) the *convergence percentage* was modified between 0.1% and 0.5%, with 0.3% being the control value. The LR_{ci} of optically-thinner layers was more sensitive (10% maximum spread or 3 sr) compared to thicker layers (5% maximum spread). Overall, the COD was modified by less than 0.004 (1–10% spread depending on the COD). Less strict *convergence percentages* (higher than 1%, not shown) were not capable of adjusting the LR_{ci} (see Eq. 4.3) with acceptable accuracy.

The impact of BSR_{ref} statistical uncertainties was also evaluated (Fig. B.2b). In the control case, the median value (BSR_{ref} = 1.03) was used, while in the perturbed cases the BSR_{ref} was increased by 0.01 (blue symbols), 0.02 (gray symbols) and 0.03 (cyan symbols). Such uncertainties were typically encountered during the analysis of different cirrus clouds (2011-2020) over Ny-Ålesund. Low COD layers (time bins 1–5) were more sensitive to the BSR_{ref} perturbations and when the BSR_{ref} was perturbed too far from the control case, it was not

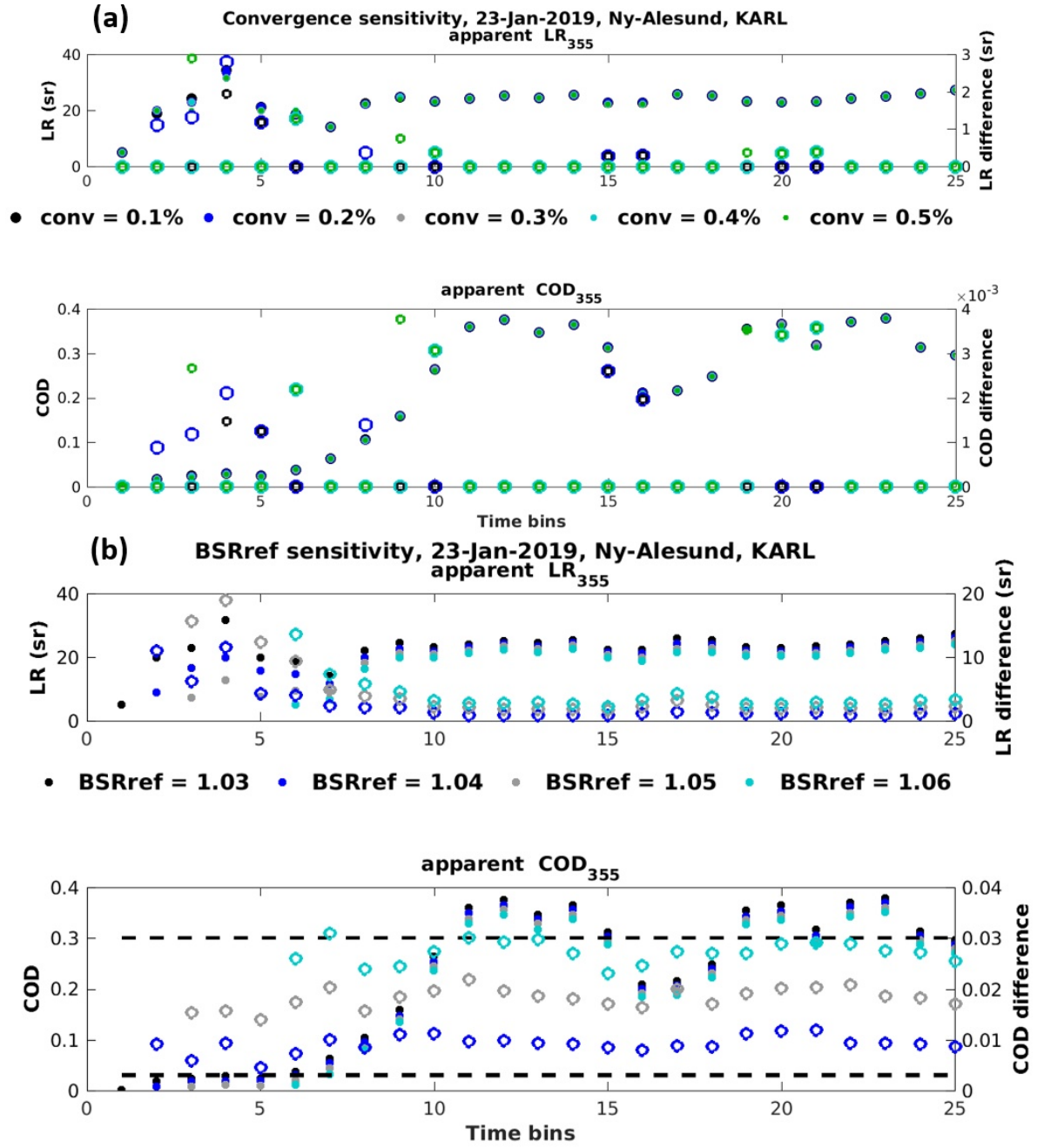

Fig. B.2: Sensitivity of optical properties to the *convergence percentage* (a) and the *reference value* (BSR_{ref}, b) parameters. Absolute differences with respect to the control case (open symbols) refer to the right axis. Dashed horizontal lines denote the optically-thin and sub-visible COD regimes.

always possible to obtain reasonable results. Therefore, an accurate *reference value* is crucial. The sensitivity of optically-thinner layers was higher in terms of LR_{ci} (60–74% or 14–19 sr). For opaque layers lower sensitivity (less than 13% or 3 sr) was found. The COD sensitivity was higher in the lower optically-thin and opaque regimes, varying between 0.02 and 0.03 (7–50% with respect to control values of 0.3 and 0.06) for the highest perturbed case (cyan symbols).

MULTIPLE-SCATTERING CORRECTION FOR CIRRUS CLOUDS

Comparison of analytical and simplified approaches

The MSC was performed for quality-assured cirrus layers (see Sec. 5.2) using the analytical model of Eloranta (1998) (Sec. 2.4.4). The MSC was also estimated from the simplified approach of Platt (1973) (Sec. 2.4.4). In Fig. C.1 the MSC LR_{ci} and COD as derived from the two approaches are presented. The comparison for different cirrus regimes is summarized in Tab. C.1.

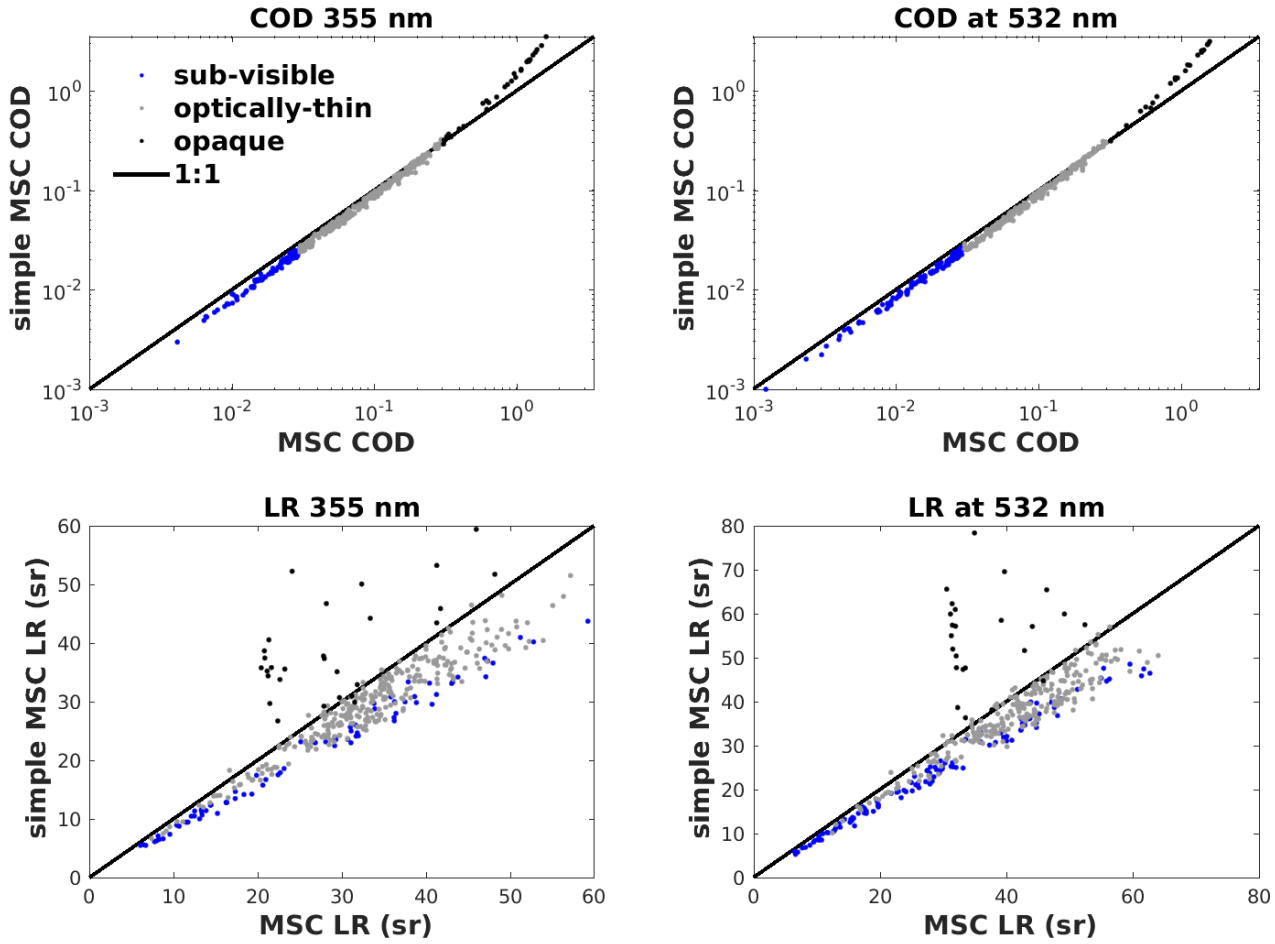

Fig. C.1: MSC COD and LR_{ci} as derived from the simplified and analytical approaches. The different cirrus regimes (based on the analytical approach) are color indicated.

For sub-visible and optically-thin cirrus layers (blue and gray symbols, respectively), the simplified approach underestimated the multiple-scattering contribution. This means that

Tab. C.1: Overview of MSC properties as derived by the analytical and simplified approaches. The differences are calculated with respect to the analytical approach. The classification into cirrus regimes is also based on the analytical approach.

sub-visible	**LR355**	**LR532**	**COD355**	**COD532**
analytical approach	26 ± 13 sr	29 ± 14 sr	0.019 ± 0.007	0.018 ± 0.008
simplified approach	21 ± 10 sr	24 ± 12 sr	0.016 ± 0.006	0.015 ± 0.007
absolute difference	5 ± 3 sr	5 ± 3 sr	0.004 ± 0.002	0.003 ± 0.002
percentage difference	***19 ± 5%***	***17 ± 5%***	***19 ± 5%***	***17 ± 5%***

optically-thin	**LR355**	**LR532**	**COD355**	**COD532**
analytical approach	34 ± 9 sr	41 ± 10 sr	0.11 ± 0.07	0.11 ± 0.07
simplified approach	30 ± 8 sr	37 ± 9 sr	0.1 ± 0.06	0.1 ± 0.07
absolute difference	4 ± 3 sr	4 ± 3 sr	0.009 ± 0.007	0.008 ± 0.007
percentage difference	***11 ± 6%***	***10 ± 7%***	***11 ± 6%***	***10 ± 7%***

opaque	**LR355**	**LR532**	**COD355**	**COD532**
analytical approach	29 ± 8 sr	37 ± 7 sr	0.87 ± 0.41	1.03 ± 0.45
simplified approach	39 ± 9 sr	55 ± 10 sr	1.34 ± 0.88	1.73 ± 1.1
absolute difference	−10 ± 7 sr	−8 ± 12 sr	−0.47 ± 0.49	−0.71 ± 0.7
percentage difference	***−40 ± 32%***	***−54 ± 36%***	***−40 ± 32%***	***−54 ± 36%***

even for cirrus layers with low COD, a correction that is solely based on the COD is not sufficient. Moreover, the relative difference was higher for the sub-visible regime (19 $\pm$ 5% at 355 nm and 17 $\pm$ 5% at 532 nm) in comparison to the optically-thin regime (11 $\pm$ 6% at 355 nm and 10 $\pm$ 7% at 532 nm, Tab. C.1). In contrast, for the opaque regime (black symbols) the simplified approach overestimated the MSC optical properties. The relative difference with respect to the analytical approach amounted to -40 ± 32% at 355 nm and -54 ± 36% at 532 nm. Thus, the simplified MSC bias is higher for the opaque regime both in absolute and relative terms. In conclusion, taking into account solely the COD for performing the MSC is not an accurate approach, especially in the opaque regime.

D

SEASONAL CIRRUS PROPERTIES: DESCRIPTIVE STATISTICS

Tab. D.1: Total and seasonal descriptive statistics of cirrus layer properties. If not stated otherwise, the median ± standard deviation is given.

Geometrical and optical properties					
	total	**winter**	**spring**	**summer**	**autumn**
GT (km)	1.9 ± 0.6	2.1 ± 1.3	1.9 ± 1.2	1.4 ± 0.9	1.4 ± 0.9
C_{base} (km)	7.3 ± 1.2	7.4 ± 1.1	6.8 ± 1.2	8.4 ± 0.8	8.2 ± 1.4
C_{top} (km)	9.6 ± 1.2	9.9 ± 1.3	9.4 ± 1	9.9 ± 0.7	9.2 ± 1.1
COD_{355}	0.07 ± 0.24	0.14 ± 0.36	0.06 ± 0.11	0.07 ± 0.07	0.07 ± 0.15
mean COD_{355}	0.14	0.25	0.09	0.09	0.12
COD_{532}	0.07 ± 0.26	0.12 ± 0.4	0.05 ± 0.11	0.07 ± 0.07	0.05 ± 0.14
mean COD_{532}	0.14	0.26	0.08	0.09	0.1
LR_{355}^{high} (sr)	33 ± 9	31 ± 7	33 ± 9	37 ± 11	41 ± 9
LR_{532}^{high} (sr)	42 ± 10	38 ± 9	43 ± 10	42 ± 13	43 ± 8
$LPDR_{355}^{high}$ (%)	15 ± 5	13 ± 5	14 ± 3	17 ± 6	22 ± 4
CR^{high}	1.4 ± 0.2	1.3 ± 0.2	1.5 ± 0.2	1.3 ± 0.2	1.4 ± 0.1
Meteorological properties					
Temper. (^oC)	**total**	**winter**	**spring**	**summer**	**autumn**
layer median	−57 ± 6	−61 ± 5	−56 ± 5	−44 ± 4	−53 ± 3
at C_{base}	−48 ± 6	−51 ± 7	−47 ± 5	−38 ± 3	−48 ± 4
at C_{top}	−65 ± 7	−66 ± 6	−66 ± 6	−49 ± 5	−57 ± 3
Winsp (ms^{-1})	**total**	**winter**	**spring**	**summer**	**autumn**
layer median	12 ± 6	23 ± 5	10 ± 4	9 ± 1	4 ± 9
at C_{base}	9 ± 6	18 ± 6	8 ± 4	9 ± 1	5 ± 8
at C_{top}	14 ± 7	28 ± 6	13 ± 4	9 ± 1	10 ± 9
Wind dir. (^{o})	**total**	**winter**	**spring**	**summer**	**autumn**
layer median	238 ± 85	243 ± 87	242 ± 77	57 ± 88	108 ± 216
median sector (-std, +std)	W/SW (S/SE–NW)	W/SW (S/SE–N/NW)	W/SW (S/SE–NW)	E/NE (N/NW–S/SE)	E/SE (NW–W/SW)

ACKNOWLEDGMENTS

After three years my PhD journey has come to an end. First of all, I would like to thank the people (Dr. Roland Neuber, Dr. Marion Maturilli and Dr. Christoph Ritter) that selected me for working on this exciting project, which made me develop professionally and personally. Besides this, I appreciate their constructive guidance, which broadened my scientific and personal perspective. At this point, I would also like to thank the additional members of my Thesis Advisory Committee (Dr. Elina Giannakaki, Dr. Mika Komppula and Prof. Markus Rex). I would also like to thank Prof. Christine Böckmann for training me on the aerosol microphysics algorithms and the kind way of sharing her knowledge with me.

The two measurement campaigns at Ny-Ålesund were rather the highlights of my PhD journey. The first person I am grateful to is Wilfried Ruhe for his intensive KARL operation training and for teaching me that hard work can be perfectly combined with fun. I would like to thank Dr. Mauro Mazzola and Prof. David Cappelletti for their friendly cooperation and provision of the tethered-balloon aerosol measurements. Of course, I couldn't forget the people I met (Rudy, Greg, Fieke, Gwen and many others) at Ny-Ålesund and the nice moments we spent there.

Another important stop of my journey was Warsaw, where I did my short-term research stay. First of all, I am grateful to the research grant of POLMAR that made this stay possible. Moreover, I want to thank Prof. Iwona Stachlewska for accepting me as a guest member of the Remote Sensing Laboratory and supporting me. Her guidance and mentoring played an important role in the rest of my journey.

At this point, I want to acknowledge the contribution and support of my co-authors. Two other contributions were those of Dr. Bärbel and Dr. Gunthner Tress. Their training on facing the challenges of a PhD and writing scientific articles made my route to PhD completion smoother and more productive. Coming closer to the end of the journey, I would like to thank Prof. Lucas Alados–Arboledas for his willingness to review my dissertation. Additionally, I am grateful to Prof. Frank Spahn, Prof. Christine Böckmann and Prof. Ricarda Winkelmann for accepting to be part of my Examination Board.

Reaching the final destination wouldn't have been possible without the support of my family and friends (especially Sofia) from Greece. Their encouragement was a vital source of motivation. In my new life in Germany, I couldn't have a better company than my partner Vasilis, who was my biggest supporter and helped me overcome any obstacle. Moreover, I want to thank my friendly colleagues (Kati, Sandro, Raphael, Daniela, Johannes and others), especially my office-mate Ralf for always having an answer to my questions. I also want to thank Mrs. Sabine Helbig for the loads of administrative support and Mrs. Siggi Debatin for taking such good care of us. For the end, I couldn't forget to thank my friends (Sara, Helene, Adrien and others) for the nice memories we created together in Potsdam.

The long-term support and technical development of KARL by Impres GmbH (Wilfried Ruhe and Ingo Beninga) are more than appreciated. I thank the ICARE Data and Services Center for providing access to the CALIOP data. I gratefully acknowledge the funding by the Deutsche Forschungsgemeinschaft (DFG, German Research Foundation) - Project Number 268020496 - TRR 172, within the Transregional Collaborative Research Center - ArctiC Amplification: Climate Relevant Atmospheric and SurfaCe Processes, and Feedback Mechanisms $(AC)^3$.

ACRONYMS

AMALi	Air-borne Mobile Aerosol lidar
AOD	Aerosol Optical Depth
APD	Avalanche Photodiode
ARE	Aerosol Radiative Effect
BSRN	Baseline Surface Radiation Network
CALIOP	Cloud-Aerosol lidar with Orthogonal Polarization
CALIPSO	Cloud-Aerosol lidar and Infrared Pathfinder Satellite Observations
CCN	Cloud Condensation Nuclei
COD	Cloud Optical Depth
CR	Color Ratio
CRE	Cloud Radiative Effect
FOV	Field of View
GT	Geometrical Thickness
HR	Heating Rate
INPs	Ice Nucleating Particles
KARL	Koldewey Aerosol Raman lidar
LPDR	Linear Particle Depolarization Ratio
LR	Lidar Ratio
MSC	Multiple Scattering Correction
PMT	Photomultiplier Tube
SNR	Signal to Noise Ratio
SZA	solar zenith angle
TOA	Top of The Atmosphere
WCT	Wavelet Covariance Transform

LIST OF TABLES

LIST OF FIGURES

BIBLIOGRAPHY

Acosta Navarro, J.C. et al. (2016). "Amplification of Arctic warming by past air pollution reductions in Europe." In: *Nat. Geosci.* 9.4, pp. 277–281.

Alexandrov, M. D. et al. (2004). "Automated cloud screening algorithm for MFRSR data." In: *Geophys. Res. Lett.* 31.4.

Ansmann, A., M. Riebesell, and C. Weitkamp (1990). "Measurement of atmospheric aerosol extinction profiles with a Raman lidar." In: *Opt. Lett.* 15.13, pp. 746–748.

Ansmann, A. et al. (1992). "Independent measurement of extinction and backscatter profiles in cirrus clouds by using a combined Raman elastic-backscatter lidar." In: *Appl. Opt.* 31.33, pp. 7113–7131.

Arnold, S. R. et al. (2016). "Arctic air pollution: Challenges and opportunities for the next decadeArctic air pollution: Challenges and opportunities for the next decade." In: *Elementa: Sci. Anthrop.* 4.

Avery, M. A. et al. (2020). "CALIOP V4 cloud thermodynamic phase assignment and the impact of near-nadir viewing angles." In: *Atmos. Meas. Tech.* 13.8, pp. 4539–4563.

Baars, H. et al. (2008). "Continuous monitoring of the boundary-layer top with lidar." In: *Atmos. Chem. Phys.*

Baars, H. et al. (2016). "An overview of the first decade of PollyNET: an emerging network of automated Raman-polarization lidars for continuous aerosol profiling." In: *Atmos. Chem. Phys.* 16, pp. 5111–5137.

Behrendt, A. and T. Nakamura (2002). "Calculation of the calibration constant of polarization lidar and its dependency on atmospheric temperature." In: *Opt. Express* 10.16, pp. 805–817.

Bellouin, N. et al. (2020a). "Bounding global aerosol radiative forcing of climate change." In: *Rev. Geophys.* 58.1, e2019RG000660.

Bellouin, N. et al. (2020b). "Radiative forcing of climate change from the Copernicus reanalysis of atmospheric composition." In: *Earth Sys. Sci. Data* 12.3, pp. 1649–1677.

Block, K. et al. (2020). "Climate models disagree on the sign of total radiative feedback in the Arctic." In: *Tellus A: Dynamic Meteorology and Oceanography* 72.1, pp. 1–14.

Böckmann, C. (2001). "Hybrid regularization method for the ill-posed inversion of multiwavelength lidar data in the retrieval of aerosol size distributions." In: *Appl. Opt.* 40.9, pp. 1329–1342.

Böckmann, C. and A. Kirsche (2006). "Iterative regularization method for lidar remote sensing." In: *Comput. Phys. Commun.* 174.8, pp. 607–615.

Borovoi, A. et al. (2014). "Layers of quasi-horizontally oriented ice crystals in cirrus clouds observed by a two-wavelength polarization lidar." In: *Opt. Express* 22.20, pp. 24566–24573.

Breider, T. J. et al. (2017). "Multidecadal trends in aerosol radiative forcing over the Arctic: Contribution of changes in anthropogenic aerosol to Arctic warming since 1980." In: *J. Geophys. Res. Atmos.* 122.6, pp. 3573–3594.

Brooks, I. M. (2003). "Finding boundary layer top: Application of a wavelet covariance transform to lidar backscatter profiles." In: *J. Atmos. Ocean. Technol.* 20.8, pp. 1092–1105.

Burton, S. et al. (2013). "Aerosol classification from airborne HSRL and comparisons with the CALIPSO vertical feature mask." In: *Atmos. Meas. Tech.* 6.5, pp. 1397–1412.

Campbell, J. R. et al. (2018). "Unusually deep wintertime cirrus clouds observed over the Alaskan subarctic." In: *Bull. Am. Meteorol. Soc.* 99.1, pp. 27–32.

Campbell, J. R. et al. (2021). "Cirrus cloud top-of-the-atmosphere net daytime forcing in the Alaskan subarctic from ground-based MPLNET monitoring." In: *J. Appl. Meteorol. Climatol.* 60.1, pp. 51–63.

Ceccaldi, M. et al. (2013). "From CloudSat-CALIPSO to EarthCare: Evolution of the DARDAR cloud classification and its comparison to airborne radar-lidar observations." In: *J. Geophys. Res. Atmos.* 118.14, pp. 7962–7981.

Chen, W. N., C. W. Chiang, and J. B. Nee (2002). "Lidar ratio and depolarization ratio for cirrus clouds." In: *Appl. Opt.* 41.30, pp. 6470–6476.

Collaud Coen, M. et al. (2020). "Multidecadal trend analysis of in situ aerosol radiative properties around the world." In: *Atmos. Chem. Phys.* 20.14, pp. 8867–8908.

Collis, R. (1966). "Lidar: a new atmospheric probe." In: *Q. J. R. Meteorol. Soc.* 92.392, pp. 220–230.

Corti, T. and T. Peter (2009). "A simple model for cloud radiative forcing." In: *Atmos. Chem. Phys.* 9.15, pp. 5751–5758.

Croft, B. et al. (2016). "Processes controlling the annual cycle of Arctic aerosol number and size distributions." In: *Atmos. Chem. Phys* 16.6, pp. 3665–3682.

D'Amico, G. et al. (2016). "EARLINET Single Calculus Chain–technical–Part 1: Pre-processing of raw lidar data." In: *Atmos. Meas. Tech.* 9.2, pp. 491–507.

Dahlke, S. and M. Maturilli (2017). "Contribution of atmospheric advection to the amplified winter warming in the Arctic North Atlantic region." In: *Adv. Meteorol.* 2017.

Dahlke, S. et al. (2020). "The observed recent surface air temperature development across Svalbard and concurring footprints in local sea ice cover." en. In: *Int. J. Climatol.* 40.12, pp. 5246–5265. ISSN: 0899-8418, 1097-0088. DOI: 10.1002/joc.6517.

Dall' Osto, M. et al. (2017). "Arctic sea ice melt leads to atmospheric new particle formation." In: *Sci. rep.* 7.1, pp. 1–10.

Dawson, K.W. et al. (2015). "Spaceborne observations of the lidar ratio of marine aerosols." In: *Atmos. Chem. Phys.* 15.6, pp. 3241–3255.

Del Guasta, M. (2001). "Simulation of LIDAR returns from pristine and deformed hexagonal ice prisms in cold cirrus by means of "face tracing"." In: *J. Geophys. Res. Atmos.* 106.D12, pp. 12589–12602.

Del Guasta, M. et al. (1993). "One year of cloud lidar data from Dumont d'Urville (Antarctica): 1. General overview of geometrical and optical properties." In: *J. Geophys. Res. Atmos.* 98.D10, pp. 18575–18587.

Delanoë, J. and R. J. Hogan (2010). "Combined CloudSat-CALIPSO-MODIS retrievals of the properties of ice clouds." In: *J. Geophys. Res. Atmos.* 115.D4. doi: https://doi.org/10.1029/2009JD012346.

Di Biagio, C. et al. (2018). "Sources, load, vertical distribution, and fate of wintertime aerosols north of Svalbard from combined V4 CALIOP data, ground-based IAOOS lidar observations and trajectory analysis." In: *J. Geophys. Res. Atmos.* 123.2, pp. 1363–1383.

Di Pierro, M., L. Jaeglé, et al. (2011). "Satellite observations of aerosol transport from East Asia to the Arctic: three case studies." In: *Atmos. Chem. Phys.* 11.5, p. 2225.

Di Pierro, M. et al. (2013). "Spatial and seasonal distribution of Arctic aerosols observed by the CALIOP satellite instrument (2006-2012)." In: *Atmos. Chem. Phys.* 13.14.

Dionisi, Davide et al. (2013). "Midlatitude cirrus classification at Rome Tor Vergata through a multichannel Raman–Mie–Rayleigh lidar." In: *Atmos. Chem. and Phys.* 13.23, pp. 11853–11868.

Donth, T. et al. (2020). "Combining atmospheric and snow radiative transfer models to assess the solar radiative effects of black carbon in the Arctic." In: *Atmos. Chem. Phys.* 20.13, pp. 8139–8156.

Doscher, R., T. Vihma, and E. Maksimovich (2014). "Recent advances in understanding the Arctic climate system state and change from a sea ice perspective: a review." In: *Atmos. Chem. Phys.* 14.24, pp. 13571–13600.

Ebell, K. et al. (2020). "Radiative effect of clouds at Ny-Ålesund, Svalbard, as inferred from ground-based remote sensing observations." In: *J. Appl. Meteorol. Climatol.* 59.1, pp. 3–22.

Eleftheriadis, K., S. Vratolis, and S. Nyeki (2009). "Aerosol black carbon in the European Arctic: measurements at Zeppelin station, Ny-Ålesund, Svalbard from 1998–2007." In: *Geophys. Res. Lett.* 36.2.

Eloranta, E. (1998). "Practical model for the calculation of multiply scattered lidar returns." In: *Appl. Opt.* 37.12, pp. 2464–2472.

Elouragini, S. and P. Flamant (1996). "Iterative method to determine an averaged backscatter-to-extinction ratio in cirrus clouds." In: *Appl. Opt.* 35.9, pp. 1512–1518.

Evangeliou, N. et al. (2016). "Wildfires in northern Eurasia affect the budget of black carbon in the Arctic – a 12-year retrospective synopsis (2002–2013)." In: *Atmos. Chem. Phys.* 16.12, pp. 7587–7604.

Fernald, F. G. (1984). "Analysis of atmospheric lidar observations: some comments." In: *Appl. Opt.* 23.5, pp. 652–653.

Ferrero, L. et al. (2019). "Aerosol optical properties in the Arctic: The role of aerosol chemistry and dust composition in a closure experiment between Lidar and tethered balloon vertical profiles." In: *Sci. Total Environ.* 686, pp. 452–467.

Flanner, M. G. et al. (2009). "Springtime warming and reduced snow cover from carbonaceous particles." In: *Atmos. Chem. Phys.* 9.7, pp. 2481–2497.

Fletcher, N. (1958). "Size effect in heterogeneous nucleation." In: *J. Chem. Phys.* 29.3, pp. 572–576.

Freud, E. et al. (2017). "Pan-Arctic aerosol number size distributions: seasonality and transport patterns." In: *Atmos. Chem. Phys.* 17.13.

Fu, Q. and K. N. Liou (1992). "On the correlated k-distribution method for radiative transfer in nonhomogeneous atmospheres." In: *J Atmos. Sci.* 49.22, pp. 2139–2156.

— (1993). "Parameterization of the radiative properties of cirrus clouds." In: *J Atmos. Sci.* 50.13, pp. 2008–2025.

Gagné, M., N. Gillett, and J. Fyfe (2015). "Impact of aerosol emission controls on future Arctic sea ice cover." In: *Geophys. Res. Lett.* 42.20, pp. 8481–8488.

Gagné, M. et al. (2017). "Aerosol-driven increase in Arctic sea ice over the middle of the twentieth century." In: *Geophys. Res. Lett.* 44.14, pp. 7338–7346.

Gamage, N. and C. Hagelberg (1993). "Detection and analysis of microfronts and associated coherent events using localized transforms." In: *J. Atmos. Sci.* 50.5, pp. 750–756.

Garrett, T., C. Zhao, and P. Novelli (2010). "Assessing the relative contributions of transport efficiency and scavenging to seasonal variability in Arctic aerosol." In: *Tellus B: Chem. Phys. Meteorol.* 62.3, pp. 190–196.

Giannakaki, E. et al. (2007). "Optical and geometrical characteristics of cirrus clouds over a Southern European lidar station." In: *Atmos. Chem. Phys.* 7, pp. 5519–5530.

Giannakaki, E. et al. (2016). "Optical and microphysical characterization of aerosol layers over South Africa by means of multi-wavelength depolarization and Raman lidar measurements." In: *Atmos. Chem. and Phys.* 16.13, pp. 8109–8123.

Gjelten, H. M. et al. (2016). "Air temperature variations and gradients along the coast and fjords of western Spitsbergen." In: *Polar Research* 35.1, p. 29878. DOI: 10.3402/polar.v35.29878.

Gouveia, D. A. et al. (2017). "Optical and geometrical properties of cirrus clouds in Amazonia derived from 1 year of ground-based lidar measurements." In: *Atmos. Chem. Phys.* 17, pp. 3619–3636.

Graßl, S. and C. Ritter (2019). "Properties of Arctic Aerosol Based on Sun Photometer Long-Term Measurements in Ny-Ålesund, Svalbard." In: *Remote Sens.* 11.11, p. 1362. ISSN: 2072-4292. DOI: 10.3390/rs11111362.

Groß, S. et al. (2013). "Aerosol classification by airborne high spectral resolution lidar observations." In: *Atmos. Chem. Phys.* 13.5, pp. 2487–2505.

Haarig, M. et al. (2017). "Dry versus wet marine particle optical properties: RH dependence of depolarization ratio, backscatter, and extinction from multiwavelength lidar measurements during SALTRACE." In: *Atmos. Chem. Phys.* 17.23, pp. 14199–14217.

Heymsfield, A. J. et al. (2017). "Cirrus clouds." In: *Meteorol. Monogr.* 58, pp. 2–1.

Hirdman, D. et al. (2010). "Long-term trends of black carbon and sulphate aerosol in the Arctic: changes in atmospheric transport and source region emissions." In: *Atmos. Chem. Phys.* 10.19, pp. 9351–9368. DOI: 10.5194/acp-10-9351-2010.

Hitschfeld, W. and J. Bordan (1954). "Errors inherent in the radar measurement of rainfall at attenuating wavelengths." In: *J Atmos. Sci.* 11.1, pp. 58–67.

Hoareau, C. et al. (2013). "A decadal cirrus clouds climatology from ground-based and spaceborne lidars above the south of France (43.9° N–5.7° E)." In: *Atmos. Chem. Phys.* 13.14, pp. 6951–6963.

Hoffmann, A. (2011). "Comparative aerosol studies based on multi-wavelength Raman LIDAR at Ny-Ålesund, Spitsbergen." PhD thesis.

Hoffmann, A. et al. (2009). "Ground-based lidar measurements from Ny-Alesund during ASTAR 2007: a statistical overview." In: *Atmos. Chem. Phys. Discuss* 9, pp. 15453–15510.

Hoffmann, A. et al. (2010). "Lidar measurements of the Kasatochi aerosol plume in August and September 2008 in Ny-Ålesund, Spitsbergen." In: *J. Geophys. Res. Atmos.* 115.D2.

Hunt, W. H. et al. (2009). "CALIPSO lidar description and performance assessment." In: *J. Atmos. Ocean. Technol.* 26.7, pp. 1214–1228.

Iarlori, M. et al. (2015). "Effective resolution concepts for lidar observations." In: *Atmos. Meas. Tech.* 8.12, pp. 5157–5176.

Illingworth, A. J. et al. (2015). "The EarthCARE satellite: The next step forward in global measurements of clouds, aerosols, precipitation, and radiation." In: *Bull. Am. Meteorol. Soc.* 96.8, pp. 1311–1332.

Jafariserajehlou, S. et al. (2019). "A cloud identification algorithm over the Arctic for use with AATSR–SLSTR measurements." In: *Atmos. Meas. Tech.* 12.2, pp. 1059–1076.

Janicka, L. et al. (2017). "Temporal variations in optical and microphysical properties of mineral dust and biomass burning aerosol derived from daytime Raman lidar observations over Warsaw, Poland." In: *Atmos. Environ.* 169, pp. 162–174.

Jocher, G. et al. (2015). "The sensible heat flux in the course of the year at Ny-Ålesund, svalbard: Characteristics of eddy covariance data and corresponding model results." In: *Adv. Meteorol.* 2015.

Josset, D. et al. (2012). "Cirrus optical depth and lidar ratio retrieval from combined CALIPSO-CloudSat observations using ocean surface echo." In: *J. Geophys. Res. Atmos.* 117.D5.

Kaleschke, L. et al. (2004). "Frost flowers on sea ice as a source of sea salt and their influence on tropospheric halogen chemistry." In: *Geophys. Res. Lett.* 31.16.

Kienast-Sjögren, E. et al. (2016). "Climatological and radiative properties of midlatitude cirrus clouds derived by automatic evaluation of lidar measurements." In: *Atmos. Chem. Phys.* 16.12, pp. 7605–7621.

Kim, M. H. et al. (2018). "The CALIPSO version 4 automated aerosol classification and lidar ratio selection algorithm." In: *Atmos. Meas. Tech.* 11.11, pp. 6107–6135.

Kinne, S. (2019). "Aerosol radiative effects with MACv2." In: *Atmos. Chem. Phys.* 19.16, pp. 10919–10959.

Klett, J. D. (1981). "Stable analytical inversion solution for processing lidar returns." In: *Appl. Opt.* 20.2, pp. 211–220.

Klonecki, A. et al. (2003). "Seasonal changes in the transport of pollutants into the Arctic troposphere-model study." In: *J. Geophys. Res. Atmos.* 108.D4.

Kokkalis, P. et al. (2020). "Application and Testing of the Extended-Kalman-Filtering Technique for Determining the Planetary Boundary-Layer Height over Athens, Greece." In: *Bound.-Layer Meteorol.* 176, pp. 125–147. DOI: https://doi.org/10.1007/s10546-020-00514-z.

Korhonen, H. et al. (2008). "A global model study of processes controlling aerosol size distributions in the Arctic spring and summer." In: *J. Geophys. Res. Atmos.* 113.D8.

Korolev, A. V., G. A. Isaac, and J. Hallett (1999). "Ice particle habits in Arctic clouds." In: *Geophys. Res. Lett.* 26.9, pp. 1299–1302.

Krämer, M. et al. (2016). "A microphysics guide to cirrus clouds–Part 1: Cirrus types." In: *Atmos. Chem. Phys.* 16.5, pp. 3463–3483.

Krämer, M. et al. (2020). "A microphysics guide to cirrus–Part 2: Climatologies of clouds and humidity from observations." In: *Atmos. Chem. Phys.* 20.21, pp. 12569–12608.

Kramshøj, M. et al. (2016). "Large increases in Arctic biogenic volatile emissions are a direct effect of warming." In: *Nat. Geosci.* 9.5, pp. 349–352.

Kübbeler, M. et al. (2011). "Thin and subvisible cirrus and contrails in a subsaturated environment." In: *Atmos. Chem. Phys.* 11.12, pp. 5853–5865.

Lanzante, J. R. (1996). "Resistant, robust and non-parametric techniques for the analysis of climate data: Theory and examples, including applications to historical radiosonde station data." In: *Int. J. Climatol.* 16.11, pp. 1197–1226.

Larroza, E. et al. (2013). "Towards an automatic lidar cirrus cloud retrieval for climate studies." In: *Atmos. Meas. Tech.* 6.11, pp. 3197–3210.

Law, K. S. and Andreas Stohl (2007). "Arctic air pollution: Origins and impacts." In: *Science* 315.5818, pp. 1537–1540.

Law, K. S. et al. (2017). "Local Arctic air pollution: Sources and impacts." In: *Ambio* 46.3, pp. 453–463.

Lawson, R. P. et al. (2019). "A review of ice particle shapes in cirrus formed in situ and in anvils." In: *J. Geophys. Res. Atmos.* 124.17-18, pp. 10049–10090.

Lisok, J. et al. (2016). "2014 iAREA campaign on aerosol in Spitsbergen–Part 1: Study of physical and chemical properties." In: *Atmos. Environ.* 140, pp. 150–166.

Liu, Z. et al. (2019). "Discriminating between clouds and aerosols in the CALIOP version 4.1 data products." In: *Atmos. Meas. Tech.* 12.1, pp. 703–734.

Lolli, S. et al. (2017a). "Daytime top-of-the-atmosphere cirrus cloud radiative forcing properties at Singapore." In: *J. Appl. Meteorol. Climatol.* 56.5, pp. 1249–1257.

Lolli, S. et al. (2017b). "Technical note: Fu–Liou–Gu and Corti–Peter model performance evaluation for radiative retrievals from cirrus clouds." In: *Atmos. Chem. Phys.* 17.11, pp. 7025–7034. DOI: 10.5194/acp-17-7025-2017.

Lolli, S. et al. (2018). "Impact of varying lidar measurement and data processing techniques in evaluating cirrus cloud and aerosol direct radiative effects." In: *Atmos. Meas. Tech.* 11.3, pp. 1639–1651.

Mace, G. G. et al. (2009). "A description of hydrometeor layer occurrence statistics derived from the first year of merged Cloudsat and CALIPSO data." In: *J. Geophys. Res. Atmos.* 114.D8.

Marquis, J. W. et al. (2017). "Estimating infrared radiometric satellite sea surface temperature retrieval cold biases in the tropics due to unscreened optically thin cirrus clouds." In: *J. Atmos. Ocean. Technol.* 34.2, pp. 355–373.

Massoli, P., M. Maturilli, and R. Neuber (2006). "Climatology of Arctic polar stratospheric clouds as measured by lidar in Ny-Ålesund, Spitsbergen (79° N, 12° E)." In: *J. Geophys. Res. Atmos.* 111.D9.

Mattis, I. et al. (2016). "EARLINET Single Calculus Chain–technical–Part 2: Calculation of optical products." In: *Atmos. Meas. Tech.* 9.7, pp. 3009–3029.

Maturilli, M. (2019a). "Basic and other measurements of radiation at station Ny-Ålesund (2019-01)." In: In: Maturilli, M (2020): Basic and other measurements of radiation at station Ny-Ålesund (2006-05 et seq). Alfred Wegener Institute - Research Unit Potsdam, PANGAEA, https://doi.org/10.1594/PANGAEA.914927. PANGAEA. DOI: 10.1594/PANGAEA.902116. URL: https://doi.org/10.1594/PANGAEA.902116.

— (2019b). *High resolution radiosonde measurements from station Ny-Ålesund (2019-01)*. https://doi.org/10.1594/PANGAEA.899965. data set. Alfred Wegener Institute - Research Unit Potsdam. DOI: 10.1594/PANGAEA.899965.

Maturilli, M., A. Herber, and G. König-Langlo (2013). "Climatology and time series of surface meteorology in Ny-Ålesund, Svalbard." In: *Earth Sys. Sci. Data* 5.1, pp. 155–163.

— (2015). "Surface radiation climatology for Ny-Ålesund, Svalbard (78.9 N), basic observations for trend detection." In: *Theor. Appl. Climatol.* 120.1, pp. 331–339.

Maturilli, M. and M. Kayser (2017). "Arctic warming, moisture increase and circulation changes observed in the Ny-Ålesund homogenized radiosonde record." In: *Theor. Appl. Climatol.* 130.1-2, pp. 1–17.

Mazzola, M. et al. (2016). "AGAP: an atmospheric gondola for aerosol profiling." In: *Rend. Lincei* 27.1, pp. 105–113.

Mei, L. et al. (2018). "The retrieval of ice cloud parameters from multi-spectral satellite observations of reflectance using a modified XBAER algorithm." In: *Remote Sens. Environ.* 215, pp. 128–144.

Mei, L. et al. (2020). "Retrieval of aerosol optical thickness in the Arctic snow-covered regions using passive remote sensing: impact of aerosol typing and surface reflection model." In: *IEEE T. Geosci. Remote*.

Monks, S. A. et al. (2015). "Multi-model study of chemical and physical controls on transport of anthropogenic and biomass burning pollution to the Arctic." en. In: *Atmos. Chem. Phys.* 15.6, pp. 3575–3603. ISSN: 1680-7324. DOI: 10.5194/acp-15-3575-2015.

Moroni, B. et al. (2018). "Mineralogical and chemical records of Icelandic dust sources upon Ny-Ålesund (Svalbard Islands)." In: *Front. Earth Sci.* 6, p. 187.

Müller, D. et al. (2016). "Microphysical particle properties derived from inversion algorithms developed in the framework of EARLINET." In: *Atmos. Meas. Tech.*

Najafi, M. R., Francis W Zwiers, and Nathan P Gillett (2015). "Attribution of Arctic temperature change to greenhouse-gas and aerosol influences." In: *Nat. Clim. Change* 5.3, pp. 246–249.

Nakoudi, K. and C. Ritter (2020). *AWI cirrus cloud retrieval scheme (v1.0.0)*. https://doi.org/10.5281/zenodo.4265007. Version v1.0.0. DOI: 10.5281/zenodo.4265007.

Nakoudi, K., I. S. Stachlewska, and C. Ritter (2021). "An extended lidar-based cirrus cloud retrieval scheme: first application over an Arctic site." In: *Opt. Express* 29.6, pp. 8553–8580.

Nakoudi, K. et al. (2019). "Planetary boundary layer height by means of lidar and numerical simulations over New Delhi, India." In: *Atmos. Meas. Tech.* 12.5, pp. 2595–2610.

Nakoudi, K. et al. (2020). "Does the Intra-Arctic Modification of Long-Range Transported Aerosol Affect the Local Radiative Budget?(A Case Study)." In: *Remote Sens.* 12.13, p. 2112.

Nazaryan, H., M. P. McCormick, and W. P. Menzel (2008). "Global characterization of cirrus clouds using CALIPSO data." In: *J. Geophys. Res. Atmos.* 113.D16.

Nicolae, D. et al. (2013). "Characterization of fresh and aged biomass burning events using multiwavelength Raman lidar and mass spectrometry." In: *J. Geophys. Res. Atmos.* 118.7, pp. 2956–2965.

Noel, V. and H. Chepfer (2010). "A global view of horizontally oriented crystals in ice clouds from Cloud-Aerosol Lidar and Infrared Pathfinder Satellite Observation (CALIPSO)." In: *J. Geophys. Res. Atmos.* 115.D4.

Nomokonova, T. et al. (2019). "Statistics on clouds and their relation to thermodynamic conditions at Ny-Ålesund using ground-based sensor synergy." In: *Atmo. Chem. Phys.* 19, pp. 4105–4126.

Ogren, J. A. et al. (2017). "Continuous light absorption photometer for long-term studies." In: *Atmos. Meas. Tech.* 10.12, pp. 4805–4818.

Ohneiser, K. et al. (2021). "Siberian fire smoke in the High-Arctic winter stratosphere observed during MOSAiC 2019–2020." In: *Atmos. Chem. Phys. Discuss.*, pp. 1–36.

Okamoto, H. et al. (2019). "Interpretation of lidar ratio and depolarization ratio of ice clouds using spaceborne high-spectral-resolution polarization lidar." In: *Opt. Express* 27.25, pp. 36587–36600.

— (2020). "Wavelength dependence of ice cloud backscatter properties for space-borne polarization lidar applications." In: *Opt. Express* 28.20, pp. 29178–29191.

Ortiz-Amezcua, P. et al. (2017). "Microphysical characterization of long-range transported biomass burning particles from North America at three EARLINET stations." In: *Atmos. Chem. Phys.* 17.9, pp. 5931–5946.

Osterloh, L. et al. (2011). "An adaptive base point algorithm for the retrieval of aerosol microphysical properties." In: *Open Atmospheric Sci. J.* 5.1.

Pandit, A. K. et al. (2015). "Long-term trend analysis and climatology of tropical cirrus clouds using 16 years of lidar data set over Southern India." In: *Atmos. Chem. Phys.* 15.24, pp. 13833–13848.

Platt, C. M . R. (1973). "Lidar and radiometric observations of cirrus clouds." In: *J. Atmos. Sci.* 30.6, pp. 1191–1204.

— (1979). "Remote sounding of high clouds: I. Calculation of visible and infrared optical properties from lidar and radiometer measurements." In: *J. Appl. Meteorol.* 18.9, pp. 1130–1143.

Quinn, PK et al. (2007). "Arctic haze: current trends and knowledge gaps." In: *Tellus B: Chem. Phys. Meteorol.* 59.1, pp. 99–114.

Rader, F. et al. (2021). "Overview of Aerosol Properties in the European Arctic in Spring 2019 Based on In Situ Measurements and Lidar Data." In: *Atmosphere* 12.2, p. 271.

Ritter, C. et al. (2016). "2014 iAREA campaign on aerosol in Spitsbergen–Part 2: Optical properties from Raman-lidar and in-situ observations at Ny-Ålesund." In: *Atmos. Environ.* 141, pp. 1–19.

Ritter, C. et al. (2018). "Microphysical properties and radiative impact of an intense biomass burning aerosol event measured over Ny-Ålesund, Spitsbergen in July 2015." In: *Tellus B: Chem. Phys. Meteorol.* 70.1, pp. 1–23.

Rothman, L. S. et al. (2003). "The HITRAN molecular spectroscopic database: edition of 2000 including updates through 2001." In: *J. Quant. Spectrosc. Radiat. Transf.* 82.1-4, pp. 5–44.

Rozanov, V. V. et al. (2014). "Radiative transfer through terrestrial atmosphere and ocean: Software package SCIATRAN." In: *J. Quant. Spectrosc. Radiat. Transf.* 133, pp. 13–71.

Ryaben'kii, V. S. and S. V. Tsynkov (2006). *A theoretical introduction to numerical analysis*. CRC Press, p. 243. ISBN: 9781584886075.

Samaras, S. et al. (2015). "Using Raman-lidar-based regularized microphysical retrievals and Aerosol Mass Spectrometer measurements for the characterization of biomass burning aerosols." In: *J. Comput. Phys.* 299, pp. 156–174.

Sand, M. et al. (2017). "Aerosols at the poles: an AeroCom Phase II multi-model evaluation." In: *Atmos. Chem. Phys.* 17, pp. 12197–12218.

Sassen, K. (1980). "Remote sensing of planar ice crystal fall attitudes." In: *J. Meteorol. Soc. Japan* 58.5, pp. 422–429.

Sassen, K. and J. R. Campbell (2001). "A midlatitude cirrus cloud climatology from the Facility for Atmospheric Remote Sensing. Part I: Macrophysical and synoptic properties." In: *J. Atmos. Sci.* 58.5, pp. 481–496.

Sassen, K. and B. S. Cho (1992). "Subvisual-thin cirrus lidar dataset for satellite verification and climatological research." In: *J. Appl. Meteorol.* 31.11, pp. 1275–1285.

Sassen, K. and J. M. Comstock (2001). "A Midlatitude Cirrus Cloud Climatology from the Facility for Atmospheric Remote Sensing. Part III: Radiative Properties." In: *J. Atmos. Sci.* 58.15, pp. 2113–2127.

Sassen, K., Z. Wang, and D. Liu (2008). "Global distribution of cirrus clouds from CloudSat/Cloud-Aerosol lidar and infrared pathfinder satellite observations (CALIPSO) measurements." In: *J. Geophys. Res. Atmos.* 113.D8.

Sassen, K. and J. Zhu (2009). "A global survey of CALIPSO linear depolarization ratios in ice clouds: Initial findings." In: *J. Geophys. Res. Atmos.* 114.D4.

Schmale, J. et al. (2018). "Local Arctic air pollution: A neglected but serious problem." In: *Earth's Future* 6.10, pp. 1385–1412.

Schmeisser, L. et al. (2018). "Seasonality of aerosol optical properties in the Arctic." In: *Atmos. Chem. and Phys.* 18.16, pp. 11599–11622.

Seinfeld, J. H. and S. N. Pandis (2016). *Atmospheric Chemistry and Physics: from air pollution to climate change*. John Wiley & Sons.

Serreze, M. C. and R. G. Barry (2011). "Processes and impacts of Arctic amplification: A research synthesis." In: *Glob. Planet. Change* 77.1-2, pp. 85–96.

Shettle, E. P. and R. W. Fenn (1979). *Models for the aerosols of the lower atmosphere and the effects of humidity variations on their optical properties*. Vol. 79. 214. Air Force Geophysics Laboratory, Air Force Systems Command, United States.

Shibata, T. et al. (2018). "Seasonal Variations in High Arctic Free Tropospheric Aerosols Over Ny-Ålesund, Svalbard, Observed by Ground-Based Lidar." In: *J. Geophys. Res. Atmos.* 123.21, pp. 12–353.

Shupe, M. D. (2011). "Clouds at Arctic atmospheric observatories. Part II: Thermodynamic phase characteristics." In: *J. Appl. Meteorol. Climatol.* 50.3, pp. 645–661.

Sicard, M. et al. (2020). "Calculation of the Overlap Function and Associated Error of an Elastic Lidar or a Ceilometer: Cross-Comparison with a Cooperative Overlap-Corrected System." In: *Sensors* 20.21, p. 6312.

Sinnhuber, B. M. et al. (2009). "The contribution of anthropogenic bromine emissions to past stratospheric ozone trends: a modelling study." In: *Atmos. Chem. Phys.* 9.8, pp. 2863–2871.

Sprenger, M. and H. Wernli (2015). "The LAGRANTO Lagrangian analysis tool–version 2.0." In: *Geosci. Model Dev.* 8.8, pp. 2569–2586.

Stachlewska, I. S. et al. (2010). "AMALi the Airborne Mobile Aerosol Lidar for Arctic research." In: *Atmos. Chem. Phys.* 10, pp. 2947–2963.

Stock, M. et al. (2012). "Springtime Arctic aerosol: Smoke versus haze, a case study for March 2008." In: *Atmos. Environ.* 52, pp. 48–55.

Stohl, A. (2006). "Characteristics of atmospheric transport into the Arctic troposphere." In: *J. Geophys. Res. Atmos.* 111.D11.

Sunilkumar, S. V. and K Parameswaran (2005). "Temperature dependence of tropical cirrus properties and radiative effects." In: *J. Geophys. Res. Atmos.* 110.D13.

Tesche, M. et al. (2009). "Vertically resolved separation of dust and smoke over Cape Verde using multiwavelength Raman and polarization lidars during Saharan Mineral Dust Experiment 2008." In: *J. Geophys. Res. Atmos.* 114.D13.

Tesche, M. et al. (2014). "Reconciling aerosol light extinction measurements from spaceborne lidar observations and in situ measurements in the Arctic." In: *Atmos. Chem. Phys.* 14.15, pp. 7869–7882.

Toon, O. B., James B Pollack, and Bishun N Khare (1976). "The optical constants of several atmospheric aerosol species: Ammonium sulfate, aluminum oxide, and sodium chloride." In: *J. Geophys. Res.* 81.33, pp. 5733–5748.

Tunved, P., J. Ström, and R. Krejci (2013). "Arctic aerosol life cycle: linking aerosol size distributions observed between 2000 and 2010 with air mass transport and precipitation at Zeppelin station, Ny-Å lesund, Svalbard." In: *Atmos. Chem. Phys.* 13.7.

Twomey, S. (1977). "The influence of pollution on the shortwave albedo of clouds." In: *J. Atmos. Sci.* 34.7, pp. 1149–1152.

Udisti, R. et al. (2016). "Sulfate source apportionment in the Ny-Ålesund (Svalbard Islands) Arctic aerosol." In: *Rend. Lincei* 27.1, pp. 85–94.

Urbanek, B. et al. (2018). "High depolarization ratios of naturally occurring cirrus clouds near air traffic regions over Europe." In: *Geophys. Res. Lett.* 45.23, pp. 13–166.

Voudouri, K. A. et al. (2020). "Variability in cirrus cloud properties using a Polly^{XT} Raman lidar over high and tropical latitudes." In: *Atmos. Chem. Phys.* 20.7, pp. 4427–4444.

WMO (1957). "Meteorology—A three-dimensional science: Second session of the commission for aerology." In: *WMO Bull.* 4.4, pp. 134–138.

Walczowski, W. and J. Piechura (2011). "Influence of the West Spitsbergen Current on the local climate." In: *Int. J. Climatol.* 31.7, pp. 1088–1093.

Wandinger, U. (1998). "Multiple-scattering influence on extinction- and backscatter-coefficient measurements with Raman and high-spectral-resolution lidars." In: *Appl. Opt.* 37.3, pp. 417–427.

Wang, D. et al. (2020). "Variability of the Boundary Layer Over an Urban Continental Site Based on 10 Years of Active Remote Sensing Observations in Warsaw." In: *Remote Sens.* 12.2, p. 340. DOI: 10.3390/rs12020340.

Wang, W. et al. (2020). "Characteristics and Seasonal Variations of Cirrus Clouds from Polarization Lidar Observations at a 30° N Plain Site." In: *Remote Sens.* 12.23, p. 3998.

Wang, Z. and K. Sassen (2002). "Cirrus Cloud Microphysical Property Retrieval Using Lidar and Radar Measurements. Part II: Midlatitude Cirrus Microphysical and Radiative Properties." In: *J Atmos. Sci.* 59.14, pp. 2291–2302.

Warneke, C. et al. (2009). "Biomass burning in Siberia and Kazakhstan as an important source for haze over the Alaskan Arctic in April 2008." In: *Geophys. Res. Lett.* 36.2.

Weitkamp, C. (2006). *Lidar: range-resolved optical remote sensing of the atmosphere*. Vol. 102. Springer Science & Business.

Wendisch, M. et al. (2017). "Understanding causes and effects of rapid warming in the Arctic." In: *Eos* 98.

Wernli, H. and H. C. Davies (1997). "A Lagrangian-based analysis of extratropical cyclones. I: The method and some applications." In: *Q. J. R. Meteorol. Soc.* 123.538, pp. 467–489.

Willis, M. D., W. R. Leaitch, and J. PD. Abbatt (2018). "Processes controlling the composition and abundance of Arctic aerosol." In: *Rev. Geophys.* 56.4, pp. 621–671.

Winker, D. M. et al. (2009). "Overview of the CALIPSO Mission and CALIOP Data Processing Algorithms." In: *J. Atmos. Ocean. Technol.* 26.11, pp. 2310–2323. ISSN: 0739-0572. DOI: 10.1175/2009JTECHA1281.1.

Winker, D. M. et al. (2013). "The global 3-D distribution of tropospheric aerosols as characterized by CALIOP." In: *Atmos. Chem. Phys.* 13.6, pp. 3345–3361.

Young, S. A. et al. (2018). "Extinction and optical depth retrievals for CALIPSO's Version 4 data release." In: *Atmos. Meas. Tech.* 11.10, pp. 5701–5727.

Zielinski, T. et al. (2020). "Study of chemical and optical properties of biomass burning aerosols during long-range transport events toward the arctic in summer 2017." In: *Atmosphere* 11.1, p. 84.

Zou, L. et al. (2020). "Revisiting global satellite observations of stratospheric cirrus clouds." In: *Atmos. Chem. Phys.* 20.16, pp. 9939–9959.

Zwaaftink, C.D. G. et al. (2016). "Substantial contribution of northern high-latitude sources to mineral dust in the Arctic." In: *J. Geophys. Res. Atmos.* 121.22, pp. 13–678.